Machine learning-based design and techno-economic assessments of adsorption processes for CO_2 capture

by

Sai Gokul Subraveti

A thesis submitted in partial fulfillment of the requirements for the degree of

Doctor of Philosophy

in

Chemical Engineering

Department of Chemical and Materials Engineering
University of Alberta

Abstract

Cyclic adsorption processes are widely considered for various industrial gas separations, including CO_2 capture. The flexibility to configure a variety of process cycles is an attractive process design feature of these processes. Despite such flexibility for process design, computationally expensive and time-consuming mathematical models used to simulate and optimize cyclic adsorption processes often limit the design to few cycle configurations. Moreover, the potential of adsorption processes for CO_2 capture is often poorly understood due to the lack of reliable techno-economic assessments. This thesis focuses on developing models of varying complexity to advance the understanding of adsorption processes for CO_2 capture.

In the first part of the thesis, viable machine learning models are developed to simulate and optimize pressure swing adsorption (PSA) and vacuum swing adsorption (VSA) processes for CO_2 capture. To this end, two hybrid optimization approaches that incorporate techniques such as artificial neural networks, partial least squares regression are proposed to accelerate the computational speeds of multi-objective optimization for a fixed PSA cycle ten times. Next, physics-based deep neural network methodology is developed to synthesize and simulate vacuum swing adsorption (VSA) processes. As a first step, a simple chromatography system is considered where the neural network model is developed to simulate the spatiotemporal dynamics of generic pulse injections in chromatography columns. In neural network training, residuals of governing partial differential equations are incorporated into the loss function. As a result, the learning process required only small amounts of training data due to the addi-

tional knowledge of physics. The results showed that the neural network predictions of column dynamics for an arbitrary pulse injection were remarkably accurate. Following this, the framework is extended to synthesize and simulate VSA cycles. Here individual neural networks are trained to learn the spatiotemporal dynamics of each constituent step. For training the models, conservation laws of mass and momentum are incorporated into the loss function. The results demonstrated that neural networks were capable of synthesizing and simulating four different VSA cycles.

The second part of the thesis focuses on developing a rigorous techno-economic optimization model for the systematic design of PVSA processes for CO_2 capture. The methodology incorporated a detailed process model, vacuum pump dynamics, rational scale-up, and cost model consistent with best practices, combined with a stochastic optimization routine to optimize process variables for determining the minimum CO_2 avoided cost. This methodology was first applied to post-combustion CO_2 capture from steam methane reformer flue gas by considering a four-step VSA process and three different adsorbents: Zeolite 13X and metal-organic frameworks, UTSA-16 and IISERP MOF2. The results showed that the four-step VSA process with IISERP MOF2 performed the best among the adsorbents considered; however, it still obtained 10% higher CO_2 avoided cost compared to the baseline monoethanolamine (MEA) based absorption process. Finally, the techno-economic optimization methodology is extended to optimize both adsorbent and process variables to determine the lowest possible CO_2 avoided costs of two PVSA cycles, namely, four-step and six-step dual reflux cycles. The techno-economic investigation is carried out at different flue gas flow rates and CO_2 compositions to identify the potential of adsorption processes for post-combustion CO_2 capture. Compared to MEA based absorption process, PVSA is attractive for flue gas streams with high CO_2 compositions $\geq$7.5%. The ideal adsorbents needed to achieve the cost limits have fairly linear CO_2 adsorption isotherms and zero N_2 adsorption.

Preface

The goal of the thesis deals with developing models to advance the understanding of cycle adsorption processes. The research conducted herein was mainly funded by Canada First Research Excellence Fund through the University of Alberta's Future Energy Systems. The second part of the thesis resulted from the collaborative effort between the University of Alberta and SINTEF Energy Research, Norway, with additional funding from the Norwegian CCS Research Centre. Compute Canada supported computations performed in the second part of the thesis. This thesis is written in a paper-based format; thus, several minor repetitions among the chapters are possible. A. Rajendran, V. Prasad, and Z. Li were the supervisory authors, and they were involved in conceptualization, methodology, and manuscript composition.

Chapter 2 of this thesis is published as: S. G. Subraveti, Z. Li, V. Prasad, A. Rajendran, Machine learning-based multiobjective optimization of pressure swing adsorption. *Ind. Eng. Chem. Res.* 2019, 58, 20412–20422. In this paper, Sai Gokul Subraveti was responsible for methodology, formal analysis, and writing the original draft of the manuscript.

Chapter 3 of this thesis will be submitted as: S. G. Subraveti, Z. Li, V. Prasad, A. Rajendran, Physics-based deep neural networks for simulation and optimization of chromatographic separations. Sai Gokul Subraveti was responsible for methodology, formal analysis, and writing the original draft of the manuscript.

Chapter 4 of this thesis will be submitted as two papers: S. G. Subraveti, Z. Li, V. Prasad, A. Rajendran, Physics-based deep neural networks for modelling cyclic ad-

sorption processes; and S. G. Subraveti, Z. Li, V. Prasad, A. Rajendran, Physics-based deep neural networks for cycle synthesis of cyclic adsorption processes. For the two papers, Sai Gokul Subraveti, was responsible for methodology, formal analysis, and writing the original draft of the manuscript.

Chapter 5 of this thesis is published as: S. G. Subraveti, S. Roussanaly, R. Anantharaman, L. Riboldi, A. Rajendran, Techno-economic assessment of optimised vacuum swing adsorption for post-combustion CO_2 capture from steam-methane reformer flue gas. *Sep. Purif. Technol.* 2021, 256, 117832. Sai Gokul Subraveti was responsible for methodology, formal analysis, and writing the original draft of the manuscript. S. Roussanaly assisted in developing the methodology by providing relevant cost functions. R. Anantharaman and L. Riboldi were involved in the methodology and the manuscript composition.

Chapter 6 of this thesis is accepted for publication as: S. G. Subraveti, S. Roussanaly, R. Anantharaman, L. Riboldi, A. Rajendran, How much can novel solid sorbents reduce the cost of post-combustion CO_2 capture? A techno-economic investigation on the cost limits of pressure-vacuum swing adsorption. *Appl. Energy*. Sai Gokul Subraveti was responsible for methodology, formal analysis, and writing the original draft of the manuscript. S. Roussanaly, R. Anantharaman, and L. Riboldi were involved in the manuscript composition.

To my parents

Acknowledgements

I express my profound gratitude to Dr. Arvind Rajendran, Dr. Vinay Prasad, and Dr. Zukui Li for presenting me with the opportunity to pursue doctoral studies under their supervision. Their insightful guidance and continual encouragement to explore new ideas pushed me to pursue different frontiers of research. The individual and group meetings have been a great learning platform to hone my skills holistically as a researcher. I am also grateful for numerous opportunities that came my way, which otherwise would not have been possible without their support. I have thoroughly enjoyed my doctoral studies under their supervision.

My sincere thanks to Mr. Simon Roussanaly, Dr. Rahul Anantharaman, and Dr. Luca Riboldi at SINTEF Energy Research for helping me transition smoothly during my research stay in Trondheim. Their valuable insights and guidance on techno-economic assessments have greatly contributed to the second part of this thesis. The discussions with other researchers at SINTEF Energy Research have helped me broaden my understanding of CCS. I also thank them for the delicious Thursday lunches.

I acknowledge the University of Alberta's Future Energy Systems (FES) funding through the Canada First Research Excellence Fund to support my doctoral studies. I also thank the Norwegian CCS Research Centre for financially supporting my research stay at SINTEF Energy Research. Thanks to Compute Canada for the resources to carry out heavy computations.

The thriving work environment I experienced was mainly because of my former and current colleagues, Bhubesh, Gywn, Jim, Lauren, Libardo, Nagesh, Nick, Rafael,

Ravi, Tai, Vishal, and Yoga. The lunch break discussions and playing Catan were memorable for me. Research visits and conference trips were exciting with Nagesh, Nick, and Tai. Thank you, Anjana, for patiently teaching me the concepts of RNN and many other things. I appreciate your support and collaboration. Advising the three summer students in my doctoral studies has been a rich experience to develop my supervisory skills.

I want to thank all my friends for giving me wonderful memories over the years. Sanat and Krishna have been amazing roommates in Edmonton. My Norwegian roommates, Even, Jørgen, and Nora, made my stay in Trondheim enjoyable, especially playing squash with Even and Jørgen was super fun. Special thanks to Ashwin for being a generous host in Zurich. All the trips with my friend Bhargav were incredible.

None of this would have been possible without the support and encouragement from my parents. I thank them for their love, trust, patience, and kindness. My brother Nikhil always pushes me to transcend my goals to newer heights. He has diligently supported me in my doctoral journey.

Table of Contents

List of Tables

List of Figures

Chapter 1

Introduction

1.1 Cyclic adsorption processes

Separation and purification of gaseous mixtures using cyclic adsorption processes are employed for many industrial applications such as gas drying [1], hydrogen purification [2, 3], air separation [4, 5], removal of impurities from gases [6], and hydrocarbon separations [7, 8]. Particularly for gas separations, cyclic adsorption processes have emerged as economic alternatives to conventional cryogenic distillation [9]. Most recently, these processes have been studied extensively for carbon dioxide capture applications [10]. From a perspective of process design, adsorption processes have more flexibility compared to other separation techniques such as distillation, absorption, etc., because of an additional degree of freedom that arises from the modular nature of the process.

The underlying principle of cyclic adsorption processes involves the molecules from the gas-phase adsorb onto the solid (adsorbent) upon contact. Since the thermodynamic interactions between the gas phase and the adsorbent depend on the type of gas molecules and the adsorbent surface selected, the difference in the affinities of the gas mixture components is usually the driving force for separation. If one of the gas mixture components has a high affinity (or stronger thermodynamic interactions) towards the adsorbent, it is usually the strongly adsorbing or the heavy component. The component with weak affinity is usually the light component in the process.

Cyclic adsorption processes typically operated in one or more fixed-beds alternate between two modes of operation: 1) adsorption, where the gas mixture that needs to be separated is introduced as feed into the adsorbent bed, and the feed mixture is separated by the preferential adsorption of the strongly adsorbing component whereas the weakly adsorbing component passes through the adsorbent bed; 2) desorption, where the adsorbent bed undergoes regeneration by varying pressure or temperature, etc. Depending on the bed regeneration strategies, several processes such as pressure swing adsorption (PSA), vacuum swing adsorption (VSA), temperature swing adsorption (TSA), temperature-vacuum swing adsorption (TVSA), concentration swing adsorption (CSA), electric swing adsorption (ESA), microwave swing adsorption (MSA), etc. can be realized. For instance, Fig. 1.1 illustrates the concept involved in PSA/VSA processes using an adsorption isotherm. An adsorption isotherm relates the gas phase and the solid phase concentrations at equilibrium. The gas component adsorbs at pressure P_{ADS} onto the adsorbent in the adsorption step, and the corresponding equilibrium solid-phase concentration (or loading) is q_{ADS}. For regenerating the bed, a desorption step is carried out to remove the adsorbed gas component from the adsorbent by utilizing the pressure swing. Since the adsorbent has a low capacity for the gas component at lower pressures than P_{ADS}, the pressure is reduced to extract the gas component from the adsorbent bed. It is worth noting that adsorption is generally exothermic, while regeneration is endothermic.

Cyclic adsorption processes for industrial applications can be used to achieve two types of separations. First, the undesired components in the gas mixture strongly adsorb onto the adsorbent, and the desired product is a weakly adsorbing component. The light product is typically collected in the adsorption step. The design and optimization of processes to obtain high purity and high recovery of the light product have been well studied and commercialized, e.g. air separation, H_2 purification, etc. Second, the desired product strongly adsorbs, and the unwanted components weakly adsorb.

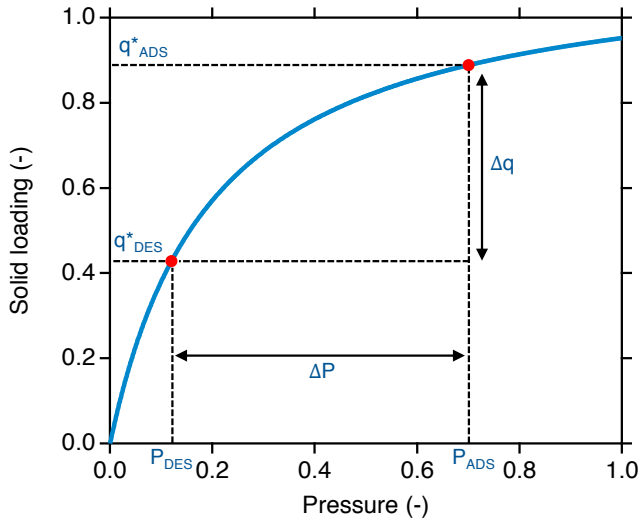

Figure 1.1: Concept of PSA/VSA processes.

Here, the heavy product is collected in the desorption step as the extract, e.g. CO_2 capture. The design and optimization of processes for the heavy product separation are still nascent and have recently gained attention for commercial implementation [11].

The purpose of this thesis is to address some key challenges involved in the design and optimization of cyclic adsorption processes, particularly for the application of CO_2 capture. This introductory chapter aims to:

- present an overview of process design and optimization strategies of cyclic adsorption processes
- provide a general introduction to CO_2 capture and the scope of adsorption processes for CO_2 capture, and
- highlight the key challenges and knowledge gaps leading to objectives of the thesis

1.2 Process design of cyclic adsorption processes

Unlike distillation and absorption, which operate under steady-state conditions, the cyclic adsorption processes are transient in nature. Steady-state operations are gov-

erned by ordinary differential equations (ODEs), where the relation between the operating variables and the process performance indicators is established by simply integrating the ODEs. However, transient systems like cyclic adsorption processes are dictated by the set of nonlinear partial differential equations (PDEs) resulting from mass, momentum and energy balances along with adsorption equilibria. Obtaining the relation between the operating variables and the process performance indicators for PDE governed systems is not straightforward [12]. Moreover, these processes undergo several steps and operate at a cyclic steady state (CSS). Therefore, designing these processes requires solving the detailed mathematical models based on nonlinear PDEs repeatedly until CCS. The key process performance indicators are then calculated based on the transient profiles of state variables (composition, pressure and temperature) at the CSS. Further, the modular nature of cyclic adsorption processes allows for flexibility in tuning several operating conditions and design parameters. Hence, process design also involves optimizing several decision (or design) variables for determining the best performance of the process.

1.2.1 Optimization of cyclic adsorption processes

Since the optimal design variables are not known a priori, the rigorous process models are often coupled with the optimization routines. The transient, cyclic nature and CSS criterion make the optimization of cyclic adsorption processes complex and challenging. Several approaches were proposed to develop optimization routines for these processes [9]. In the equation-oriented approach [13–15], the PDEs are completely discretized in time and space. The resulting large number of algebraic equations coupled with the objective functions and constraints are solved using a non-linear optimization solver. This approach resulted in 30000 - 50000 optimization variables, making optimization challenging [9]. Alternatively, the simultaneous tailored approach [16] involves incorporating the CSS condition as a constraint while optimizing design vari-

ables and initial states. Here the CSS condition is guaranteed only at the optimal point, saving computational efforts for other points [9].

Finally, in the commonly used black-box approaches [17–20], the optimizer selects a set of decision variables for every trial point. The objective functions and constraints are calculated based on the rigorous process models at the CSS condition. The objective function evaluations are returned to the optimizer, and based on this information, it takes a new search direction [9]. The detailed PSA model runs inside an inner loop each time the optimizer calls the black-box function. Although black-box approaches are computationally expensive, global search methods such as non-dominated sorting genetic algorithms (NSGA) are widely used for single [21] or multi-objective [19, 22–25] optimization problems.

1.3 Applications for CO_2 capture

An increase in atmospheric CO_2 concentration levels over the years has led to global warming and climate change [26]. In the sixth assessment report, the Intergovernmental Panel on Climate Change (IPCC) considered various emission scenarios limiting global warming to 1.5 °C [26]. To meet this target, it is necessary to achieve net-zero CO_2 emissions by mid-century [27]. The decarbonization of global energy and industrial sectors is essential for achieving climate goals. Carbon dioxide capture and storage (CCS) remains promising for mitigating CO_2 emissions from these sectors in the near future and long term [28]. CCS involves capturing the CO_2 emitted from point sources (e.g. flue gas in power generation) or directly from air (direct air capture). The captured CO_2 is compressed to a dense phase for transporting to a geological storage site.

There are several technological options for capturing CO_2 from point sources: post-combustion capture, pre-combustion capture and oxy-fuel combustion. In post-combustion capture, CO_2 from flue gases produced by the combustion of fossil fuels is concentrated

from 3.5-30% to over 95%, usually at atmospheric pressures. The post-combustion technology is mature and has been commercialized. The pre-combustion capture involves separating CO_2 from syngas produced by the combustion of fuel with air or oxygen at high pressures (10 - 50 bar). The clean syngas is later used as fuel to generate electricity. Pre-combustion technologies have gained tremendous attention with an increased interest in a hydrogen economy. Oxy-fuel combustion involves the separation of nitrogen from the air, followed by the combustion of coal in pure oxygen. In this type of combustion, the flue gas stream comprises 70-85% of CO_2 and the remaining H_2O. Several factors such as CO_2 composition, pressure, the flow rate of the CO_2-containing stream, system-level integration aspects etc. determine the feasibility of CSS deployment in energy and industry sectors [29]. For example, post-combustion CO_2 capture can be retrofitted into existing chemical/power plants in a rather straightforward manner without restructuring the plant layout and has been identified as one of the viable technologies in the short- to medium-term [30].

Adsorption-based processes have emerged as an attractive technology for CO_2 capture for their applicability over a wide range of temperatures and pressures [10]. The potential applications of cyclic adsorption processes are explored in each of the CO_2 capture technologies: post-combustion CO_2 capture, pre-combustion CO_2 capture, and oxy-fuel combustion. For instance, the VSA technology was commercially demonstrated for CO_2 capture from syngas in an SMR-based plant at Valero Port Arthur Refinery (Texas, USA) [31]. However, the bottleneck for the successful commercialization of any technology is the associated energy penalty and cost expenditure for capturing CO_2. Major improvements have been made to develop adsorption technology for CO_2 capture [10]. Adsorbents are one of the key factors for determining the performance of cyclic adsorption processes. To this end, significant efforts have been directed to develop different types of adsorbents for CO_2 capture. Among them, activated carbons, zeolites are the commercially used adsorbents. Activated carbons exhibit high adsorp-

tion capacities at higher pressures and are preferred for pre-combustion CO_2 capture [25, 32, 33]. Zeolites are microporous crystalline aluminosilicates extensively studied for CO_2 capture because of their ability to separate CO_2 based on the molecular sieving effect and the strong interactions between CO_2 and alkali-metal cations [34]. Particularly, numerous studies were carried out on the current benchmark material, Zeolite 13X, for CO_2 capture [19, 35–38]. Moreover, recent developments in material science have allowed material chemists to discover several new classes of adsorbents, such as metal-organic frameworks (MOFs), covalent-organic frameworks (COFs), etc., that can be highly tuned for a variety of gas separations [30]. Each class usually consists of hundreds of thousands of materials, including both real and hypothetical structures.

The design of cyclic adsorption processes for recovering the heavy product such as CO_2 is an active topic of ongoing research. Several cycle configurations have been proposed for CO_2 capture. While most of the configurations designed and optimized for the operating conditions are based on heuristics [22, 25, 39–45], a superstructure approach was also proposed to optimize both the cycle configuration and the operating conditions simultaneously [18, 46]. Although not an exhaustive review, few relevant studies are discussed here. Reynolds et al. [39] evaluated nine different PSA cycles with heavy reflux steps for post-combustion CO_2 capture from stack and flue gas at a high temperature (575 K). A 5-bed 5-step cycle containing heavy and light reflux steps yielded the best separation performance. Agarwal et al. [18] demonstrated a superstructured-based optimal synthesis of PSA cycles for post-combustion CO_2 capture. Using this approach, a 2-bed 8-step PSA cycle with pressure equalization and heavy reflux steps gave low power consumption while achieving high CO_2 recovery and CO_2 purity. Haghpanah et al. developed and optimized six different VSA cycle configurations for post-combustion CO_2 capture. A four-step VSA cycle with countercurrent light product pressurization yielded the lowest energy consumption for given CO_2 recovery and CO_2 purity constraints. Joss et al. [43] developed four TSA cycles

for post-combustion CO_2 capture with comparable regeneration energies to solvent-based processes. Khurana and Farooq proposed a six-step VSA cycle with dual reflux steps to overcome the deep vacuum and low productivity limitations in single-stage VSA cycles. On the other hand, Casas et al. [22] developed and optimized PSA cycles with pressure equalization steps to achieve high CO_2 purity and CO_2 recovery for pre-combustion CO_2 capture. Subraveti et al. [25] proposed and optimized three PSA cycles with steam purge to achieve low energy and high productivity while achieving CO_2 purity and CO_2 recovery requirements for pre-combustion CO_2 capture.

1.4 Motivation

Computational challenges in process design. Despite such a rapid growth of this separation technique for many practical applications, there are still inherent challenges associated with process design that need to be overcome to promote innovations in adsorption process technology. For instance, detailed mathematical models are often required to design cyclic adsorption processes with the accuracy and reliability needed for industrial applications. As previously mentioned, process simulations based on these rigorous models require solving the set of nonlinear PDEs repeatedly in time and space until the process reaches CSS. Typically, the CSS criterion in one simulation is achieved after simulating the process for hundreds of cycles. Hence, adsorption process simulations are computationally intensive. Moreover, process design involves optimizing design variables that yield the best process performance, where thousands of process simulations are carried out. Given that the process undergoes several sequence of steps in one or more fixed-beds (with or without interactions), this modular nature allows configuring different processes by altering the sequence of steps or interactions among the fixed-beds. Despite such flexibility available for process design, the computational burden of designing and optimizing each process configuration limited the design to few process configurations for practical applications [25, 40]. Since

a successful adsorptive gas separation process is generally an optimum combination of adsorbent and process design [1], the selection of suitable adsorbents and the right process is crucial for assessing the potential of adsorptive gas separations. With the recent discovery of hundreds of thousands of adsorbents for gas separations [30], the current simulation tools based on rigorous mathematical models are computationally inadequate to handle several thousands of combinations of adsorbents and processes for process design and evaluation.

Techno-economic feasibility. Although adsorption technology for light component separations is commercialized, adsorption processes for CO_2 capture are still in the R&D stage [10]. To promote commercial interest, assessments of technical viability and process economics are essential to determine the potential of adsorption technology for CO_2 capture. While several studies demonstrated the technical viability of this technology [22, 25, 35, 41, 43, 44, 47], the scarcity of techno-economic analyses and system-level integrated process studies resulted in knowledge gaps in the economic feasibility of adsorption processes for CO_2 capture. Techno-economic assessments play a significant role in comparing various technologies, evaluating the complexities associated with process scale-up, guiding adsorbents/processes selection in the early stages of process design. While few techno-economic analyzes have been carried out previously [21, 48–51], a wide range of financial parameters were used for cost estimations, making the comparison of adsorption processes with other technologies challenging. Therefore, a detailed techno-economic model based on established financial guidelines together with accurate and reliable adsorption process design is absolutely necessary for comparing the cost performance of adsorption processes with other capture technologies.

1.5 Objectives

One of the ways forward to overcome the computational burden of simulating cyclic adsorption processes using rigorous mathematical models is to develop simplified faster models so that the process features and the accuracy are not lost. The latest groundbreaking advances in modern data science techniques like machine learning opened up a new paradigm of modelling physical systems in science and engineering through surrogates as faster approximations to rigorous mathematical models. The first part of this thesis leverages the recent developments in machine learning to develop viable methodologies for modelling and optimizing cyclic adsorption processes. With this new alternative to rigorous process modelling, the following systematic studies are carried out:

- Two hybrid approaches incorporating machine learning methods into optimization routines are proposed to accelerate the process optimization of a fixed cycle configuration for the case of pre-combustion CO_2 capture
- A modern physics-based deep learning framework is developed for simulating physical phenomena characterized by adsorption equilibria where deep neural networks are trained to learn the underlying PDEs
- The physics-based deep learning models are first implemented for simpler systems such as chromatography to simulate spatiotemporal dynamics of generic pulse injections in chromatography columns
- The physics-based deep learning modelling is extended to construct and simulate cyclic adsorption processes for post-combustion CO_2 capture
- Finally, cycle synthesis capabilities of physics-based deep learning methodology are demonstrated for the case of post-combustion CO_2 capture

The second part of the thesis aims to develop a rigorous techno-economic optimization methodology for the systematic design of P/VSA processes for post-combustion CO_2 capture. The techno-economic model developed herein obeys both technical and economic recommendations for adsorption processes and is consistent with best practices to obtain reliable cost values for comparing with other CO_2 capture technologies. The following studies are carried out based on the techno-economic model:

- Assessed the techno-economic performance of optimized VSA process for post-combustion CO_2 capture from steam methane reformer dried flue gas
- A techno-economic investigation is carried out to determine the cost limits of PVSA processes for post-combustion CO_2 capture to evaluate the potential of adsorptive CO_2 capture

1.6 Structure of the thesis

The thesis is structured in two parts. The first part of the thesis, titled *Machine learning* (Chapters 2 to 4), deals with machine learning applications. The second part of the thesis, titled *Techno-economic assessments* (Chapters 5 to 6), focuses on techno-economic assessments for post-combustion CO_2 capture.

Chapter 2 focuses on developing two different hybrid approaches that incorporate machine learning methods into process optimization routines for accelerating the computational speeds of process optimization. The accuracy, robustness, and reliability of these approaches are tested by considering a complex eight-step PSA process for pre-combustion CO_2 capture.

In Chapter 3, a deep learning framework that incorporates underlying governing laws of physics to learn the spatiotemporal dynamics of generic pulse injections in chromatography columns is proposed. The framework's effectiveness is demonstrated by validating the predicted results with detailed model simulations.

Chapter 4 deals with developing physics-based deep learning models to construct and simulate cyclic adsorption processes. Individual models are trained for each constituent step in cyclic adsorption processes to learn the spatiotemporal solutions of state variables while obeying the underlying conservation laws of mass and momentum. The proposed methodology is first tested on the four-step VSA cycle for post-combustion CO_2 capture. Next, the ability of physics-based deep learning models to synthesize and simulate different cyclic adsorption processes is explored. The predictive capabilities of this approach are demonstrated by constructing four VSA cycles for post-combustion CO_2 capture and validating the results produced with the detailed process model.

In Chapter 5, a rigorous techno-economic optimization methodology is developed to systematically design P/VSA processes for post-combustion CO_2 capture. The techno-economic model incorporates both the latest improvements in process modelling and the best practices for costing CCS systems. Based on this model, techno-economic assessments are carried out to determine the CO_2 avoided costs of the optimized four-step VSA cycle for post-combustion CO_2 capture from steam methane reformer flue gas.

Chapter 6 extends the techno-economic optimization model to simultaneously optimize both adsorbent and process variables to determine the cost limits of PVSA processes for post-combustion CO_2 capture. The potential of adsorptive CO_2 capture is assessed by identifying the cost limits for different industrial flue gas CO_2 compositions and flow rates and comparing them with the cost performances of solvent-based CO_2 capture.

Finally, Chapter 7 summarizes the key findings of this thesis and provides ways forward for future research that could lead to potential improvements.

Chapters 2 to 6 are standalone works and are presented in a complete form with required definitions wherever deemed necessary.

Part I

Machine learning

Chapter 2

Machine learning-based multi-objective optimization of pressure swing adsorption

2.1 Introduction

Pressure-swing adsorption (PSA) processes are widely employed for a variety of industrial gas separations [1, 2, 4, 5, 7, 8] owing to their flexibility in operation and the ability to achieve high separation trade-offs [1, 52]. The inherent feature of PSA is the cyclic mode of operation between preferential adsorption of one or more gases in a gaseous mixture at high pressures and regeneration at low pressures. To this end, fixed-beds packed with a suitable adsorbent undergo a sequence of multiple steps such as adsorption, blowdown, feed pressurization, etc., to realize the PSA cycle. Such processes reach a cyclic steady state (CSS). As part of PSA modelling and optimization, a set of stiff nonlinear partial differential equations (PDEs) must be solved repeatedly in time and space until the system attains CSS. Owing to the modular nature of PSA processes, various configurations (called "cycles") can be synthesized by constituting basic operational steps. Depending on the cycle, many decision variables can arise that have to be tuned to meet the separations goals. For this reason, the optimization of PSA

The results presented in this chapter have been reported in: S.G. Subraveti, Z. Li, V. Prasad, A. Rajendran. Machine learning-based multi-objective optimization of pressure swing adsorption. *Ind. Eng. Chem. Res.* **2019**, *58*, 44, 20412-20422.

processes is inherently complex. Further, hard constraints on separation trade-offs, e.g. product purity, recovery etc., make optimization more challenging.

PSA optimization has been a topic of interest over the years [13, 14, 16, 17, 19, 20, 46, 53]. In most cases, the PDEs are solved until CSS each time the optimizer calls for objective function evaluations. Therefore, obtaining solutions to the dynamic optimization problem is computationally demanding since several PSA simulations are required. Over the past two decades, reduced-order or surrogate models have been considered for objective function calculations in PSA optimization [18, 48, 54–60]. Surrogate models are mathematical models constructed using statistical techniques and avoid the computational costs associated with expensive PSA simulations, thereby improving the convergence speeds of PSA optimization routines [9]. To this end, kriging-based algorithms [57, 58, 60] and artificial neural networks [54, 55, 59] have been reported for PSA design and optimization. Further, Agarwal et al. developed and incorporated a proper orthogonal decomposition-based reduced-order model into optimization routines [18]. When surrogate models are used for function evaluations, it is important to ensure that the chosen model converges to the global optimum or near the optimum of the detailed PSA model [61]. However, the accuracy of these models depends on factors such as the number of samples used and the position of samples in the design space. Although the performance of surrogate models can be improved with more samples, computational efforts significantly increase alongside, owing to the high dimensional design space. In the context of surrogate-based PSA optimization, an initial random sampling (e.g. Latin hypercube sampling) over the entire design space is first carried out; then, surrogate models are constructed based on those samples and incorporated into optimization routines. Previous work on constructing surrogate models based on efficient sampling strategies is minimal. Furthermore, research on integrating machine learning techniques with PSA optimization routines to reduce the dimensionality of the optimization problem is still nascent.

Recent advances in model-based engineering supported by modern data science techniques like machine learning accelerate the development of adsorption technology for gas separations [62]. So, the present chapter aims to address the issues of computational costs associated with PSA optimization by efficiently incorporating machine learning principles into the optimization routines. Two approaches, named surrogate-assisted optimization (*SOpt*) and dimensional reduction-based optimization (*DROpt*), are proposed in this chapter. The novelty of *SOpt* lies in the construction of surrogates based on the large number of samples accumulated during the optimization runs. The main advantage of this efficient sampling strategy is to guarantee the search direction for the optimization while spending minimal computational efforts on poor designs. In *DROpt*, data-based methods are utilized to reduce the dimensionality of the search space for improving the computational run-times of the PSA optimization. Further, dimensional reduction-based surrogate-assisted optimization (*DR-SOpt*), a third approach that is based on the combination of *DROpt* and *SOpt* is also considered.

The remainder of the chapter is organized as follows: Section 2.2 describes the case study considered in this chapter and also formulates the optimization problem. The modelling of the PSA process is explained in Section 2.3. Section 2.4 introduces the approaches proposed in the present chapter. Finally, the accuracy and reliability of these approaches are discussed in Section 2.5 by applying them to the case study considered.

2.2 Problem statement

The PSA optimization for carbon dioxide capture and storage is challenging owing to strict regulatory requirements for achieving high separation trade-offs, namely, CO_2 purity and recovery. To this end, a complex PSA process designed for pre-combustion CO_2 capture applications [25] was considered as a case study to apply the proposed optimization approaches. The PSA cycle aims to separate CO_2 and H_2 efficiently under pre-combustion CO_2 capture conditions [25]. The feed consists of a binary mixture

of 40 mol % CO_2 and 60 mol % H_2 at 34.5 bar and 240 °C. The process configuration comprises a high pressure *adsorption step* (where the separation occurs and light product H_2 is removed from the column), *two pressure equalization steps* (i.e. depressurization and pressurization via pressure equalization of two columns), a *counter-current blowdown* and a *steam purge* to remove the heavy product CO_2 from the column at low pressure, and *light-product pressurization* in order to pressurize the column back to high pressure. The process schematic is illustrated in Fig. 2.1. The adsorbent used for the PSA process is activated carbon which has been demonstrated to have high stability and good CO_2/H_2 selectivity [33]. The CO_2 and H_2 isotherms on activated carbon were expressed in terms of the Sips model and the related adsorption isotherm parameters used are those reported in the literature [25, 32]. The Sips isotherm model and the related parameters for CO_2 and H_2 are provided in Appendix B.

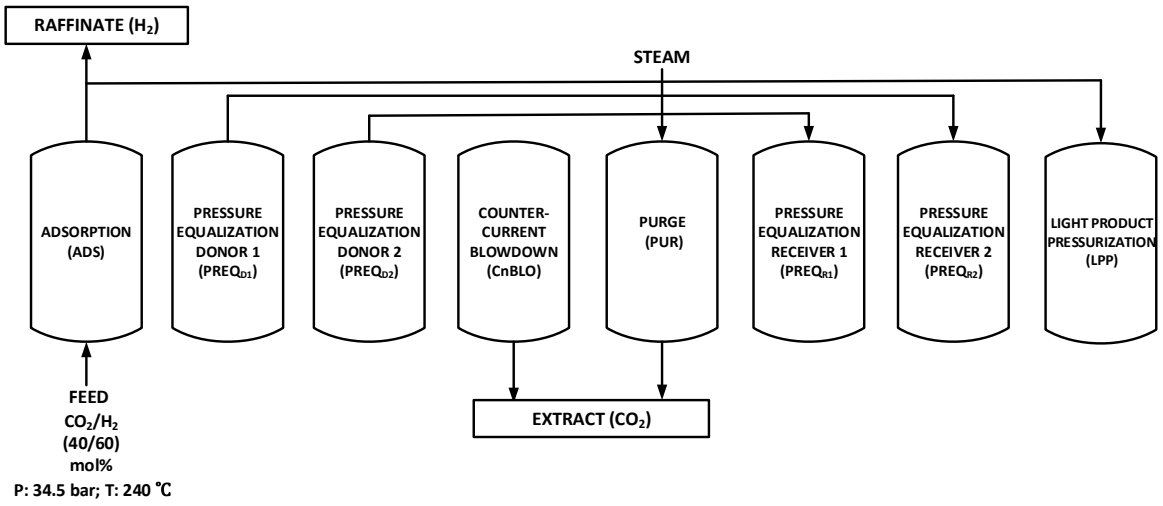

Figure 2.1: PSA cycle designed for pre-combustion CO_2 capture [25] used as the case study in this chapter.

Owing to the fact that cyclic adsorption processes feature multiple conflicting performance indicators, multi-objective optimization problems are formulated for PSA process optimization [20]. For the case study considered, it is important to identify the optimal design and operating variables for which the PSA process meets the US Department of Energy (US-DOE) requirements of 95% CO_2 purity and 90% recovery.

Therefore, a nonlinear multi-objective optimization problem was formulated as:

$$\begin{aligned} &\begin{cases} \max\limits_{x} & Pu \\ \max\limits_{x} & Re \end{cases} \\ &\text{subject to:} \quad lb \leq x \leq ub \\ &\qquad\qquad x \in \Re^n \end{aligned} \tag{2.1}$$

where

$$Pu, (\%) = \frac{\text{Total moles of } CO_2 \text{ in the extract product within one cycle}}{\text{Total moles of gas in the extract product within one cycle}} \times 100 \tag{2.2}$$

$$Re, (\%) = \frac{\text{Total moles of } CO_2 \text{ in the extract product within one cycle}}{\text{Total moles of } CO_2 \text{ fed into the column within one cycle}} \times 100 \tag{2.3}$$

x is a vector of decision variables that includes the adsorption step time (t_{ADS}), the first and second pressure equalization step times (t_{PREQ1} and t_{PREQ2}, respectively), the counter-current blowdown step time (t_{CnBLO}), the purge step time (t_{PUR}), the low pressure (P_{L}), the feed velocity (v_0) and the purge velocity (v_{PUR}). lb and ub are the lower and upper bounds on the decision variables x. Although t_{PREQ1} and t_{PREQ2} are not decision variables from a practical perspective, it is assumed in the simulations that they can be controlled independently. In this chapter, the column dimensions are fixed to those of the pilot-scale unit reported in a different study. Hence, the goal here was to demonstrate the use of surrogate modelling rather than to perform a comprehensive design of a new PSA unit. However, it is important to note that within the framework described in this chapter, other decision variables such as the column dimensions can be incorporated in a rather straightforward manner.

2.3 Adsorption process model

The mathematical model for simulating adsorption column dynamics consists of nonlinear PDEs obtained by solving mass, momentum, and energy balances. A detailed one-dimensional model developed in earlier work was used to simulate the PSA process [19]. The model assumes an axially dispersed plug flow to describe the bulk gas

flow through the column. No radial gradients were considered for concentration, temperature and pressure across the column. The model also assumes that the gas obeys ideal behaviour and an instantaneous thermal equilibrium between the gas and the solid. The adsorbent properties and bed voidage remain uniform throughout the column while heat transfer across the walls was considered. The model accounts for frictional pressure drop across the column using Darcy's law, and the solid phase mass transfer was described using a linear driving force (LDF) model. The model used in this chapter has been validated experimentally both at the lab-scale [47] and the pilot-scale [35]. The model equations and appropriate boundary conditions are provided in Appendix A.

The spatial terms in the PDEs were discretized into 30 finite volumes using the van-Leer flux limiter [19]. The resulting ordinary differential equations (ODEs) were solved using *ode23s*, a stiff solver in MATLAB. All simulations were performed assuming that a single bed undergoes all cycle steps in a sequence. The criterion for reaching CSS was when a mass balance error equal to 0.5% or less was observed for five consecutive cycles. The coupled cycle steps in the PSA cycle were solved by storing the stream information in data buffers. The model provided detailed gas phase, solid phase and temperature profiles across the column, which were essential for calculating performance indicators of a given PSA process. The simulation parameters are provided in Table 2.1. Note that the uni-bed approach has been used successfully in the literature to simulate the PSA process. In order to adopt the process for continuous operation, appropriate sequencing needs to be included. Such a sequencing might result in idle steps to ensure that at least one column in the system receives the feed.

Table 2.1: PSA simulation parameters used in the present chapter [25].

Parameter	Value
Column properties	
Length, L (m)	0.83
Outer radius, r_{o} (cm)	5.715
Inner radius, r_{i} (cm)	5.118
Particle radius, r_{p} (mm)	0.3
Bed voidage, ε (-)	0.4
Particle voidage, ε_{p} (-)	0.57
Physical properties	
Adsorbent density, ρ_{s} (kg m^{-3})	1361.00
Specific heat capacity of adsorbent, $C_{\mathrm{p,s}}$ (J kg^{-1} K^{-1})	1877.20
Specific heat capacity of gas phase, $C_{\mathrm{p,g}}$ (J kg^{-1} K^{-1})	1010.60
Molecular diffusivity, D_{m} (mm^2 s^{-1})	0.0481
Fluid viscosity, μ (cP)	0.0251
Effective gas thermal conductivity, K_{z} (J m^{-1} K^{-1} s^{-1})	0.09
Inside heat transfer coefficient, h_{in} (J m^{-2} K^{-1} s^{-1})	0
Outside heat transfer coefficient, h_{out} (J m^{-2} K^{-1} s^{-1})	2.5
Universal gas constant, R (m^3 Pa mol^{-1} K^{-1})	8.314
Mass transfer coefficient, CO_2, $k_{\mathrm{avg,CO_2}}$ (s^{-1})	0.53
Mass transfer coefficient, H_2, $k_{\mathrm{avg,H_2}}$ (s^{-1})	10
Heat of adsorption CO_2, $\Delta H_{\mathrm{CO_2}}$ (kJ mol^{-1})	20.5
Heat of adsorption H_2, $\Delta H_{\mathrm{H_2}}$ (kJ mol^{-1})	9.8 [32]
Operating parameters	
Syngas feed pressure P_{feed} (bar)	34.5
High pressure P_{H} (bar)	34.5
Feed composition (CO_2/H_2), y_{feed} (-)	0.4/0.6
Feed temperature, T_{feed} (°C)	240

2.4 Optimization approaches

2.4.1 Traditional optimization (TradOpt) framework

One of the ways to solve the multi-objective optimization problem described in Eq. 2.1 involves the implementation of global search methods, such as the non-dominated sorting genetic algorithm II (NSGA-II) coupled with detailed PSA models. This rigor-

ous methodology was successfully implemented for PSA optimization in several studies [19, 23, 40] and has been validated experimentally [47]. This is referred to as the traditional optimization (*TradOpt*) procedure in the present chapter. In *TradOpt*, the optimizer sends a population of decision variables to the detailed PSA model, which calculates and returns the objective functions. NSGA-II improves the population of individuals by mimicking the process of evolution. The result of this multi-objective optimization problem is the set of Pareto optimal solutions that represent the best trade-off between CO_2 purity and recovery.

The *TradOpt* procedure was implemented using MATLAB global optimization and parallelization toolboxes. Pareto solutions were generated based on all individuals evaluated during the optimization run. It should be noted that although this methodology is easy to implement, a large number of NSGA-II function evaluations using the detailed PSA model make it computationally expensive.

2.4.2 Surrogate-assisted optimization (SOpt)

In this approach, surrogate models replaced the computationally expensive detailed PSA model for function evaluations within NSGA-II optimization routines. Surrogates are alternate representations of the multivariate mapping structure of the input-output space constructed based on samples obtained either from experimental or simulation data. Surrogate models serve as faster approximations of PSA process metrics without solving PDEs repeatedly until the CSS condition is met. Therefore, coupling surrogate models with an optimization algorithm should reduce the computational costs significantly. Single or multiple surrogate models can be employed depending on the optimization problem. Many surrogate modelling methods have been studied for engineering design and optimization purposes [63–66]. Artificial neural networks (ANN), kriging, support vector regression (SVR) and response surface methods are the popular techniques. For the current chapter, artificial neural networks were chosen as global

surrogate models within the NSGA-II optimization algorithm because of their ability to approximate any continuous function if properly constructed and trained [67].

There are a few ways to incorporate ANN models within an evolutionary algorithm framework. One way is to construct ANN models in a pre-processing phase based on systematic design of experiments such as Latin hypercube (LHC) sampling. Later, couple those models with an optimization routine. An alternative approach involves constructing ANN models based on the population evolved within an evolutionary algorithm during the optimization process. The latter approach exploits the genes and fitness values of individuals obtained during optimization for training the ANN models. It also allows the ANN models to learn the promising regions better than the other areas in the design space, based on the characteristics of individuals present in the training data. The main idea of this approach lies in implementing the NSGA-II optimization using the detailed PSA model for function evaluations in the first few generations of the optimization process so that the ANN models are trained based on the individuals evaluated, and then the PSA model can be replaced with the ANN models to evaluate the fitness values in the subsequent generations of the optimization algorithm. Other examples of constructing surrogate models based on the population generated during optimization runs can be found elsewhere in the literature in the context of engineering design and optimization [68].

The surrogate-assisted optimization (*SOpt*) approach proposed in the present chapter is described as follows:

1. Implement *TradOpt* for the first N generations of the NSGA-II optimization.

2. Construct ANN models for purity and recovery, respectively, based on the simulation data generated in Step 1.

3. Implement ANN-based NSGA-II function evaluations for the remaining number of generations until the stopping criterion is met

4. Compute the final Pareto front using all individuals generated in Step 3.

5. Re-evaluate the Pareto solutions using the detailed PSA model for final validation

An individual ANN model was developed for each objective (purity and recovery). Since the inputs have different units, they were normalized before being fed to the network as shown below:

$$\bar{x} = \frac{x - \min x}{\max x - \min x} \tag{2.4}$$

A systematic learning-validation procedure was followed during ANN model construction, where 70% of samples were used for learning purposes while the remaining 30% were used for validation. Conventional learning methods adopt mean-squared error (MSE) between the original and the predicted data as the performance function for error minimization of the network, which leads to overfitting problems (i.e. lower bias and large variance) [69]. When the error on the training set is driven to extremely small values, often, there arises a situation where new data presented to the network results in large errors because the network was trained to memorize only training examples. Hence, to improve the generalization capacity of the ANN model, Bayesian regularization (BR) was employed. BR is commonly used for improving generalization ability and robustness while training ANN models [70]. Details of the ANN structure, training and implementation are provided in Appendix B. The Levenberg-Marquardt algorithm with BR was implemented using the Neural Network Toolbox in MATLAB 2018a.

Transformation of the output space

The PSA cycle considered as the case study was designed to achieve high purities and recoveries, respectively. Hence, initial generations of an evolutionary algorithm can produce purities and recoveries as high as 100%. To this end, a transformation (as shown in Eq. 2.5) was applied to the training output data in order 1) to avoid ANN model predictions violating the physical bounds of the outputs by imposing

asymptotic behaviour at the boundaries through the transformation, and 2) to make the best prediction of the highly skewed region of the training data that was generated from the evolutionary algorithm. The transformation was implemented using,

$$u = -\frac{1}{\zeta}\log\left[\left(\frac{\kappa-\chi}{y-\chi}\right)^{\nu} - 1\right] \tag{2.5}$$

where u is the transformed output, y is the original output data, κ and χ are the upper and lower asymptotes, respectively, and ζ and ν are other constants. It is worth mentioning that $y \in$ [0,1] while u lies in the interval [0, 1+] on the real line. The predictions are again transformed back using: $\hat{y} = \chi + (\kappa - \chi)/(1 + \exp(-\zeta\hat{u}))^{1/\nu}$. Similar transformations were utilized by Beck et al. [58] to improve model robustness within a multi-objective optimization framework.

2.4.3 Dimensionality reduction-based optimization (DROpt)

The second approach proposed in the present chapter focuses on reducing the dimensionality of the design space. The PSA process consists of multiple cycle steps operating in a sequence. The number of decision variables for the optimization problem depends on the number of design (or operating) variables pertaining to different constituent steps. For example, the PSA process considered in this chapter has eight steps and eight decision variables for optimization. The high dimensionality of the variable space poses a challenge for the global-search method (NSGA-II) due to the significant computational efforts incurred to investigate the entire space, thereby increasing the burden on the cost of optimization.

The curse of dimensionality in PSA optimization problems can be addressed by selecting a limited number of relevant decision variables for optimization. Data-driven methods have recently gained attention for addressing the issue of high dimensionality in many applications. Common algorithms for dimensionality reduction include principal component analysis (PCA) and partial least squares (PLS) regression, which are feature extraction methods. In the current chapter, PLS regression was employed

to identify the most relevant variables. Once the most relevant decision variables for the optimization problem are identified, the others are discarded as decision variables and held constant. The basic idea involves the hybridization of PLS-based dimensional reduction and NSGA-II optimization using the detailed PSA model. The dimensional reduction-based optimization (*DROpt*) approach proposed in this chapter is as follows:

1. Implement *TradOpt* for the first N generations of the NSGA-II optimization.
2. Carry out the dimensionality reduction using PLS regression based on simulation data generated in Step 1 to identify the most relevant input variables.
3. Perform NSGA-II optimization for the remaining number of generations until the stopping criterion is met using the important inputs identified in Step 2 as decision variables while holding the remaining inputs constant at the sample means of the data used in Step 2.
4. Compute the final Pareto based on all individuals from Step 3.

Note that there is no separate validation step for *DROpt* since the function evaluations are carried out using the detailed PSA model. It is worth noting that simulation data generated within an optimization framework was utilized to reduce dimensionality. However, any sampling technique can be used to implement dimensionality reduction techniques. More details on the theory of PLS regression are provided in Appendix B. In the present chapter, the PLS regression was performed using the built-in function '*plsregress*' in the Statistics and Machine Learning Toolbox in MATLAB 2018a.

2.4.4 Dimensional reduction-based surrogate optimization (DR-SOpt)

The main idea of this approach lies in combining *DROpt* and *SOpt* methods. This approach incorporates both dimensional reduction tools and surrogate models for the NSGA-II optimization. The dimensional reduction-based surrogate-assisted optimization (*DR-SOpt*) approach proposed here is as follows:

1. Implement *TradOpt* for the first N generations of the NSGA-II optimization.

2. Carry out the dimensionality reduction using PLS regression based on simulation data generated in Step 1 to identify the most relevant input variables.

3. Perform detailed model-based NSGA-II optimization for the next K generations using the important inputs identified in Step 2 as decision variables while holding other inputs constant at the sample means of the data used in Step 2.

4. Construct ANN models for purity and recovery, respectively, based on the simulation data generated in Step 3.

5. Perform ANN-based NSGA-II function evaluations for the remaining number of generations until the stopping criterion is met.

6. Compute the final Pareto based on all individuals from Step 5.

7. Re-evaluate the Pareto solutions using the detailed model for final validation.

2.5 Results and discussion

2.5.1 Benchmarking

The performances of proposed hybrid optimization routines, *SOpt*, *DROpt* and *DR-SOpt*, are compared to the conventional *TradOpt*. The stopping criteria in all optimization routines were set to a total of 50 generations. An initial population for NSGA-II was generated using LHC sampling, and the population size was specified to be 24 times the number of decision variables. Other NSGA-II parameters were kept the same for all cases. The ranges for the decision variables are as follows: t_{ADS} (s): 20-100, t_{PREQ1} (s): 30-180, t_{PREQ2} (s): 30-180, t_{CnBLO} (s): 30-180, t_{PUR} (s): 10-80, P_{L} (bar): 1-17.3, v_0 (m s^{-1}): 0.08-0.5 and v_{PUR} (m s^{-1}): 0.1-1.

2.5.2 Pareto computation using SOpt

As described in Section 2.4.2, the first step in the proposed *SOpt* approach involves implementing the detailed PSA model-based-NSGA-II optimization for the first N generations. The simulation results obtained in this step are used as the training dataset to construct ANN surrogate models for purity and recovery, respectively. It is worth mentioning that the training data comprises eight input variables (t_{ADS}, t_{PREQ1}, t_{PREQ2}, t_{CnBLO}, t_{PUR}, P_{L}, v_0 and v_{PUR}) and two output variables, Pu and Re. The predictive capabilities of ANN surrogate models depend on the choice of N. Since there is no rule of thumb for determining the ideal N, empirical tests were performed to choose N. To this end, simulation data generated by the *TradOpt* routine after 50 generations were utilized. Out of 50 generations of simulation data, the first 20 generations were kept aside for training purposes; generations 21-50 were used as test samples T and were not involved in ANN training. Different subsets of training samples, $G^{(i)}$, were generated by considering the first i generations, where $i \in$ [1,20]. For each training subset, $G^{(i)}$, ANN models were trained for purity and recovery, respectively, based on the procedure outlined in Section 2.4.2. During this learning procedure, the number of hidden neurons used in the ANN models was ten, and it was kept the same throughout the process. The ANN training process was stopped after 1000 iterations. The trained ANN models of purity and recovery were tested on the test dataset T. The root-mean-squared error (RMSE) of the test dataset served as the metric to choose N. The RMSE was defined as:

$$\text{RMSE}, (\%) = \sqrt{\frac{1}{T}\sum_{j=1}^{T}\left(\hat{y}_{j,\,\text{ANN}} - y_{j,\,\text{DM}}\right)^2} \times 100 \tag{2.6}$$

where $\hat{y}_{\text{ANN}}$ is the ANN model prediction (purity or recovery) of the test sample, y_{DM}, is the detailed PSA model output in the test sample, and the set T consists of 5622 samples.

Figure 2.2 illustrates the RMSE for both purity and recovery, respectively, as a func-

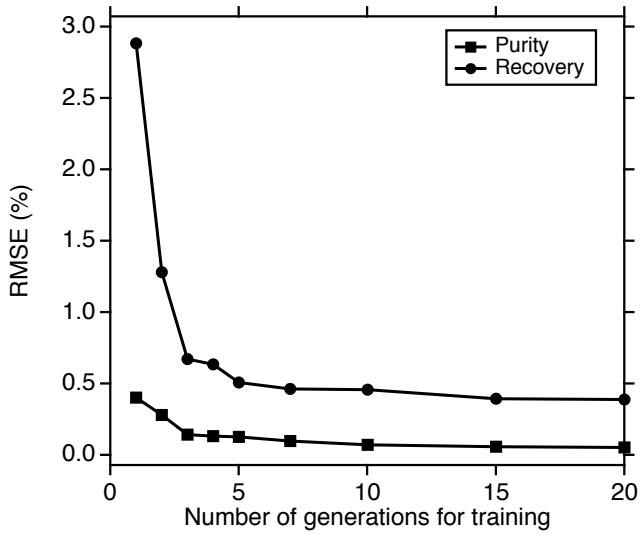

Figure 2.2: RMSE for purity and recovery ANN models as a function of the number of generations to determine adequate N in *SOpt*.

tion of the number of generations. The RMSE for recovery models has a steep decrease initially with an increase in the number of generations, and after five generations, the change in RMSE was not significant. On the other hand, the RMSE for purity models remains relatively constant after N=3 generations. This suggests that a choice of $N \geq$5 generations should generate accurate ANN models for both purity and recovery, respectively, with the ability to provide good predictions for later generations when used in an optimization framework. Therefore, N=5 with 1122 samples was chosen as this was the smallest value of N for which the RMSE was nearly constant. Another consideration is the probability distribution of the training data. The univariate probability distribution of key input variables, t_{ADS}, P_{L}, and v_0, and the outputs, Pu and Re, (as shown in Fig. B.2 in Appendix B) illustrates that the uniformly distributed individuals in the initial generation evolve towards the most promising regions (i.e. regions where there is a high probability of finding solutions that belong to the optimized Pareto front) in the subsequent generations. As seen from the figure, the probability distribution started advancing towards the promising areas of the search space from N=5. This indicates that sampling the individuals accumulated in the first five generations

can provide a promising search direction for ANN model-based NSGA-II optimization. In other words, ANN models trained based on this sampling strategy can predict the promising region reasonably well, thereby guarantee convergence to the global or near optimum during function evaluations of the NSGA-II optimization. Besides, the bivariate joint probability distributions of input and output variables for individuals accumulated in the first 5 and 20 generations (as shown in Figs. B.4 and B.5, respectively, in Appendix B) reinforce the observation that the probability distribution obtained based on the individuals present in the first five generations proceed towards the promising areas of the solution space. Table 2.2 presents the error summary of the trained ANN models for N=5 generations along with the coefficient of determination (R^2). As can be seen from the table, the models achieve high R^2 values of about 0.98.

Table 2.2: Summary of the training and validation accuracy of the purity and recovery ANN models.

Model	E_{train}	E_{val}	R^2	N_{neurons}
Purity	2.05×10^{-4}	4.15×10^{-4}	0.98	10
Recovery	1.7×10^{-3}	7.4×10^{-3}	0.98	10

In the next stage of the *SOpt* framework, the detailed PSA model-based function evaluations are replaced with ANN models of purity and recovery, respectively, after five generations for determining the Pareto front. The surrogate-based NSGA-II multi-objective optimization was carried out for the remaining number of generations until the stopping criterion was met. It should be noted that this stage of the optimization was completed within a few seconds of CPU time. After that, the Pareto front was computed independently based on all individuals evaluated during the ANN model-based NSGA-II implementation and is shown in Fig. 2.3(a). The Pareto solutions obtained from the average of three independent runs are reported. Figure 2.3(a) also illustrates the Pareto front obtained using the *TradOpt* approach for comparison. It can be seen that the Pareto fronts overlap significantly, indicating that the trained ANN models of

purity and recovery have good predictive capabilities. However, towards the top right corner of the Pareto region, it can be observed that the optimal points generated using the *SOpt* approach slightly underestimate the front from *TradOpt*. This can be due to the fact that ANN model-based NSGA-II has not converged for the given stopping criteria. Nevertheless, the stopping criteria for both approaches were kept the same for a fair comparison of computational efforts and accuracy, as explained in Section 2.5.5. In order to understand the input-output mapping structure of the Pareto solutions obtained from *SOpt*, the key decision variables (t_{ADS}, P_{L}, and v_0) corresponding to the Pareto solutions in Fig. 2.3(a) are illustrated in Fig. 2.3(b). Decision variables t_{ADS} and v_0 are jointly shown as the product $t_{\mathrm{ADS}} \cdot v_0$. It can be seen that the *SOpt*, in addition to predicting the Pareto, also captures the mapping of optimal decision variables to the performance indicators, purity and recovery. Note that a parallel coordinate representation of the selected optimal solutions obtained using *TradOpt* and *SOpt* are also illustrated in Fig. B.10 in Appendix B.

To demonstrate the reliability of the *SOpt*-based Pareto front, optimal decision variables obtained using ANN model-based NSGA-II implementation were re-evaluated using the detailed PSA model for final validation. Figure 2.4 shows the comparison of purities and recoveries obtained using the detailed PSA model with that of predicted purities and recoveries from the ANN models, respectively, for the optimal decision variables. Any point that lies on the 45-degree line indicates that both models predict the same target value. It can be observed that most of the points lie along the line. The maximum relative difference between the PSA model and ANN model for purity and recovery was found to be 0.9% and 5.1%, respectively. In the region of interest ($Pu > 95\%$ and $Re > 90\%$), the ANN model prediction is highly accurate in reproducing the detailed PSA model's estimates.

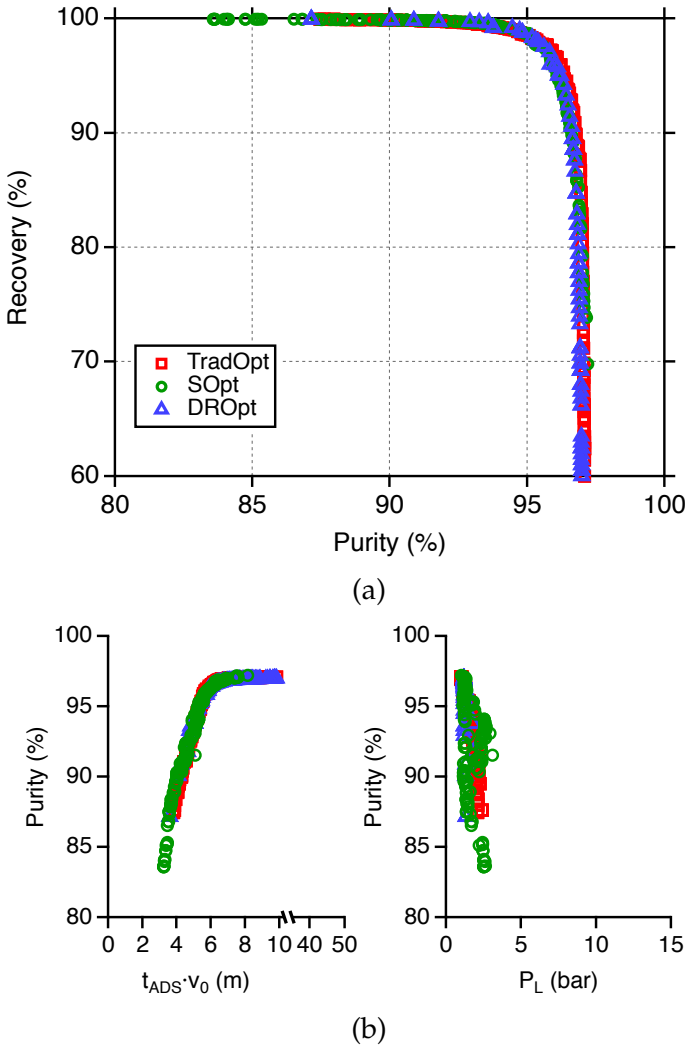

Figure 2.3: Comparison of (a) Pareto fronts obtained with *SOpt* (circles), *DROpt* (triangles) and *TradOpt* (squares) approaches and (b) the corresponding key optimal decision variables obtained. Note that the bounds on $t_{\mathrm{ADS}} \cdot v_0$ and P_{L} in the optimization were varied from 1.6 to 50 m and 1 to 17.3 bar, respectively.

2.5.3 Maximization of purity and recovery based on DROpt

Within the *DROpt* framework, PLS regression was first implemented to reduce the high dimensional design space to a lower dimension. The initial data to perform the dimensional reduction was obtained by implementing *TradOpt* for the first N=2 generations, comprising 576 samples (or simulations). Each sample in the data generated by *TradOpt* implementation consists of eight design variables and two output vari-

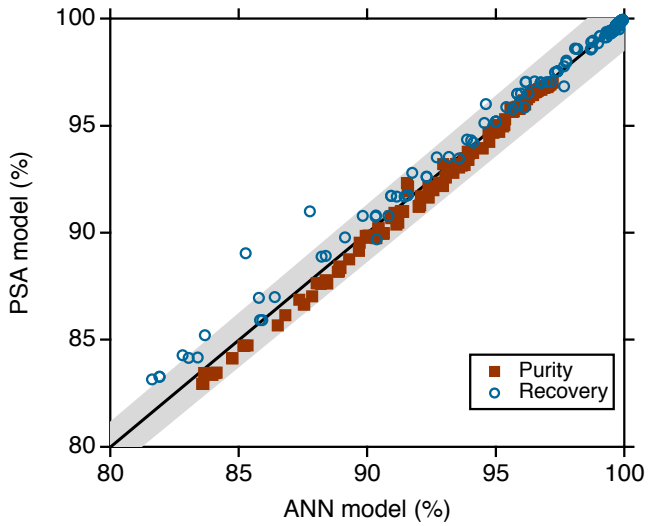

Figure 2.4: Purity-recovery parity plots corresponding to the optimal design variables computed using *SOpt*. The shaded region represents an error range of $\pm 1.5\%$.

ables, Pu and Re. The scope of PLS in this approach involves identifying important input variables, and the posterior outcomes of this technique (i.e. regression models) were not used elsewhere in this approach. An essential part of PLS modelling involves finding the minimum number of latent variables (n_{LV}) that best explains the variance from the original data. A popular approach to choose an optimal value of n_{LV} involves constructing a PLS model with maximum n_{LV} and subsequently analyzing the contributions towards RMSE and variance in the output y by each of the latent variables [71]. To this end, a maximum of n_{LV}=8 could be extracted as the rank of the input matrix is 8 for the given case. Therefore, a PLS model with maximum n_{LV} was developed using the entire dataset gathered from *TradOpt* implementation. During the training process, a 10-fold cross-validation procedure was followed to validate the model. It was found that the first three latent variables were sufficient to describe the PLS model as the remaining latent variables had negligible contribution with respect to both decreasing the overall RMSE value of the model and increasing the total variance explained in the output space (as shown by Figs. B.6 and B.7 in Appendix B). Based on the above analysis, it was concluded that the optimum n_{LV} is 3. A final PLS model was then

constructed with n_{LV}=3 using the entire dataset. To understand the influence of the original input variables on the PLS latent variables, the PLS weights were inspected. The PLS weights are simply the linear combinations of the original variables that form a latent variable. Figure 2.5 shows the weights of the first two latent variables plotted against each other. Since the contribution of the third latent variable towards lowering the RMSE is relatively smaller than that of the first two latent variables, only the first two latent variables were considered for easy interpretation. Data labels provided in Fig. 2.5 correspond to the original input variables. It should be noted that the higher the weight, the stronger the latent variable depends on the original variable. The original input variables with high loadings on the first two latent variables were considered to contribute most to the PLS regression model. From Fig. 2.5, it can be seen that variables t_{ADS}, P_{L} and v_0 are far away from the origin (i.e. have high loading) in both the latent variables, indicating that these variables have a strong influence on the PLS model while the remaining variables t_{PREQ1}, t_{PREQ2}, t_{CnBLO}, t_{PUR}, and v_{PUR} are clustered closer to the origin, indicating negligible contributions to both the latent variables. Table 2.3 shows the regression coefficients obtained from the PLS model. As can be seen from the table, the regression coefficients for t_{ADS}, P_{L} and v_0 are higher than those for the remaining variables. Therefore, it can be deduced that the variables t_{ADS}, P_{L} and v_0 contribute significantly to explaining the variance in both purity and recovery. To this end, the remaining variables are discarded from the optimization problem by holding them at constant values, which are: t_{PREQ1} = 100.4 s, t_{PREQ2} = 103.7 s, t_{CnBLO} = 104.4 s, t_{PUR} = 45.5 s, and v_{PUR} = 0.5 ms^{-1}. These values were obtained based on the sample means of the data used for PLS regression. Subsequently, the search space dimension of the NSGA-II optimizer is reduced from 8 to 3.

The next step in *DROpt* involves the multi-objective NSGA-II optimization using the detailed PSA model for function evaluations given the three input variables, t_{ADS}, P_{L} and v_0. The final Pareto computation was done when the stopping criterion was

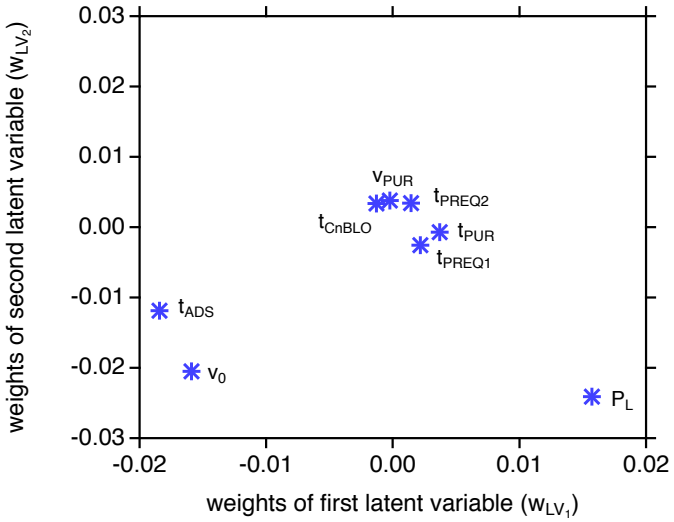

Figure 2.5: PLS weights for the first two latent variables in *DROpt*. Data labels represent the original input variables.

Table 2.3: PLS regression coefficients for n_{LV}=3.

	Pu	Re
t_{ADS}	0.33	-0.44
t_{PREQ1}	0.01	-0.02
t_{PREQ2}	0.04	0.02
t_{CnBLO}	-0.07	0.07
t_{PUR}	-0.02	0.03
P_{L}	-0.41	0.09
v_0	0.43	-0.58
v_{PUR}	0.04	0.02

met for the aforementioned optimization after 50 generations. Figure 2.3(a) also shows the Pareto front (triangles) obtained using the *DROpt* approach. The bounds for decision variables t_{ADS}, P_{L} and v_0 used in *DROpt* were kept the same as in *TradOpt*. *DROpt* was reliable in predicting the purity-recovery optimal solutions, as the Pareto fronts of *DROpt* and *TradOpt* overlap. It is also interesting to note that the optimal points generated by *DROpt* are spread throughout the Pareto space of *TradOpt*. The key decision variables corresponding to the Pareto solutions in Fig. 2.3(a) are again illustrated in Fig. 2.3(b). It can be noticed that *DROpt* captures the mapping of the optimal input

space reasonably well.

2.5.4 Pareto computation based on DR-SOpt

In *DR-SOpt*, data was gathered from the first two generations of *TradOpt* implementation to carry out the dimensional reduction. For the process considered, the important variables remain the same as in *DROpt*. Thereafter, PSA model-based NSGA-II optimization was implemented based on the important variables, t_{ADS}, P_{L} and v_0, as decision variables for the next K generations. The simulations performed herein were used as the training data to construct ANN models of purity and recovery. The K value was again determined using the RMSE of the test samples, which were all individuals from generations 21-50 obtained in *DROpt*. K was varied between 2 to 20, and the influence of K on the RMSE of the purity and recovery, respectively, is illustrated in Fig. B.8 in Appendix B. As can be observed, K has no influence on the RMSE of the purity and recovery models after eight generations. The smallest value of K (=8) for which trained ANN models of purity and recovery showed good accuracy was chosen. It is worth noting that the inputs to the ANN models in this approach are t_{ADS}, P_{L} and v_0 while the output was purity or recovery, depending on the ANN model used.

The remaining 40 generations of NSGA-II optimization were carried out based on ANN models of purity and recovery, respectively. Subsequently, the optimization was terminated after the stopping criterion was attained. All individuals generated during ANN model-based NSGA-II implementation were considered for determining the Pareto front. Figure 2.6(a) shows the Pareto solutions obtained using this hybrid approach. The results obtained were the average of three independent runs. The *TradOpt*-based Pareto is also shown for comparison. It can be seen that *DR-SOpt* predicts the Pareto reasonably well. Although most of the points are slightly underestimated compared to the Pareto generated with *TradOpt*, the computational gains achieved through this approach are significant. Figure 2.6(b) compares the purities and recoveries ob-

tained from the detailed PSA model to the predicted purities and recoveries from ANN models based on optimal decision variables, t_{ADS}, P_{L} and v_0. The relative error for both purity and recovery was found to be less than 1%. This approach also shows good performance in predicting the optimal decision variable space (as shown in Fig. B.9 in Appendix B) for the Pareto solutions illustrated in Fig. 2.6(a).

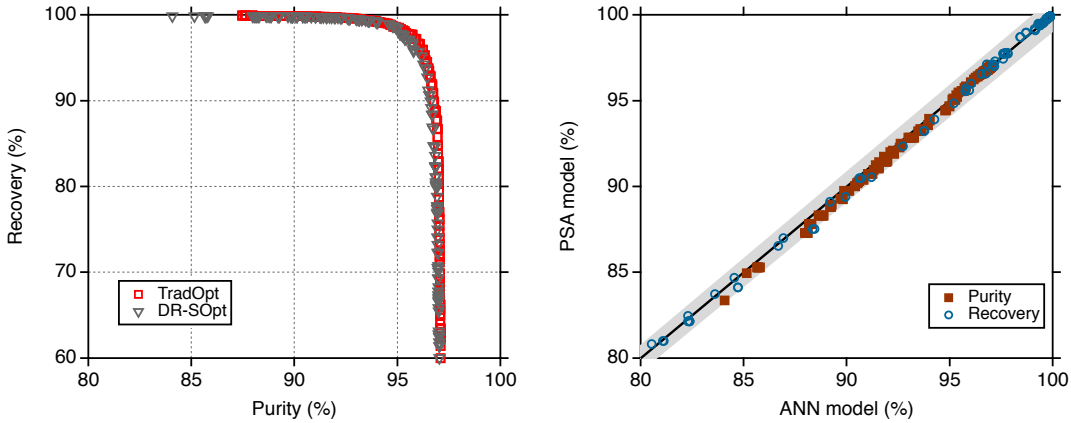

Figure 2.6: (a) Comparison of Pareto fronts obtained with *DR-SOpt* (inverted triangles) and *TradOpt* (squares). (b) Purity-recovery parity plots corresponding to the optimal design variables computed using *DR-SOpt*. The shaded region represents an error range of $\pm 1\%$.

2.5.5 Performance of the different optimization approaches

The overall performance of the three approaches studied in the present chapter was compared in terms of 1) computational costs incurred for computing the final Pareto front after 50 (total) generations in each approach, and 2) accuracy of predicting the original Pareto (obtained using *TradOpt*). The run-times are reported in terms of single-core computation hours. It is worth noting that *TradOpt* and *DROpt* runs were carried out using multiple CPUs run in parallel but were converted to single-core hours for a fair comparison with other approaches. The accuracy of the Pareto curve obtained in each approach was quantified in terms of the normalized area between Pareto fronts

($\mathcal{A}$), which is defined as:

$$\mathcal{A}, [\%] = \frac{AUC_{\text{TradOpt}} - AUC}{AUC_{\text{TradOpt}}} \times 100 \tag{2.7}$$

where AUC_{TradOpt} corresponds to the area under the curve of the *TradOpt*-generated Pareto front in the region Pu $\geq$90% & Re $\geq$85% in Fig. 2.3(a); AUC represents the area under the curve of the Pareto generated based on a given proposed approach, i.e. *SOpt*, *DROpt* and *DR-SOpt*. Based on Eq. 2.7, the Pareto fronts obtained in each of the proposed approaches were respectively compared to the Pareto front generated in *TradOpt*.

Figure 2.7(a) shows the single-core hours (SCH) equivalent run-times of each optimization approach after 50 generations of function evaluations. As expected, *TradOpt* incurred high computational costs while the other approaches showed significant improvement in run-times. In *SOpt*, only five generations of function evaluations were performed using the detailed PSA model, while the remaining 45 generations were evaluated based on the developed ANN models. Because of this, computationally intensive PSA model-based function evaluations were avoided for 45 generations, which resulted in only $\approx$10% of computational demands as compared to *TradOpt*. Dimensionality reduction in *DROpt* from eight variables to three variables also showed good run-time performance. The first two generations used all eight variables; after that, optimization was carried out with a search space of only three dimensions; this showed $\approx$50% of improvement in run-time performances when compared to *TradOpt*. Finally, *DR-SOpt* also demanded less computational resources of about $\approx$12% of *TradOpt*. To determine the accuracies of the Pareto fronts obtained in each of the approaches, $\mathcal{A}$ was plotted as a function of SCH in Fig. 2.7(b). A lower $\mathcal{A}$ implies that the Pareto front of the proposed approach and *TradOpt* are very close, while a higher $\mathcal{A}$ implies that the two Pareto fronts are far from each other. A value of $\mathcal{A}$=0 represents the exact overlap of the Pareto fronts on each other. Any point that lies in the bottom-left region of the figure corresponds to an ideal optimization approach with high accuracy and low

computational efforts. The accuracies of Pareto fronts obtained after every generation in the *TradOpt* (also shown as open markers in Fig. 2.7(b)) are used for comparison. As can be seen from the figure, *SOpt* has relatively lower $\mathcal{A}$ and lower SCH when compared to other approaches. To provide context, the accuracy of the Pareto front computed based on the *SOpt* is the same as the Pareto front obtained in the *TradOpt* after 46 generations (as can be observed from Fig. 2.7(b)), but the computational costs incurred are approximately nine times less than that of the latter approach. *DROpt* has comparable $\mathcal{A}$ performance to *SOpt*; however, the computational costs associated with this approach are relatively higher than that of the *SOpt*, yet, two times faster than that of the *TradOpt*. Of all the proposed approaches, *DR-SOpt* has the highest $\mathcal{A}$ (similar to that of the *TradOpt* after 42 generations), indicating that the Pareto front generated underestimates the conventional Pareto front. Nevertheless, all the proposed approaches showed good performance in predicting the Pareto fronts with small computational demands.

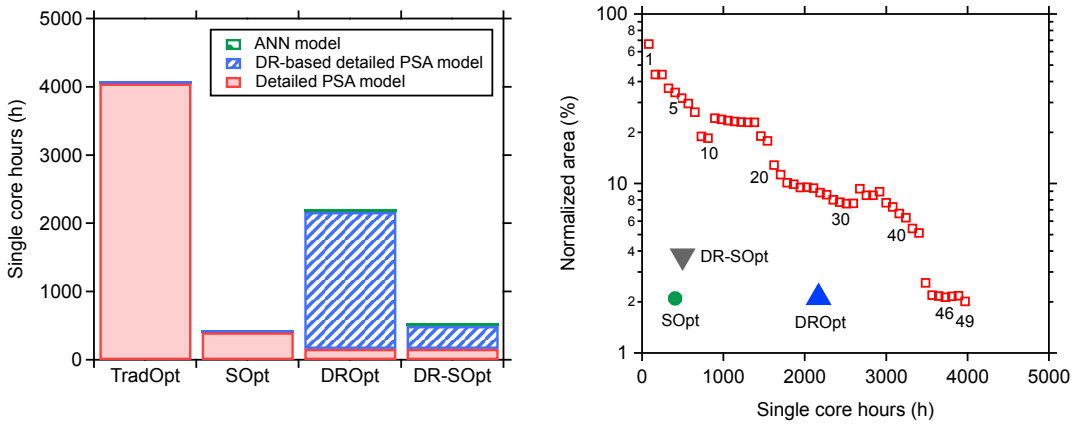

(a) (b)

Figure 2.7: Comparative performance of the proposed approaches in terms of (a) computational costs incurred, (b) normalized area between Pareto fronts ($\mathcal{A}$). $\mathcal{A}$ as a function of the number of generations in *TradOpt* (open squares) are also illustrated for comparison.

2.6 Conclusions and outlook

This chapter demonstrated the hybridization of the detailed PSA model and machine learning principles for the multi-objective optimization of PSA processes. Two approaches, *SOpt* and *DROpt*, are proposed for accelerating the computation of Pareto optimal solutions within the NSGA-II optimization framework. The proposed approaches were tested for accuracy, robustness and reliability by considering a complex PSA cycle that was designed for pre-combustion CO_2 capture as the case study.

The *SOpt* approach exploits nonlinear artificial neural networks as surrogate models, which act as alternate representations of the multivariate mapping between design variables and performance indicators. The ANN models substitute the original PSA model to achieve very fast NSGA-II function evaluations in the later generations of the multi-objective optimization problem. Empirical tests were carried out to determine the minimum number of generations required for ANN models to predict the latter generations with high accuracy and stability. The Pareto front computed using this approach overlaps with the Pareto front obtained using the conventional procedure. The fact that the surrogate optima lie in the close vicinity of the optima from conventional methods can be attributed to the efficient sampling strategy and high accuracy of the ANN models. Another interesting aspect of this approach is the accurate prediction of optimal decision variables. The re-evaluation of optimal design variables using the detailed PSA model demonstrated the reliability of this approach. As far as computational run-times are concerned, this approach utilized only about 10% of the run-time required for the conventional optimization procedure.

The second methodology, *DROpt*, focuses on solving the issue of high-dimensionality in PSA multi-objective optimizations. By employing PLS regression, relevant variables for the optimization problem were identified. The optimization was carried out with these important variables, reducing the computational costs associated with the high-dimensional design space. The *DROpt*-based Pareto front was shown to be similar

to that of the original Pareto. In addition, the input-output mapping structure in the optimal design space was also captured well. The dimensional reduction from 8 to 3 improved the computational speeds of the optimization by $\sim$50%.

A third approach, *DR-SOpt*, that exploits both dimensionality reduction and ANN model-based function evaluations, has also been investigated. Initially, sufficient data was gathered from the first few generations to perform PLS regression for dimensional reduction. Subsequently, based on the relevant variables, the optimization was carried out for the next few generations using the detailed PSA model. The large number of samples accumulated were then used to train the ANN models for function evaluations in the later generations. It was found that the *DR-SOpt* predicts the original Pareto front reasonably well by facilitating faster computations.

In the context of PSA design and optimization, the major barrier for solving the multi-objective optimization problems has been the associated computational costs incurred. The present chapter shows the ability of machine learning in accelerating the discovery of optimal operating conditions when efficiently incorporated into the optimization routines. With the increased interest in model-based engineering for material discovery and process development, the current work demonstrates the importance of machine learning towards rapid progress in adsorption technology for different gas separations.

Chapter 3

Physics-based deep neural networks for simulation and optimization of chromatographic separations

3.1 Introduction

Many physical phenomena in science and engineering are mathematically described by partial differential equations (PDEs). To this end, solving PDEs is of great research interest for simulating and thorough understanding of scientific and engineered systems. Due to the lack of analytical solutions, the PDE solutions are often approximated using numerical approaches such as finite difference, finite element, and finite volume methods. However, the numerical solvers take significant computational time and resources to obtain the solutions with the desired accuracy, especially if many repeated simulations are needed. To avoid the computational burdens, surrogate models are used as fast approximations to the high-fidelity numerical simulations. The latest groundbreaking advances in artificial intelligence, machine and deep learning have allowed for the development of viable methodologies for surrogate modelling [72]. For instance, neural networks are one of the machine learning algorithms widely employed for learning the input-output mapping structures of complex systems [73, 74]. The neural networks consist of hidden layers with neurons which gives them the ability to capture nonlinear dynamics. If the network has more than two hidden lay-

ers, typically, it is called a deep neural network. The enhanced ability of deep neural networks with several hidden layers in capturing very complex nonlinear dynamics has spurred a lot of interest recently in modelling physical systems - particularly the idea of learning PDEs through constraint-based loss functions [75–77]. For instance, Raissi *et al.* [77] developed a physics-based neural network framework in which fully connected deep neural networks can learn the PDE solutions anywhere on the domain with few training points by incorporating a physics-constrained loss function. One of the advantages of this approach includes the presence of PDE-based terms in the loss function, which automatically enables the physics regularization of the neural networks. The philosophy of physics constraining the loss function was later adopted for various applications [78–80].

As mentioned previously in Chapter 1, gas adsorption systems governed by a system of nonlinear PDEs are computationally expensive to solve using numerical methods. To this end, physics-based neural network models can be potential alternatives to simulate adsorption processes rapidly. Before implementing these approaches for modelling such complex processes, a simpler physical phenomenon such as chromatography with the same underlying principles of gas adsorption processes is considered in this chapter to test the feasibility of implementing physics-based neural networks for simulating column dynamics. Preparative chromatography is a powerful technique employed in pharmaceutical, food, and agrochemical industries [81]. In most cases, the binary solute mixture that needs to be separated is dissolved in a solvent (mobile phase) and introduced into single or multiple chromatography columns containing adsorbent particles (stationary phase). The driving force for the separation is the difference in the affinity of the solute mixture components towards the stationary phase. To quantitatively describe the complex behaviour of solute movement inside the column, hyperbolic PDEs must be solved, sometimes repeatedly. Due to the lack of analytical solutions, especially when dispersive and mass transfer effects are present, the PDE

solutions are often approximated using time-consuming numerical solvers to obtain the desired accuracy. Most previous studies on physics-based neural networks have shown their capabilities to learn a single PDE solution, i.e. for given initial and boundary conditions, physical parameters, etc. However, the neural network models must be retrained if the initial or boundary conditions or simulation parameters change. Retraining the models every time does not provide the computational advantage for chromatography systems because the numerical solver is computationally less expensive than retraining the models. Therefore, a more generalized framework is required to implement the physics-based neural networks for chromatography systems.

This chapter explores the ability of the physics-based neural network to predict the complex dynamics of chromatography columns for generic pulse injections. Specifically, the feed concentrations of binary solute mixtures and injection volumes profoundly impact the solute movement along the column [81]. Different concentration transitions arise depending on feed concentrations and pulse injection volumes that will influence how the solute components interact with each other along the column [81]. Therefore, a generic model that can quantitatively describe the solute movement for any given binary mixture feed concentration and injection volume is desired for the rapid design of chromatographic systems. To this end, the goal of the physics-based neural network is to predict the binary solute mixture dynamics and capture critical features such as the formation and propagation of shocks, waves, concentration transitions and their evolution within the column. The predictive capabilities of the physics-based neural network are assessed by comparing the results produced with the high-fidelity numerical simulations. Ultimately, the neural network model is coupled with the optimization routine to determine optimal conditions for baseline separation of solute components of the feed mixture.

3.2 Governing partial differential equations

The conservation of mass governs the solute transport in chromatographic columns. Under the assumption of negligible mass transfer resistance, an equilibrium-dispersive model is employed to describe the mass balance of each solute component in a binary mixture along with adsorption equilibria [82]. In this model, there exists an instantaneous equilibrium between the fluid and the solid phases. Moreover, dilute solute concentrations are considered so that the velocity of the fluid phase remains constant along the column. Based on these assumptions, the mass balance equation for each component is given by

$$\frac{\partial c_i}{\partial t} = D_{\text{ax}} \frac{\partial^2 c_i}{\partial z^2} - v \frac{\partial c_i}{\partial z} - \frac{1-\varepsilon}{\varepsilon} \frac{\partial q_i^*}{\partial t} \quad i = 1, 2 \tag{3.1}$$

where c_i is the concentration of the solute i in the fluid phase; q_i^* is the equilibrium solid-phase concentration of the solute i; D_{ax} is the axial dispersion coefficient that accounts for both axial dispersion and mass transfer resistance due to non-equilibrium effects; ε is the void fraction of the bed; and v is the interstitial velocity. The equilibrium solid-phase concentration, q_i^*, is calculated using a competitive single-site Langmuir (SSL) isotherm model as shown below:

$$q_i^* = \frac{H_i c_i}{1 + \sum_i b_i c_i} \quad i = 1, 2 \tag{3.2}$$

In the above equation, H_i and b_i are the Henry constant and the adsorption equilibrium constant. The second component is assumed to be the strongly adsorbing component, i.e., $H_2 > H_1$. Equations 3.1 and 3.2 together result in a system of two coupled non-linear PDEs. For well-posed systems, appropriate initial and boundary conditions are required. Normally, the chromatographic columns are initially saturated with a non-adsorbing solvent, giving rise to an initial condition, $c_i(z, 0)$=0. Binary concentration pulses are injected into the column where Eq. 3.1 is subjected to the following bound-

ary conditions at the column inlet and outlet, respectively:

$$c_i(0,t) = \begin{cases} c_i^0 & 0 \leq t \leq \tau \\ 0 & t > \tau \end{cases} \tag{3.3}$$

$$\left.\frac{\partial c_i}{\partial z}\right|_{z=L} = 0 \tag{3.4}$$

where c_i^0 represents the concentration of the solute i injected into the column, and τ is the time of injection.

3.3 Methodology

3.3.1 Physics-based neural network

Physics-based neural networks are based on advanced deep learning algorithms that can solve supervised learning tasks while obeying the laws of physics as described by general nonlinear partial differential equations [77]. The basic idea involves training the neural networks to match the labelled data while also minimizing the residuals of PDEs to enforce the physics-based constraints. As previously mentioned, the solution of Eq. 3.1 is unique for given inlet feed concentrations (c_1^0, c_2^0) and the injection time τ. For computing the neural network approximated solutions of Eq. 3.1 at any c_1^0, c_2^0, and τ, the neural network model is trained based on N_k different combinations of c_1^0, c_2^0, and τ to enable generalized capabilities. Therefore, the physics-based neural network model developed herein aims to learn the following mapping:

$$[z, t, c_1^0, c_2^0, \tau] \xrightarrow{\theta} [c_1(z,t), c_2(z,t)] \tag{3.5}$$

Here the neural network takes five inputs: spatiotemporal coordinates (z, t), inlet feed concentrations (c_1^0, c_2^0) and the injection time τ, while the solute concentrations $c_1(z,t)$, $c_2(z,t)$ are the outputs. The equilibrium solid concentrations $q_1^*(z,t)$, $q_2^*(z,t)$ can be expressed in terms of $c_1(z,t)$, $c_2(z,t)$ based on Eq. 3.2 and are not explicitly considered as the outputs.

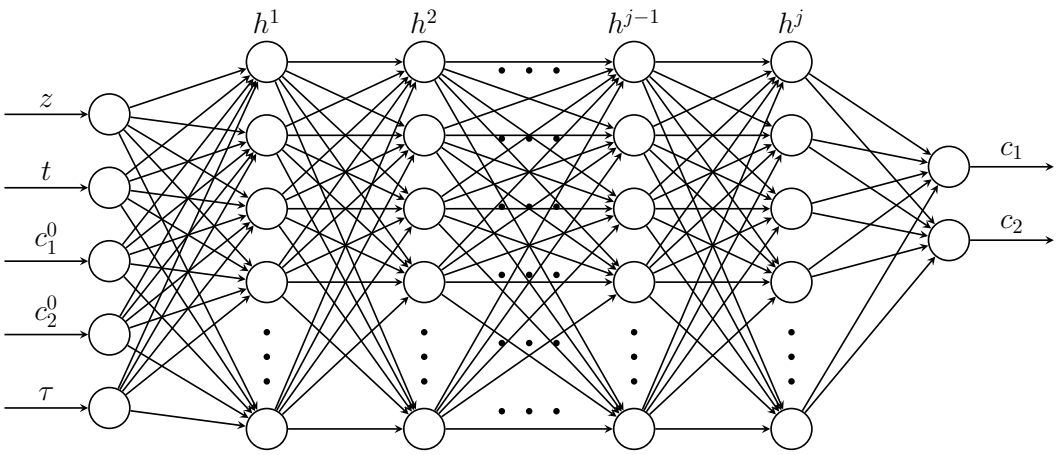

Figure 3.1: Deep neural network architecture.

Neural network architecture

This study employs a feed-forward, fully connected deep neural network to construct a physics-based neural network model for chromatography. Figure 3.1 illustrates the architecture of the deep neural network comprising N_h+2 layers with one input layer, N_h hidden layers, and one output layer. Moreover, each layer has a predefined number of neurons that are interconnected through a set of coefficients called weights. In addition to weights, each neuron also has a bias term. Each neuron combines the inputs, weights and biases through a nonlinear activation function as shown below:

$$X_l = \sigma_l(X_{l-1}W_l + b_l) \tag{3.6}$$

where X_{l-1} is the output of the $l-1$ layer; W_l and b_l represent the weight matrix and bias vector of layer l, respectively and; X_l is the output of l layer. The dimensions of weight matrix W_l and bias vector b_l are $N_{l-1} \times N_l$ and N_l, respectively, where N_{l-1} and N_l are the number of neurons in $l-1$ and l layer, respectively. This way each layer receives outputs from the previous layer as inputs and feeds forward to the next layer. All the hidden parameters of the neural network are denoted as θ, i.e. ($\mathbf{W}$, $\mathbf{b}$) $\in \theta$. Here, the activation function, σ_l, number of hidden layers, N_h, number of hidden neurons, N_l form hyperparameters.

Loss function

To enable such a mapping given in Eq. 3.5, the hidden parameters, θ, need to be determined by optimizing the loss function. To this end, the loss function constructed herein consists of two terms. Each part of the loss function is described in detail as follows:

Loss function: Labelled data. This part of the loss function constrains the predictions of the neural network to match the labelled data. Herein, the labelled data refers to the training data that needs to be obtained either from experiments or simulations. The initial and the boundary data from the simulations is introduced as the labelled data [77]. The loss term expressed as the mean-squared error (MSE) between the neural network predictions and the labelled data (for case #k) can be written as

$$\mathcal{L}_{data}^{k} = \frac{1}{N_i^k}\sum_{i=1}^{N_i^k}\left[\frac{\hat{c_1}(z_i^k, t_i^k, c_1^{0,k}, c_2^{0,k}, \tau^k, \theta) - c_1(z_i^k, t_i^k, c_1^{0,k}, c_2^{0,k}, \tau^k)}{\tau^k}\right]^2 + \frac{1}{N_i^k}\sum_{i=1}^{N_i^k}\left[\frac{\hat{c_2}(z_i^k, t_i^k, c_1^{0,k}, c_2^{0,k}, \tau^k, \theta) - c_2(z_i^k, t_i^k, c_1^{0,k}, c_2^{0,k}, \tau^k)}{\tau^k}\right]^2 \tag{3.7}$$

where $\hat{c_1}$ and $\hat{c_2}$ are the neural network predictions, whereas c_1 and c_2 denote the labelled data of two solute concentrations obtained using high-fidelity simulations. N_i^k represents the number of labelled initial and boundary data points. z_i^k and t_i^k are spatiotemporal coordinates on the bottom, left and right boundaries of the spatiotemporal domain. Finally, $k = 1, 2.., N_k$, represent different cases of $c_1^{0,k}, c_2^{0,k}, \tau^k$.

Loss function: PDE residuals. This part of the loss function introduces the physics regularization of the neural networks. To this end, the PDE residuals of Eq. 3.1 for two solute components are defined as follows:

$$\begin{aligned} r_1(z,t) &: \frac{\partial c_1}{\partial t} + v\frac{\partial c_1}{\partial z} - D_{\text{ax}}\frac{\partial^2 c_1}{\partial z^2} + \frac{1-\varepsilon}{\varepsilon}\frac{\partial q_1^*}{\partial t} \\ r_2(z,t) &: \frac{\partial c_2}{\partial t} + v\frac{\partial c_2}{\partial z} - D_{\text{ax}}\frac{\partial^2 c_2}{\partial z^2} + \frac{1-\varepsilon}{\varepsilon}\frac{\partial q_2^*}{\partial t} \end{aligned} \tag{3.8}$$

For evaluating the above mentioned residuals, N_r collocation points (i.e. (z_r, t_r)) within the spatiotemporal domain are used. These collocation points are randomly chosen

using Latin hypercube sampling. Notably, this part of the loss function requires no additional training data from the simulations because the collocation points are just auxiliary points that help calculate the partial derivatives. The loss term corresponding to the residuals given in Eq. 3.8 can be written as

$$\mathcal{L}^k_{residual} = \frac{1}{N^k_r}\sum_{r=1}^{N^k_r} r_1(z^k_r, t^k_r, c^{0,k}_1, c^{0,k}_2, \tau^k, \theta) + \frac{1}{N_r}\sum_{r=1}^{N_r} r_2(z^k_r, t^k_r, c^{0,k}_1, c^{0,k}_2, \tau^k, \theta) \tag{3.9}$$

where N^k_r is the number of collocation points for case #k. r^k_1 and r^k_2 correspond to the residuals of first and second solute component mass balances for case #k, where $k = 1, 2.., N_k$.

Overall Loss function. By combining the loss terms Eqs. 3.7 and 3.9, the overall loss function takes the following form:

$$\mathcal{L} = \lambda_{data}\sum_{k=1}^{N_k}\mathcal{L}^k_{data} + \lambda_{residual}\sum_{k=1}^{N_k}\mathcal{L}^k_{residual} \tag{3.10}$$

In the above equation, individual terms $\mathcal{L}^k_{data}$ and $\mathcal{L}^k_{residual}$ obtained for each case #k are together summed over N_k cases of different combinations of $c^{0,k}_1, c^{0,k}_2, \tau^k$. The rationale here is to constrain the neural network to match the labelled data and reduce the PDE residuals close to zero for each case #k, then minimize the MSE values obtained from all cases considered so that the neural network learns the unique spatiotemporal solutions corresponding to different $c^{0,k}_1, c^{0,k}_2, \tau^k$. λ_{data} and $\lambda_{residual}$ are the weight terms ([0, ∞]) in the loss function. The neural network learning process and the accuracy are dependent on the choice of the weights. Although there is no rule of thumb for choosing the optimal weights, limited numerical experimentation is carried out to estimate the weights that give better accuracy.

Learning procedure

The neural network training aims to determine the optimal weights and biases (θ) by minimizing the loss function described in Eq. 3.10. The weights are initialized using

Xavier initialization [83], a standard strategy for neural network initialization, and the biases are initialized with zeros. Equation 3.10 is minimized using L-BFGS, a quasi-Newton full-batch gradient-based optimization method. During the training, the gradients of the loss function with respect to each training weight are backpropagated based on the chain rule, and after each iteration, the weights and biases are updated. This procedure repeats until convergence is achieved. Although the convergence to the global minimum with thousands of adjustable parameters is not guaranteed using this approach, it is shown that the correct parameters for weights and biases that can result in good prediction accuracies can be obtained [77].

To compute the partial derivatives in the PDE residuals, automatic differentiation (AD) is used [84]. In AD, the partial differential operators are approximated using the chain rule through backpropagation of derivatives from the output layer to the input layer. Well-established modules are available to implement AD in deep learning frameworks such as Tensorflow [85] and PyTorch [86]. In this study, the partial differential operators are computed using "tf.gradients()" in Tensorflow.

3.3.2 Non-dimensionalization and normalization

The physical quantities in Eq. 3.1 have different orders of magnitude, which can lead to difficulties while calculating backpropagated gradients during neural network training [78, 87]. In order to avoid this, non-dimensionalization of physical quantities with appropriate scaling (i.e. $\sim \mathcal{O}(1)$) is essential. Here, the non-dimensionalized quantities are defined as:

$$\bar{c}_1 = \frac{c_1}{c_1^0}, \quad \bar{c}_2 = \frac{c_2}{c_2^0}, \quad \bar{q}_1^* = \frac{q_1^*}{c_1^0}, \quad \bar{q}_2^* = \frac{q_2^*}{c_2^0}, \quad \bar{v} = \frac{v}{v_0} \tag{3.11}$$

where v_0 is the interstitial velocity (m s^{-1}), and the inputs are normalized to lie in the range of [-1,1] as follows:

$$\bar{z} = 2\frac{z}{L} - 1, \quad \bar{t} = 2\frac{t}{t_0} - 1, \quad \bar{c^0} = 2\frac{c^0}{c_{max}^0} - 1, \quad \bar{\tau} = 2\frac{\tau}{\tau_0} - 1 \tag{3.12}$$

L is the length of the chromatography column (m), t_0 is the total duration for which the solute movement is tracked (s), c^0_{max} is the maximum inlet concentration, and τ_0 is the maximum injection time considered (s).

Based on the non-dimensionalized variables, Eq. 3.1 takes the form:

$$\frac{\partial \bar{c}_i}{\partial \bar{t}} = -\nu_1 \bar{v} \frac{\partial \bar{c}_i}{\partial \bar{z}} + \nu_2 \frac{\partial^2 \bar{c}_i}{\partial \bar{z}^2} - \nu_3 \frac{\partial \bar{q}^*_i}{\partial \bar{t}} \quad i = 1, 2 \tag{3.13}$$

In the above equation, $\nu_1 = \dfrac{v_0 t_0}{L}$, $\nu_2 = \dfrac{D_{ax} t_0}{L^2}$, and $\nu_3 = \dfrac{1-\varepsilon}{\varepsilon}$.

The non-dimensionalization and the normalization ensures that all the variables and inputs are scaled to order $\mathcal{O}(1)$. Before the training, the data provided to the neural network is scaled based on Eqs. 3.11 and 3.12. The predicted quantities are finally reverted to their original form.

3.3.3 Data generation: high fidelity ED model simulations

For generating both training and validation data, high-fidelity simulations are carried out to solve Eqs. 3.1 and 3.2 together. The spatial terms in Eq. 3.1 are discretized into 200 finite volumes using a finite volume method. Although fewer finite volume elements would generally suffice, high-efficiency separations require finer discretization. The resulting ordinary differential equations are integrated in time using *ode15s* in MATLAB 2021a. Finally, the high fidelity simulations provided the entire spatiotemporal solutions of $c_1(z,t)$ and $c_2(z,t)$. Although the data generated in simulations can be massive, only a tiny portion is gathered to train the neural network models. The simulation data is also used to evaluate the neural network model's accuracy. Since the framework employed herein also has c^0_1, c^0_2 and, τ as inputs, multiple simulations are carried out at different combinations of c^0_1, c^0_2 and, τ to have variation in the inputs, thereby enabling the desired mapping in Eq. 3.5.

3.3.4 Optimization

The neural network models are coupled with a non-dominated sorting genetic algorithm II (NSGA-II), a stochastic optimizer, to optimize chromatographic separations. The optimizer selects a population of decision variables for the neural network model to evaluate objective functional values. Based on this information, the optimizer improves the population by mimicking the evolution to carry out operations such as crossover, mutation, etc., for obtaining the optimum solution. NSGA-II has been successfully implemented for single-objective optimization problems [21, 88].

3.4 Results and discussion

3.4.1 Neural network training

The physics-based neural networks are trained to learn the column dynamics for generic pulse injections by considering multiple training cases with varying c_1^0, c_2^0 and, τ. Here ten training cases are considered where each case represents a unique combination of c_1^0, c_2^0 and, τ and a unique solution to Eq. 3.1. The values of c_1^0, c_2^0 and, τ are chosen such that several important features such as propagation of shocks, waves, concentration transitions, along with interactions between adsorption and desorption fronts can be noticed. To this end, both c_1^0 and c_2^0 are varied between 0.3 and 5 mg ml^{-1}, whereas τ is changed between 100 and 550 seconds, respectively. Table 3.1 shows the ten different combinations of c_1^0, c_2^0 and, τ generated using Latin-hypercube sampling. The high fidelity simulations are carried out for these cases based on the parameters provided in Table 3.2 to generate the simulation data.

The data acquisition for training involves gathering the simulation data from each case and subjecting both the inputs and the physical quantities to normalization and non-dimensionalization, respectively, as outlined previously. Following this, the initial and boundary concentration data of two solute components from all training cases are

gathered to form the labelled data, as illustrated in Fig. 3.2. To be more specific, 251 equidistant time steps of concentration profile at each boundary and initial concentration at 102 spatial locations are extracted from each training case. The total number of labelled data points fed to the network can be visualized in Fig. 3.2. To infer the PDE solution within the spatiotemporal domain, N_r=2000 collocation points are randomly generated using Latin-hypercube sampling for each training case. It is worth reiterating that no additional simulation data is required for the collocation points.

Table 3.1: Training cases generated using Latin hypercube sampling.

Case	c_1^0 (mg ml^{-1})	c_2^0 (mg ml^{-1})	τ (s)
1	4.93	4.33	266.88
2	2.94	1.05	181.52
3	3.51	4.01	529.78
4	0.38	2.93	143.97
5	3.90	1.51	314.04
6	4.08	4.71	330.91
7	2.27	0.31	391.21
8	2.08	2.08	418.86
9	0.77	3.42	461.17
10	1.68	2.52	208.66

The neural network architecture employed herein consists of one input layer with five neurons, five hidden layers with 50 neurons each, one output layer with two neurons and a hyperbolic tangent function for the nonlinear activation. The weight terms λ_{data} and $\lambda_{residual}$ in the overall loss function (Eq. 3.10) are chosen as 100 and 1, respectively. It is worth noting that the choice of hyperparameters is based on a series of systematic studies presented in the following section. The learning procedure is implemented in Tensorflow v1.15 [85], and the computations are performed based on a single Telsa P100 GPU card where it took almost 15 minutes to train the neural network model.

Table 3.2: Simulation parameters.

Parameters	**Value**
Column length, L (cm)	20
Interstitial feed velocity, v_0 (cm s^{-1})	0.075
Total porosity, ε (-)	0.4
Axial dispersion, D_{ax} (mm^2 s^{-1})	0.087
Maximum injection time, τ_0 (s)	550
Total duration, t_0 (s)	2000
Maximum inlet concentration, c^0_{max} (mg ml^{-1})	5
Henry constant of 1^{st} component, H_1 (-)	1
Henry constant of 2^{nd} component, H_2 (-)	2
Adsorption equilibrium constant of 1^{st} component, b_1 (-)	0.1
Adsorption equilibrium constant of 2^{nd} component, b_2 (-)	0.1

Hyperparameter selection

The selection of the hyperparameters is essential before the neural network training. The hyperparameters determine the model structure and can significantly affect the model's prediction accuracy. Since there is no rule of thumb to determine the right hyperparameters, a series of systematic studies are carried out. For the neural network methodology employed herein, the activation function, σ_l, number of hidden layers, N_h, number of hidden neurons, N_l, and weight term, λ_{data}, can be identified as the hyperparameters. Since the network used here is relatively shallow, the hyperbolic tangent activation function can lead to better results [87]. Numerical experiments are carried out to choose appropriate N_h, N_l, and λ_{data}. In each numerical experiment, the neural network model is trained based on certain values of hyperparameters, and the performance of the trained model is compared with the simulation data based on relative $\mathcal{L}_2$ error defined as follows:

$$\mathcal{L}_2 = \frac{\sqrt{\sum_{j=1}^{N_f}(\hat{c}(z_j,t_j) - c(z_j,t_j))^2}}{\sqrt{\sum_{j=1}^{N_f} c(z_j,t_j)^2}} \tag{3.14}$$

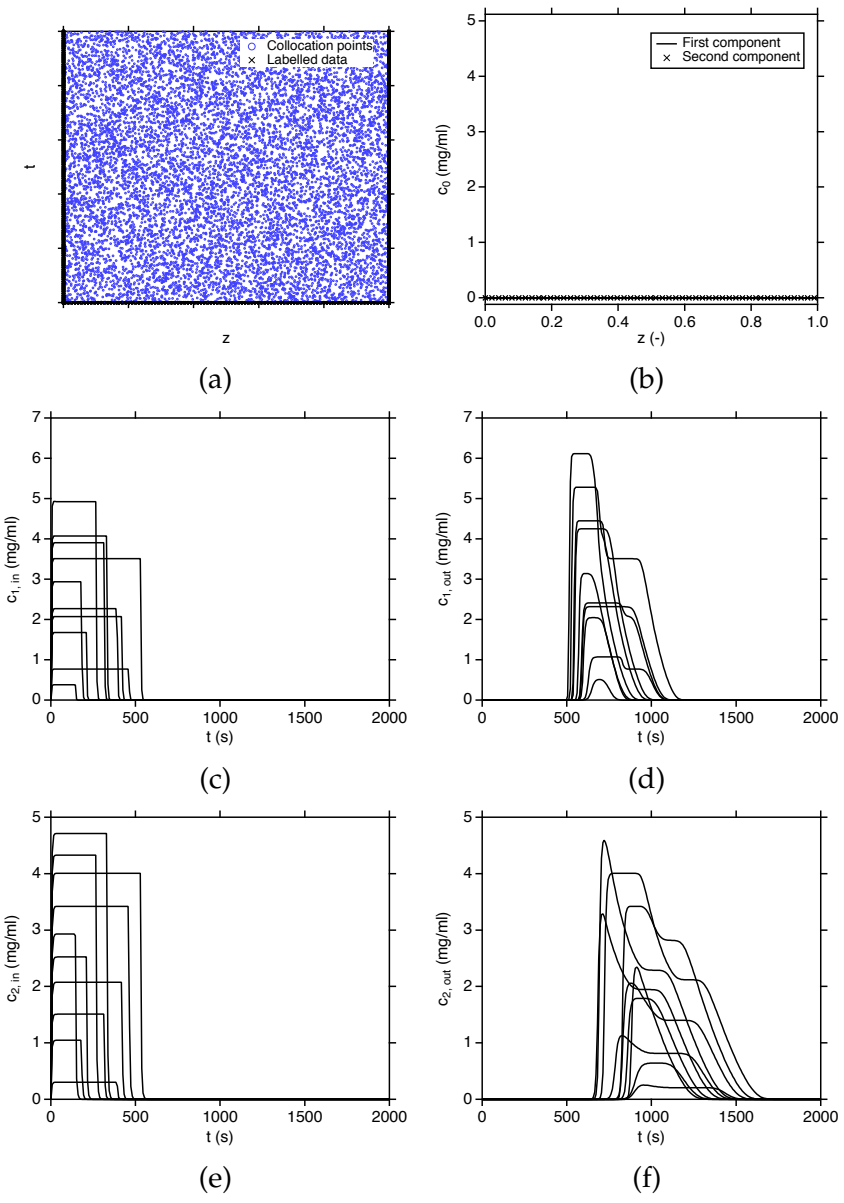

Figure 3.2: Visualization of (a) spatiotemporal domain. (b) initial and (c)-(f) boundary labelled data of the first and the second component concentrations fed to the network training.

where $\hat{c}$ is the predicted concentration and c is the concentration obtained from high fidelity simulations. N_f represents the number of spatiotemporal points.

The first set of numerical experiments are performed to select λ_{data}. For this, other hyperparamters are set to: N_h=5; N_l=50. Table 3.3 summarizes the relative $\mathcal{L}_2$ error between the predicted and ED model concentrations of two solute components for all

training cases. Although the variation in λ_{data} did not impact the prediction accuracies, λ_{data}=100 resulted in a marginally better result. In the second set of numerical experiments (see Table 3.4), the number of hidden layers is varied from 3 to 7 while keeping λ_{data}=100, N_l=50. Again, the general trend suggests that the $N_h \geq 5$ gave slightly lower $\mathcal{L}_2$ errors for most training cases. Finally, the third set of experiments, illustrated in Table 3.5, are carried out to select N_l by setting λ_{data}=100 and N_h=5. Here, N_l=20 gave marginally higher $\mathcal{L}_2$ errors for most training cases. These results show that the hyperparameters have minimal influence on the overall model prediction accuracies, which can be attributed to the efficient regularization achieved in the neural network training due to the presence of physics-constrained loss terms.

Comparison of predicted and ED model solutions for training cases

The results produced by the trained physics-based neural network for the training cases are first compared with high fidelity ED model simulations. Since the initial and boundary data from the training cases are already used in the neural network training, the emphasis remains on whether the neural network has accurately learned the interior of the spatiotemporal domain. For the sake of brevity, the neural network predictions for training cases 3 and 4 representing large- and small-volume pulse injections, respectively, are discussed here. The rationale behind this is to find out the neural network's ability in capturing different behaviors of solute movement that occur in chromatography columns for large- and small-volume pulse injections. Since other training cases are also examples of either large- or small-volume pulse injections, the discussion will not be substantially different.

Figure 3.3 illustrates the comparison between neural network predicted and ED model concentration solutions of both solutes when subjected to a large-volume injection (training case 3). Consider the propagation of the first solute component, for instance (Fig. 3.3(a)). Since the first solute component has a weaker affinity, it travels

Table 3.3: Relative $\mathcal{L}_2$ norm between the neural network predicted and the ED model solution of solute concentrations ($c_1(z,t)$, $c_2(z,t)$) obtained based on all training cases by changing λ_{data}. Note that the number of layers and the number of neurons are fixed to 5 and 50, respectively.

λ_{data}	1	10	100
$c_1(z,t)$			
Case 1	$3.36e-02$	$3.05e-02$	$3.08e-02$
Case 2	$3.54e-02$	$3.06e-02$	$3.98e-02$
Case 3	$2.96e-02$	$2.54e-02$	$2.50e-02$
Case 4	$5.02e-02$	$3.86e-02$	$3.54e-02$
Case 5	$3.15e-02$	$2.76e-02$	$2.93e-02$
Case 6	$3.84e-02$	$3.07e-02$	$3.99e-02$
Case 7	$3.54e-02$	$2.53e-02$	$2.28e-02$
Case 8	$3.74e-02$	$2.56e-02$	$2.38e-02$
Case 9	$2.69e-02$	$2.65e-02$	$2.60e-02$
Case 10	$4.80e-02$	$3.86e-02$	$3.35e-02$
$c_2(z,t)$			
Case 1	$3.10e-02$	$3.46e-02$	$2.03e-02$
Case 2	$4.74e-02$	$3.69e-02$	$2.68e-02$
Case 3	$2.01e-02$	$2.61e-02$	$1.66e-02$
Case 4	$5.39e-02$	$4.98e-02$	$4.21e-02$
Case 5	$3.60e-02$	$2.71e-02$	$1.59e-02$
Case 6	$3.14e-02$	$2.87e-02$	$2.19e-02$
Case 7	$3.53e-02$	$2.60e-02$	$1.68e-02$
Case 8	$2.59e-02$	$2.45e-02$	$1.88e-02$
Case 9	$2.41e-02$	$3.55e-02$	$2.41e-02$
Case 10	$4.53e-02$	$3.56e-02$	$2.88e-02$

relatively faster than the second solute component along the column. In large-volume pulse injections, this naturally causes an overshoot in the concentration, i.e. concentration greater than the feed concentration, in the regions where only a weaker component is present. As can be seen from the figure, the physics-based neural network accurately captures this phenomenon inside the spatiotemporal domain even in the absence of labelled data. The neural network also describes the dispersion related to the desorption on the rear-end of the pulse propagation. In Fig. 3.3(b), the spatiotemporal solution

Table 3.4: Relative $\mathcal{L}_2$ norm between the neural network predicted and the ED model solution of solute concentrations ($c_1(z,t)$, $c_2(z,t)$) obtained based on all training cases by changing the number of hidden layers. Note that the number of neurons are fixed to 50 and the λ_{data}=100.

# hidden layers	3	4	5	6	7
$c_1(z,t)$					
Case 1	$4.92e-02$	$5.11e-02$	$3.08e-02$	$3.89e-02$	$3.10e-02$
Case 2	$4.03e-02$	$2.84e-02$	$3.98e-02$	$3.55e-02$	$2.97e-02$
Case 3	$2.38e-02$	$2.37e-02$	$2.50e-02$	$2.68e-02$	$2.78e-02$
Case 4	$3.71e-02$	$3.09e-02$	$3.54e-02$	$3.45e-02$	$3.84e-02$
Case 5	$3.26e-02$	$3.22e-02$	$2.93e-02$	$3.23e-02$	$2.83e-02$
Case 6	$5.00e-02$	$5.07e-02$	$3.99e-02$	$4.03e-02$	$3.98e-02$
Case 7	$2.51e-02$	$2.12e-02$	$2.28e-02$	$2.55e-02$	$2.11e-02$
Case 8	$2.57e-02$	$2.13e-02$	$2.38e-02$	$2.42e-02$	$2.07e-02$
Case 9	$2.29e-02$	$1.98e-02$	$2.60e-02$	$2.19e-02$	$2.33e-02$
Case 10	$3.27e-02$	$3.33e-02$	$3.35e-02$	$3.27e-02$	$3.44e-02$
$c_2(z,t)$					
Case 1	$2.31e-02$	$2.08e-02$	$2.03e-02$	$2.25e-02$	$2.26e-02$
Case 2	$2.45e-02$	$2.24e-02$	$2.68e-02$	$2.60e-02$	$2.32e-02$
Case 3	$1.76e-02$	$1.73e-02$	$1.66e-02$	$1.85e-02$	$1.88e-02$
Case 4	$5.54e-02$	$7.36e-02$	$4.21e-02$	$4.57e-02$	$4.46e-02$
Case 5	$1.75e-02$	$1.48e-02$	$1.59e-02$	$1.64e-02$	$1.67e-02$
Case 6	$2.37e-02$	$2.36e-02$	$2.19e-02$	$2.26e-02$	$2.32e-02$
Case 7	$1.75e-02$	$1.48e-02$	$1.68e-02$	$1.68e-02$	$1.81e-02$
Case 8	$1.93e-02$	$1.83e-02$	$1.88e-02$	$1.79e-02$	$1.71e-02$
Case 9	$2.39e-02$	$2.21e-02$	$2.41e-02$	$2.35e-02$	$2.35e-02$
Case 10	$3.39e-02$	$3.00e-02$	$2.88e-02$	$3.18e-02$	$2.77e-02$

of the concentration of second solute component obtained from both neural networks and ED model is illustrated. The neural network predictions are remarkable, especially, the intermediate transition plateau on the desorption front of the pulse injection is well described. Finally, the relative $\mathcal{L}_2$ error between the predicted and ED model concentrations of two solute components are given in Tables 3.3-3.5.

Moreover, the ability of neural networks to predict the spatiotemporal concentration solutions of first and second solute components in the case of short pulses can be

Table 3.5: Relative $\mathcal{L}_2$ norm between the neural network predicted and the ED model solution of solute concentrations ($c_1(z,t)$, $c_2(z,t)$) obtained based on all training cases by changing the number of hidden neurons. Note that the number of layers are fixed to 5 and the λ_{data}=100.

# neurons per layer	20	50	100
$c_1(z,t)$			
Case 1	$2.90e-02$	$3.08e-02$	$4.19e-02$
Case 2	$3.42e-02$	$3.98e-02$	$4.00e-02$
Case 3	$3.04e-02$	$2.50e-02$	$2.42e-02$
Case 4	$3.89e-02$	$3.54e-02$	$3.89e-02$
Case 5	$3.11e-02$	$2.93e-02$	$3.05e-02$
Case 6	$5.48e-02$	$3.99e-02$	$5.40e-02$
Case 7	$2.87e-02$	$2.28e-02$	$2.44e-02$
Case 8	$2.11e-02$	$2.38e-02$	$2.18e-02$
Case 9	$2.25e-02$	$2.60e-02$	$2.20e-02$
Case 10	$3.08e-02$	$3.35e-02$	$3.46e-02$
$c_2(z,t)$			
Case 1	$2.38e-02$	$2.03e-02$	$2.28e-02$
Case 2	$2.35e-02$	$2.68e-02$	$2.35e-02$
Case 3	$1.95e-02$	$1.66e-02$	$1.70e-02$
Case 4	$5.73e-02$	$4.21e-02$	$5.29e-02$
Case 5	$1.92e-02$	$1.59e-02$	$1.39e-02$
Case 6	$2.63e-02$	$2.19e-02$	$2.33e-02$
Case 7	$1.93e-02$	$1.68e-02$	$1.49e-02$
Case 8	$2.05e-02$	$1.88e-02$	$1.73e-02$
Case 9	$2.17e-02$	$2.41e-02$	$3.44e-02$
Case 10	$3.17e-02$	$2.88e-02$	$3.07e-02$

visualized in Fig. 3.4. Owing to small pulses, the waves from adsorption and desorption fronts interact within the column, leading to a more dispersed concentration band, especially for the second component, which the neural network model captured well. Again, this can be attributed to the fact that the neural network learned the governing coupled PDEs well along with the constraints of matching the labelled data.

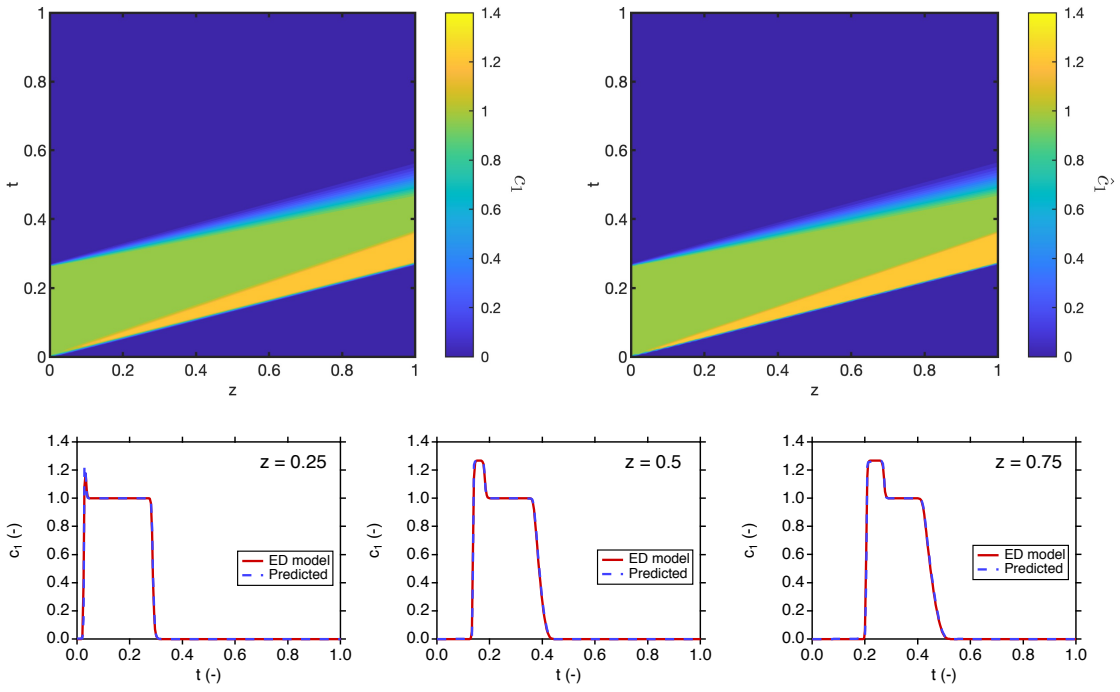

(a)

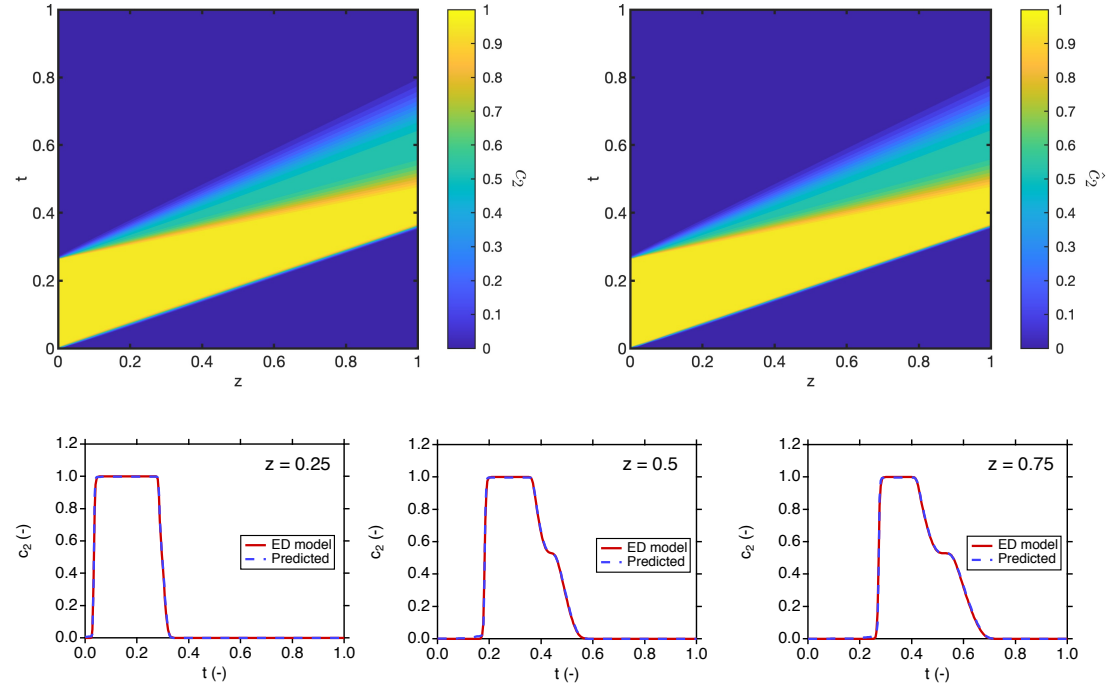

(b)

Figure 3.3: Comparison between the neural network predicted and the ED model spatiotemporal solutions of solute concentrations of (a) the first and (b) the second components for training case #3.

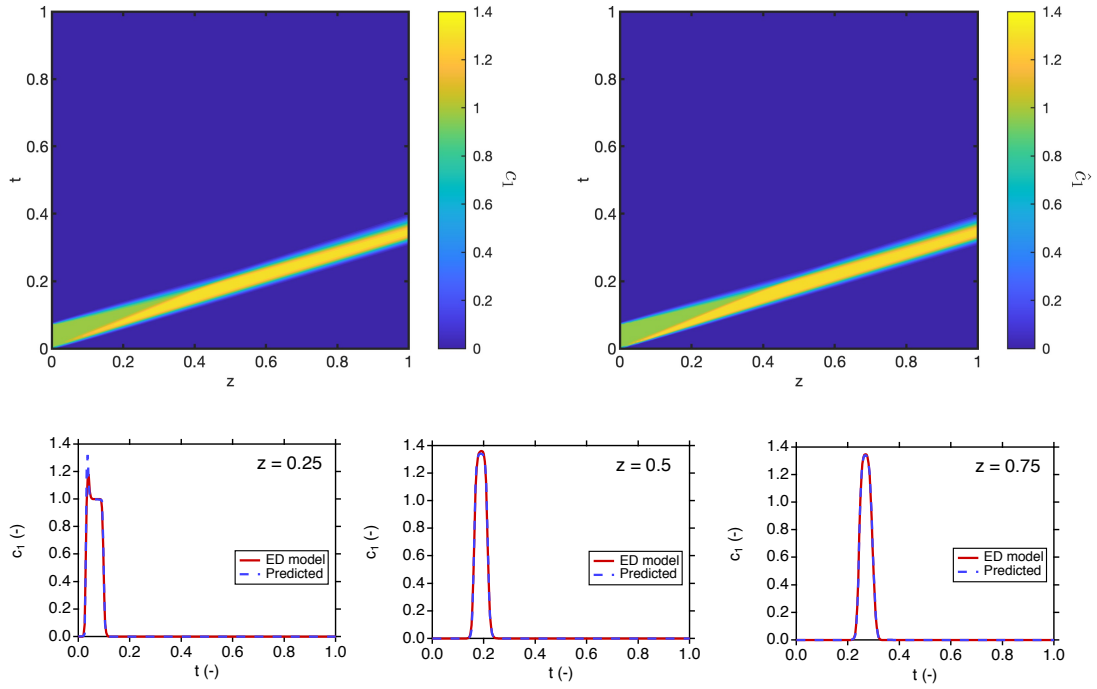

(a)

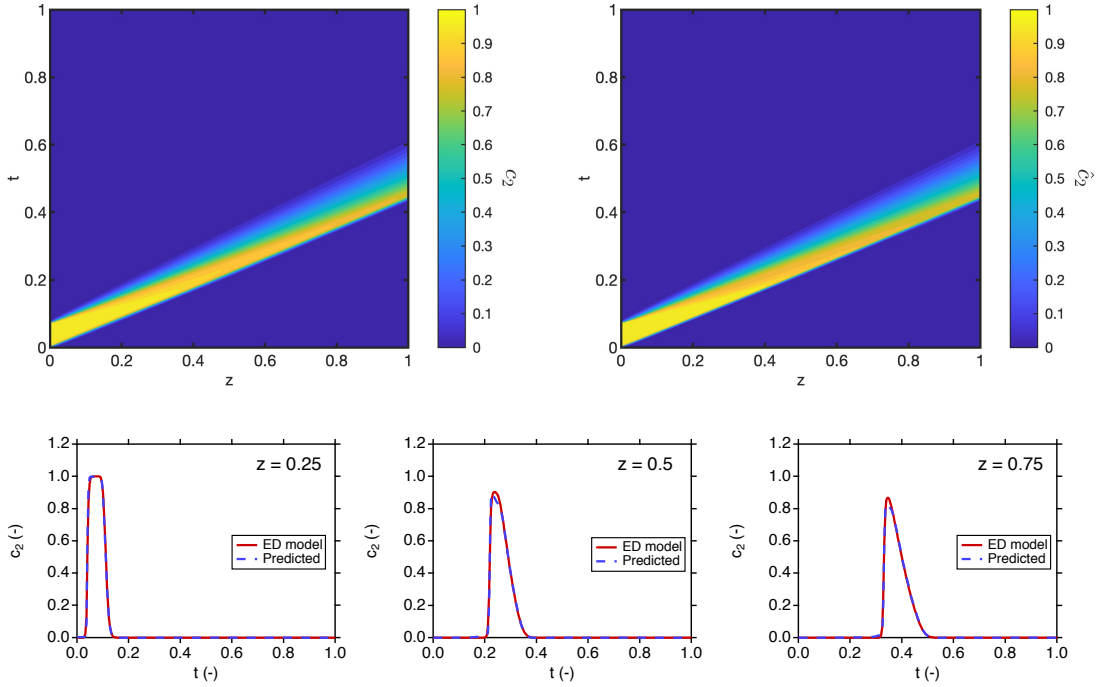

(b)

Figure 3.4: Comparison between the neural network predicted and the ED model spatiotemporal solutions of solute concentrations of (a) the first and (b) the second components for training case #4.

3.4.2 Model performance for test cases

The neural network model prediction abilities are evaluated by considering two test cases. The two test cases considered herein are as follows: *Test case 1:* c_1^0 = 3.5 mg ml^{-1}, c_2^0 = 2.5 mg ml^{-1}, and τ = 477 s; *Test case 2:* c_1^0 = 4 mg ml^{-1},c_2^0 = 3.5 mg ml^{-1}, and τ = 265 s. The test cases that are different from training cases (provided in Table 3.1) are randomly chosen to determine the model's generic ability to capture the complex dynamics of solute transport in chromatography columns. The spatiotemporal concentration solutions are obtained based on the trained neural network and ED models. The solutions from high fidelity ED model simulations serve as the reference for comparing predicted results from the neural network model. It is worth mentioning that the neural network model predictions are almost instantaneous and up to 500 times faster than the ED model simulations.

Figure 3.5 illustrates the spatiotemporal solutions of two solute concentrations obtained by the neural network model for test case 1. Here, test case 1 is an example for large-volume pulse injections. As can be seen from the figure, the predictions from neural network and ED models are in excellent agreement. The relative $\mathcal{L}_2$ error between the predicted and the ED model concentrations for the first and the second components are $1.35e-02$ and $9.20e-03$, respectively. Similar to training cases, the important features such as overshoot in the concentration profiles of the first component, plateaus on the desorption front of the second component are well captured. The test case 2 represents the dynamics of solute transport when subjected to a pulse injection between small- and large-volumes. In Fig. 3.6, the predictions from the neural network model are illustrated where the relative $\mathcal{L}_2$ error between the neural network predicted and the ED model concentrations for the first and the second components are $1.76e-02$ and $9.6e-03$, respectively. Since the width of the pulse injection is not large enough, the first component moves faster than the second component such that the entire peak of the pulse overshoots, unlike in the previous test case, where a portion of pulse of

the first component returns to the feed concentration as it traverses along the column. The neural network accurately describes this feature, even for new values of c_1^0, c_2^0, and τ where no information on the spatiotemporal domains was provided. This again indicates that the neural network model remarkably learned the underlying physical laws.

Extrapolation capabilities

The goal here is to investigate the extrapolation capabilities of the trained neural network model. To this end, two additional test cases are introduced. The values of c_1^0, c_2^0, and τ are chosen such that they fall outside the limits of the training range (i.e. outside of 0.3 and 5 mg ml^{-1} for c_1^0, c_2^0, and outside of 100 and 550 s for τ). The two additional test cases are as follows: *Test case 3:* c_1^0 = 0.1 mg ml^{-1},c_2^0 = 5.5 mg ml^{-1}, and τ = 50 s; *Test case 4:* c_1^0 = 5.5 mg ml^{-1},c_2^0 = 0.1 mg ml^{-1}, and τ = 600 s. High fidelity ED model simulations are also carried out on these cases for comparison. The neural network model predictions for the additional test cases are illustrated in Figs. 3.7 and 3.8. The relative $\mathcal{L}_2$ error between the neural network predicted and the ED model concentrations for the first component in test cases 3 and 4 are $1.08e+00$ and $1.35e-01$, respectively, whereas for the second component, the $\mathcal{L}_2$ error was calculated to be $7.18e-01$ and $1.66e-01$ in test cases 3 and 4, respectively. While the $\mathcal{L}_2$ error is higher compared to previous cases, the overall model performance is reasonably good. For instance, in Fig. 3.7, the neural network predicted dynamics of small pulse injection for two solute components is in good agreement with the ED model. Especially, the movement and width of the solute bands are captured very well by the neural network model. One feature that the neural network model failed to describe is concentration peaks of the first and the second component as it traverses along the column. In the other test case where the pulse injection is very large, the neural network predictions are comparable to the spatiotemporal solutions obtained from the ED model. Solute movement, inter-

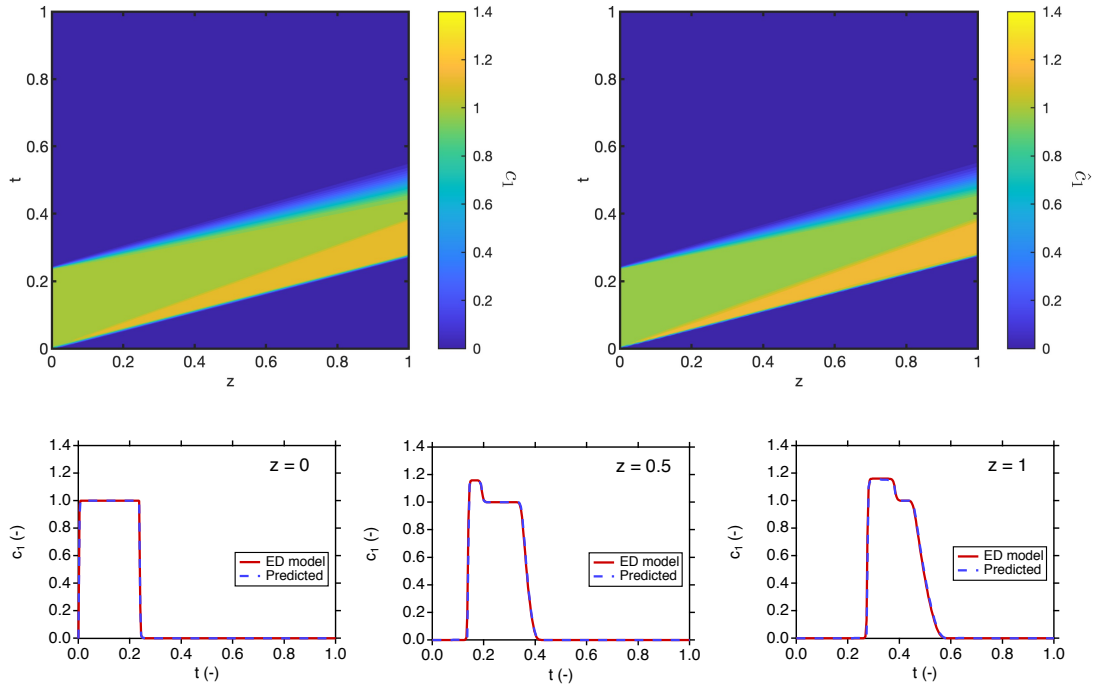

(a)

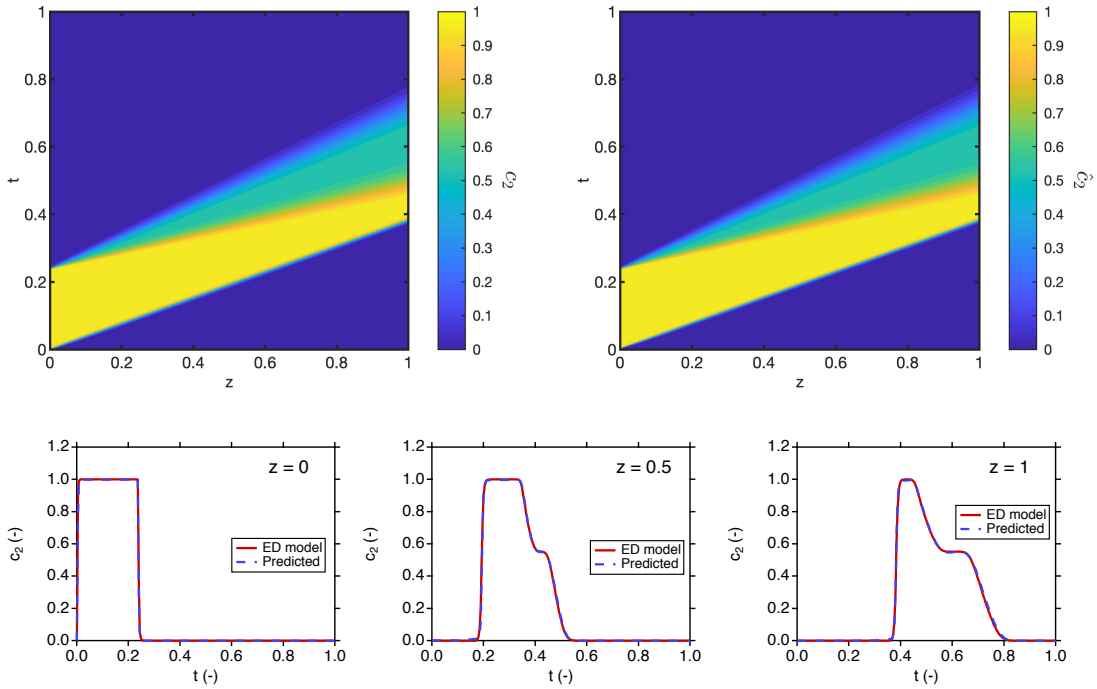

(b)

Figure 3.5: Comparison between the neural network predicted and the ED model spatiotemporal solutions of solute concentrations of (a) the first and (b) the second components for the test case #1.

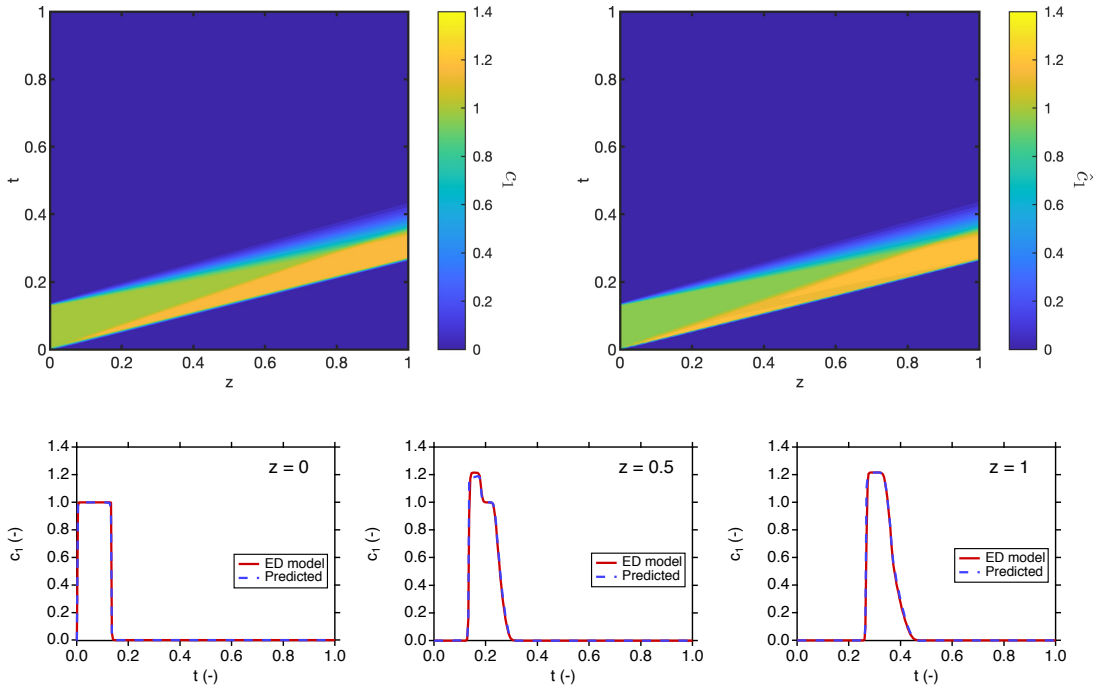

(a)

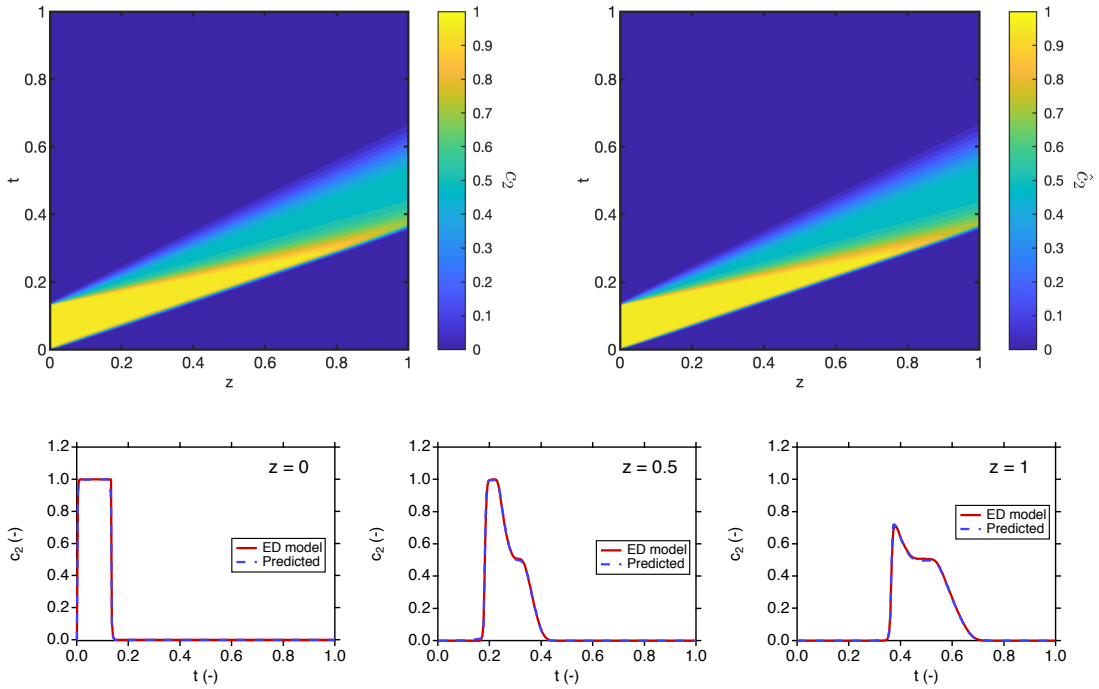

(b)

Figure 3.6: Comparison between the neural network predicted and the ED model spatiotemporal solutions of solute concentrations of (a) the first and (b) the second components for the test case #2.

mediate plateaus are reasonably predicted well, although not identical to the ED model solutions. Probably, increase in the number of training cases or labelled data could potentially improve the model's accuracy to capture these fine details. The incorporation of the physics-based constraints in the neural network training, as opposed to traditional approaches, has definitely contritubed to the model extrapolation capabilities.

3.4.3 Process optimization of a chromatographic separation

In most practical separations, the operation of chromatography cycles to achieve complete separation of solute components with shorter cycle times is desired, thus enabling rapid baseline separation of the components of the feed mixture. To this end, appropriate pulse injection times (τ) must be determined such that the outlet concentration profiles of the solute components are baseline separated, i.e, the baseline of the desorption front of the first component at the outlet overlaps with the baseline of the adsorption front of the second component's outlet concentration profile. Although equilibrium theory can rapidly estimate τ for ideal cases with no dispersion [81], computationally expensive numerical simulations based on the ED model are often coupled with optimization routines to determine optimal τ for practical systems with finite dispersion. Here the trained neural network model is coupled with the NSGA-II algorithm to quickly optimize τ for baseline separation of four randomly chosen binary feed concentration mixtures shown in Table 3.6. For each case, unique optimizations, comprising 300 NSGA-II evaluations, are carried out to determine optimal τ that leads to baseline separation. In these optimizations, the objective function J is minimized as follows:

$$J = \chi_1(t_{\mathrm{D},1} - t_{\mathrm{A},2})^2 + \frac{\chi_2}{\tau} \tag{3.15}$$

where $t_{\mathrm{D},1}$ is the residence time of the baseline (defined as the 2% of the concentration peak) of the desorption front of the first component at the outlet and $t_{\mathrm{A},2}$ is the residence time of the baseline of the adsorption front of the second component at the outlet. χ_1 and χ_2 are the penalty factors. The second term in the objective function

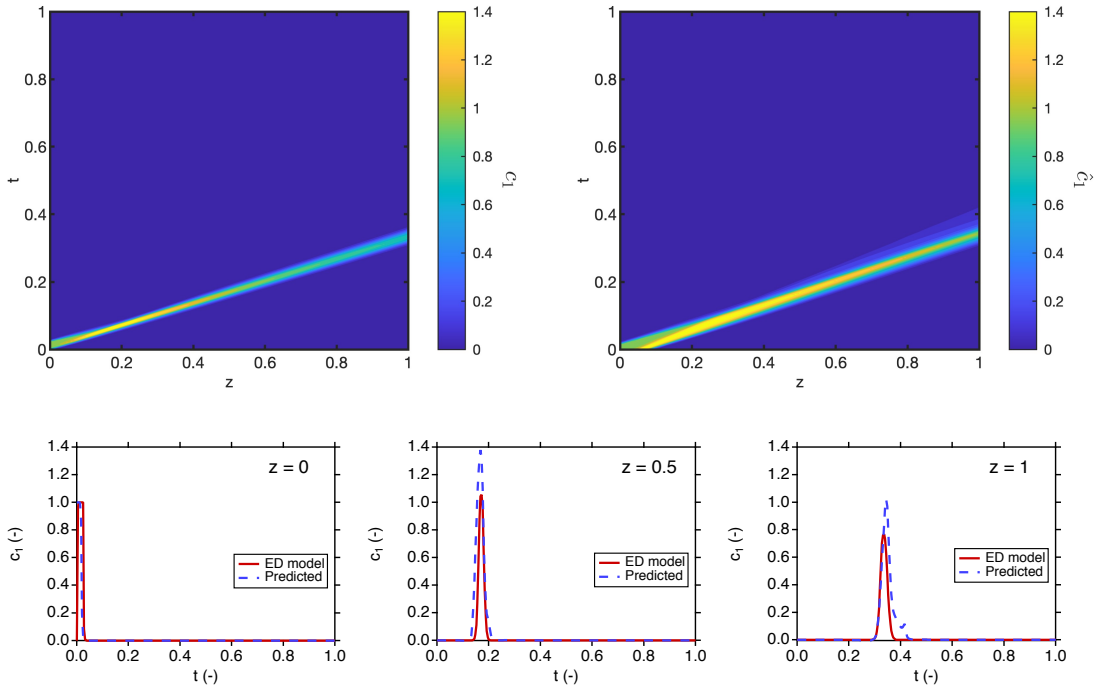

(a)

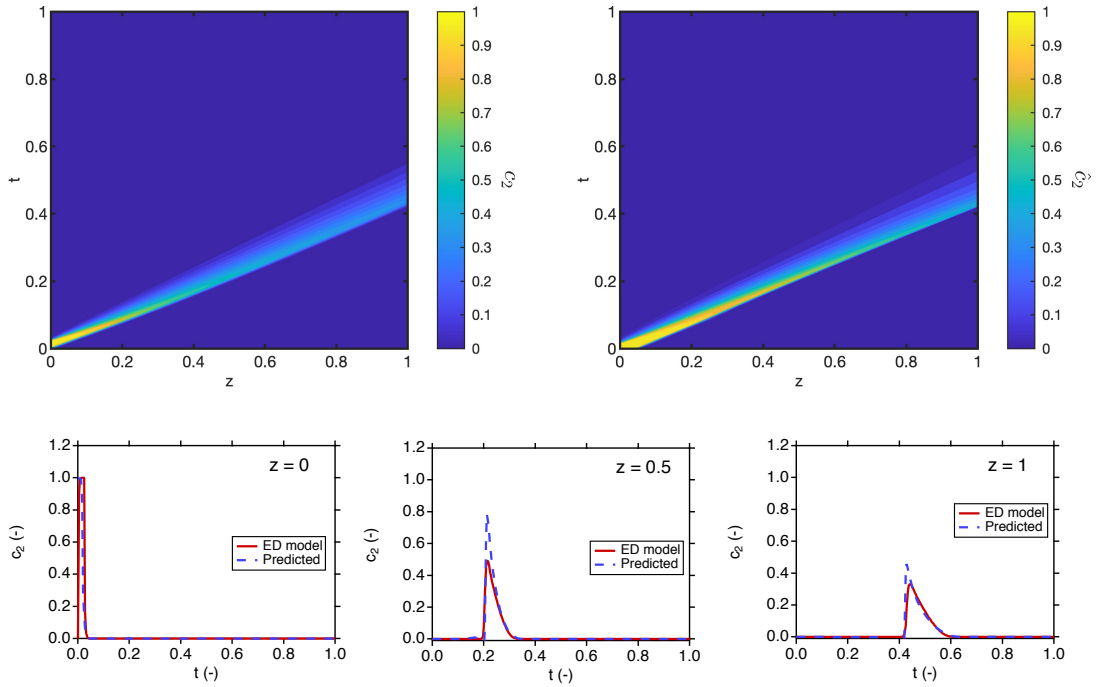

(b)

Figure 3.7: Test of extrapolation capability of the neural network model. Comparison between the neural network predicted and the ED model spatiotemporal solutions of solute concentrations of (a) the first and (b) the second components for the test case #3.

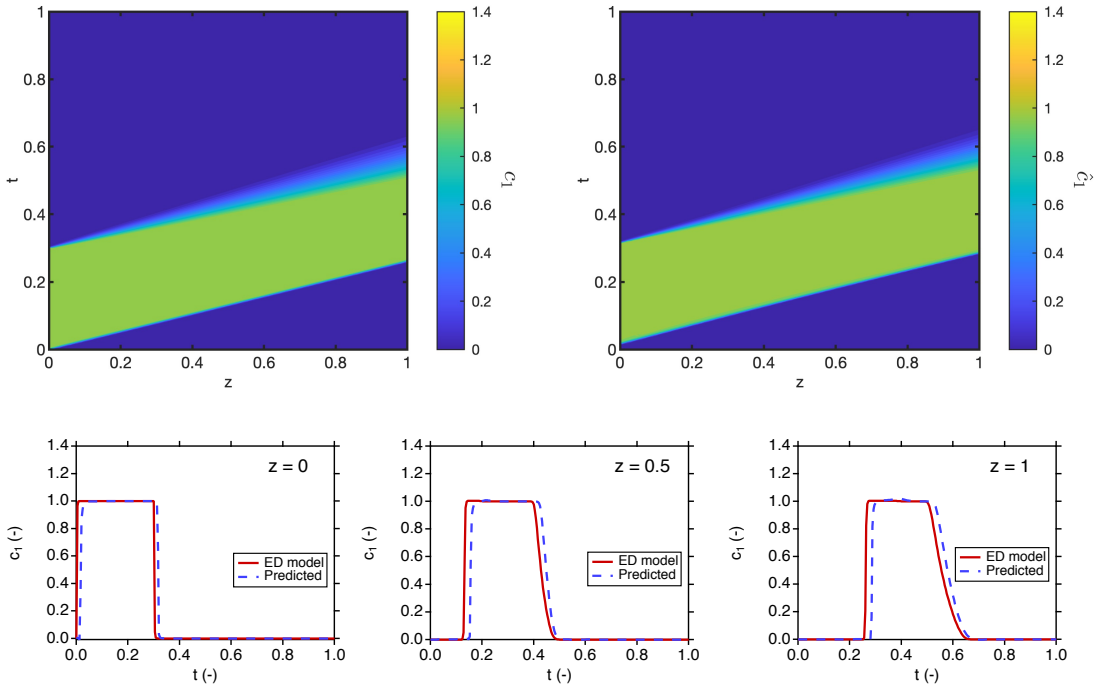

(a)

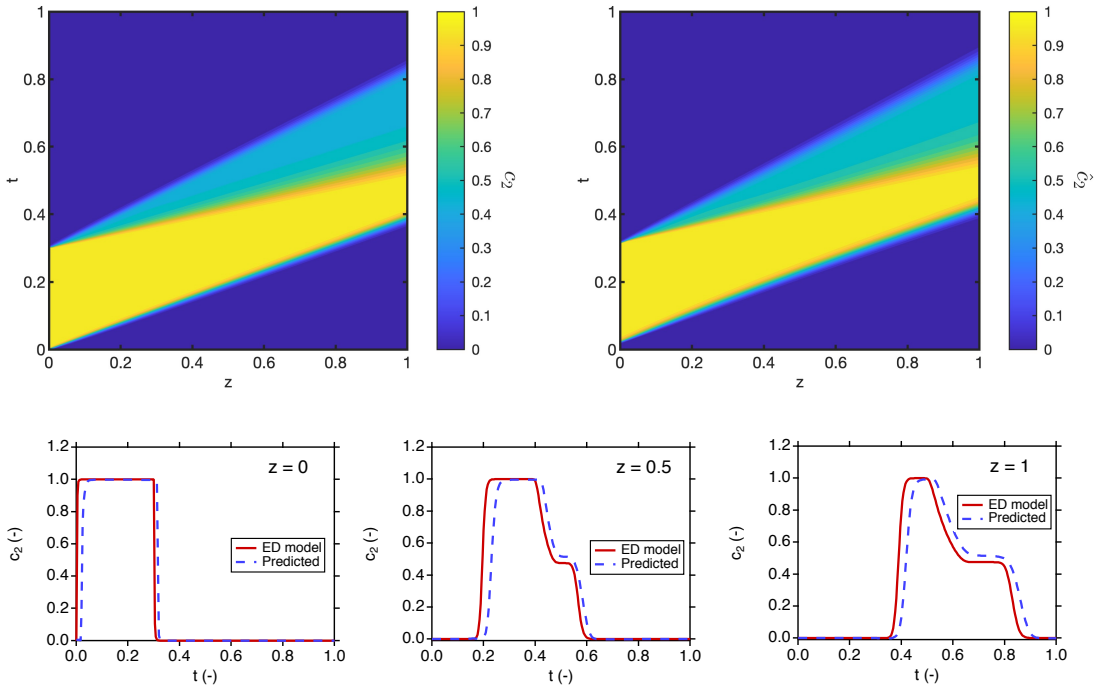

(b)

Figure 3.8: Test of extrapolation capability of the neural network model. Comparison between the neural network predicted and the ED model spatiotemporal solutions of solute concentrations of (a) the first and (b) the second components for the test case #4.

ensures that the maximum possible injection time is chosen to achieve baseline separation.

Table 3.6: Different binary feed concentration mixtures considered for the optimization of pulse injection times to achieve baseline separation.

c_1^0 (mg ml^{-1})	c_2^0 (mg ml^{-1})
2.04	3.16
3.66	1.28
3.51	3.07
0.57	3.87

Figure 3.9 illustrates the baseline separated outlet concentration curves of the two components of four different feed concentration mixtures based on optimal pulse injection times obtained from neural network-based optimizations. The corresponding outlet concentration curves calculated based on ED model simulations are shown for comparison. The optimal pulse injection times obtained in each case are reported in Fig. 3.9. As can be seen from the figure, the neural networks were accurate in predicting the optimal injection times for baseline separation of the four different feed concentration mixtures considered. It is worth noting that the neural network-based optimizations took minimal computational time. In fact, the time required to complete the entire optimization, comprising 300 evaluations, was shorter than the time required to run one simulation using the ED model.

3.5 Conclusions

This study demonstrated the effectiveness of physics-based neural networks to predict the complex dynamics of generic pulse injections in chromatography columns. The capabilities of physics-based neural networks were tested by investigating the impact of feed concentrations of binary solute mixtures and injection volumes on the solute movement along the column. To this end, a generic neural network model was devel-

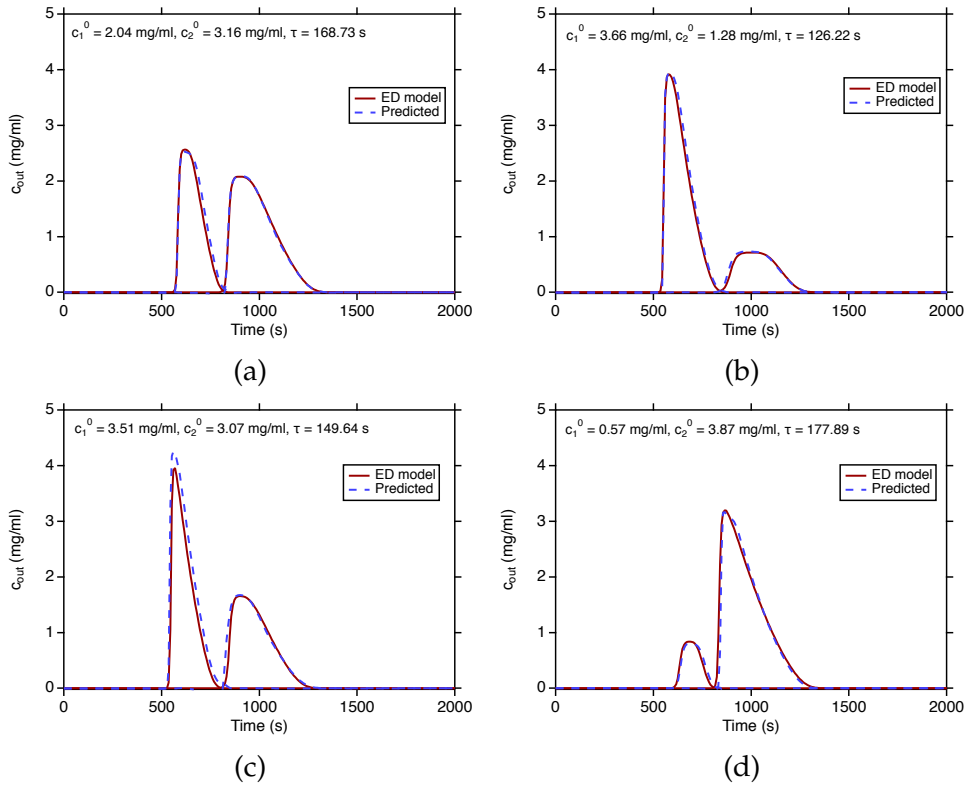

Figure 3.9: Baseline separated outlet concentration profiles (dashed lines) of the two components of four different feed concentration mixtures based on optimal pulse injection times obtained from the neural network-based optimizations. For comparison, ED model simulation-based outlet concentration profiles (solid lines) are also shown.

oped that takes five inputs, namely, spatiotemporal coordinates, inlet binary feed concentrations, and the injection time to predict the spatiotemporal solutions of two solute concentrations. A deep neural network architecture consisting of 7 layers with 50 hidden neurons was trained using ten different cases representing a unique combination of inlet binary feed concentrations, the injection time, and a unique spatiotemporal solution. For the neural network learning, labelled data comprising the initial and boundary data from the high fidelity simulations was first gathered across all training cases and then, the inputs and the physical quantities are non-dimensionalized and normalized, respectively, to ensure appropriate scaling. Subsequently, a loss function that accounts for terms constraining the predictions of the neural network to match the labelled data and the PDE residuals was minimized.

The results demonstrated that the trained neural network accurately predicts the solute movement in chromatography columns. Particularly, important features such as concentration transitions, front interactions typically encountered in chromatography systems were well-captured by the neural network model, even though no information inside the spatiotemporal domains were provided. Compared to traditional neural network approaches, physics-based modelling requires only a small amount of data. In terms of computational speeds, the neural network-based simulations are approximately 500 times faster than the ED model simulations. Although the physics-based neural networks are applied for a specific case study, the framework, in principle, can be extended to represent a more general system. For instance, adsorption isotherm parameters, mass transfer coefficients, column sizes, and operating parameters can also be introduced as input variables. Such models can be used for applications such as online monitoring, control, etc.

Chapter 4

Physics-based deep neural networks for synthesizing and simulating cyclic adsorption processes

4.1 Introduction

Cyclic adsorption processes are particularly attractive for their flexibility in process configurations and hence, are extensively used in industrial gas separations such as hydrogen purification, oxygen enrichment, methane purification, carbon dioxide removal, etc. [1, 12]. In the most commonly used processes such as pressure swing adsorption (PSA), vacuum swing adsorption (VSA), temperature swing adsorption (TSA), etc., one or more fixed bed adsorption columns (with or without interactions) packed with a suitable adsorbent undergo several sequence of steps through a cyclic variation of pressure or temperature in order to perform the separation. Several process configurations (or cycles) can be synthesized by altering the sequence of steps or interactions among the adsorption columns. Given the transient and modular nature, adsorption processes are rather complex and operate at cyclic steady state (CSS). Rigorous mathematical models based on the underlying physical laws are required to better understand, simulate and design such complex processes [19]. Process simulations involve solving these rigorous models characterized by a system of coupled nonlinear partial differential equations (PDEs) repeatedly in time and space until CSS. Further,

each process configuration needs to be thoroughly optimized where thousands of simulations are carried out in order to identify the optimal set of design variables that yield the best process performance. Inherently, this makes the design and optimization of cyclic adsorption processes computationally expensive, thereby limiting the design to few process configurations for practical applications [25, 40]. With the recent discovery of hundreds of thousands of adsorbents for gas separations [30], the current simulation and optimization tools based on rigorous mathematical models are computationally inadequate to handle such huge databases of adsorbents for process design and optimization.

To address the computational challenges posed by adsorption process design and optimization, the use of machine learning techniques such as artificial neural networks (ANNs) have emerged as alternatives to rigorous mathematical models. To this end, Sant Anna et al. [59] developed three-layer feed-forward ANN (input layer, one hidden layer and one output layer) models for the separation of methane and nitrogen using PSA. Using these models in the optimization, the authors show that the computational times significantly reduced from 15.7 h to 50 s. Subraveti et al. [73] constructed three-layer feed-forward ANN models initially within an optimization framework and subsequently used them to determine the Pareto solutions of multi-objective maximization of CO_2 purity and recovery for a complex eight-step PSA cycle designed for pre-combustion CO_2 capture. As a result, the relative error of Pareto solutions in both objectives was less than 1% and accelerated the optimization routine by ten times. Xiao et al. [89] instead used a multi-output feed-forward ANN architecture to predict process performances in the PSA optimizations. Pai et al. [74] extended the use of feed-forward ANN models to predict the axial profiles of the intensive variables for a four-step VSA process at CSS, and the models were experimentally validated. Furthermore, Oliveira et al. [90] developed a real-time soft sensor for a PSA unit based on neural network models. Three types of ANN architectures, namely, feed-forward,

recurrent and long short-term memory (LSTM) based on multi-input and a single output, are used to predict the PSA process performance over the number of cycles. The LSTM-based deep neural networks were found to be reliable for optimization, control and online measurements of PSA units. However, in these studies, ANN models were trained to learn the mapping between the inputs and the outputs for a fixed process configuration. This means that the models need to be retrained if the process configuration is changed. Therefore, a more generalized framework is required in order to facilitate the adsorption cycle synthesis and allow for the evaluation of several process configurations. For instance, Leperi et al. [45] used ANN to model individual steps in typical PSA processes for post-combustion CO_2 capture. Each step was modelled using 12 four-layer ANN (input layer, two hidden layers and multi-output layer). The trained ANN models predicted the five state variables, i.e. absolute pressure, CO_2 gas phase mole fraction, CO_2 molar loading, N_2 molar loading and column temperature, at ten different locations across the column. In the ANN models training, the normalized mean squared error between the neural network predictions and the training data from rigorous simulations was minimized. While this approach allowed synthesis of different PSA cycles, such models can require a large amount of training data to obtain accurate predictions.

The latest groundbreaking advances in artificial intelligence, machine and deep learning have allowed for the development of viable methodologies to model various physical systems comprising governing PDEs [72]. To this end, ANNs with several hidden layers, also known as deep neural networks (DNNs), have shown an enhanced ability to capture very complex nonlinear dynamics that led to tremendous interest for modelling physical systems. Particularly the idea of learning PDEs through constraint-based loss functions [75–77]. For instance, Raissi *et al.* [77] developed a physics informed neural network framework in which fully connected DNNs are capable of learning the PDE solutions anywhere on the spatiotemporal domain with few

training points by incorporating a physics-constrained loss function. The presence of PDE-based terms in the loss function inherently facilitates the physics-constrained regularization of the neural networks. Owing to the additional knowledge of physics, the learning process for neural networks require only small amounts of training data, compared to the complexity of the systems described. The philosophy of physics constraining the loss function was later adopted for several applications [78–80]. However, most of these studies focused on demonstrating the capabilities of physics-based neural networks to learn a single PDE solution, i.e. for given initial and boundary conditions. If initial or boundary conditions change, then the physics-based neural networks have to be retrained. In cyclic adsorption processes, the initial condition of each step depends on the previous step's final condition that changes every cycle. This means that the PDE solutions differ from step to step and also every cycle. Therefore, a more generalized framework is required to implement the physics-based neural networks for cyclic adsorption systems.

In the present chapter, a physics-based neural network modelling framework is developed to synthesize and simulate different adsorption processes. By choosing the appropriate training philosophy, the framework developed herein does not require any system-specific inputs *such as isotherm parameters*. Accordingly, unique neural networks models are trained for different *constituent steps* typically encountered in cyclic adsorption processes. The trained neural network model for each constituent step aims to predict the entire spatiotemporal solutions of state variables for a given initial gas composition profile and step-parameters obeying underlying physical laws. The proposed methodology is first tested by constructing and simulating a four-step VSA cycle for post-combustion CO_2 capture. The performance of neural network models is then assessed by comparing the results from the neural network predictions with rigorous process simulations for a variety of operating conditions. Subsequently, the methodology is extended to synthesize and simulate four different VSA cycles for post-

combustion CO_2 capture. The cycle synthesis capabilities of this approach are demonstrated by comparing the neural network- and the detailed process model-based simulations based on the four VSA cycles considered.

4.2 VSA governing equations

The one-dimensional mathematical model describes the adsorption column dynamics in VSA cycles after incorporating the following assumptions:

1. Axially dispersed plug flow model to describe the gas phase.
2. No radial gradients exist for composition and pressure across the column.
3. The gas-phase behaves ideally.
4. Uniform bed properties along the column.
5. The linear driving force model accounts for the solid-phase mass transfer.
6. Pressure drop calculations are based on Darcy's law (valid for the column sizes and the operating conditions considered here).
7. System operated under isothermal conditions.

Based on the above assumptions, the model comprises a system of coupled nonlinear PDEs based on the conservation of mass and momentum and takes the form:

$$\frac{\partial c_i}{\partial t} = \frac{\partial}{\partial z}\left[cD_{\mathrm{L}}\frac{\partial y_i}{\partial z} - c_i v\right] - \frac{1-\varepsilon}{\varepsilon}\frac{\partial q_i}{\partial t} \tag{4.1}$$

$$\frac{1}{P}\frac{\partial P}{\partial t} = -\frac{1}{P}\frac{\partial (Pv)}{\partial z} - \frac{RT_0}{P}\frac{1-\varepsilon}{\varepsilon}\sum_{i=1}^{n_{\mathrm{comp}}}\frac{\partial q_{\mathrm{i}}}{\partial t} \tag{4.2}$$

$$-\frac{\partial P}{\partial z} = \frac{150}{4}\frac{1}{r_{\mathrm{p}}^2}\Big(\frac{1-\varepsilon}{\varepsilon}\Big)^2 \mu v \tag{4.3}$$

Here Eqs. 4.1 and 4.2 are component and overall mass balances for the gas phase, respectively. In Eq. 4.1, c_i, y_i, q_i are the gas-phase concentration, the gas-phase molar

composition, and the solid-phase loading of the component i, v is the interstitial velocity, ε is the bed void fraction, and D_{L} is the axial dispersion coefficient. The ideal gas law relates c_i and y_i as follows: $c_{\mathrm{i}} = \frac{y_{\mathrm{i}} P}{R T_0}$, where P is the total pressure, R is the universal gas constant, and T_0 is the reference temperature. Using Eqs. 4.1 and 4.2, the gas-phase molar composition of the first component, y_1, and the the total pressure P are calculated, respectively. From the solution of y_1, the gas-phase molar composition of the second component can be obtained simply by: $y_2 = 1 - y_1$. Equation 4.3 represents the Darcy's law for calculating the pressure drop throughout the column, where r_{p} and μ are the particle radius and the gas-phase viscosity.

In addition to above equations, the linear driving force model describes the mass transfer in the solid phase:

$$\frac{\partial q_{\mathrm{i}}}{\partial t} = k_{\mathrm{i}}(q_{\mathrm{i}}^{*} - q_{\mathrm{i}}) \tag{4.4}$$

where q^* is the equilibrium loading and k is the mass transfer coefficient expressed, based on the assumption that the molecular diffusion in the macropores controls the transport into the solid phase, as follows:

$$k_{\mathrm{i}} = \frac{c_{\mathrm{i}}}{q_{\mathrm{i}}^{*}} \frac{15 \varepsilon_{\mathrm{p}} D_{\mathrm{p}}}{r_{\mathrm{p}}^2} \tag{4.5}$$

The adsorption equilibria was quantified using the competitive dual-site Langmuir (DSL) isotherm model as shown below:

$$q_i^{*} = \frac{q_{\mathrm{sb},i} b_i c_i}{1 + \sum_i b_i c_i} + \frac{q_{\mathrm{sd},i} d_i c_i}{1 + \sum_i d_i c_i} \tag{4.6}$$

where q_i^* is the equilibrium solid-phase loading of the component i, $q_{\mathrm{sb},i}$ and $q_{\mathrm{sd},i}$ are saturation capacities for the two sites and, b_i and d_i are the adsorption equilibrium constants. It is worth noting that the heat effects that are prominent in gas adsorption systems are deliberately not considered in the present chapter for simplicity. In the future, heat effects will be accounted for to represent gas adsorption processes accurately.

4.3 Physics-based neural networks

Physics-based neural networks adopt modern deep learning techniques to infer the underlying physical laws that involve PDEs [77]. The framework used for this study is illustrated in Fig. 4.1. Here the neural networks are trained to learn the conservation laws of mass and momentum along with adsorption equilibria. To this end, the residuals of PDEs are incorporated into the loss function so that the neural networks are trained to match the labelled data while penalizing them for violation of physical laws. Such formulation allows the neural networks to learn the spatiotemporal solutions with small amounts of labelled data. It is worth noting that the labelled data represents the training data obtained from the high fidelity simulations.

The spatiotemporal solutions of PDEs are unique to initial and boundary conditions. Since the position of valves at the two ends of adsorption columns in VSA processes periodically change to implement different steps in the cycle, boundary conditions in each constituent step are different. Depending on the state (open or close) of the valves, constituent steps can be categorized into generalized boundary conditions, such as open-open, open-closed, closed-open, etc. Hence, it is reasonable to construct separate neural network models to predict the dynamics of each step. Moreover, in a cyclic process, the initial condition for each step depends on the final condition of the preceding step. This means that the initial conditions change based on the sequence and the duration of steps. To account for such variations in initial conditions, neural network models of each step type must be able to learn the solutions for an arbitrary initial condition. Another feature that affects the dynamics of adsorption columns is the step parameters such as operating pressures, inlet gas conditions, etc. Here the neural network models are trained based on N_k different initial profiles and the step parameters to have generalized capabilities.

One deep neural network is defined for each constituent step s in the VSA process,

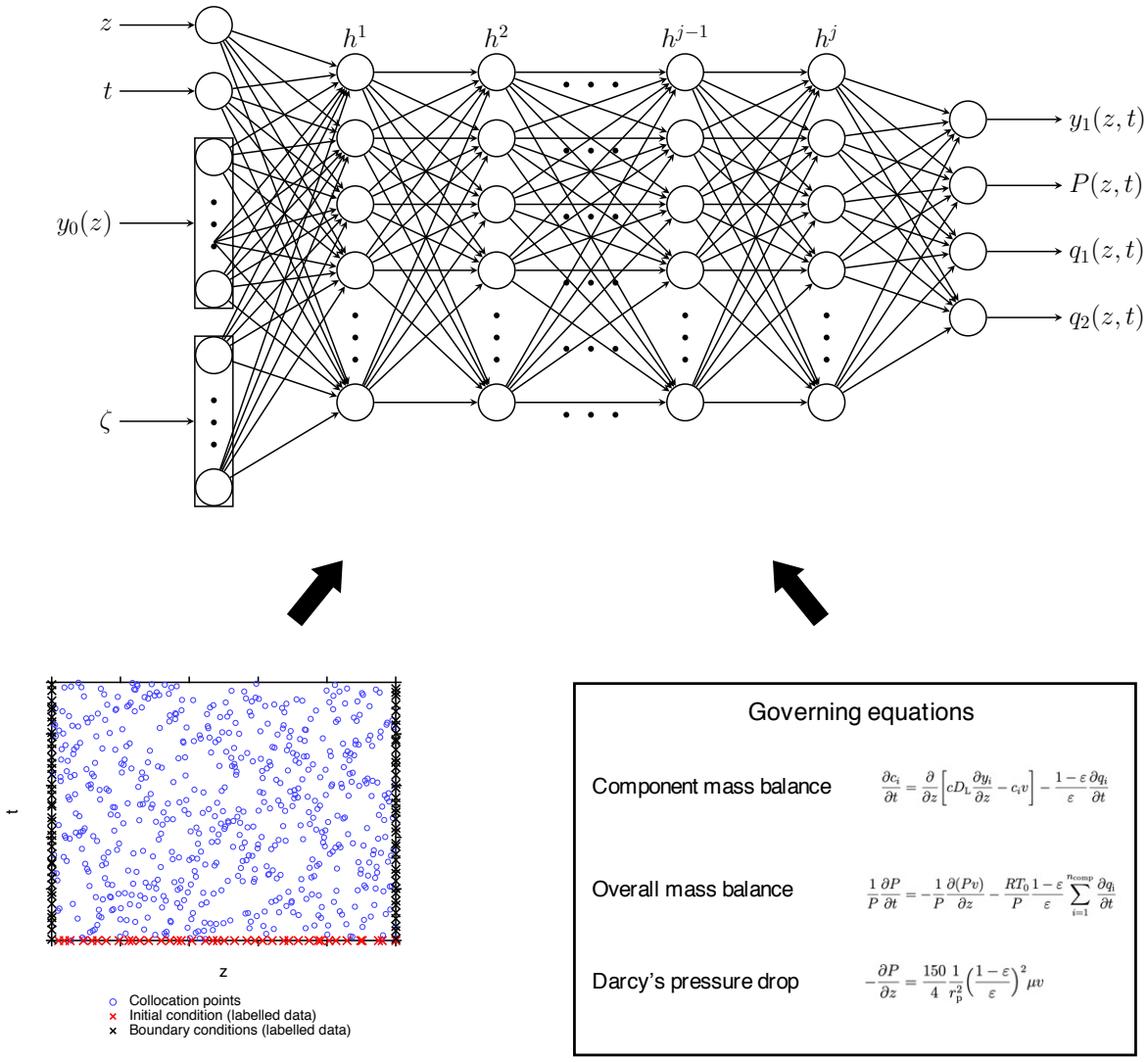

Figure 4.1: The physics-based neural network framework used for simulating each constituent step in cyclic adsorption processes. *Top:* Deep neural network architecture. *Bottom left:* Spatiotemporal domain with collocation points (blue), initial (red) and boundary (black) data from the simulations. *Bottom right:* Underlying governing equations of cyclic adsorption processes.

and the goal of the neural network is to learn the following mapping:

$$[z, t, y_0^s(z), \zeta^s] \xrightarrow{\theta^s} [y_1^s(z,t), P^s(z,t), q_1^s(z,t), q_2^s(z,t)] \tag{4.7}$$

Here the neural network takes the following inputs: spatiotemporal coordinates (z, t), initial gas-phase molar composition profile, $y_0^s(z)$, of the first component, and step parameters, ζ^s, for the step s. The neural network $f^s(z, t, y_0^s(z), \zeta^s, \theta^s)$ outputs the four

state variables, namely, gas-phase composition of the first component, $y_1^s(z,t)$, the column total pressure, $P^s(z,t)$, and solid loadings, $q_1^s(z,t)$ and $q_2^s(z,t)$. The symbol θ^s represents the parameters of the neural network used for the individual step s. In other words, the neural network approximates the spatiotemporal solutions of four state variables of the step s for a given initial gas composition profile $y_0^s(z)$ and step parameters ζ^s based on θ^s.

Based on the component and overall mass balances in Eqs. 4.1 and 4.2, the residuals can be defined as follows:

$$\begin{aligned} r_c(z,t) :=& \frac{\partial c_1}{\partial t} + \frac{\partial}{\partial z}\left[c_1 v - cD_{\mathrm{L}}\frac{\partial y_1}{\partial z}\right] + \frac{1-\varepsilon}{\varepsilon}\frac{\partial q_1}{\partial t} \\ r_p(z,t) :=& \frac{1}{P}\frac{\partial P}{\partial t} + \frac{1}{P}\frac{\partial (Pv)}{\partial z} + \frac{RT_0}{P}\frac{1-\varepsilon}{\varepsilon}\left[\frac{\partial q_1}{\partial t} + \frac{\partial q_2}{\partial t}\right] \end{aligned} \tag{4.8}$$

And $v = \frac{4}{150\mu}\left(\frac{\varepsilon}{1-\varepsilon}\right)^2 r_{\mathrm{p}}^2\left(-\frac{\partial P}{\partial z}\right)$ is directly substituted in Eq. 4.8 to account for Darcy's pressure drop through the column without defining Eq. 4.3 as a separate residual. Moreover, Eqs. 4.4-4.6 are not required to calculate $q_1(z,t)$ and $q_2(z,t)$. Instead, the neural networks are expected to learn solutions for $q_1(z,t)$ and $q_2(z,t)$ through constraints imposed on the right hand side of Eq. 4.8 to be zero while also matching the labelled data corresponding to q_1 and q_2. More details on the neural network architecture, the loss function, and the learning procedure are provided below.

4.3.1 Neural network architecture

Feed-forward deep neural networks are considered in this chapter, comprising N_{layers} layers (one input layer, N_{layers} - 2 hidden layers and one output layer) with a predefined number of neurons. The neurons are interconnected to form a fully-connected complex network as shown in Fig. 4.1. The inputs to each neuron are combined with a set of coefficients called weights which can either dampen or amplify the input depending on its significance. In addition to weights, each neuron also has a bias. The inputs, weights and biases are combined in each neuron through a nonlinear activation function as

shown below:

$$X_{\mathrm{l}} = \sigma_{\mathrm{l}}(X_{\mathrm{l}-1}W_{\mathrm{l}} + b_{\mathrm{l}}) \tag{4.9}$$

where $X_{\mathrm{l}-1}$ is the output of the $l-1$ layer; W_{l} and b_{l} represent the weight matrix and bias vector of the layer l, respectively and; X_{l} is the output of the l layer. The dimensions of weight matrix W_{l} and bias vector b_{l} are $N_{\mathrm{l}-1} \times N_{\mathrm{l}}$ and N_{l}, respectively, where $N_{\mathrm{l}-1}$ and N_{l} are the number of neurons in the $l-1$ and l layer, respectively. Collectively, the weight matrices (**W**) and biases (**b**) of the entire neural network are denoted using θ, i.e., (**W**, **b**) $\in \theta$. In this way, each layer receives the outputs of a previous layer as inputs and feeds forward to the next layer. The number of hidden layers, N_{layers}, number of hidden neurons, N_{l}, and the activation functions (such as tanh, sine, sigmoid, etc.) are considered model hyperparameters and selected based on limited numerical experimentation.

4.3.2 Loss function

For enabling the mapping in Eq. 4.7, the hidden parameters, θ, need to determined by optimizing the loss function. The loss function constructed herein comprises two parts. Details of each part of the loss function are provided below:

Loss term: Labelled data

In this part of the loss function, the predictions of the neural network are constrained to match the labelled data. Here the labelled data refers to the training data obtained from the high fidelity simulations. The PDE solutions are unique to initial and boundary conditions of the each step s and proper enforcement of initial and boundary conditions is essential to have well-posed systems. Hence, the initial and the boundary data from the simulations are introduced as the labelled data. The loss term is expressed as the mean-squared error (MSE) between the neural network predictions and

the labelled data. The loss term (for index #k) can be written as

$$\mathcal{L}^k_{data,0} = \frac{1}{N^k_{i,0}}\Bigg[\lambda_{0,y_1}\sum_{i=1}^{N^k_{i,0}}\Big[\hat{y_1}(z^k_i,0,y^k_0(z),\zeta^k,\theta^s) - y_1(z^k_i,0,y^k_0(z),\zeta^k)\Big]^2 + \lambda_{0,P}\sum_{i=1}^{N^k_{i,0}}\Big[\hat{P}(z^k_i,0,y^k_0(z),\zeta^k,\theta^s) - P(z^k_i,0,y^k_0(z),\zeta^k)\Big]^2 + \lambda_{0,q_1}\sum_{i=1}^{N^k_{i,0}}\Big[\hat{q_1}(z^k_i,0,y^k_0(z),\zeta^k,\theta^s) - q_1(z^k_i,0,y^k_0(z),\zeta^k)\Big]^2 + \lambda_{0,q_2}\sum_{i=1}^{N^k_{i,0}}\Big[\hat{q_2}(z^k_i,0,y^k_0(z),\zeta^k,\theta^s) - q_2(z^k_i,0,y^k_0(z),\zeta^k)\Big]^2\Bigg] \tag{4.10}$$

$$\mathcal{L}^k_{data,lb} = \frac{1}{N^k_{i,b}}\Bigg[\lambda_{lb,y_1}\sum_{i=1}^{N^k_{i,b}}\Big[\hat{y_1}(z^k_{lb},t^k_i,y^k_0(z),\zeta^k,\theta^s) - y_1(z^k_{lb},t^k_i,y^k_0(z),\zeta^k)\Big]^2 + \lambda_{lb,P}\sum_{i=1}^{N^k_{i,b}}\Big[\hat{P}(z^k_{lb},t^k_i,y^k_0(z),\zeta^k,\theta^s) - P(z^k_{lb},t^k_i,y^k_0(z),\zeta^k)\Big]^2 + \lambda_{lb,q_1}\sum_{i=1}^{N^k_{i,b}}\Big[\hat{q_1}(z^k_{lb},t^k_i,y^k_0(z),\zeta^k,\theta^s) - q_1(z^k_{lb},t^k_i,y^k_0(z),\zeta^k)\Big]^2 + \lambda_{lb,q_2}\sum_{i=1}^{N^k_{i,b}}\Big[\hat{q_2}(z^k_{lb},t^k_i,y^k_0(z),\zeta^k,\theta^s) - q_2(z^k_{lb},t^k_i,y^k_0(z),\zeta^k)\Big]^2\Bigg] \tag{4.11}$$

$$\mathcal{L}^k_{data,rb} = \frac{1}{N^k_{i,b}}\Bigg[\lambda_{rb,y_1}\sum_{i=1}^{N^k_{i,b}}\Big[\hat{y_1}(z^k_{rb},t^k_i,y^k_0(z),\zeta^k,\theta^s) - y_1(z^k_{rb},t^k_i,y^k_0(z),\zeta^k)\Big]^2 + \lambda_{rb,P}\sum_{i=1}^{N^k_{i,b}}\Big[\hat{P}(z^k_{rb},t^k_i,y^k_0(z),\zeta^k,\theta^s) - P(z^k_{rb},t^k_i,y^k_0(z),\zeta^k)\Big]^2 + \lambda_{rb,q_1}\sum_{i=1}^{N^k_{i,b}}\Big[\hat{q_1}(z^k_{rb},t^k_i,y^k_0(z),\zeta^k,\theta^s) - q_1(z^k_{rb},t^k_i,y^k_0(z),\zeta^k)\Big]^2 + \lambda_{rb,q_2}\sum_{i=1}^{N^k_{i,b}}\Big[\hat{q_2}(z^k_{rb},t^k_i,y^k_0(z),\zeta^k,\theta^s) - q_2(z^k_{rb},t^k_i,y^k_0(z),\zeta^k)\Big]^2\Bigg] \tag{4.12}$$

Here $\mathcal{L}^k_{data,0}$, $\mathcal{L}^k_{data,lb}$, and $\mathcal{L}^k_{data,lb}$ represent the MSE on the initial, the left and the right boundary data, respectively. $\hat{y_1}$, $\hat{P}$, $\hat{q_1}$, and $\hat{q_2}$ are the neural network predictions whereas

y_1, P, q_1, and q_2 denote the labelled data of four state variables. $N^k_{i,0}$ and $N^k_{i,b}$ represent the number of labelled initial and boundary data points. z^k_{lb} and z^k_{ub} are spatial coordinates on the left and the right boundary of the spatiotemporal domain. $k = 1, 2.., N_k$, represents different cases of initial profile and operating parameters. Finally, λ_0, λ_{lb}, and λ_{rb} are the weight terms ([0, ∞]). The choice of weights influence the constraints of matching the labelled data. Although, there is no rule of thumb for choosing the optimal weights, limited numerical experimentation is carried out to estimate the weights that tend to give better accuracies. In addition to initial and boundary data, final column profiles of gas-phase composition are also provided in the training to improve prediction accuracies. The corresponding loss term, $\mathcal{L}^k_{data,f}$, for index #k can be written as

$$\mathcal{L}^k_{data,f} = \frac{\lambda_{f,y_1}}{N^k_{i,0}} \sum_{i=1}^{N^k_{i,0}} \left[\hat{y_1}(z^k_i, t^k_f, y^k_0(z), \zeta^k, \theta^s) - y_1(z^k_i, t^k_f, y^k_0(z), \zeta^k) \right]^2 \tag{4.13}$$

Combining the four terms above leads to the first part of the loss function as shown below:

$$\mathcal{L}^k_{data} = \mathcal{L}^k_{data,0} + \mathcal{L}^k_{data,lb} + \mathcal{L}^k_{data,rb} + \mathcal{L}^k_{data,f} \tag{4.14}$$

Loss term: PDE residuals

This part of the loss function introduces the physics regularization of the neural networks. The PDE residuals defined in Eq. 4.8 are incorporated here. For evaluating these residuals, N_r collocation points, i.e., (z_r, t_r), within the spatiotemporal domain are used as illustrated in Fig. 4.1. These collocation points are randomly chosen using Latin hypercube sampling. Notably, this part of the loss function requires no additional labelled data from the simulations because the collocation points are just auxiliary points that help calculate the partial derivatives. The loss term for index #k expressed as the MSE is shown below:

$$\mathcal{L}^k_{residual} = \frac{1}{N^k_r} \left[\lambda_{r,c} \sum_{r=1}^{N^k_r} r^k_c(z^k_r, t^k_r, y^k_0(z), \zeta^k, \theta^s) + \lambda_{r,p} \sum_{r=1}^{N_r} r^k_p(z^k_r, t^k_r, y^k_0(z), \zeta^k, \theta^s) \right] \tag{4.15}$$

where N_r^k is the number of collocation points for case #k. r_c^k and r_p^k correspond to the residuals of component and overall mass balances for case #k, where $k = 1, 2.., N_k$. $\lambda_{r,c}$ and $\lambda_{r,p}$ are the weight terms.

Overall loss function

The overall MSE $\mathcal{L}$ defined by combining the loss terms from Eqs. 4.14 and 4.15 takes the following form:

$$\mathcal{L} = \sum_{k=1}^{N_k} \left[\mathcal{L}_{data}^k + \mathcal{L}_{residual}^k \right] \tag{4.16}$$

Here, individual terms $\mathcal{L}_{data}^k$ and $\mathcal{L}_{residual}^k$ obtained in each case k are together summed over N_k cases of different initial profiles $y_0^s(z)$ and operating parameters ζ^s for step s. The idea here is to minimize $\mathcal{L}$ such that the neural network aims to learn the unique spatiotemporal solutions corresponding to different initial profiles and operating parameters. Hence, the constraints of matching the labelled data and reducing the PDE residuals close to zero are imposed for each case k and together minimize the MSE values obtained from all cases considered.

4.3.3 Training

The objective of training the deep neural networks is to determine the optimized weights and biases associated with each neuron in such a way that minimizes the loss function described in Eq. 4.16. Initially, the weights are specified using Xavier initialization [83] and the biases are initialized with zeroes. The training follows a backpropagation approach where the gradients of loss function with respect to each of the training weight computed based on the chain rule along with the learning rate are used to update the weights and the biases. This procedures continues to iterate until convergence is achieved. The loss function was minimized using L-BFGS, a quasi-Newton full-batch gradient-based optimization method. It is worth noting that the convergence to the global minimum with hundreds of thousands of adjustable parameters and the com-

plex loss function may not be possible, however, studies show that this approach is capable of determining the correct parameters for weights and biases to obtain good prediction accuracies provided an appropriate selection of hyperparamters are made [77].

Since the loss function requires computation of residuals of the PDEs, the spatial and temporal derivatives of outputs of the neural network are calculated using automatic differentiation [84]. Automatic differentiation uses chain rule to approximate the partial differential operators in the governing equations through backpropagation of derivatives from the output layer to the input layer. The analytically defined connections between the layers of the deep neural network enable the implementation of this technique. In terms of accuracy, the automatic differentiation offers higher accuracy compared to the numerical differentiation as errors arising from the truncation and rounding-off errors are avoided [84]. Automatic differentiation has been well-implemented in the deep learning frameworks such as Tensorflow [85] and PyTorch [86]. The training procedure was implemented using the deep learning library Tensorflow and the partial differential operators are computed using "tf.gradients()" in Tensorflow. It is important to reiterate that the neural network model is trained for each step defined by a unique set of boundary conditions and the cycles are not used for the training.

4.3.4 Non-dimensionalization and normalization

The state variables, $y_1^s(z,t)$, $P^s(z,t)$, $q_1^s(z,t)$, and $q_2^s(z,t)$ have different orders of magnitude that can lead to difficulties while calculating backpropagated gradients during neural network training [78, 87]. Hence, the physical quantities are non-dimensionalized in Eqs. 4.1 - 4.3 to have an appropriate scaling, i.e.$\sim \mathcal{O}(1)$. The non-dimensionalized quantities are defined as follows:

$$\bar{P} = \frac{P}{P_0}, \quad \bar{c_i} = \frac{y_i \bar{P}}{P_0} \quad \bar{q_1} = \frac{q_1}{q_{s1,0}}, \quad \bar{q_2} = \frac{q_2}{q_{s2,0}}, \quad \bar{v} = \frac{v}{v_0} \tag{4.17}$$

Here P_0 is the reference atmospheric pressure, $q_{s1,0}$ and $q_{s2,0}$ are the equilibrium loadings of the first and the second component at feed conditions, and v_0 is the feed interstitial velocity (m s^{-1}). Since the gas-phase composition y is a molar fraction that lies in [0,1], this state variable is not non-dimensionalized.

The inputs are normalized to scale between [-1,1] to enhance the robustness of the neural network training [77, 78, 87] as follows:

$$\bar{z} = 2\frac{z}{L} - 1, \quad \bar{t} = 2\frac{t}{t_0} - 1, \quad \bar{y_0}(z) = 2\frac{y_0(z) - min(y_0(z))}{max(y_0(z)) - min(y_0(z))} - 1 \tag{4.18}$$

where $\bar{z}$, $\bar{t}$, and $\bar{y_0}(z)$ are the normalized inputs to the neural network. The operating parameters ζ are scaled such that the values lie in the range of [0,1].

Based on the non-dimensionalized variables, Eqs. 4.1-4.3 can be rewritten as

$$\frac{\partial \bar{c_i}}{\partial \bar{t}} = \frac{\partial}{\partial \bar{z}}\left[- \psi_1 \bar{c_i} \bar{v} + \psi_2 \frac{\partial y_i}{\partial \bar{z}} \right] - \omega_i \frac{\partial \bar{q_i}}{\partial \bar{t}} \tag{4.19}$$

$$\frac{1}{\bar{P}}\frac{\partial \bar{P}}{\partial \bar{t}} = -\psi_1 \frac{1}{\bar{P}}\frac{\partial (\bar{P}\bar{v})}{\partial \bar{z}} - \sum_{i=1}^{n_{comp}} \omega_i \frac{\partial \bar{q_i}}{\partial \bar{t}} \tag{4.20}$$

$$- \frac{\partial \bar{P}}{\partial \bar{z}} = \psi_3 \bar{v} \tag{4.21}$$

The dimensionless groups in the above equations are given by

$$\psi_1 = \frac{v_0 t_0}{L}, \quad \psi_2 = \frac{D_L t_0}{L^2}, \quad \psi_3 = \frac{150}{4}\frac{1}{r_{\mathrm{p}}^2}\left(\frac{1-\varepsilon}{\varepsilon}\right)^2 \frac{\mu v_0 L}{P_0}, \quad \omega_i = \frac{R T_0 q_{s,i,0}}{P_0}\frac{1-\varepsilon}{\varepsilon}$$

The non-dimensionalization and the normalization ensures that all the variables and inputs are scaled to order $\mathcal{O}(1)$. Before the training, the labelled data provided to the neural network is scaled based on Eqs. 4.17-4.18 and the residuals are defined based on Eqs. 4.1-4.21. The predicted quantities are finally reverted to their original form.

4.3.5 Detailed model simulations

The VSA cycles are simulated using our detailed one-dimensional mathematical model [19]. The system of coupled nonlinear PDEs are numerically solved by discretizing the

spatial terms into 50 finite volumes using the total variation diminishing (TVD) scheme with van-Leer flux limiter. The resulting ordinary differential equations (ODEs) are integrated in time based on *ode23s* solver in MATLAB. Individual steps are simulated by imposing appropriate boundary conditions [19]. All cycle simulations are carried out using standard unibed approach, i.e. a single column undergoes all steps in the cycle sequentially, until it reaches CSS. The CSS was considered to be achieved when the mass balance error for the entire cycle equals to 0.5% or less in the five consecutive cycles. The simulations provide detailed composition, pressure and temperature spatiotemporal profiles from the initial cycle to CSS which are then used to calculate process performance indicators. It is worth noting that the detailed simulations are validated elsewhere against both lab-scale [47] and pilot-scale experiments [35].

4.4 Results and discussion

4.4.1 Case study

Four simple VSA cycles, illustrated in Fig. 4.2, are considered to demonstrate the ability of the proposed methodology to synthesize and simulate different cyclic adsorption processes. The feed consists of a binary mixture of 20 mol% CO_2 and 80 mol% N_2 at 1 bar and 25 °C. The constituent steps used to construct these cycles can be categorized into four different step types: the adsorption step, the blowdown step, the evacuation step and the pressurization step. The first cycle, shown in Fig. 4.2(a), is a simple three-step VSA cycle consisting of the following steps: 1) In the adsorption step (ADS), the feed mixture introduced in the column with constant interstitial velocity (v_0) at $P_{\mathrm{H}} = 1$ bar undergoes separation through preferential adsorption of the heavy component CO_2. On the other hand, the light component N_2 leaves the column. 2) In the evacuation step (EVAC), the column pressure is reduced to a low pressure (P_{L}) in the counter-current direction using a vacuum pump with constant interstitial velocity (v_{EVAC}) at the boundary, similar to realistic conditions [21, 88], to collect the CO_2 rich

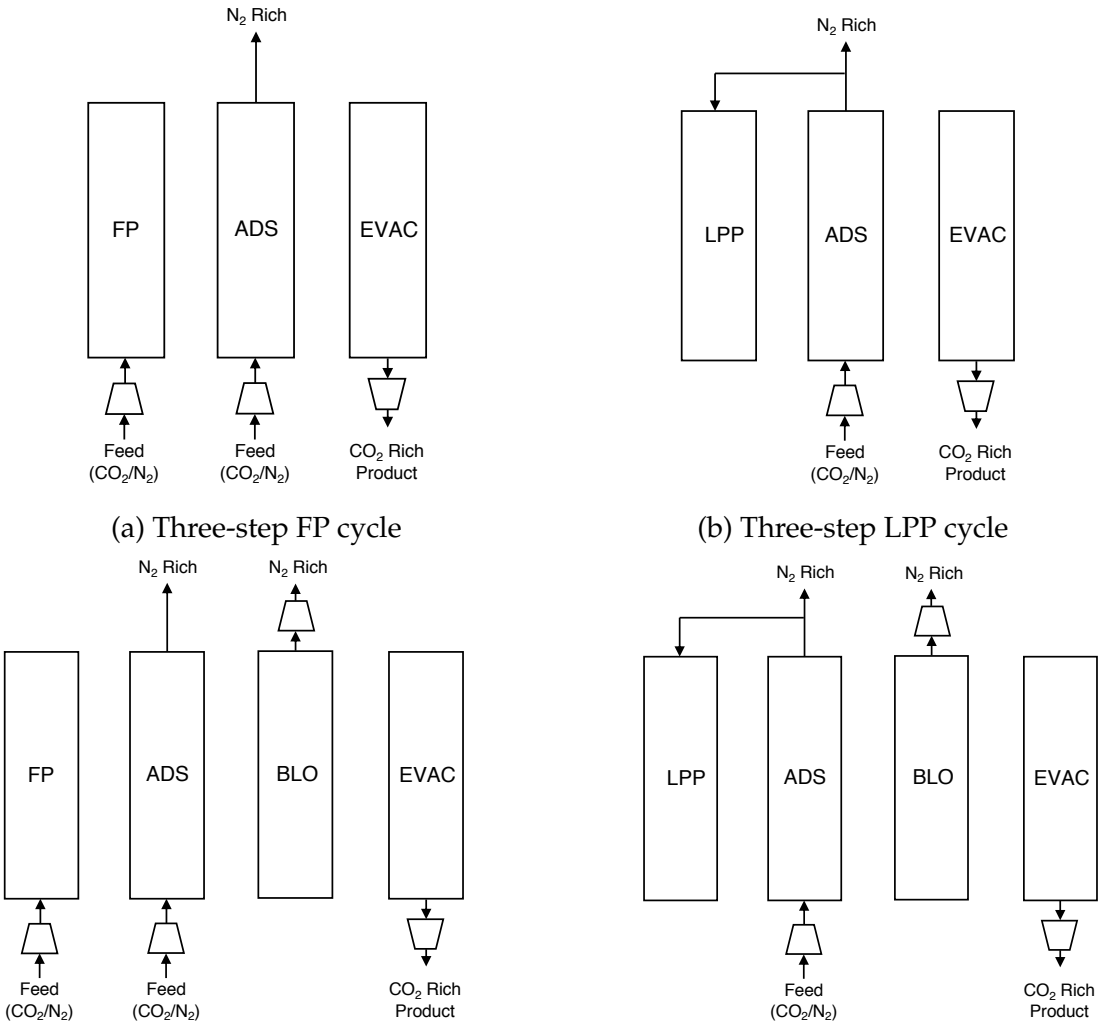

(a) Three-step FP cycle

(b) Three-step LPP cycle

(c) Four-step FP cycle

(d) Four-step LPP cycle

Figure 4.2: Four different VSA cycles considered for demonstrating the cycle synthesis capabilities of physics-based neural networks.

product at the feed end of the column. 3) The feed pressurization step (FP) pressurizes the column to 1 bar using the feed mixture through a blower with constant interstitial velocity at the boundary, v_{FP}. The second cycle in Fig. 4.2(b) is a variant of the first cycle. Instead of using the fresh feed for pressurizing the column in the pressurization step, the light product from the adsorption step is used to pressurize the column from the light product end. In the third and the fourth cycles, the blowdown step is included after the adsorption step in the first and the second cycles to depressurize

the column to an intermediate pressure P_{I} in the co-current direction through the light product end to remove N_2 from the column. The vacuum pump is used to remove the gas by implementing a constant interstitial velocity (v_{BLO}) boundary condition at the light product end. Although the underlying constituent steps are the same in these cycles, in principle, these cycles can yield different performances and considered unique from a process design perspective. The VSA cycle performs the separation with IISERP MOF2, a novel metal-organic framework, as an adsorbent. Previous screening studies have shown superior performance of IISERP MOF2 for post-combustion CO_2 capture [88, 91]. The CO_2 and N_2 isotherms on IISERP MOF2 at 25 °C are shown in Fig. 4.3 and the DSL isotherm parameters are reported in Table 4.1. Each step in the VSA cycle can be distinguished based on boundary conditions provided in Table 4.2. Hence, separate neural network models are developed for each step to predict its spatiotemporal dynamics. As can be seen from Table 4.2, the durations of blowdown, evacuation, and pressurization step can be calculated through implementation of a constant velocity boundary condition based on the pressures P_{H}, P_{I}, and P_{L}.

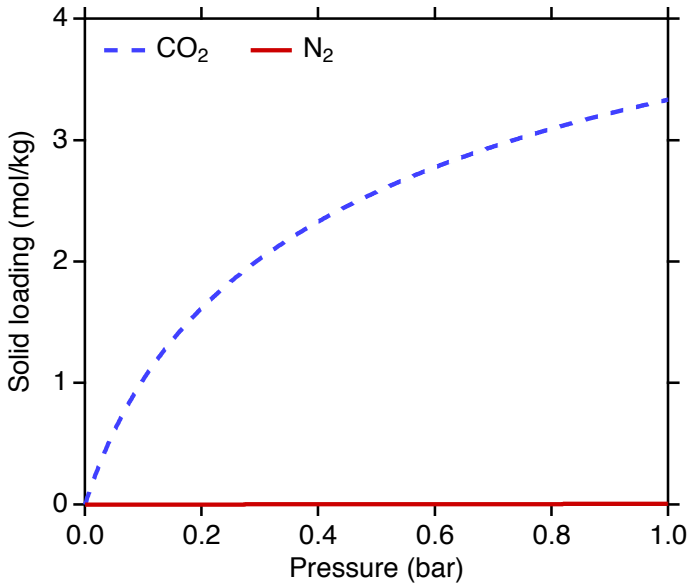

Figure 4.3: CO_2 and N_2 isotherms on IISERP MOF2 at 298.15K [91].

The VSA cycle performance can be tuned based on the following operating param-

Table 4.1: Dual-site Langmuir isotherm parameters.

Parameter	**CO_2**	**N_2**
q_{sb} (mol kg^{-1})	3.29	3.29
q_{sd} (mol kg^{-1})	1.89	1.89
b_0 (m^3 mol^{-1})	9.39×10^{-8}	2.55×10^{-7}
d_0 (m^3 mol^{-1})	5.23×10^{-7}	2.55×10^{-7}
ΔU_{b} (J mol^{-1})	-31135	-11890
ΔU_{d} (J mol^{-1})	-31135	-11890

Table 4.2: Boundary conditions for different steps considered in this study.

Step	**z=0**	**z=L**
Adsorption	$v\vert_{z=0} = v_{\mathrm{feed}}$	$P\vert_{\mathrm{z=L}} = P_{\mathrm{ADS}}$
	$D_{\mathrm{L}}\ \frac{\partial y_i}{\partial z}\big\vert_{\mathrm{z=0}} = -v\vert_{\mathrm{z=0}}\left(y_{i,\mathrm{feed}} - y_i\vert_{\mathrm{z=0}}\right)$	$\frac{\partial y_i}{\partial z}\big\vert_{\mathrm{z=L}} = 0$
Blowdown	$\frac{\partial P}{\partial z}\big\vert_{\mathrm{z=0}} = 0$	$v\vert_{\mathrm{z=L}} = v_{\mathrm{BLO}}$
	$\frac{\partial y_i}{\partial z}\big\vert_{\mathrm{z=0}} = 0$	$\frac{\partial y_i}{\partial z}\big\vert_{\mathrm{z=L}} = 0$
Evacuation	$v\vert_{\mathrm{z=0}} = v_{\mathrm{EVAC}}$	$\frac{\partial P}{\partial z}\big\vert_{\mathrm{z=L}} = 0$
	$\frac{\partial y_i}{\partial z}\big\vert_{\mathrm{z=0}} = 0$	$\frac{\partial y_i}{\partial z}\big\vert_{\mathrm{z=L}} = 0$
Pressurisation	$v\vert_{\mathrm{z=0}} = v_{\mathrm{FP}}$	$\frac{\partial P}{\partial z}\big\vert_{\mathrm{z=L}} = 0$
	$D_{\mathrm{L}}\ \frac{\partial y_i}{\partial z}\big\vert_{\mathrm{z=0}} = -v\vert_{\mathrm{z=L}}\left(y_{i,\mathrm{feed}} - y_i\vert_{\mathrm{z=L}}\right)$	$\frac{\partial y_i}{\partial z}\big\vert_{\mathrm{z=L}} = 0$

eters. For the adsorption step, feed velocity (v_0) and duration of the adsorption step (t_{ADS}) can be varied. In blowdown and evacuation steps, pressures P_{I}, P_{L}, and vacuum

pump velocities, v_{BLO}, v_{EVAC} are the variables. The pressurization inlet velocity, v_{FP}, is an operating parameter in the pressurization step. In the present study, v_0, v_{BLO}, v_{EVAC}, and v_{FP} are held constant and are not considered operating parameters in neural network training. In other words, the VSA cycle simulations are restricted to fixed vacuum pump and blower sizes.

4.4.2 Neural network training

Unique neural networks are trained to learn the spatiotemporal dynamics of four different constituent steps: the pressurization step, the adsorption step, the co-current blowdown step, and the counter-current evacuation step. To gather training data for each model, individual steps are separately simulated. Since initial column profiles and step parameters are inputs to the neural network, each step must be simulated at different initial column profiles and step parameters to enable the mapping in Eq. 4.7. As previously mentioned, the column profiles drastically change depending on the sequence of steps implemented, step parameters, and the number of times the cycle is simulated until CSS. To ensure appropriate sampling of different initial column profiles for training, knowledge of various column profiles encountered in cyclic adsorption processes is essential. One way to learn about the types of column profiles typically encountered is to simulate various adsorption processes using the detailed model and gather different column profiles of individual steps for various operating conditions. The other approach involves synthetically generating different types of column profiles based on mathematical functions, splines, etc. The drawback of the latter approach is the loss of column profile characteristics specific to adsorption processes. Here, the former approach is used to gather different initial profiles by first simulating different VSA cycles using the detailed model based on the simulation parameters provided in Table 4.3. The detailed model-based cycle simulations are carried out at different operating conditions generated randomly using Latin hypercube sampling.

For each set of operating conditions, VSA cycle simulations are carried out until the CSS. At the same time, the gas-phase composition column profiles after every step are gathered from the initial cycle to the CSS. From these, N_k=60 different initial column profiles and the corresponding step parameters of each step are randomly chosen and used for training the model. Figure 4.4 illustrates the different initial profiles used in the neural network training for each step.

Table 4.3: VSA simulation parameters used for this study [19].

Parameter	**Value**
Column length, L (m)	1
Inner column radius, r_{i} (m)	0.1445
Outer column radius, r_{o} (m)	0.1620
Particle radius, r_{p} (mm)	1
Column void fraction, ε (-)	0.37
Tortuosity, τ (-)	3.0
Adsorbent particle density, ρ_{s} (kg m^{-3})	1442.6 [91]
Molecular diffusivity, D_{m} (cm^2 s^{-1})	0.16
Fluid viscosity, μ (cP)	0.0172
Universal gas constant, R (m^3 Pa mol^{-1} K^{-1})	8.314
Adsorption pressure, P_{H} (bar)	1
Reference temperature, T_0 (K)	298.15
Adsorption feed velocity, v_0 (m s^{-1})	0.5
Pressurization feed velocity, v_{FP} (m s^{-1})	0.2
Blowdown vacuum pump velocity, v_{BLO} (m s^{-1})	0.05
Evacuation vacuum pump velocity, v_{EVAC} (m s^{-1})	1

Next, individual steps are separately simulated based on these initial profiles and step parameters to obtain the labelled data for model training. The temporal domains defined for the individual steps in the step simulations are larger than the typical operating ranges used in the cycles. For instance, the blowdown and the evacuation steps are simulated for durations where the column pressures reach lower than the desired pressures in the cycles. The rationale behind defining such large temporal domains in the individual step simulations is the flexibility to extract different slices of temporal

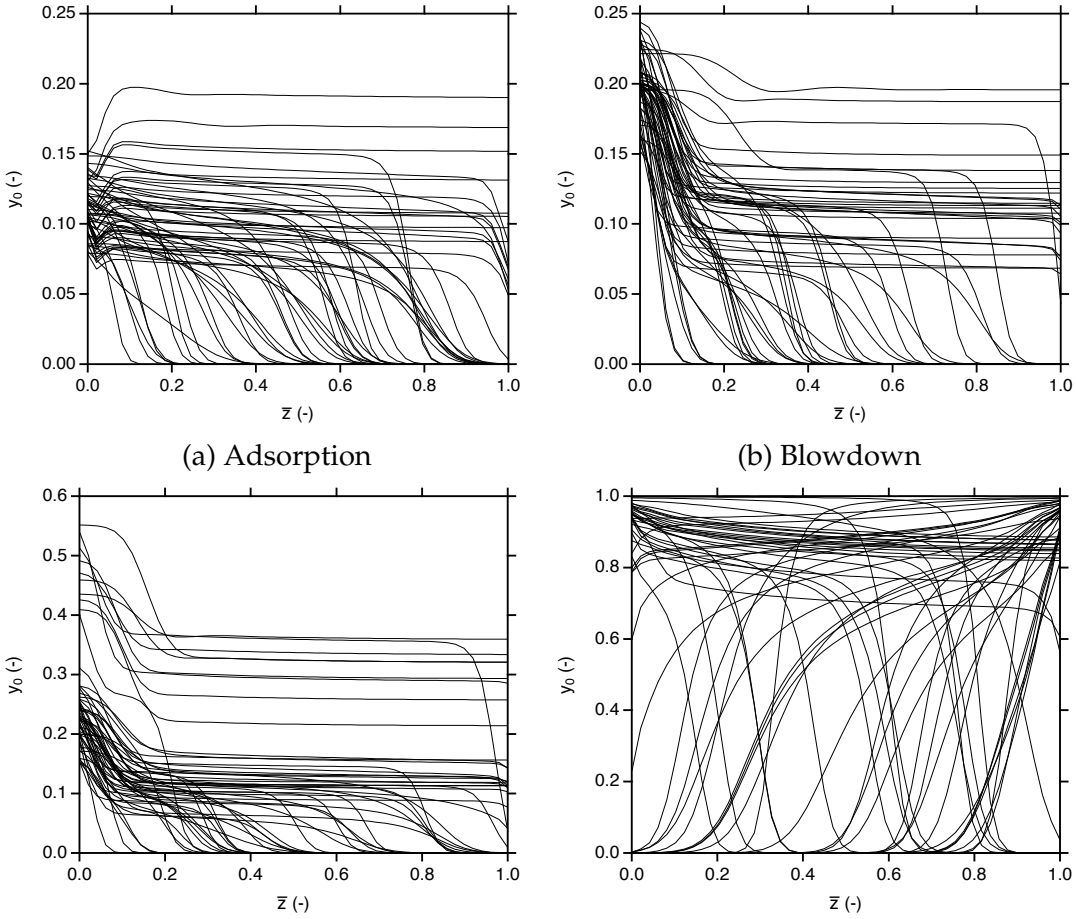

(a) Adsorption (b) Blowdown

(c) Evacuation (d) Pressurization

Figure 4.4: Different initial profiles used in neural network training.

solutions within the larger domain, when using a trained neural network. It is worth noting that a unique simulation is carried out for each set of initial profiles and step parameters. In the data acquisition procedure, the simulation data from each case is first gathered, and then the inputs and the physical quantities are subjected to normalization and non-dimensionalization, respectively. Following this, the initial and the boundary data of four state variables based on N_k = 60 cases are gathered for each step to form the labelled data. Although the data generated in simulations is massive, only a tiny portion is extracted as the labelled data. As an example, the labelled data fed to the blowdown step model training can be visualized in Fig. 4.5. For inferring the PDE solution within the spatiotemporal domain, $N_r = 250$ collocation points are randomly

generated using Latin hypercube sampling for each initial profile and step parameter. It is worth reiterating that no additional simulation data is required for the collocation points.

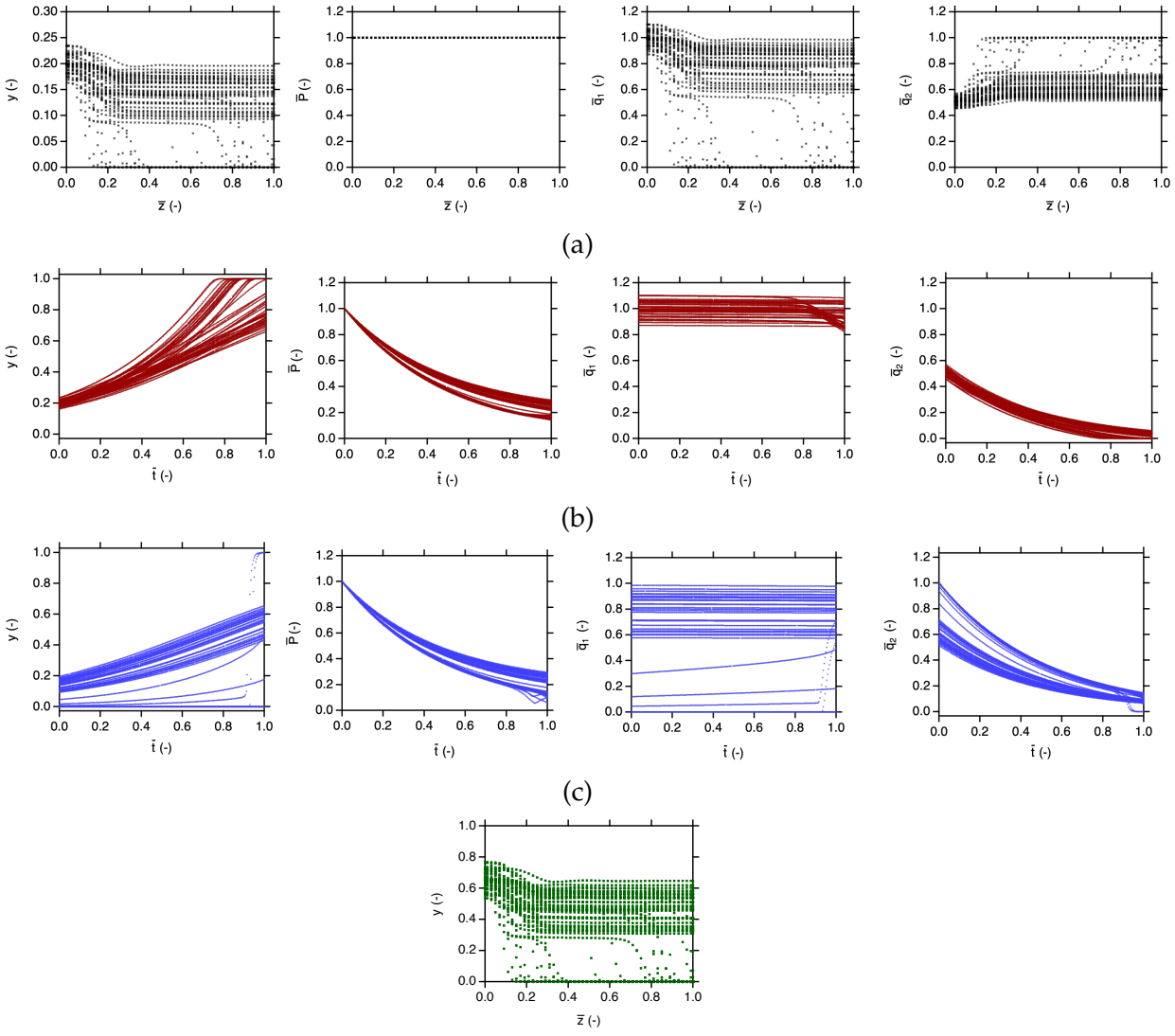

Figure 4.5: Labelled data fed to the blowdown step neural network training. Labelled data corresponds to (a) the initial (b) left boundary (c) right boundary data of four state variables and (d) final column profile of CO_2 gas-phase composition.

The neural network architecture employed for all steps consists of an input layer, ten hidden layers with 100 neurons each, and one output layer with four neurons (four state variables). However, the number of neurons in the input layer varies from step to

step. The common inputs for all steps are the spatiotemporal coordinates (z, t), and the initial gas composition at 50 spatial locations (based on the finite volume discretization of the detailed model). In addition to these 52 inputs, other inputs related to the step parameters are included depending on the step. For this study, the only variable in the adsorption step is the step duration t_{ADS}. Since time t is already one of the inputs to the neural networks, the variation of t_{ADS} can be achieved by extracting different slices of spatiotemporal solutions of the four state variables. Therefore, t_{ADS} is explicitly not considered as step parameter input. As the blowdown step occurs after the adsorption step, the column pressure at the $z = 1$ boundary is always at 1 bar initially. Subsequently, it reduces to a final column pressure, P_{I}, when subjected to a constant vacuum pump flow. Similar to the adsorption step, slices of spatiotemporal solutions can be extracted for any P_{I}. Again, there is no need for an additional step parameter. In the evacuation step, the initial column pressure, P_0, will be either P_{H} or P_{I} and then depressurizes to P_{L}. Here initial column pressure, P_0, depends on the preceding step and the spatiotemporal solutions of evacuation step are dependent on P_0. Hence, P_0 is considered as an input to the evacuation step model. Similarly, the initial column pressure, P_0, in the pressurization step is also an input for the pressurization step model. Moreover, the inlet gas-phase composition ($y_{in,P}$) in the pressurization step can be a variable depending on the stream (i.e. feed or light product) used for pressurizing the column. This makes $y_{in,P}$ a pressurization step parameter. Hence, P_0 and $y_{in,P}$ are the additional inputs for the pressurization step. To summarize, the adsorption and the blowdown step neural networks have 52 inputs, the evacuation step neural neural network has 53 inputs, and the pressurization step input has 54 inputs. Since the proposed approach requires the calculation of first and second order derivatives using automatic differentiation, the nonlinear activation in the neural networks must be differentiable. Hence, a hyperbolic tangent function is used for the nonlinear activation in the adsorption and sinusoidal function for other steps. It is worth noting that the neural network

hyperparameters such as the number of hidden layers, the number of hidden neurons, activation function, and weight terms ($\lambda_{data,0}$, $\lambda_{data,lb}$, $\lambda_{data,rb}$, $\lambda_{data,f}$, $\lambda_{r,c}$, and $\lambda_{r,p}$) are chosen based on limited numerical experimentation. The learning procedure is implemented in Tensorflow v1.15 [85] and the computations are performed based on a single Telsa P100 GPU card where it took approximately 4-8 hours training each model. It is worth reiterating that no system-specific inputs such as mass transfer coefficients, CO_2 and N_2 isotherm parameters are fed to the neural networks in the learning process.

After training the models for each step, the capabilities of physics-based neural networks in learning the spatiotemporal solutions of the four state variables are assessed for different initial profiles and step parameters used in training. For this, the results produced by the trained physics-based neural networks are compared with the detailed model solutions and the averaged relative $\mathcal{L}_2$ error between the neural network predictions and the detailed model solutions across all training cases is used as the metric to quantify the performance of the trained models. The averaged relative $\mathcal{L}_2$ error for state variable $\mathcal{S}$ is defined as:

$$\mathcal{L}_2 = \frac{1}{N_k}\sum_{k=1}^{N_k}\frac{\sqrt{\sum_{j=1}^{N_f}|\hat{\mathcal{S}}_{j,k}-\mathcal{S}_{j,k}|^2}}{\sqrt{\sum_{j=1}^{N_f}|\mathcal{S}_{j,k}|^2}}, \quad \mathcal{S} = y, P, q_1, q_2 \tag{4.22}$$

where $\hat{\mathcal{S}}$ is the neural network predicted state variable and $\mathcal{S}$ is the corresponding detailed model solution. N_f represents the number of spatiotemporal points. Table 4.4 summarizes the averaged relative $\mathcal{L}_2$ error between the neural network predictions and the detailed model solutions across all training cases for the four state variables. As can be seen from the table, the prediction accuracies of the neural network models for each step are very good. For instance, the adsorption step model can predict the $y_1^s(z,t)$ spatiotemporal solutions of N_k=60 different training simulation cases with an 4.31% averaged deviation from the original solutions. It is worth noting that the evacuation step averaged relative $\mathcal{L}_2$ error for $q_2^s(z,t)$ is higher compared to others because the original solution itself has values close to zero.

Table 4.4: Averaged relative $\mathcal{L}_2$ norm between the neural network predicted and the detailed process model spatiotemporal solutions of four state variables ($y_1^s(z,t)$, $P^s(z,t)$, $q_1^s(z,t)$, and $q_2^s(z,t)$) based on N_k=60 different training cases.

Step	$y_1^s(z,t)$	$P^s(z,t)$	$q_1^s(z,t)$	$q_2^s(z,t)$
Pressurization	$6.70e-02$	$1.30e-03$	$8.80e-02$	$2.77e-02$
Adsorption	$4.31e-02$	$6.60e-03$	$4.36e-02$	$1.38e-02$
Blowdown	$2.73e-02$	$4.92e-04$	$3.40e-02$	$1.40e-02$
Evacuation	$6.03e-02$	$1.36e-02$	$6.58e-02$	$1.24e-01$

The effectiveness of the neural network models in learning the spatiotemporal solutions of VSA governing equations can be visualized in Fig. 4.6, where the spatiotemporal solutions based on both neural network predictions and detailed model simulations are compared for one initial profile used in the training. For the discussion, the blowdown step is shown as an example. Here, the emphasis remains on whether the neural network model has accurately learnt the interior of the spatiotemporal solutions of the four state variables by simply using the initial, final and boundary data in the training. As can be seen from the figure, the results produced by the physics-based neural networks are in very good agreement with the detailed model solutions for all four state variables. Remarkably, this also means that the neural networks accurately learnt the underlying interdependencies of each state variable in the VSA process. The prediction accuracies indicate that the methodology employed herein can successfully enable the desired coupling of the state variables by simultaneously minimizing the residuals of component and overall mass balances along with labelled data. It is worth reiterating that the use of physics-based residuals in the loss function has allowed the neural networks to learn the adsorption column dynamics with one fully connected multi-output architecture instead of conventional approaches of having multiple surrogate models for each state variable. Another interesting feature is the ability of predicting q_1 and q_2 solutions. The detailed model calculations of q_1 and q_2 require the adsorption isotherm and the linear driving force model. In the present methodology, instead

of explicitly providing these equations, the initial, final and boundary data of q_1 and q_2 are provided. By simultaneously allowing the neural networks to match this data along with minimizing the overall PDE residuals, the q_1 and q_2 terms in the PDEs are forced to obey the imposed constraints, thereby predicting the interior solutions of q_1 and q_2 reasonably well.

4.4.3 Application: Cycle simulation of four-step FP cycle

The four neural network models constructed for the constituent steps are used to simulate the four-step FP cycle at various operating conditions to test the effectiveness of the proposed methodology. These operating conditions are randomly generated using Latin hypercube sampling such that t_{ADS} is varied from 20 to 100 seconds, P_{I} and P_{L} range between 0.3-0.5 bar and 0.1-0.2 bar, respectively, and are independent of the training operating conditions. Here the neural network predicted profiles of the state variables are first compared with the detailed model simulations. Later on, performance metrics such as CO_2 purity and CO_2 recovery calculated from the neural network predicted profiles are validated against the detailed model calculations. The CO_2 purity and CO_2 recovery are defined as follows:

$$\text{CO}_2 \text{ purity} = \left[\frac{\text{mole}_{\text{out,CO}_2}|_{\text{evac}}}{\text{mole}_{\text{out,total}}|_{\text{evac}}}\right] \times 100 \tag{4.23}$$

$$\text{CO}_2 \text{ recovery} = \left[\frac{\text{mole}_{\text{out,CO}_2}|_{\text{evac}}}{\text{mole}_{\text{in,CO}_2}|_{\text{press}} + \text{mole}_{\text{in,CO}_2}|_{\text{ads}}}\right] \times 100 \tag{4.24}$$

where

$$\text{mole}_{\text{in,CO}_2} = \frac{P_0 v_0}{RT_0}\varepsilon A \int_0^{\bar{t}_{step}} \left[\bar{v}_{\bar{z}=0}(\bar{t}) y_{\bar{z}=0}(\bar{t}) \bar{P}_{\bar{z}=0}(\bar{t})\right] d\bar{t} \tag{4.25}$$

$$\text{mole}_{\text{out,CO}_2} = \frac{P_0 v_0}{RT_0}\varepsilon A \int_0^{\bar{t}_{step}} \left[\bar{v}_{\bar{z}=1}(\bar{t}) y_{\bar{z}=1}(\bar{t}) \bar{P}_{\bar{z}=1}(\bar{t})\right] d\bar{t} \tag{4.26}$$

$$\text{mole}_{\text{out,total}} = \frac{P_0 v_0}{RT_0}\varepsilon A \int_0^{\bar{t}_{step}} \left[\bar{v}_{\bar{z}=1}(\bar{t}) \bar{P}_{\bar{z}=1}(\bar{t})\right] d\bar{t} \tag{4.27}$$

For a fair comparison, both neural networks and the detailed model are initialized with the same initial condition and simulated from the initial cycle to CSS for each set of

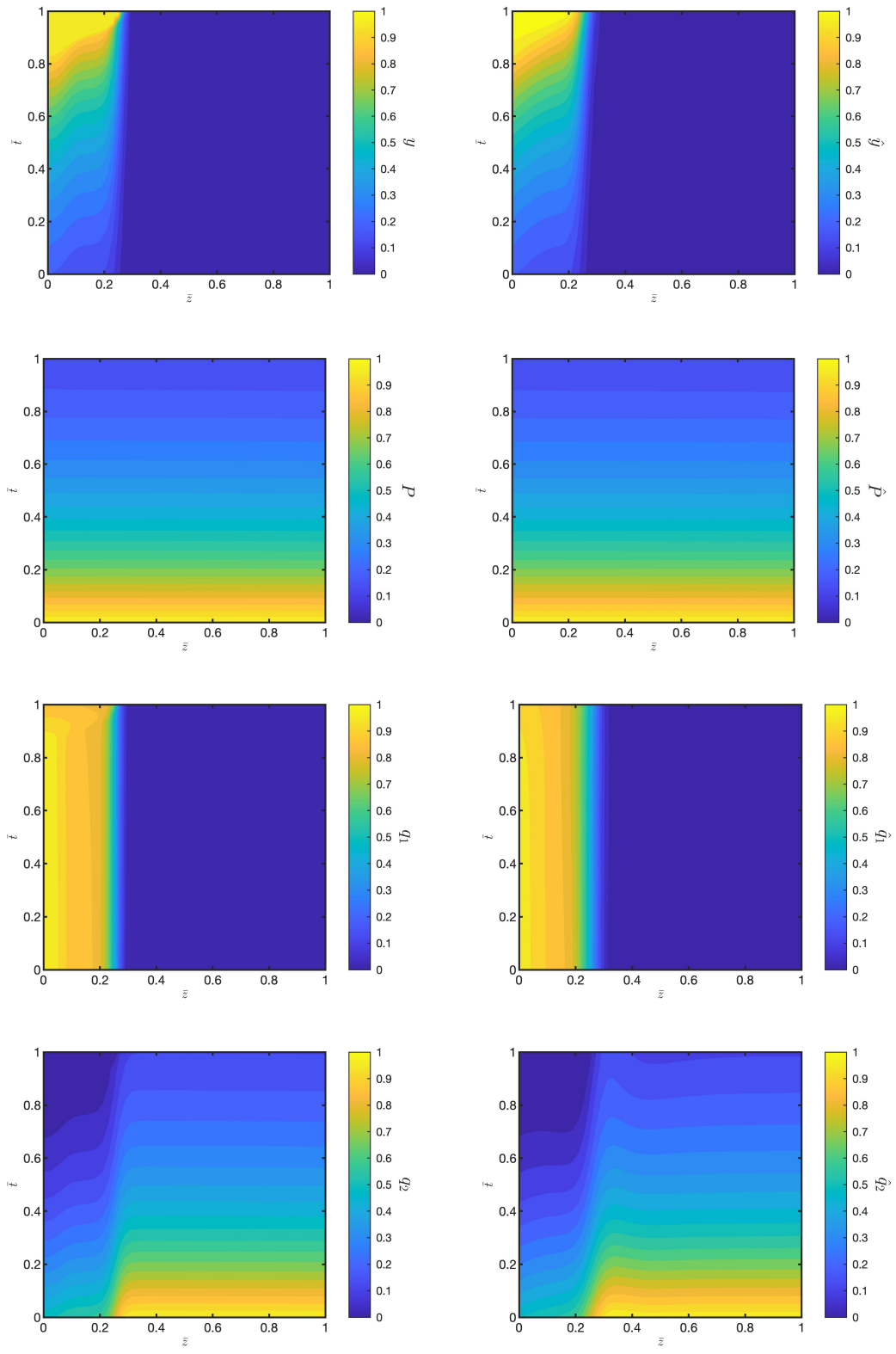

Figure 4.6: Comparison of spatiotemporal solutions of the four state variables based on the detailed process model (left hand panel) and the blowdown step neural network predictions (right hand panel) for one of the initial column profiles used in training. In both the simulations, the blowdown step is initialized with a column pressure of 1 bar.

operating conditions. In both neural networks and detailed model-based simulations, different steps of the cycle are simulated such that the final state for each step will be the initial condition for the next step in the cycle. To achieve CSS criterion, the PDEs are repeatedly solved for each step of the cycle in detailed simulations until the mass balance error equals 1% or less for five consecutive cycles. At CSS, the profiles of state variables across the column in each step and the process performance indicators remain invariant when cycling repeatedly. In neural network-based simulations, the CSS is assumed to be achieved when there is no variation in the column dynamics of each step in the cycle and the process performance indicators remain constant during repeated cycling. It is worth noting that the moles in or out integrated in each step based on neural network approximations may not necessarily lead to overall mass balance convergence less than 1% due to small deviations in the predictions of profiles. In such cases, the CSS was assumed to be achieved if the overall mass balance error is less than 5%.

For the sake of brevity, let us consider one specific operating condition: t_{ADS}=45 s, P_{I} = 0.37 bar, and P_{L} = 0.13 bar for the discussion. Both the neural network and the detailed model simulations are carried out for this operating condition from the initial cycle until the CSS. The column profiles after cycle #1 and at CSS obtained from the two models are illustrated in Figs. 4.7 and 4.8, respectively. As can be seen from the figure, the predictive capabilities of the neural network models are remarkable. It is worth reiterating that both neural network and the detailed model simulations are initialized with the same initial condition. Interestingly, the neural network simulations have accurately captured the dynamics from the initial cycle to the CSS. Such predictive capabilities of neural network simulations can be attributed to the use of different initial profiles as inputs in the neural network training of each step. The results also demonstrate that this methodology successfully predicted the CSS profiles for the given initial profile and operating conditions by simultaneously minimizing the resid-

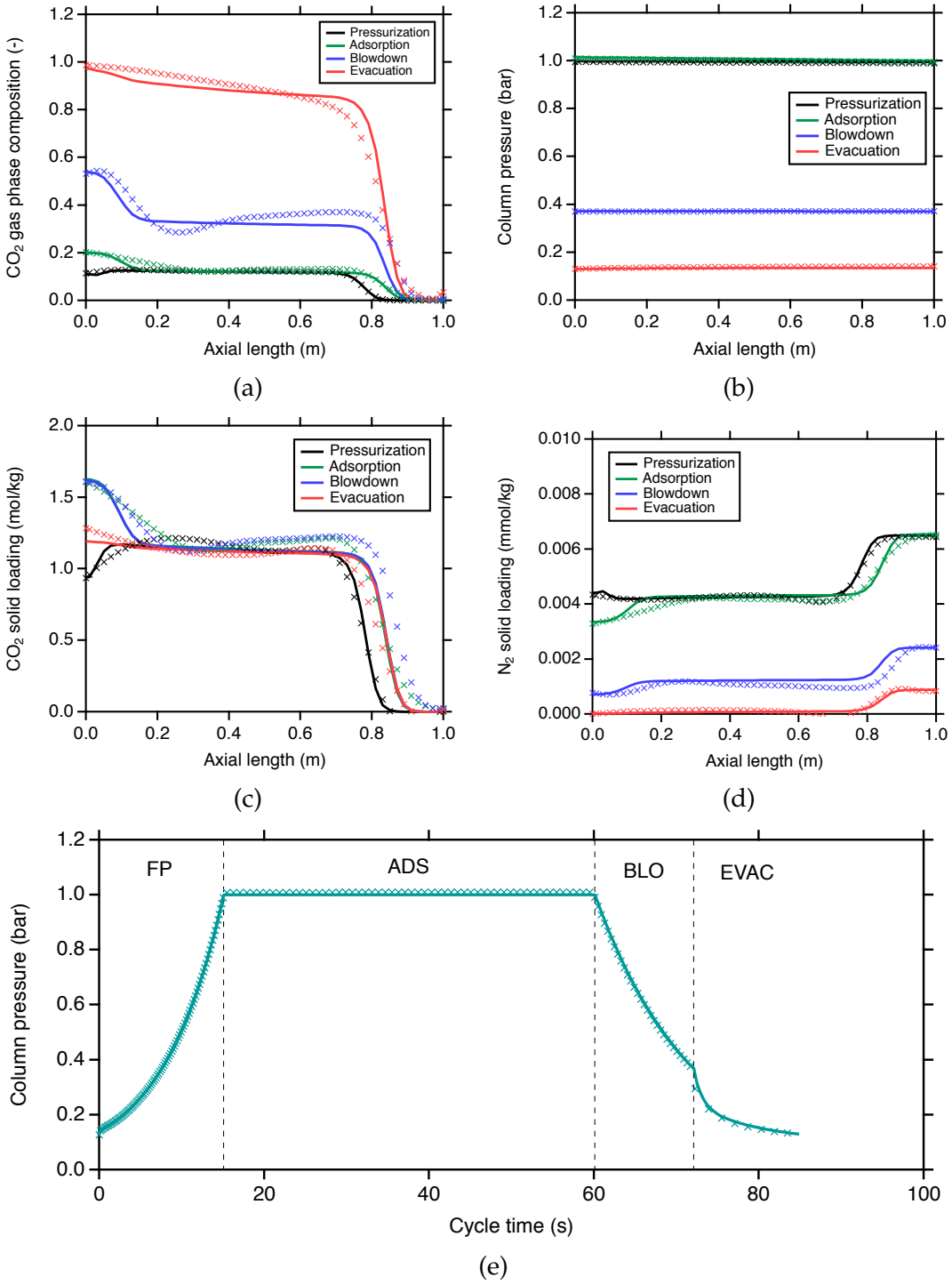

Figure 4.7: Comparison of cycle #1 profiles of four state variables obtained from the neural network (markers) and the detailed model (lines) simulations for the operating condition: t_{ADS}=45 s, P_{I} = 0.37 bar, and P_{L} = 0.13 bar.

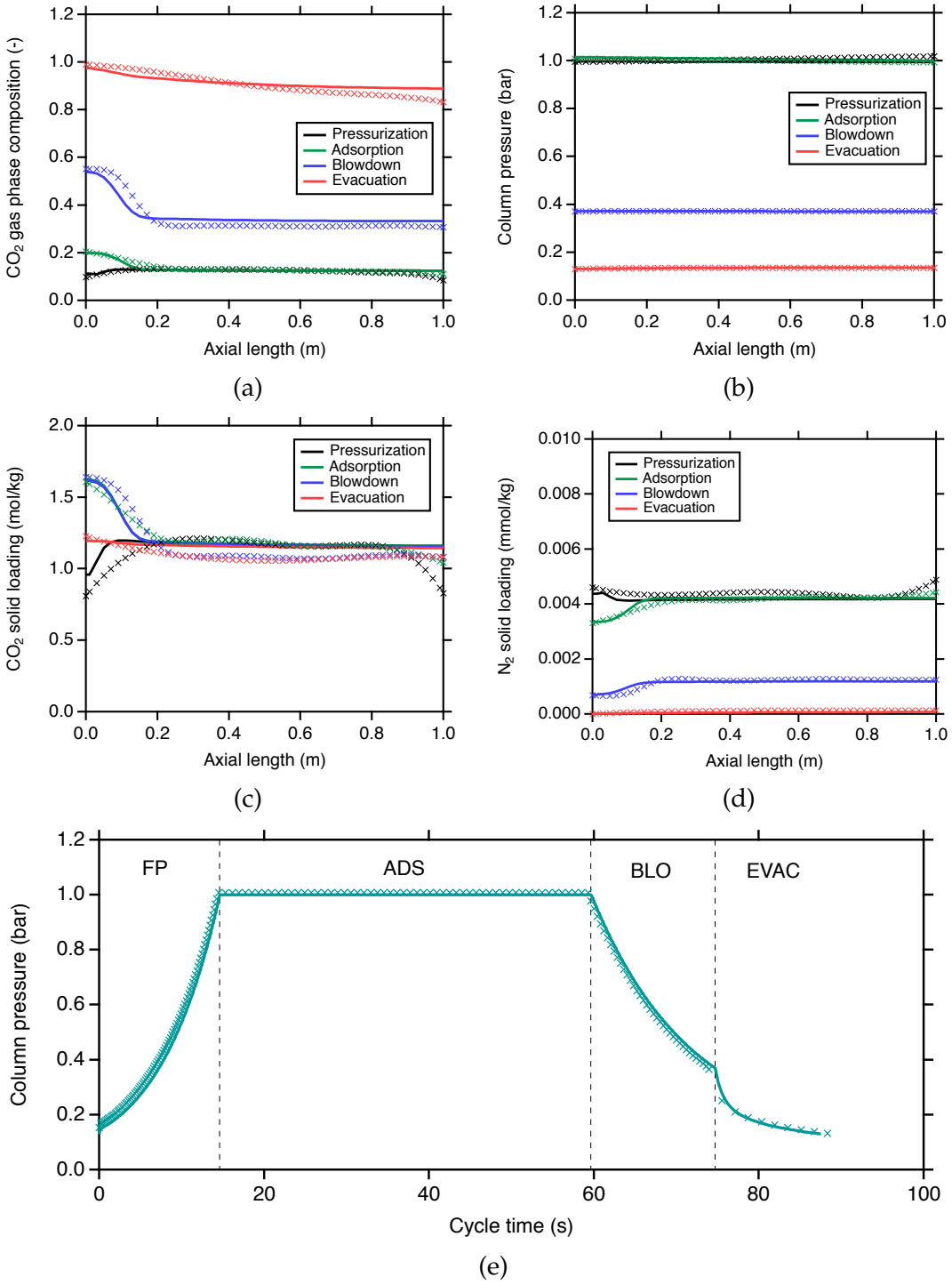

Figure 4.8: Comparison of cyclic steady state (CSS) profiles of four state variables obtained from the neural network (markers) and the detailed model (lines) simulations for the operating condition: t_{ADS}=45 s, P_{I} = 0.37 bar, and P_{L} = 0.13 bar.

uals of PDEs and the labelled data across all initial profiles and operating conditions. The calculated moles in each step and the performance indicators for this case are reported in Table 4.5. The CO_2 recovery from the neural network simulations is higher than one calculated from the detailed model simulations because the neural networks slightly overestimated the duration of the evacuation step, as can be seen in Fig. 4.8(e). In terms of computational efficiencies, the neural network simulations were almost 40 times faster than the detailed model simulations.

Table 4.5: Summary of moles calculated from the state variables at CSS based on neural networks and detailed process model simulations for the operating condition: t_{ADS}=45 s, P_{I} = 0.37 bar, and P_{L} = 0.13 bar. The number of cycles to reach CSS and the computational time are also reported. Note that CPU seconds on a 128 GB and 3.10 GHz workstation.

	Detailed model	Neural network
$\mathrm{mole}_{\mathrm{in,CO_2}}\vert_{\mathrm{FP}}$	0.25	0.26
$\mathrm{mole}_{\mathrm{in,CO_2}}\vert_{\mathrm{ADS}}$	4.53	4.50
$\mathrm{mole}_{\mathrm{out,CO_2}}\vert_{\mathrm{ADS}}$	2.56	2.21
$\mathrm{mole}_{\mathrm{out,CO_2}}\vert_{\mathrm{BLO}}$	0.18	0.17
$\mathrm{mole}_{\mathrm{out,CO_2}}\vert_{\mathrm{EVAC}}$	2.03	2.47
CO_2 purity (%)	88.4	90.2
CO_2 recovery (%)	42.5	51.9
mass balance error (%)	0.02	1.79
#cycles to CSS (-)	17	5
Computational time (s)	125.9	2.9

Next, the simulations are extended to 200 different operating conditions spanning the entire range. The neural network's predictive ability is expressed in terms of CO_2 purity and CO_2 recovery obtained at CSS. Figure 4.9 illustrates the parity plot for CO_2 purities and CO_2 recoveries between the detailed model and the neural network simulations. As shown, the purity predictions from the neural network simulations are within the 6% error margin. On the other hand, the some of the recovery predictions from the neural network simulations slightly have a higher error margin of 20%. As

mentioned previously, this discrepancy can be attributed to the slight overestimation of the duration of the evacuation step neural network model. Nevertheless, the accuracy of the results produced by the neural network simulations are very good for designing and optimizing different cycles for initial material screening purposes. Based on these 200 simulations, the neural network simulations were 30 times faster than the detailed model simulations on a 128 GB and a 3.10 GHz workstation. It is expected that the computational advantages will be more significant when optimizing different cycle designs.

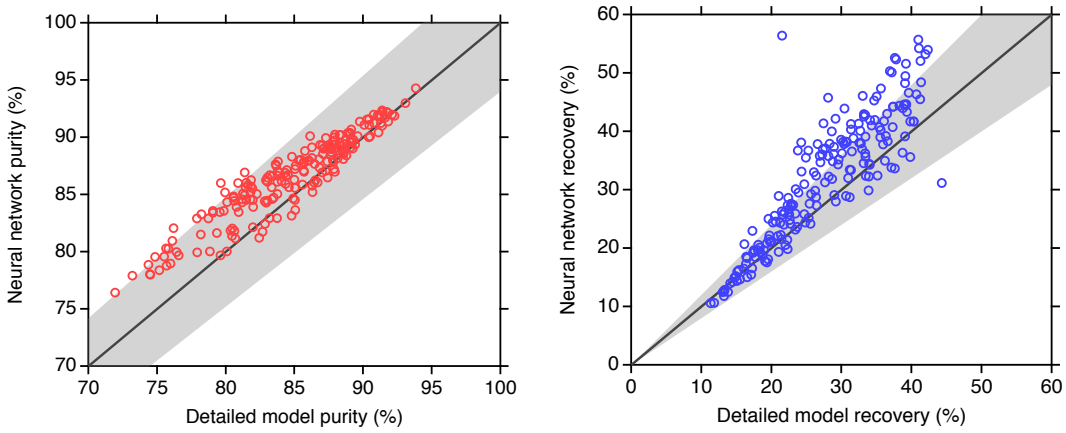

Figure 4.9: Parity plots of CO_2 purity and CO_2 recovery based on 200 different simulations between the detailed process model- and the neural network-based simulations. The error margin for CO_2 purity and CO_2 recovery are 6% and 20%, respectively.

4.4.4 Application: Cycle synthesis

In the previous section, the neural network models successfully demonstrated the simulation capabilities for one VSA cycle. Here, the effectiveness of the proposed approach is tested for cycle synthesis by constructing and simulating the four VSA cycles illustrated in Fig. 4.2. For this, the cycle simulations are carried out in slightly different operating ranges of t_{ADS}, P_{I} and P_{L} by varying them between 5-45 seconds, 0.7-0.99 bar and 0.08-0.13 bar, respectively. Both neural networks and the detailed process are

simulated until CSS and the results produced by the two approaches are compared at CSS. In detailed process simulations, the CSS condition is reached when the overall mass balance error equals 1% or less for five consecutive cycles. The CSS was assumed to be achieved in neural network-based simulations when there is no variation in the column dynamics of each step in the cycle during repeated cycling or the overall mass balance error is less than 5%.

Simulation of three-step FP cycle

First, a simple three-step VSA cycle with feed pressurization (FP) is constructed based on the individual feed pressurization, adsorption, and evacuation step models. A specific process operating condition: t_{ADS} = 25 s, P_{L}=0.1 bar is considered randomly to test the ability of neural network-based simulations to predict CSS profiles. Figures 4.10 and 4.11 illustrate the column profiles of four state variables after cycle #1 and at CSS from neural network- and detailed process model-based simulations, respectively. Overall, there is an excellent agreement between the two results. However, the neural network model over-predicted the CO_2 gas-phase composition profile at the end of evacuation step at CSS. Moreover, CO_2 solid loadings of adsorption step are also slightly overestimated. In Table 4.6, the CO_2 purity and CO_2 recovery calculated based on both neural network and detailed process simulations are reported. Moreover, the number of cycles to reach CSS and the computational times are also provided. The neural network-based calculations of CO_2 purity and CO_2 recovery have an error deviation of 13% and 43%, respectively. Such a high CO_2 recovery difference is because the neural network simulations overestimated the duration of the evacuation step (see Fig. 4.11(e)), which resulted in the calculation of higher moles out of the evacuation step. Since the constant velocity boundary condition is used in the evacuation step, the step duration also depends on the initial CO_2 gas-phase composition in the column, apart from intermediate and low pressures. Owing to this, the smallest deviation in

the final CO_2 gas-phase composition profile in the preceding adsorption step can significantly affect the evacuation step duration calculated by the neural network model. The neural networks simulations are almost 35 times faster than the detailed model simulations.

Table 4.6: Summary of CO_2 purity and CO_2 recovery calculated based on neural networks (NN) and detailed process model (DM) simulations for the operating condition: t_{ADS}=25 s and P_{L} = 0.1 bar. For four-step cycles, P_{I} = 0.75 bar was used. The number of cycles to reach CSS and the computational time are also reported. Note that CPU seconds on a 128 GB and 3.10 GHz workstation.

VSA cycles	CO_2 purity (%)		CO_2 recovery (%)		#cycles to CSS		Computational time (s)	
	DM	NN	DM	NN	DM	NN	DM	NN
Three-step FP cycle	62.5	70.7	64.0	91.6	37	13	250.4	7.4
Three-step LPP cycle	64.8	67.9	78.5	87.5	42	5	265.1	3.2
Four-step FP cycle	69.5	76.3	62.6	88.9	35	10	258.8	7.2
Four-step LPP cycle	71.8	73.6	77.3	81.1	25	7	183.1	5.3

Simulation of three-step LPP cycle

Another three-step cycle can be constructed by pressurizing the column using light product from the adsorption step instead of feed pressurization, as illustrated in Fig. 4.2(b). In the light product pressurization (LPP) step, the inlet CO_2 gas-phase composition depends on the outlet stream of the adsorption step. For simplicity, it is assumed that the outlet stream of the adsorption step is first directed into a well-mixed tank before feeding to pressurize the column in the LPP step. Both neural network and detailed process model simulations are carried out based on this additional assumption. The same operating condition as earlier is used to compare the CSS profiles from both models. Figures 4.12 and 4.13 illustrate the column profiles of four state variables after cycle #1 and at CSS from both simulations, respectively. The neural network profile predictions are remarkable. The impact of pressurizing the column with outlet stream of the adsorption step can be visualized from the CO_2 gas-phase compositions/solid loadings at the light product end. The final CO_2 solid loading at $z = 1$ at the end of

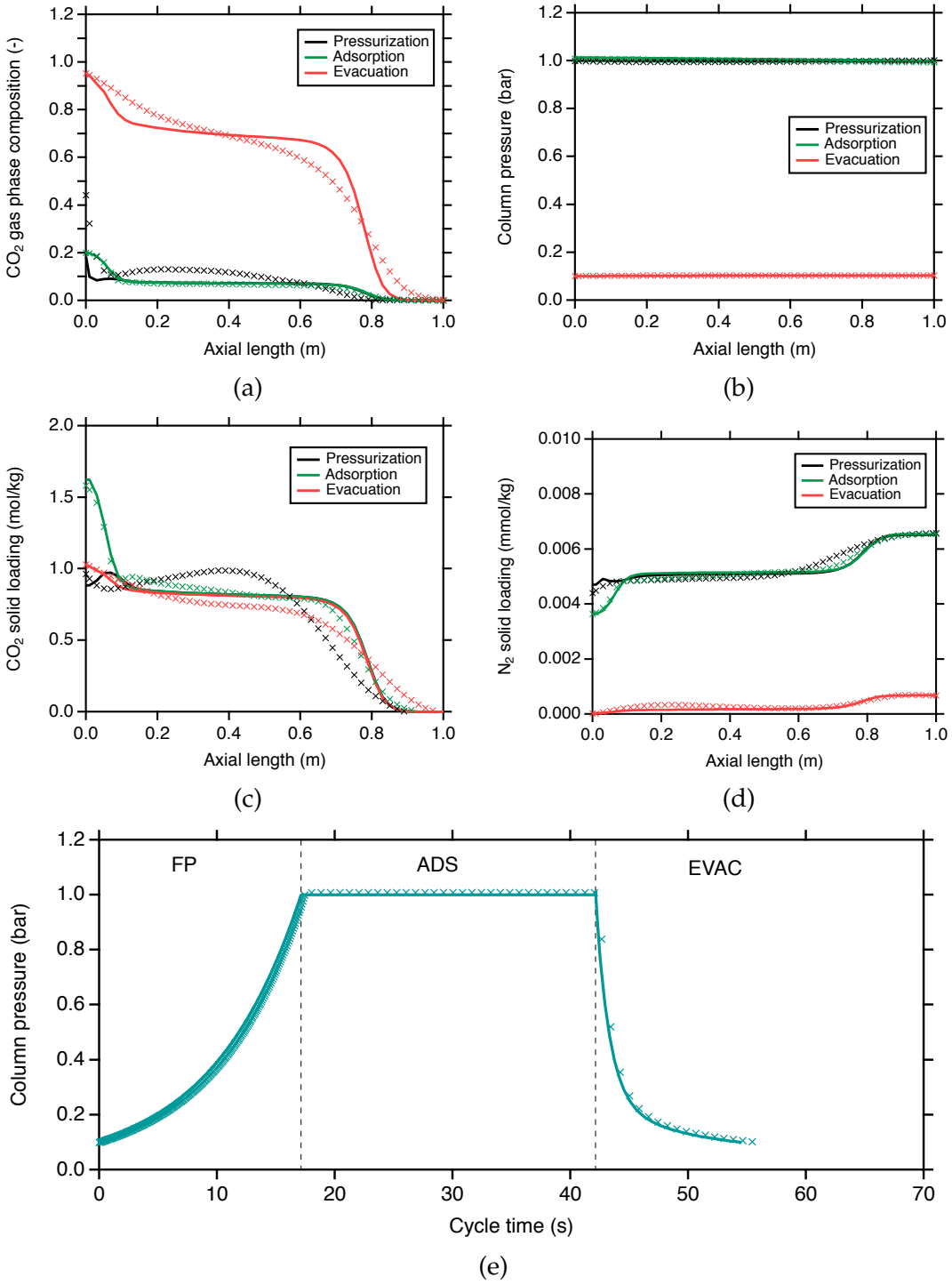

Figure 4.10: Comparison of cycle #1 profiles of four state variables obtained from the neural network (markers) and the detailed model (lines) simulations of three-step FP cycle for the operating condition: t_{ADS}=25 s and P_{L} = 0.1 bar.

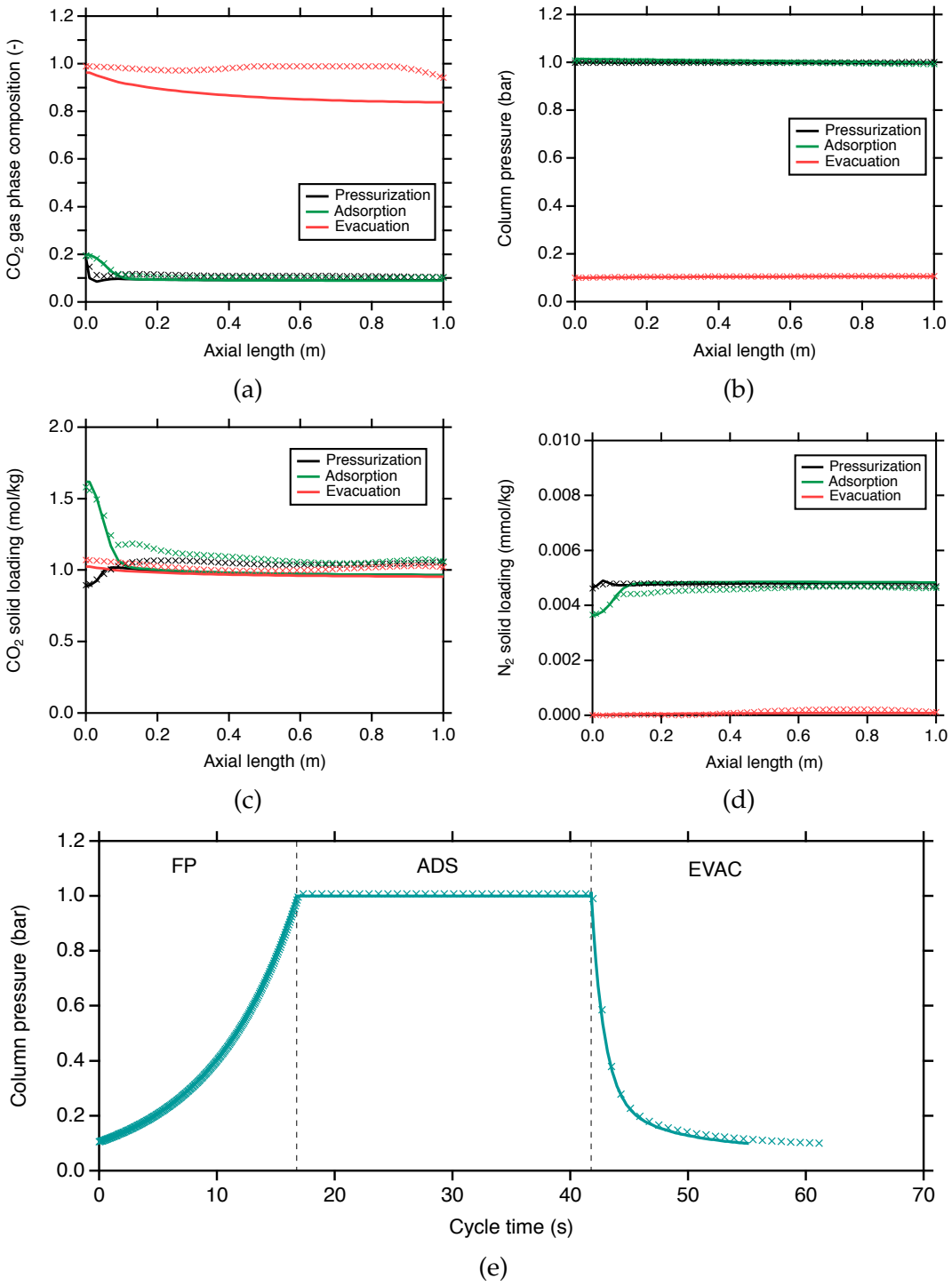

Figure 4.11: Comparison of cyclic steady state (CSS) profiles of four state variables obtained from the neural network (markers) and the detailed model (lines) simulations of three-step FP cycle for the operating condition: t_{ADS}=25 s and P_{L} = 0.1 bar.

the LPP step at CSS is $\approx$ 0.5 mol kg^{-1}, whereas in the previous case with FP, the final CO_2 solid loading at $z = 1$ at CSS is $\approx$ 1 mol kg^{-1}. It is worth mentioning that the pressurization step neural network model learnt the impact of inlet CO_2 gas-phase composition on the spatiotemporal dynamics very well. As can be seen from Table 4.6, the calculated CO_2 purity and CO_2 recovery from the neural network simulations are 5% and 11% higher than the values from the detailed model simulations. The detailed model took 85 cycles to reach CSS wheres the neural network simulations took 5 cycles. As a result, the computational speeds for neural networks simulations were up to 80 times faster than the detailed model simulations.

Simulation of four-step FP cycle

Here the four-step FP cycle, shown in Fig. 4.2(c), is constructed using the pressurization, the adsorption, the blowdown, the evacuation step models. For the operating condition of t_{ADS} = 25 s, P_{I}=0.75 bar, and P_{L}=0.1 bar, the column profiles after cycle #1 and at CSS from both neural network- and detailed model-based simulations can be visualized in Figs. 4.14 and 4.15, respectively. The profiles calculated from both the simulations are in good agreement, although the neural networks over-predicted the CO_2 gas-phase composition at the end of the evacuation step. As can be seen from Table 4.6, the inclusion of the blowdown step between the adsorption and the evacuation step improved the CO_2 purity while the CO_2 recovery remained almost the same compared to the first case. This is because the blowdown step removed some residual N_2 from the column, as can be seen from the increase in the CO_2 gas-phase compositions across the column before the evacuation step. Finally, the CO_2 purity and the CO_2 recovery from the neural network simulations are overestimated by 10% and 42%, respectively, compared to the detailed model simulations. Such high error in the CO_2 recovery can be attributed to the slight over-prediction of the evacuation step duration by the neural network model, as illustrated in Fig. 4.15. Nevertheless, the overall ef-

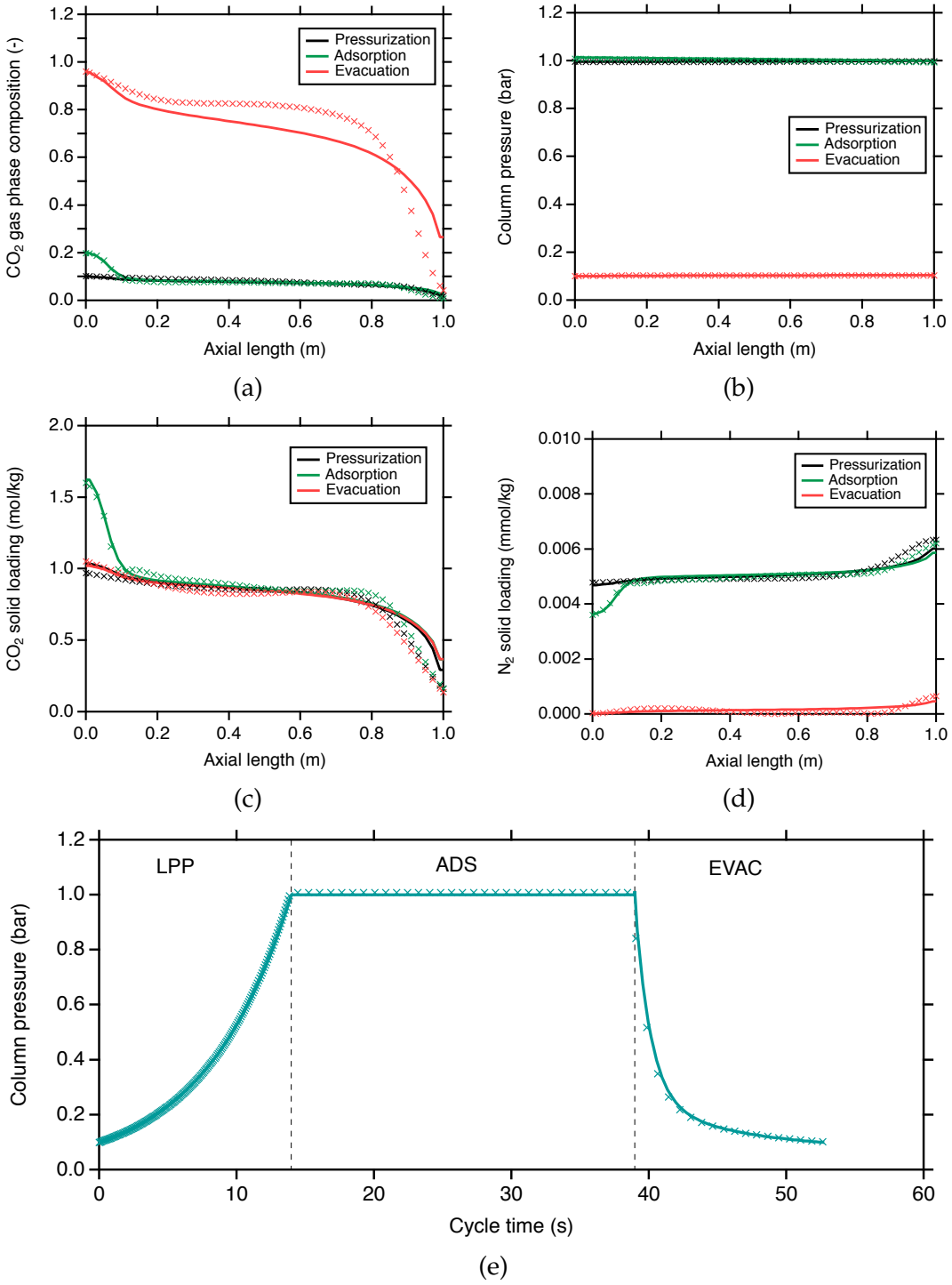

Figure 4.12: Comparison of cycle #1 profiles of four state variables obtained from the neural network (markers) and the detailed model (lines) simulations of three-step LPP cycle for the operating condition: t_{ADS}=25 s and P_{L} = 0.1 bar.

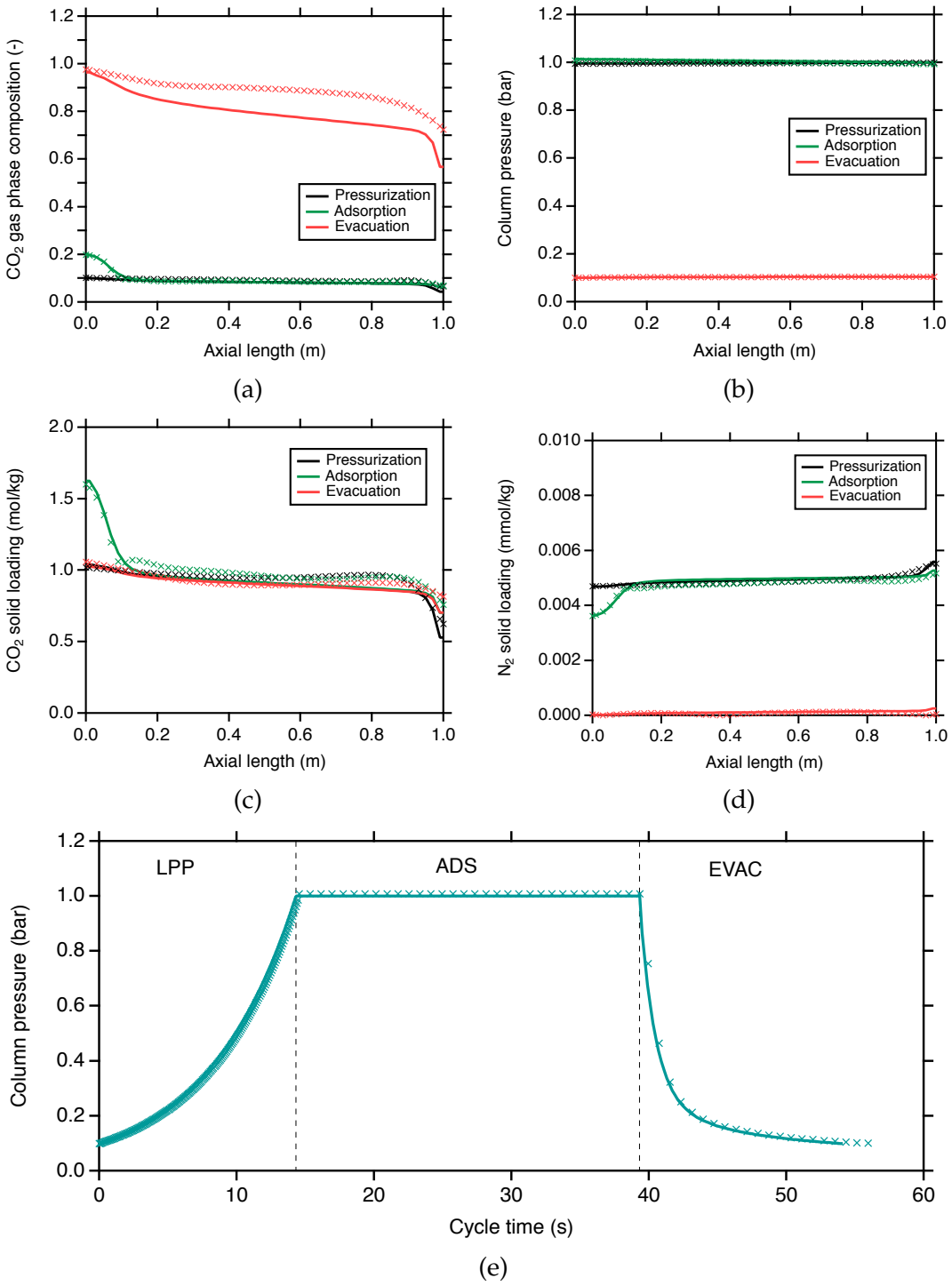

Figure 4.13: Comparison of cyclic steady state (CSS) profiles of four state variables obtained from the neural network (markers) and the detailed model (lines) simulations of three-step LPP cycle for the operating condition: t_{ADS}=25 s and P_{L} = 0.1 bar.

fectiveness of the neural network models in predicting the CSS profiles are excellent. In terms of computational efficiency, neural networks simulations saved up to 35 times the computational run-time.

Simulation of four-step LPP cycle

Finally, the four-step LPP cycle is constructed and simulated for the operating condition: t_{ADS} = 25 s, P_{I}=0.75 bar, and P_{L}=0.1 bar. The profiles of four step variables after cycle #1 and at CSS are shown in Figs. 4.16 and 4.17, respectively. Again, the predictions from the neural network simulations are in good agreement with the detailed model simulations. The CO_2 gas-phase composition final profile of the evacuation step is overestimated by the neural network models. Based on Table 4.6, the CO_2 purity and the CO_2 recovery are overestimated by 3% and 5%, respectively. The computational speeds achieved were 35 times higher than the detailed model.

Comparative performance for various operating conditions

The performance of the neural network models are tested based on 50 different randomly chosen operating conditions spanning the entire range considered for cycle synthesis study. Here, CO_2 purity and CO_2 recovery calculated at CSS from neural network and detailed process model simulations are compared. Figure 4.18 compares the CO_2 purities obtained from both the models and the error band represents 10% deviation. For all the cycles, the CO_2 purity calculated based on neural network simulations lie within the 10% error. On the other hand, the parity plot for CO_2 recovery illustrated in Fig. 4.19 show that the most of the predictions based on neural network simulations are within the 20% error margin. It is anticipated that the accuracy of CO_2 recovery calculated from the neural network simulations can be improved by increasing N_k, i.e., the number of different initial profiles and step parameters, in the neural network training. Finally, the computational times incurred for 50 simulations of all four cycles are reported in Table 4.7.

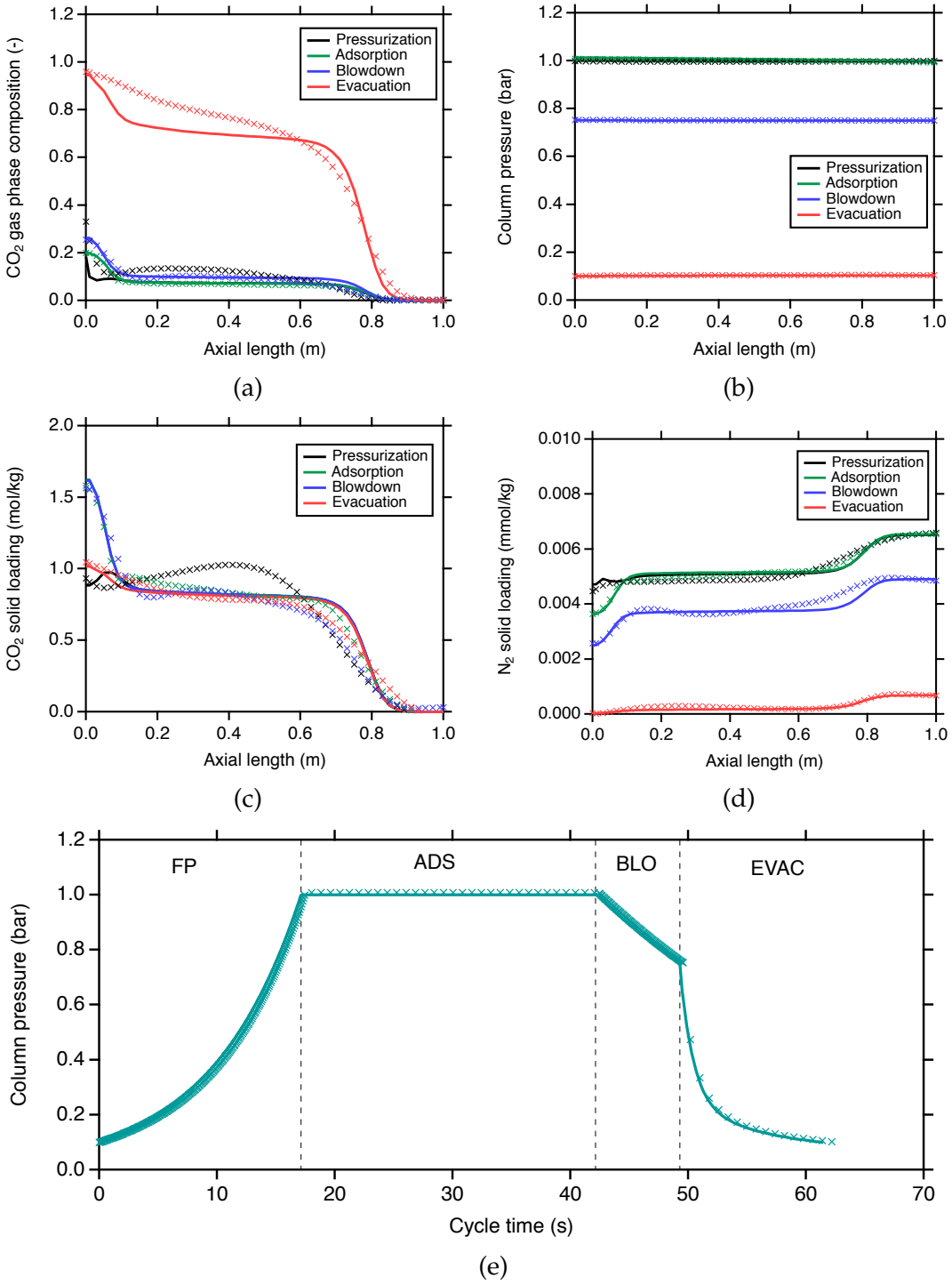

Figure 4.14: Comparison of cycle #1 profiles of four state variables obtained from the neural network (markers) and the detailed model (lines) simulations of four-step FP cycle for the operating condition: t_{ADS}=25 s, P_{I} = 0.75 bar, and P_{L} = 0.1 bar.

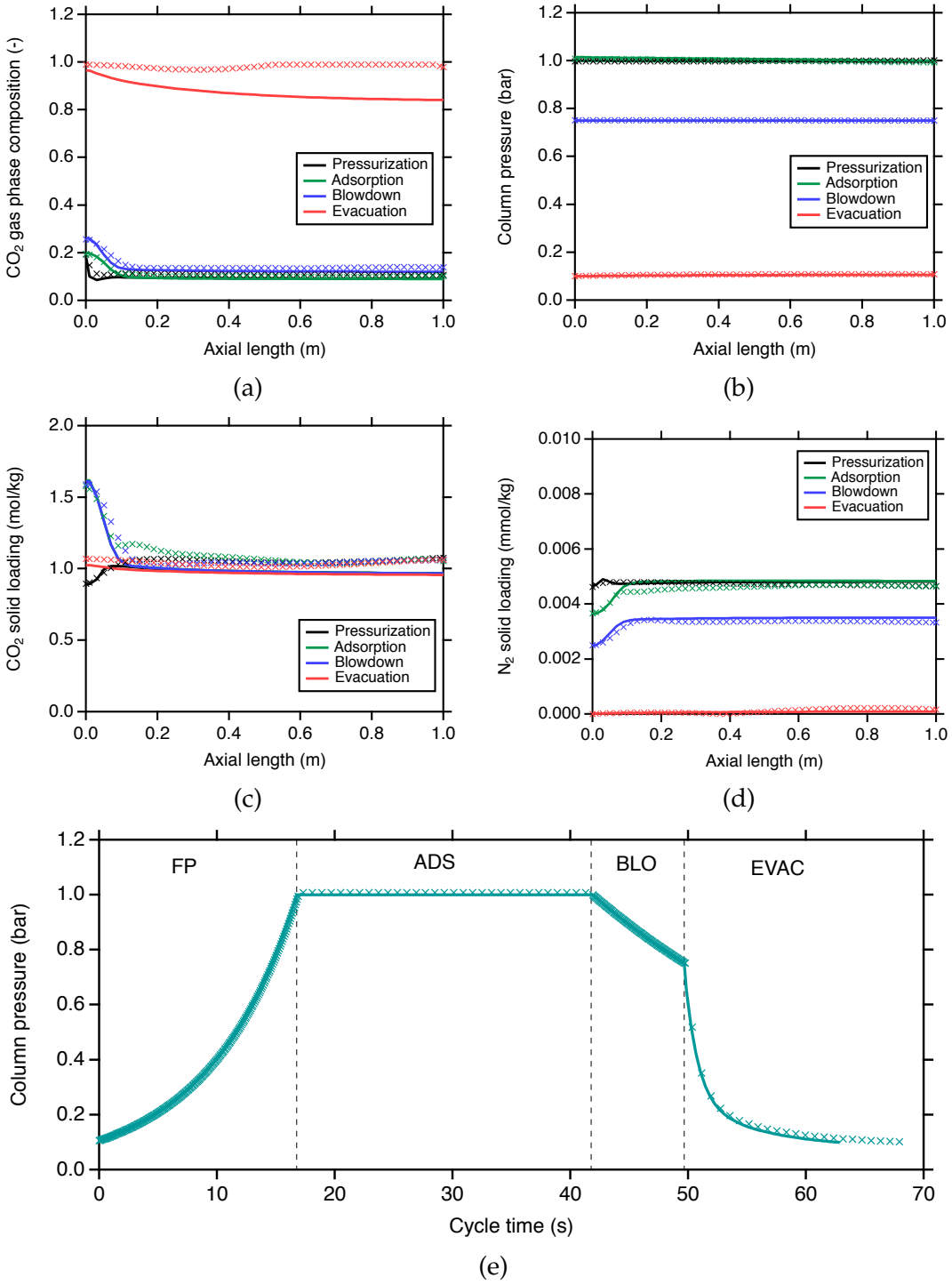

Figure 4.15: Comparison of cyclic steady state (CSS) profiles of four state variables obtained from the neural network (markers) and the detailed model (lines) simulations of four-step FP cycle for the operating condition: t_{ADS}=25 s, P_{I} = 0.75 bar, and P_{L} = 0.1 bar.

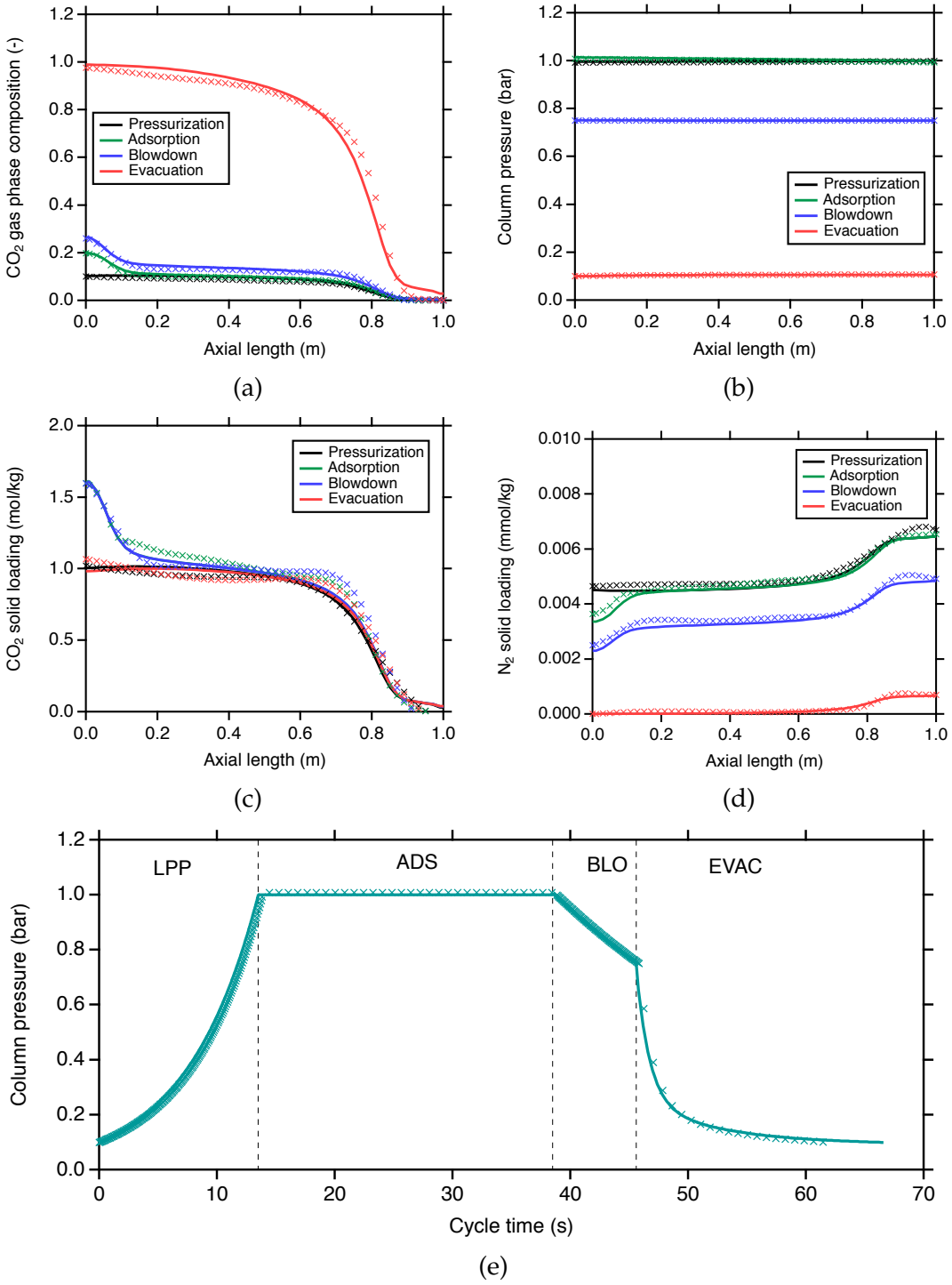

Figure 4.16: Comparison of cycle #1 profiles of four state variables obtained from the neural network (markers) and the detailed model (lines) simulations of four-step LPP cycle for the operating condition: t_{ADS}=25 s, P_{I} = 0.75 bar, and P_{L} = 0.1 bar.

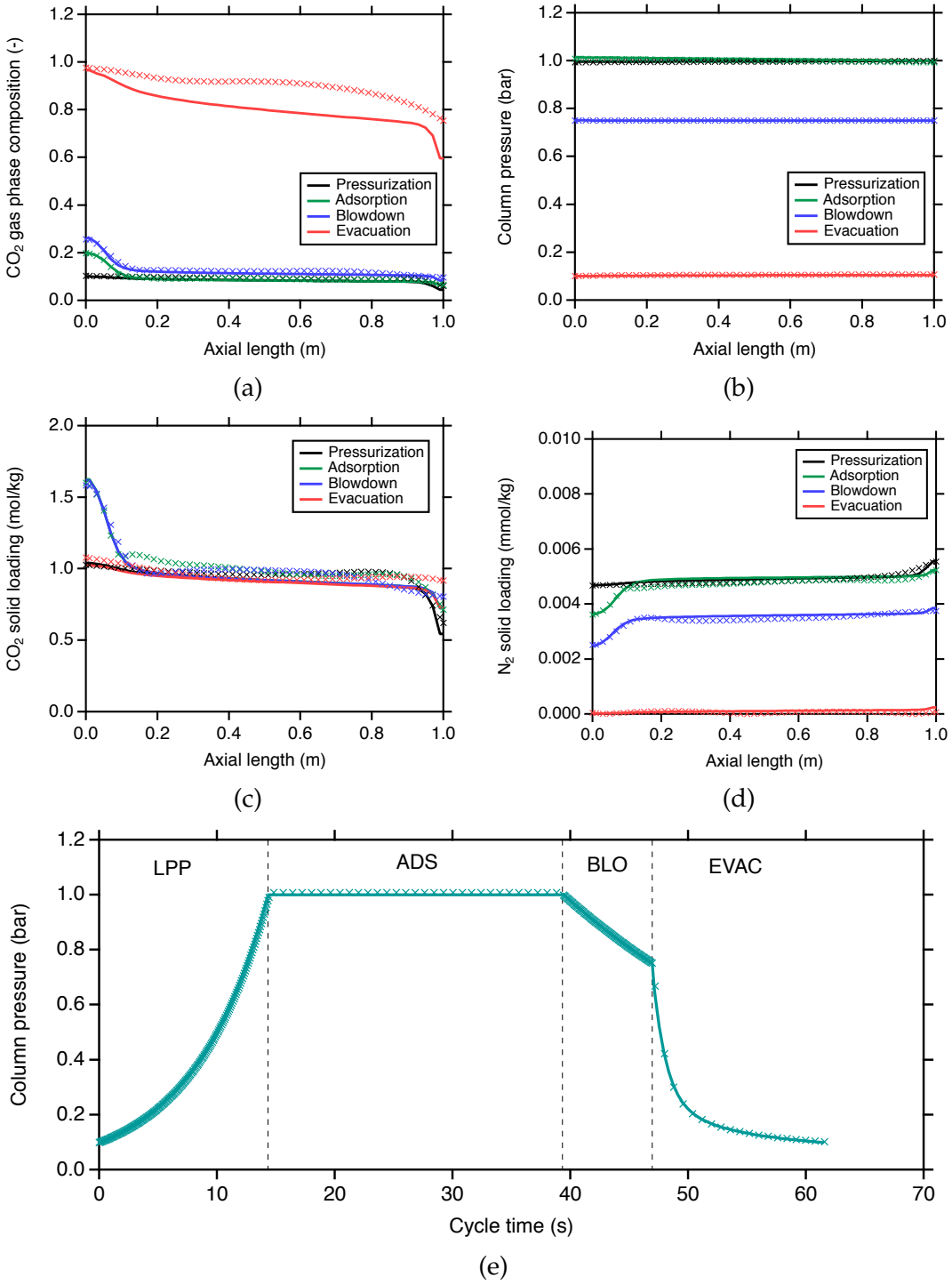

Figure 4.17: Comparison of cyclic steady state (CSS) profiles of four state variables obtained from the neural network (markers) and the detailed model (lines) simulations of four-step LPP cycle for the operating condition: t_{ADS}=25 s, P_{I} = 0.75 bar, and P_{L} = 0.1 bar.

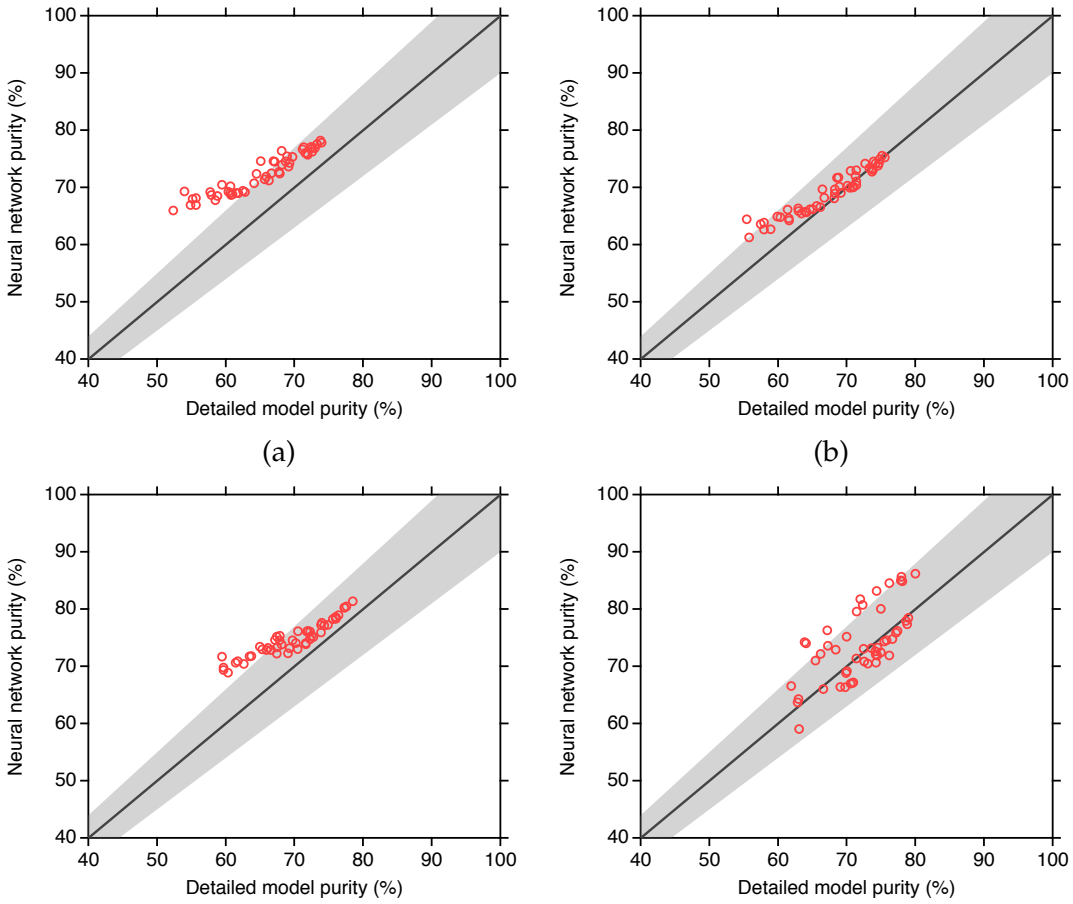

Figure 4.18: Parity plots of CO_2 purity obtained from the detailed process model- and the neural network-based simulations of (a) three-step FP cycle (b) three-step LPP cycle (c) four-step FP cycle (d) four-step LPP cycle at 50 different operating conditions. The error band represents 10%.

Table 4.7: Summary of computational times for carrying out 50 simulations using neural networks and the detailed process model. Note that CPU seconds on a 128 GB and 3.10 GHz workstation.

VSA cycles	Computational time (s)	
	Detailed model	Neural network
Three-step FP cycle	15771	384
Three-step LPP cycle	29499	166
Four-step FP cycle	16573	989
Four-step LPP cycle	30137	626

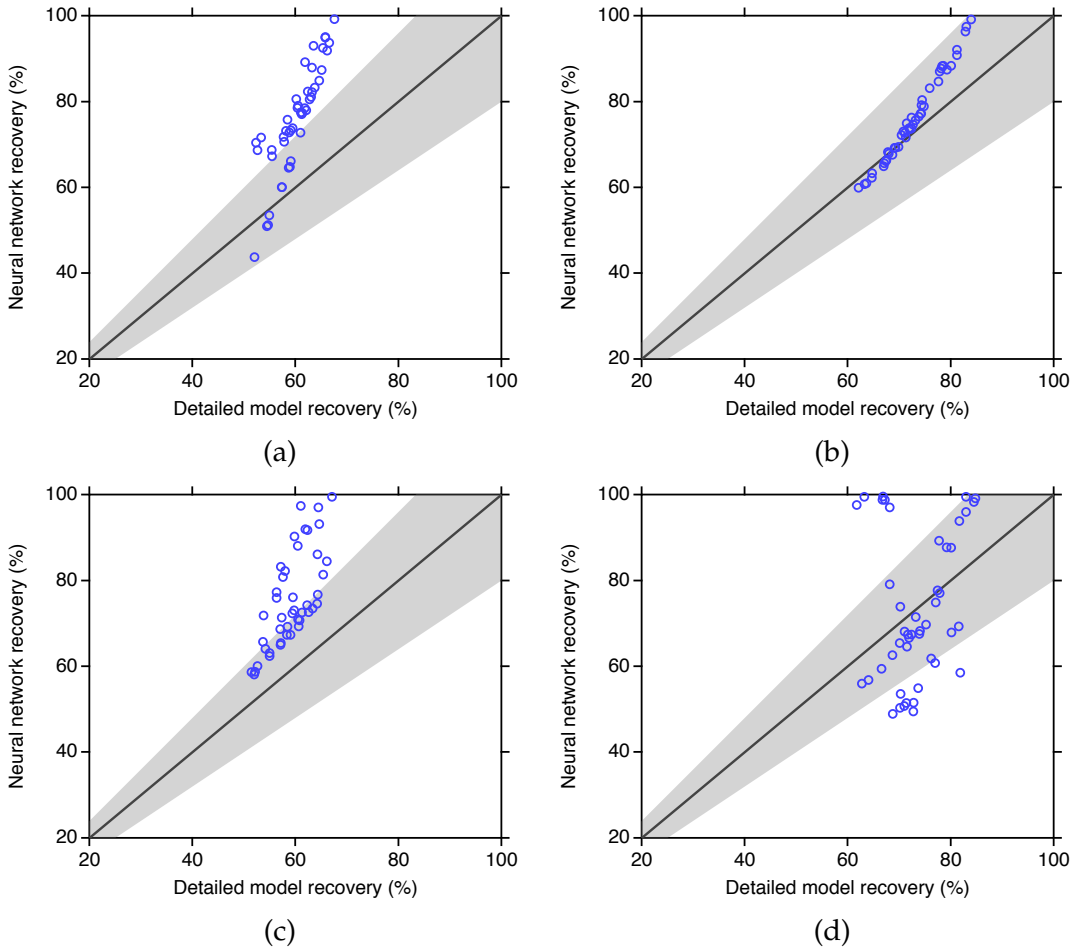

Figure 4.19: Parity plots of CO_2 recovery obtained from the detailed process model- and the neural network-based simulations of (a) three-step FP cycle (b) three-step LPP cycle (c) four-step FP cycle (d) four-step LPP cycle at 50 different operating conditions. The error band represents 20%.

4.5 Conclusions

For the first time, physics-based neural networks based on modern deep learning techniques are developed to rapidly synthesize and simulate cyclic adsorption processes. The deep neural networks employed herein are trained to learn the full spatiotemporal solutions of different state variables in cyclic adsorption processes by obeying the underlying conservation laws of mass and momentum along with adsorption equilibria. Unique neural networks are trained for different constituent steps of cyclic adsorption processes. The generalization capabilities are enabled by training the neural network

models based on different initial conditions and operating parameters. In the present study, the proposed methodology was tested on the case of post-combustion CO_2 capture by first constructing and simulating a four-step VSA cycle using individual neural network models of each step. Subsequently, individual neural network models are utilized to synthesize four simple VSA cycles for post-combustion CO_2 capture.

The results demonstrated that the trained neural network accurately predicts the spatiotemporal solutions of four state variables: CO_2 gas phase composition, column pressure, CO_2 solid loading, and N_2 solid loading. Particularly, the dynamics of state variables interior of the spatiotemporal domain were well-captured, even though no labelled data was provided. Moreover, the column profiles predicted by the neural network models at the cyclic steady state were in excellent agreement with the profiles obtained from the detailed model simulations. The effectiveness of the neural network-based simulations was further demonstrated by comparing the CO_2 purities and the CO_2 recoveries predicted at various operating conditions with the detailed model calculations.

With this initial success, the methodology was extended to demonstrate the cycle synthesis capabilities of neural network models. Using the trained neural network models, a three-step VSA cycle with feed pressurization, adsorption, and evacuation steps are constructed and simulated. The results showed that the neural network-based simulations accurately predicted the CSS profiles of each step in the cycle. Later on, the a three-step VSA cycle with light product pressurization is simulated and the neural network predictions were found to be in excellent agreement with the detailed process simulations. Finally, the complexity was increased by synthesizing two four-step VSA cycles with feed and light product pressurization steps. The comparative performances between the neural network and the detailed model simulations were found to be in good agreement, although the evacuation CO_2 gas-phase composition final profiles and step durations were slightly over-predicted by the neural networks.

Nevertheless, the results demonstrated the effectiveness of the proposed methodology to synthesize and simulate different cycles, a step towards superstructure-based optimal cycle synthesis. In the future, this methodology will be extended to incorporate more steps in order to synthesize and optimize complex adsorption cycles. In terms of computational speeds, the neural network simulations were at least 40 times faster than the detailed model simulations. The proposed methodology will be extended to synthesize and optimize different cyclic adsorption processes.

Part II

Techno-economic assessments

Chapter 5

Techno-economic assessment of optimized vacuum swing adsorption for post-combustion CO_2 capture from steam methane reformer flue gas

5.1 Introduction

Hydrogen is a clean fuel that plays an important role in the transition towards a low-carbon sustainable energy future. With growing demands in various sectors such as power, heating, industry, transportation, global hydrogen production is expected to increase in the next few decades substantially [92]. Although hydrogen can be produced through renewable sources, over 95% of global hydrogen production relies on fossil fuels [92, 93]. Since this production route involves high CO_2 emissions, CO_2 capture and storage (CCS) is a path forward to enable large-scale hydrogen production with low-carbon emissions in hydrogen plants to meet growing demands. Steam methane reforming (SMR) of natural gas is the leading technology for large-scale hydrogen production [11], accounting for almost 50% of the hydrogen produced globally [94]. In SMR-based hydrogen plants, natural gas undergoes steam-reforming followed by a

The results presented in this chapter have been reported in: S.G. Subraveti, S. Roussanaly, R. Anantharaman, L. Riboldi, A. Rajendran. Techno-economic assessment of optimised vacuum swing adsorption for post-combustion CO_2 capture from steam-methane reformer flue gas. *Sep. Purif. Technol.* **2021**, *256*, 117832.

water-gas shift to obtain shifted syngas. Owing to the highly endothermic reforming reactions, combustion of natural gas in the reformer remains inevitable [11]. Pressure swing adsorption (PSA) then purifies the shifted syngas to produce ultrapure hydrogen. Based on the aforementioned process steps, CO_2 sources can be associated with SMR furnace flue gas and shifted syngas from reforming and water-gas shift reactions. While up to 60% CO_2 can be captured from shifted syngas [92], post-combustion CO_2 capture from SMR furnace flue gas must be deployed to achieve higher overall capture rates from SMR-based hydrogen plants [11], thus enabling low-carbon-footprint hydrogen. The current state-of-the-art separation technology for post-combustion CO_2 capture in SMR plants involves monoethanolamine (MEA) based absorption [11].

Alternative post-combustion CO_2 capture technologies such as membrane separation and vacuum swing adsorption (VSA) have emerged as promising technologies currently in the R&D stage [10]. The VSA technology was also commercially demonstrated for CO_2 capture from syngas in an SMR-based plant at Valero Port Arthur Refinery (Texas, USA) [31]. With growing interest in developing adsorption technology for CO_2 capture, major improvements have been made to develop new adsorbents and processes [10]. Recent model-based material screening studies have enabled the discovery of potential adsorbents for CO_2 capture applications [23, 45, 95, 96]. Alongside, novel processes that are efficient in terms of energy and productivity are being developed [40]. It is worth noting that majority of studies in the literature focus on the development of materials. Most process studies have focused either on developing novel processes or the screening/evaluation of adsorbents. These studies often perform assessments based on process metrics such as parasitic energy consumption and productivity. While these are important metrics, they seldom provide an idea of the cost of capture. Without a proper estimate of the cost, it is problematic to compare various technologies, evaluate the complexities involved in scale-up, etc. Hence, it is important that process studies go beyond evaluating process metrics and consider the

cost of capture. Such detailed analyses are not common in the literature, with a few exceptions that are discussed here.

Table 5.1 summarizes a sample of relevant techno-economic studies that focused on P/VSA technology for post-combustion CO_2 capture. As can be seen from the table, many studies have focused mainly on coal-fired power plants, and there are no studies reported for post-combustion CO_2 capture in hydrogen plants using the VSA technology. Most previous studies also overlooked the dynamics of the vacuum pump in P/VSA simulations which can lead to two major concerns. Typically, predefined pressure histories used to approximate the dynamics of vacuum pumps can significantly overestimate the productivity of the capture plant. Another shortcoming comes from the assumption of high vacuum pump efficiencies to calculate the VSA energy consumption. This is a critical aspect since the production of high purity CO_2 at high recovery requires very low vacuum pressures at which pump efficiencies are known to drop dramatically [35, 97]. Practical considerations on the vacuum pump performance are often omitted in cost estimations. Previous research has not considered the scale-up and proper column scheduling in their optimal cost estimations, with a notable exception being the work of Khurana and Farooq [21]. Given the complexity of the CO_2 capture problem, multiple trains of VSA columns are required to treat the flue gas. Under such circumstances, it is important to carefully perform the column scheduling and the scale-up to ensure continuous feed. One more limitation relates to the adsorbent cost. As can be seen from Table 5.1, some studies estimated the costs of novel adsorbents such as metal-organic frameworks to be the same as that of Zeolite 13X. This assumption may no longer be valid, especially when the raw materials used to synthesize these adsorbents are expensive. Further, a wide range of financial parameters were used for cost estimations which makes the comparison of VSA performance with other technologies challenging. The P/VSA cost estimations are not straightforward, and the literature has not rigorously assessed the techno economics apart from

the work of Khurana and Farooq [21]. Therefore, a detailed cost model based on established financial guidelines together with the full complexity of VSA remains essential in order to compare VSA with other capture technologies. Improvements in VSA modelling in recent years to perform reliable calculations are another factor to consider for the need for up-to-date cost estimation. In order to enable cost-efficient designs, integrating the detailed cost model with the design and optimization is essential [98].

In the present chapter, an integrated techno-economic optimization model is developed that takes into account a detailed VSA process model, peripheral component models, vacuum pump performance and a comprehensive costing model. This model is used to assess the techno-economic performance of an optimized VSA process for post-combustion CO_2 capture in SMR-based hydrogen plants. Three different adsorbents are evaluated for their technical and cost performances based on a four-step VSA cycle with light product pressurization and tested for their competitiveness by comparing with state-of-the-art MEA-based absorption. In addition, different optimization cases are considered to highlight (1) the critical choice of process design objectives, (2) the importance of incorporating vacuum pump performance into the techno-economic optimization model, (3) the effect of adsorption column sizing and (4) the influence of adsorbent costs.

Table 5.1: Summary of selected techno-economic studies for P/VSA.

Study	Case/application	CO_2 composition	Process	Adsorbent(s)	KPI	Lowest CO_2 capture cost	Scale-up/scheduling	MOF cost	Purity/recovery Constraints	Comments
Ho et al. (2008) [99]	500 MW power plant	13%	Skarstorm PSA/VSA	Zeolite 13X	CO_2 avoided cost	US$51 per ton of CO_2 avoided	Simple	-	None	Short-cut model with many simplifying assumptions Preliminary analysis, which is only indicative
Hasan et al. (2012) [48]	Generic	Wide range	4-step PSA/VSA	Zeolite 13X	Total annualized cost	Wide range	No	-	90%/90%	Vacuum pump dynamics not considered Column scheduling and scale-up not considered
Susarla et al. (2015) [49]	500 MW power plant	15%	4-step PVSA	Zeolite 13X	Total annualized cost	US$33.4 per tonne of CO_2 avoided	Extensive	-	90%/90%	Dry flue gas considered
Leperi et al. (2016) [50]	30 MW coal power plant	14.1%	Two-stage modified Skarstorm cycle	Zeolite 13X Zeolite 5A Ni-MOF-74 HKUST-1	Total annualized cost	US$ 34.1 per ton of CO_2 captured	No	Based on metal prices	90%/90%	Small-scale power plant No column scheduling
Khurana & Farooq (2019) [21]	550 MW power plant	15%	4-step VSA 6-step VSA	Zeolite 13X UTSA-16 Min. cost adsorbent	Levelized cost of electricity	US$26.3 per tonne of CO_2 avoided	Extensive	Fixed to Zeolite 13X	95%/90%	Based on a dry flue gas Framework also facilitates the search for the lowest cost adsorbent MOF costs assumed to be same as that of the Zeolite 13X
Danaci et al. (2020) [51]	400 MW natural gas power plant 500 MW coal power plant 1 MM TPA cement plant 4 MM TPA steel plant	4.38% 12.5% 21% 25.5%	3-step VSA	25 Adsorbents incl. UTSA-16, Zeolite 13X	Annualized capture cost	Wide range	No	Fixed to Zeolite 13X	None	Simplified VSA model that does not consider column dynamics MOF cost estimations based on bulk metal prices performed for UTSA-16
This chapter	450 TPD SMR H_2 plant	20%	4-step VSA	Zeolite 13X UTSA-16 IISERP MOF2	CO_2 avoided cost	33.6 € per tonne of CO_2 avoided	Extensive	Based on metal prices	95%/90%	Vacuum pump performance incorporated into VSA simulation Adsorbent manufacturing factor considered in estimating MOF costs Comprehensive cost model consistent with best practices

5.2 Case study

The SMR process for hydrogen production without CO_2 capture considered in this chapter is based on a single steam methane reforming train with a production capacity of 450 tonnes of hydrogen per day. A simplified process flow diagram of the SMR-based hydrogen production system is shown in Fig. 5.1. First, natural gas is converted to syngas through a pre-reformer and a reformer. After the reformer, the CO in the syngas is converted to CO_2 through a high-temperature and a low-temperature water-gas shift. It is also worth noting that the water-gas shift enables the production of HP steam used to generate electricity. A PSA unit then separates H_2 from the rest of the converted syngas to produce high purity hydrogen (the main product of the plant). The PSA tail gas is sent back to the furnace to burn with the natural gas and deliver heat for the reforming process. Without CO_2 capture, the hydrogen plant results in an exhaust flue gas of 233.9 kg/s at 1.02 bar and 353.15 K and the following molar composition: 16.23% CO_2, 63.31% N_2, 17.87% H_2O, 1.84% O_2, 0.75% Ar [100]. The scope of this chapter is identified in Fig. 5.1.

To benchmark the adsorption-based process, a standard MEA-based CO_2 capture is considered as the reference technology, as illustrated in Fig. D.1 in Appendix D. After CO_2 capture, the CO_2 is pressurized to 200 bar before being transported to an offshore saline aquifer located 140 km away. While a summary of the performances of the hydrogen plant with and without MEA-based CCS is presented in Table D.1 in Appendix D, more details can be found elsewhere [100].

5.3 Systematic design of VSA systems

An integrated techno-economic optimization framework is proposed for the design of VSA processes. Most VSA studies for CO_2 capture deal with process optimizations involving either energy reduction or productivity maximization, or both. While these

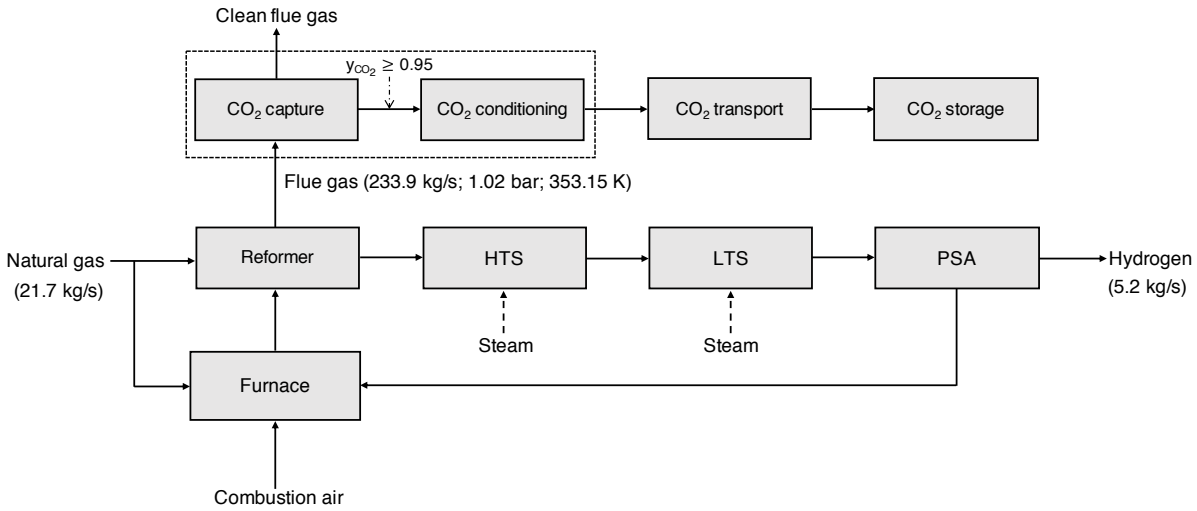

Figure 5.1: Process flow diagram of the hydrogen production plant and the overview of CCS chain. The dotted box represents the scope of this chapter.

are good proxies for operating and capital costs, the true estimate of technology should be based on a thorough techno-economic study that accurately incorporates the trade-offs involved. In this chapter, a techno-economic analysis coupled with a rigorous process optimization approach is used. The key features of this approach are following:

1. The use of a process cycle demonstrated at a pilot plant facility to produce high CO_2 purity and recovery.

2. Rigorous modelling of the adsorption process that explicitly accounts for full transient column dynamics and cyclic-steady state performance of the process.

3. A rational scale-up approach that determines the number of columns and parallel trains to ensure continuous operation.

4. A costing framework that is consistent with best practices in order to improve the reliability of the cost values.

The framework used for this chapter is illustrated in Fig. 5.2. The inputs to this framework are technical and economic design basis, VSA cycle and physiochemical properties such as adsorption isotherms. Based on the inputs provided, integrated

simulation and costing framework coupled with stochastic optimization output the cost optimal design of the VSA process. More details of these components are presented below.

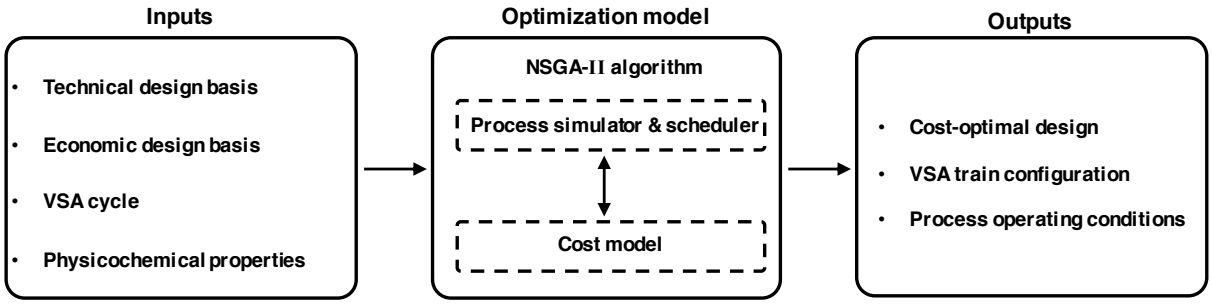

Figure 5.2: Integrated techno-economic optimization methodology.

5.3.1 VSA capture system

Process layout

The process layout of adsorption-based CO_2 capture is illustrated in Fig. 5.3. Given the detrimental nature of water on many adsorbents, the wet flue gas of the hydrogen plant is first cooled to 313.15 K by a direct contact cooler and then dehydrated using a molecular sieve to remove the water [98]. The dry flue gas requires compression to overcome the pressure drop in VSA columns. Two identical single-stage compressors are employed to compress the entire dry flue gas to the desired pressures. Coolers follow each compression unit to cool the feed mixture to 298.15 K.

A feed header splits the dry flue gas as feed into M identical VSA units [49]. The feed mixture to VSA units is considered to contain 20% CO_2, 77% N_2, 2% O_2, 1% Ar. For simplicity, a binary mixture of 20% CO_2 and 80% N_2 was used to simulate the VSA process. This can be justified by the fact that both O_2 and Ar adsorb weaker than N_2 on most adsorbents, specifically those considered in this chapter and hence, can be considered to be adequately represented by N_2. Each VSA unit consists of N identical columns operating out of phase to implement the cycle operation. Several switching

valves, dedicated vacuum pumps are employed to remove N_2 and collect CO_2 separately. The CO_2 after capture undergoes a multi-stage compression with intercooling from 1 bar and 298.15 K to the target conditions prior to offshore pipeline transport (200 bar and 318.15 K). More details on the technical modelling of various peripheral components are summarized in Appendix D.

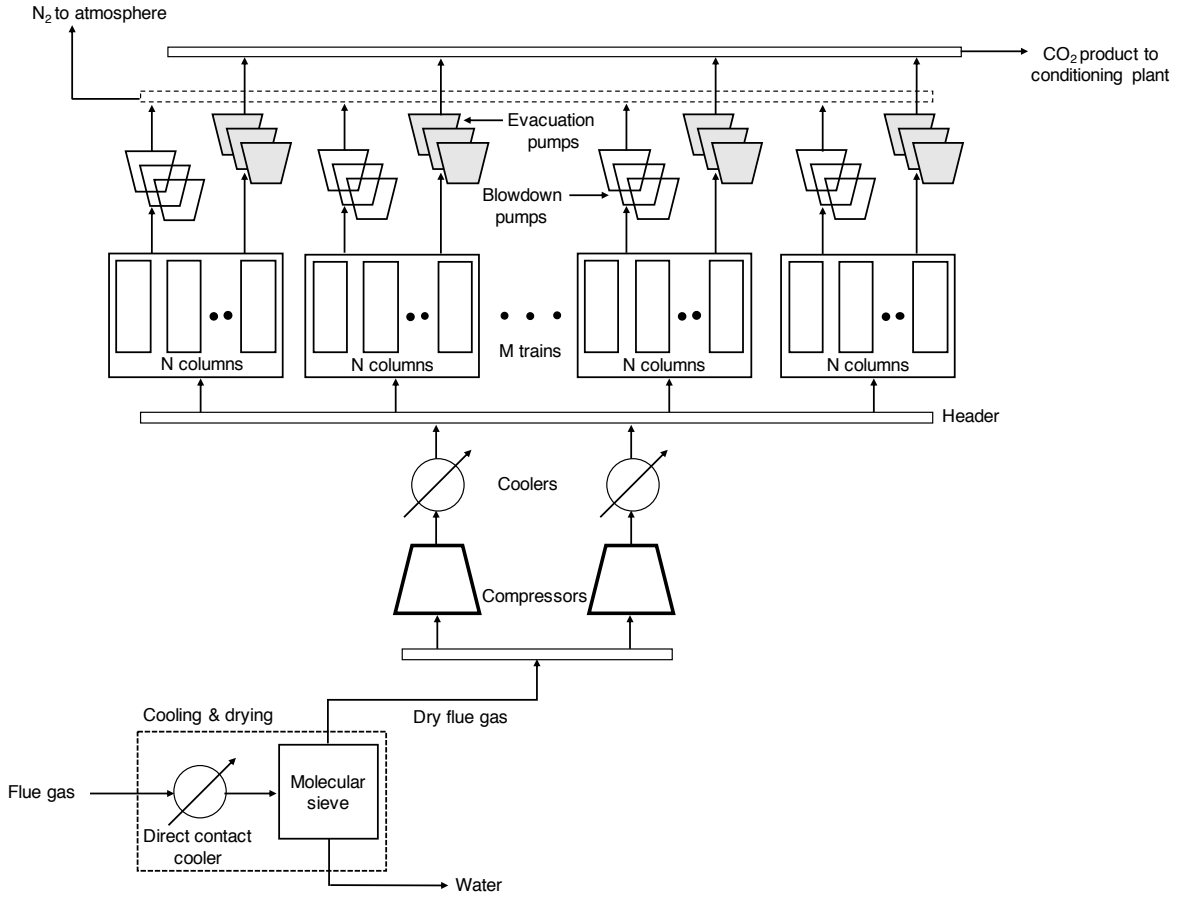

Figure 5.3: Process layout for CO_2 capture using vacuum swing adsorption.

Four-step VSA cycle

The cycle configuration considered in this chapter is illustrated in Fig. 5.4. It is worth noting that this process is widely used in the research community as a benchmark cycle and has been successfully demonstrated at a pilot scale [21, 24, 35, 101, 102]. Naturally, more complex cycles can be synthesized, resulting in better performance. However, it

is anticipated that for a process of this scale, simple cycles would be preferred. The cycle consists of adsorption (ADS), co-current blowdown (BLO), counter-current evacuation (EVAC) and light product pressurization (LPP) steps. The separation of feed mixture occurs in the adsorption step at atmospheric pressure (P_{H}) where the heavy product CO_2 adsorbs in the column, and N_2 leaves the column as a light product. Although the adsorption step occurs at atmospheric pressure, the feed mixture needs to be compressed to a higher pressure (P_{F}) to overcome the pressure drop across the column. In the co-current blowdown step, the column pressure is reduced to an intermediate vacuum (P_{I}) in order to remove N_2 present in the column. The column pressure is further reduced to a low vacuum (P_{L}) in the counter-current evacuation step to collect the heavy product CO_2 at the feed end of the column. The light product from the adsorption step is used to pressurize the column back to atmospheric pressure.

Adsorbent materials

Three adsorbents were considered: Zeolite 13X [19], the current benchmark material for CO_2 capture [35, 36]; Metal-organic frameworks, UTSA-16 [103], a widely studied metal-organic framework for CO_2 capture [21, 24, 51, 104]; and IISERP MOF2 [105], which showed a better performance than Zeolite 13X and other MOFs in terms of energy consumption and productivity in a recent screening study [91]. The adsorption equilibria for all these adsorbents were described using a competitive form dual-site Langmuir (DSL) model (for each component i):

$$q_i^* = \frac{q_{\mathrm{sb},i} b_i c_i}{1 + \sum_i b_i c_i} + \frac{q_{\mathrm{sd},i} d_i c_i}{1 + \sum_i d_i c_i} \tag{5.1}$$

where $q_{\mathrm{sb},i}$ and $q_{\mathrm{sd},i}$ are the saturation loadings for the two sites and, b_i and d_i are the adsorption equilibrium constants with Arrhenius temperature dependence as follows:

$$b_i = b_0 e^{\left(-\frac{\Delta U_{\mathrm{b},i}}{RT}\right)} \tag{5.2a}$$

$$d_i = d_0 e^{\left(-\frac{\Delta U_{\mathrm{d},i}}{RT}\right)} \tag{5.2b}$$

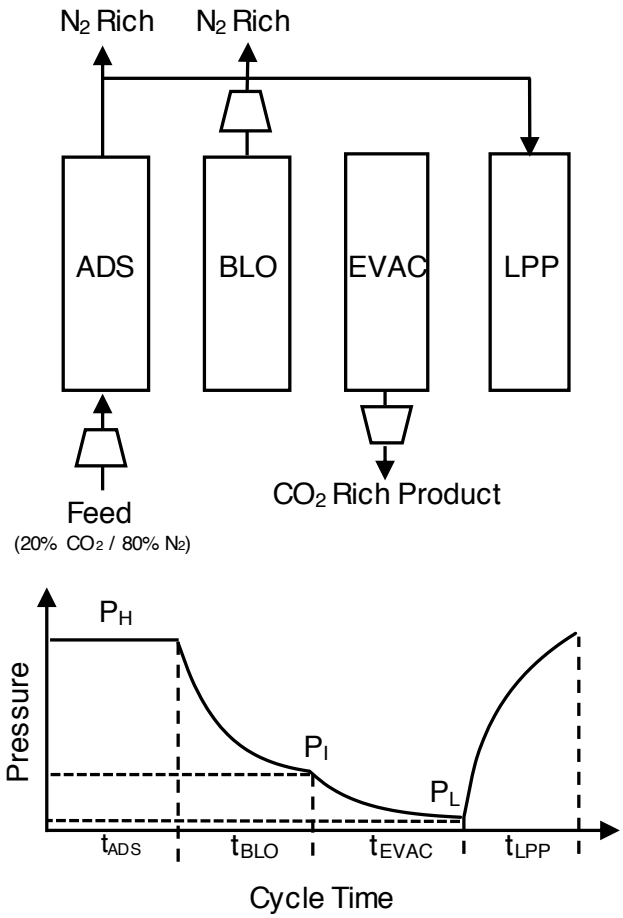

Figure 5.4: Four-step VSA cycle schematic.

$\Delta U_{\mathrm{b},i}$ and $\Delta U_{\mathrm{d},i}$ are the internal energies of the two sites. It is worth mentioning that the extended dual-site Langmuir isotherm model in Eq. 5.1 explicitly takes into account the competition between CO_2 and N_2. In this chapter, the equal energy site (EES) form of the DSL isotherm is used [101]. In this formalism, the saturation capacity of each site is kept identical for both components and the enthalpy of adsorption for N_2 is kept identical for both sites. Experimental evidence supports this for the case of Zeolite 13X [47]. The DSL isotherm parameters for Zeolite 13X pellets were obtained based on previously performed experiments [19]. The CO_2 and N_2 isotherm parameters for UTSA-16 extrudates and IISERP MOF2 were obtained from the literature [91, 104]. Note that the IISERP MOF2 was assumed to form uniform particles of 1.5 mm using a structuring agent (binder). Figure 5.5 shows the CO_2 and N_2 single component

isotherms for all three adsorbents, and related isotherm parameters are provided in Table D.2 in Appendix D.

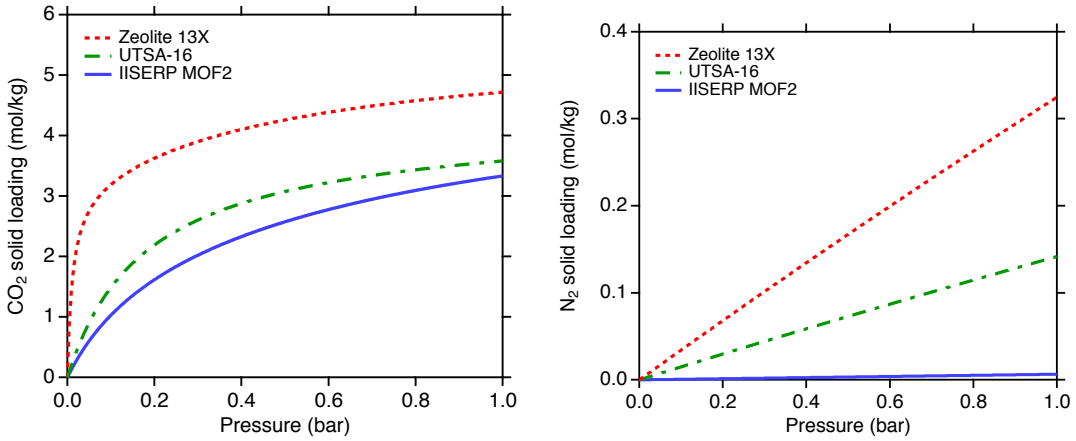

Figure 5.5: Single component (a) CO_2 and (b) N_2 isotherms on the three adsorbents at 298.15 K.

5.3.2 Technical modelling

VSA process model

A non-isothermal, one-dimensional mathematical model obtained by solving mass, momentum and energy balances was used to simulate the VSA process [19]. Both lab-scale and pilot-scale experiments have been reported in the literature to validate the model [35, 47]. The model assumes that the gas behaves ideally, and an axially dispersed plug flow model represents the bulk flow. No radial gradients exist for composition, pressure and temperature across the column. Adsorbent properties and bed porosity remain uniform throughout the column. There also exists an instantaneous thermal equilibrium between the gas and the solid. The linear driving force model describes the solid-phase mass transfer, and Ergun's equation accounts for the pressure drop across the column. The adiabatic operation, i.e. no heat transfer across the walls, remains valid given the large column sizes considered. The resulting governing equations are listed in Appendix A.

Appropriate boundary conditions were defined to solve each cycle step (provided in Table D.3 in Appendix D). Unlike previous studies [19, 25], the volumetric flow rate of vacuum pumps was assigned as boundary conditions at the exit of the column to simulate blowdown and evacuation steps instead of using predefined exponential pressure histories. This modification allows for reliable estimations of cycle times and the vacuum pump size/cost. Note that most of the vacuum pump costs are based on volumetric flow rates [21]. In addition, recent studies also show that incorporating vacuum pump volumetric flow rate-based boundary conditions improve the overall accuracy of the model to predict process performance indicators [21, 106]. Therefore, the volumetric flow rate of vacuum pumps was given as inputs, and the model calculated the times of blowdown and evacuation.

The partial differential equations (PDEs) were numerically solved by discretizing the spatial terms using the finite volume method with a weighted essentially non-oscillatory (WENO) scheme as a flux limiter [19]. The PDEs were discretized into 30 finite volumes, and the resulting ordinary differential equations were integrated using a stiff ode solver, *ode23tb*, in MATLAB. All simulations were initialized with a feed mixture at P_{L} and were performed based on a unibed approach, i.e. a single bed undergoes all cycle steps in a sequence, a standard technique used in P/VSA simulations. The coupled cycle steps were modelled by using data buffers to store the stream information. The blowdown and evacuation steps were terminated once the column pressure reaches the desired pressure. The cyclic steady state (CSS) criterion was when the mass balance error equal to 1% or less was observed for five consecutive cycles. Simulations were run for a large number of cycles to confirm that this criterion was adequate. If the system fails to attain the CSS criterion, simulations were performed until a maximum of 500 cycles after which it was assumed that the CSS was attained. At CSS, the model provided a detailed composition, temperature and pressure profiles that were essential to calculate key performance indicators. The simulation parameters are provided

in Table D.4 in Appendix D.

Column scheduling

Owing to the transient nature of the VSA system, scheduling the cycle with the minimum number of columns is required to make the operation continuous. The scheduling procedure proposed by Khurana and Farooq [21] was adopted. The main considerations are summarized here: (1) Continuous feed with constant throughput. (2) Separate blowdown and evacuation vacuum pumps to avoid contamination of effluents from respective steps and to maintain the modular nature of the process. (3) Coupled steps must occur simultaneously in two columns in order to avoid storage. (4) At any given time, one vacuum pump serves only one column. More details on calculating the number of columns per unit train (N), the number of vacuum pumps per unit train (N_{v}) and the number of parallel trains (M) are provided in Sections D.3.1 and D.3.2.

Vacuum pumps

Vacuum pumps were assumed to deliver constant volumetric flow rates over wide vacuum ranges. Although vacuum pump flow rates obey specific performance curves in practice, a constant volumetric flow rate assumption allows for a more generic design framework employed herein. It is worth mentioning that the vacuum pump efficiency was considered to be dependent on the vacuum level instead of a fixed value. Based on earlier studies, it was found that the vacuum pump performance significantly drops at deep vacuum levels ($<$0.1 bar) while it remains constant for moderate vacuum ($>$0.1 bar) [35, 97]. Although the true vacuum pump efficiency depends on the specific vacuum pump, a generalized vacuum pump efficiency function regressed based on vacuum levels between 0.01 bar and 1 bar after analyzing the several vacuum pump performance curves in a previous study [97] was used. The relation for vacuum pump

efficiency is defined as follows:

$$\eta_{\mathrm{V}} = \frac{15.84P}{1 + 19.80P} \tag{5.3}$$

where P, in bar, is the suction pressure. Note that Eq. 5.3 was was used to quantify the vacuum pump performance in this chapter unless otherwise stated. The efficiency, η_{V}, includes that of the driver.

5.3.3 Cost assessment

The cost assessment was performed on the basis of an Nth Of A Kind (NOAK) approach wherein it was assumed that the VSA technology was mature for CO_2 capture and demonstrated on a commercial scale [107]. The cost methodology for VSA technology involves the estimation of both capital costs (CAPEX) and operating costs (OPEX). All costs are provided in €$_{2016}$ price levels. Costs based on older estimates than 2016 were updated using Chemical Engineering Plant Cost Index (CEPCI) and inflation.

Capital costs

A bottom-up approach was adopted to estimate the capital costs and is illustrated in Fig. 5.6 [108]. First, the direct cost of process equipment was estimated using Aspen Process Economic Analyzer®. The direct cost of each equipment represents both equipment and installation costs. The estimation was carried out based on key design characteristics of each equipment, such as pressure, diameter, flow rate, etc. For easier implementation within the optimization framework, cost functions were regressed for each type of equipment and were directly used to assess the direct cost of each equipment of the process. Multiple economic evaluations were performed based on a wide range of relevant key design characteristics for each equipment. The accuracy of cost functions remains valid for different operating conditions evaluated in the optimization (see Appendix C for more details). In addition to process equipment, initial

adsorbent purchase, transport and installation costs were also accounted for in the total direct cost (TDC).

A process contingency factor of 15% of total direct cost without contingencies, which is in line with NETL guidelines, was added to the total direct cost to calculate the total direct cost with process contingency (TDCPC) [109]. Then, indirect costs and project contingencies were added to the total direct cost with process contingencies to obtain the total plant cost (TPC). Indirect costs, which include engineering costs, consultancies, service facilities, yard improvement, building and sundries, were set to 14% of TDCPC. The project contingencies were set to 20% of TDCPC in accordance with NETL guidelines [109]. Finally, the owner costs and interest over construction are added to the TPC to calculate the total capital requirement (TCR). The owner costs are considered to represent 7% of TDCPC [110]. The interest over construction is calculated assuming that the construction costs are shared over a three-year construction period following a 40/30/30 allocation.

Due to its specificity, it is worth noting that the direct cost of each adsorbent was estimated differently than presented above. While the cost of an adsorbent is key for the design and evaluation of adsorption-based CO_2 capture processes, estimating the cost of an adsorbent can be challenging in practice, especially if the material has not been commercialized. Amongst the adsorbents considered in this chapter, Zeolite 13X is the only one that has been deployed industrially, and its purchase cost was estimated to 1500 € per tonne [51]. However, UTSA-16 and IISERP MOF2, and more generally MOFs, are still in early development stages with no information on large-scale production and thus with no well-established cost. While the cost of synthesizing MOFs is currently very high, as these are mainly grams-level quantities synthesized at the lab scale. The potential for scale-up through an application like CCS would be expected to significantly reduce the production cost for MOFs reaching the commercial stage [51]. Under such circumstances, the cost of raw materials could be expected to repre-

sent a similar level of the MOF cost to the synthesis cost. Therefore, in this chapter, the purchase cost of MOFs was assumed to be twice the cost of metals used to synthesize them as the metals of these MOFs can be expected to be the main material cost as they typically are orders of magnitude more expensive than the organic components. For both UTSA-16 and IISERP MOF2, the costs of their underlying metals, cobalt and nickel, respectively, were determined based on bulk prices per tonne from the United States Geological Survey website [111]. Based on the assumptions mentioned above, the potential purchase costs at a larger production scale were estimated in terms of relative metal content and calculated to be 16640 and 4440 € per tonne for UTSA-16 and IISERP MOF2, respectively. Finally, in addition to adsorbent purchase costs, transport and installation costs associated with adsorbents were set to 1500 € per tonne for all adsorbents to reach the adsorbent direct cost, irrespective of the adsorbent considered. For commercial adsorbents, transport and installation costs are usually in the same range as the adsorbent purchase cost. This was set as the cost of Zeolite 13X.

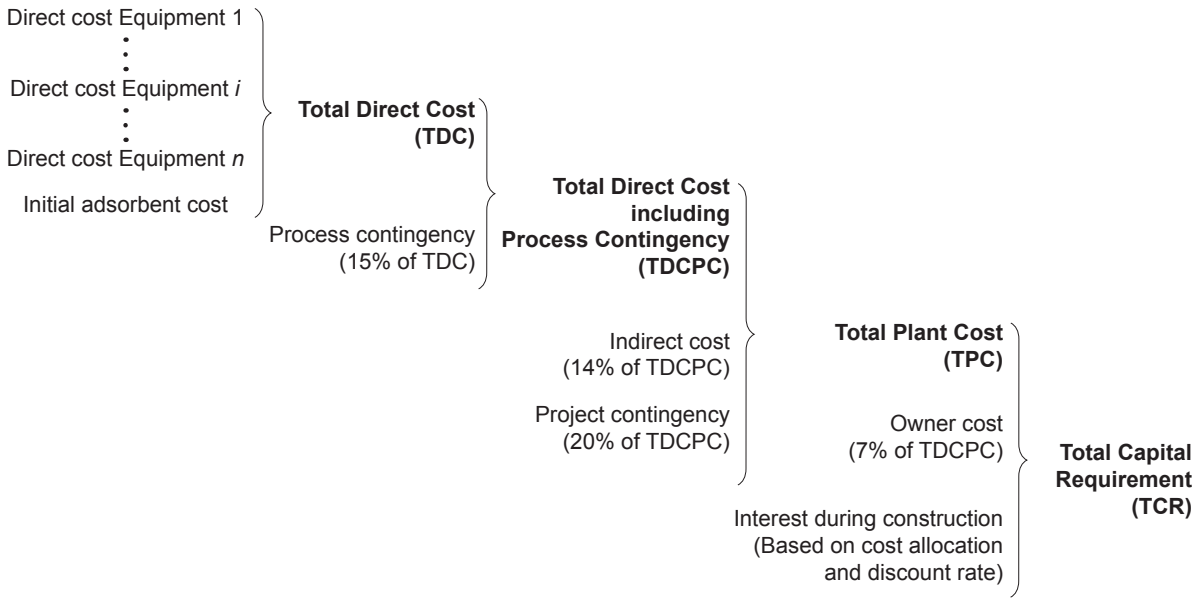

Figure 5.6: Illustration of the adopted bottom-up approach for calculating investment costs [108].

Operating costs

Operating costs consist of fixed and variable operating costs. The annual fixed operating costs include maintenance, labour, insurance and administrative costs. The annual maintenance cost was calculated as 2.5% of TPC, of which the maintenance labour cost accounts for 40%. The annual insurance and location taxes, including overhead and miscellaneous regulatory fees were set to 2% of TPC. The labour costs were calculated based on the assumption that the CO_2 capture unit requires five operators (5 shift patterns with one operator per shift as adsorption processes are highly automated) with an annual salary of 60000 € per person. Administrative costs were set to 30% of the operating and maintenance labour cost.

One important operating cost can be associated with adsorbent replacement over time due to thermal or mechanical degradation. While some commercial adsorbents can be operated for up to 20 years without replacement by careful design and proper control strategies [112], the lifetime of MOFs is still unknown. Hence, to be conservative, the replacement time for all adsorbents was set to 5 years [50, 51]. The adsorbent replacement costs, which include purchase, transport and installation costs, are incurred every five years after the start of the plant to replace the adsorbent.

Variable operating costs include utilities, electricity, cooling water, and adsorbent replacement. The annual cost for utilities was calculated based on estimated consumption from process simulations. The unit costs of utilities are provided in Table 5.2.

Table 5.2: Unit costs of utilities

Utility	**Price**
Electricity (€ $\cdot MW^{-1}h^{-1}$)	58.1 [113]
Specific direct emissions (kg CO_2 $\cdot MW^{-1}h^{-1}$)	38 [100]
Cooling water (€ $\cdot m^{-3}$)	0.039 [113]

5.3.4 Key performance indicators

Key technical performance indicators

The CO_2 purity, CO_2 recovery, overall power consumption, specific energy consumption and productivity were defined as follows:

$$\text{CO}_2 \text{ purity (\%)} = \frac{\text{total moles of CO}_2 \text{ in the product step}}{\text{total moles of gas in the product step}} \cdot 100 \tag{5.4a}$$

$$\text{CO}_2 \text{ recovery (\%)} = \frac{\text{total moles of CO}_2 \text{ in the product step}}{\text{total moles of CO}_2 \text{ in the feed step}} \cdot 100 \tag{5.4b}$$

Overall power consumption (P_{el}) was defined as the product of the power consumption in each unit train and the number of parallel trains (M) [21].

$$\text{Overall power consumption, } P_{\text{el}}\ (\text{MW}_\text{e}) = M \cdot \left(N_{\text{ADS}} \cdot \frac{E_{\text{ADS}}(\text{J}_\text{e})}{t_{\text{ADS}}(\text{s}) \cdot 10^6} + N_{\text{BLO}} \cdot \frac{E_{\text{BLO}}(\text{J}_\text{e})}{t_{\text{BLO}}(\text{s}) \cdot 10^6} + N_{\text{EVAC}} \cdot \frac{E_{\text{EVAC}}(\text{J}_\text{e})}{t_{\text{EVAC}}(\text{s}) \cdot 10^6} \right) \tag{5.4c}$$

The power consumption in the unit train was calculated by averaging the energy consumed in each step of the VSA cycle over the duration of each step. In other words, it represents the integral average of the power demand in each step of the VSA cycle. In Eq. 5.4c, N_{ADS}=1 in the adsorption step; N_{BLO} represents the number of dedicated vacuum pumps per unit train for the blowdown step and; N_{EVAC} represents the number of dedicated vacuum pumps per unit train for the evacuation step.

It is worth noting that the power demand calculated based on Eq. 5.4c assumes that all movers operate continuously throughout the cycle duration. This always holds true for the compressor in the adsorption step due to continuous feed consideration in the column scheduling. On the contrary, the number of blowdown and evacuation vacuum pumps that are active will be less than or equal to N_{BLO} and N_{EVAC}, respectively, at any given time of the cycle duration. To elaborate, consider, for instance, evacuation vacuum pumps. There would be a certain portion of the cycle schedule that operates with exactly N_{EVAC} vacuum pumps, yet, there also exists other portions of the cycle

schedule which would operate with fewer than N_{EVAC} vacuum pumps. Under such circumstances, the power demand from the evacuation step will be based on vacuum pumps, less than N_{EVAC}, operating actively to implement the cycle. Moreover, there will be no power consumption from the remaining evacuation vacuum pumps that are inactive. Accounting for such variations in the power consumption for blowdown and evacuation steps may provide a slightly lower estimate for the overall power consumption, albeit the assumption that all vacuum pumps operate continuously performing the same work throughout the cycle duration will conservatively estimate the overall power consumption and will also comply with the realistic operation. In addition to overall power consumption, specific energy consumption was also defined as follows:

$$\text{Specific energy consumption (kWh}_\text{e}\ \text{t}_{\text{CO}_2}{}^{-1}) = \frac{\text{Overall power consumption (kW}_\text{e}) \cdot \text{Operating hours (h year}^{-1})}{\text{CO}_2\ \text{captured (tonne year}^{-1})} \tag{5.4d}$$

Productivity was defined by considering the entire VSA capture unit as shown below:

$$\text{Productivity, } Pr\ (\text{mol m}^{-3}\ \text{s}^{-1}) = \frac{\text{CO}_2\ \text{capture rate for the plant (mol s}^{-1})}{\text{total adsorbent volume used in the plant (m}^3)} \tag{5.4e}$$

Note that CO_2 capture rate (mol s^{-1}) was defined as the product of CO_2 recovery (-) and CO_2 molar flow rate in the flue gas (mol s^{-1}).

Key economic performance indicators

The CO_2 avoided cost was considered as the key economic performance indicator to compare the cost performance of adsorption-based CO_2 capture technology with MEA-based CCS. It approximates the average discounted CO_2 tax or quota over the duration of the project that would be required as income to match the net present value of additional capital and operating costs due to CCS infrastructure [107]. Since the implementation of CCS does not impact the hydrogen production of the plant (key product), CO_2 avoided cost was calculated through a net present value approach [114]. The CO_2

avoided cost, in €/$t_{CO_2\ avoided}$ (where $t_{CO_2\ avoided}$ is metric tonnes of CO_2 avoided), is defined as shown below:

$$CO_2 \text{ avoided cost} = \frac{\text{Net present value of the CCS implementation cost}}{\text{Net present value of the } CO_2 \text{ avoided}} \tag{5.5}$$

Or more specifically,

$$CO_2 \text{ avoided cost} = \frac{\sum_i \frac{\text{TCR}_{\text{CCS implementation}}\ (i) + \text{Annual OPEX}_{\text{CCS implementation}}\ (i)}{(1+d)^i}}{\sum_i \frac{\text{Annual amount of } CO_2 \text{ emissions avoided by the CCS implementation } (i)}{(1+d)^i}} \tag{5.6}$$

where i is the year index (-).

The amount of CO_2 emissions avoided by CCS implementation was defined as the difference of the annual amount of CO_2 captured by CCS implementation and direct emissions due to heat and electricity associated with CCS implementation. Direct emissions due to electricity can be calculated using the following equation:

$$\text{Direct emissions} = e_{\text{el}} \cdot P_{\text{el}}\ (\text{MW}_\text{e}) \cdot \text{Operating hours (h year}^{-1}) \tag{5.7}$$

where e_{el} is the specific CO_2 emissions associated with each unit of electric power consumed (kg CO_2 MW_e^{-1} h^{-1}). By taking into account direct emissions, the equivalent CO_2 avoided indicates the true overall reduction in CO_2 emissions of the SMR plant when adsorption capture technology is implemented and allows for a fair comparison with different capture technologies [113]. The financial parameters used to calculated CO_2 avoided cost are listed in Table 5.3.

The CO_2 capture cost was also considered to optimize the VSA process and to compare the cost performances of different adsorbents. The CO_2 capture cost, in €/$t_{CO_2\ avoided}$ is defined as follows:

$$CO_2 \text{ capture cost} = \frac{\sum_i \frac{\text{TCR}_{\text{VSA capture plant}}\ (i) + \text{Annual OPEX}_{\text{VSA capture plant}}\ (i)}{(1+d)^i}}{\sum_i \frac{\text{Annual amount of } CO_2 \text{ emissions avoided by the VSA capture plant } (i)}{(1+d)^i}} \tag{5.8}$$

It is worth noting that the CO_2 capture cost corresponds to the CO_2 avoided cost in Eq. 5.6 without the cost of flue gas cooling and drying, CO_2 conditioning, CO_2 transport and storage, since these costs are expected to be identical for all adsorbents.

Table 5.3: Financial parameters used for calculating CO_2 avoided costs [100].

Parameter	**Value**
Economic lifetime (years)	25
Capacity factor (%)	91.3
CO_2 capture plant construction time (years)	3
Allocation of CO_2 capture construction costs by year (%)	40/30/30
Discount rate (%)	8

5.3.5 Techno-economic optimization model

The VSA process design was approached as an integrated techno-economic optimization framework by identifying optimal design and operating variables of the process, as illustrated in Fig. 5.2. The optimization methodology integrates process and material aspects with cost models in order to minimize CO_2 capture cost while ensuring a minimum of 90% CO_2 recovery and 95% CO_2 purity. The set of variables include adsorption step duration (t_{ADS}), blowdown step interstitial velocity (v_{B}), evacuation step interstitial velocity (v_{E}), intermediate vacuum (P_{I}), evacuation vacuum (P_{L}), interstitial feed velocity (v_0) and column length (L).

The choice of design and operating variables depends on the VSA cycle and the adsorbent used. For the four-step VSA cycle considered, t_{ADS} and v_0 can be tuned in the adsorption step to control the feed flow rate and also the CO_2 front propagation along the column. Since this step operates at atmospheric pressure, the feed pressure can be calculated based on Ergun's equation. For blowdown and evacuation steps, vacuum levels, P_{I} and P_{L}, respectively are variables. In addition, volumetric flow rates of blowdown (S_{B}) and evacuation vacuum pumps (S_{E}) can be also varied for respective steps. To this end, S_{B} and S_{E} were implicitly varied in terms of the interstitial velocities, v_{B} and v_{E}, respectively. This was done to provide an appropriate vacuum pump sizing range for the columns, and also, a limit of 20000 $m^3\ h^{-1}$ was implicitly enforced on the maximum vacuum pump size. It is worth mentioning that the durations of blowdown

and evacuation steps are calculated by the model based on S_{B} and S_{E}, respectively. Finally, the duration of light product pressurization depends on t_{ADS} and is not considered as the variable in the optimization. Owing to the scale-up design, the column length, L was considered as a variable. As both column length and column diameter can be varied simultaneously, the column length-to-diameter (L/D) ratio was kept constant in the optimizations. The lower and upper bounds defined for the variables are provided in Table 5.4.

Table 5.4: Decision variable bounds used in the optimization.

	t_{ADS} (s)	v_{B} (m s^{-1})	v_{E} (m s^{-1})	P_{I} (bar)	P_{L} (bar)	v_0 (m s^{-1})	L (m)
Lower bound	50	0.2	0.2	P_{L} + 0.01	0.01	0.1	3
Upper bound	400	3	3	0.9	0.05	1.2	9

The constrained optimization problem was transformed into an unconstrained problem by adding penalty terms to the objective function, which impose high costs when constraints are violated and was solved using a non-dominated sorting genetic algorithm II (NSGA-II), a global search method that converges towards an optimal solution(s) by mimicking the process of evolution. In other words, the algorithm initializes a unique set of decision variables chosen within the bounds using Latin hypercube sampling and evaluates for objective functional values based on the integrated VSA process and cost models. This set of decision variables represents a generation. NSGA-II improves the objective functional values by utilizing some additional operations such as mutation and crossover over multiple generations. Global optimization and parallelization toolboxes in MATLAB 2018b were employed to implement the optimization. The population size was set to 24 times the number of variables, and the stopping criterion for the optimization was 50 generations.

5.4 Results and discussion

5.4.1 Design and cost of the optimal adsorptive CO_2 capture

The VSA process for each adsorbent was optimized for the minimum CO_2 capture cost with requirements of 95% CO_2 purity and 90% CO_2 recovery. Table 5.5 shows the process variables optimized for the minimum capture cost together with technical performances and other design details of the VSA process. In these optimizations, for the base-case scenario, the length-to-diameter ratio of adsorption columns was fixed at 3. For the cycle considered, all three adsorbents met the purity-recovery requirements by demanding a deep vacuum, i.e. ≤ 0.036 bar, to evacuate the CO_2 product out of the column. It can be observed that the size requirement of the vacuum pump depends on the intermediate vacuum (P_{I}) and low vacuum (P_{L}) levels. Owing to the larger swing between P_{I}=0.31 bar and P_{L}=0.036 bar for IISERP MOF2 in the evacuation step, the optimizer chose very large evacuation vacuum pump (>16000 $m^3\ h^{-1}$) to avoid long durations of the evacuation step, thereby, limiting the number of columns and evacuation vacuum pumps needed for scheduling. For Zeolite 13X and UTSA-16, vacuum pumps of capacity $\approx$ 8500-13000 $m^3\ h^{-1}$ seemed to be sufficient to reduce the vacuum levels from P_{I} of 0.11 bar to P_{L} of 0.022 and 0.026 bar, respectively, in the evacuation steps. Although larger vacuum pumps might perhaps be used for these cases, it can be inferred that the optimizer found the trade-off between the size requirement and the vacuum pump power consumption as the optimal flow rates have not approached the limits of the specified ranges in the optimization. The non-linear nature of the CO_2 isotherms on Zeolite 13X and UTSA-16 compared to linear CO_2 isotherm on IISERP MOF2 could have also contributed to this choice. Similar observations can be made for optimizer's choice of blowdown vacuum pumps based on the intermediate vacuum (P_{I}). As can be seen from the table, longer columns (>5 m) are needed to reduce the total number of columns. Also, interstitial feed velocities for all cases are either close

to or at the upper bound to reduce the number of parallel trains. Due to long columns and high interstitial velocities, the flue gas is compressed (>1.5 bar) to overcome the pressure drops across the column. Though the upper limit for the column length was kept at 9 m, power losses due to large pressure drops and very long evacuation times might have discouraged the optimizer from choosing column lengths in close proximity to the upper limit.

Table 5.5: Process performances of the four-step VSA cycle for different materials that were optimized for the minimum capture cost.

	Base case		
Adsorbent	Zeolite 13X	UTSA-16	IISERP MOF2
Vacuum pump efficiency	Variable	Variable	Variable
Objective function	Min. cost	Min. cost	Min. cost
Operating conditions			
Adsorption time (s)	212	159	118
Blowdown pump flow rate ($m^3\ h^{-1}$)	7784	6086	5434
Evacuation pump flow rate ($m^3\ h^{-1}$)	12682	8631	16341
Maximum feed pressure (bar)	1.92	1.53	2.03
Intermediate pressure (bar)	0.11	0.11	0.31
Low pressure (bar)	0.022	0.026	0.036
Feed velocity ($m\ s^{-1}$)	1.14	1.20	1.20
Column length (m)	8.0	5.4	8.8
Length-to-diameter ratio (-)	3.0	3.0	3.0
Train configuration			
Number of columns per train (-)	7	4	4
Number of blowdown pumps per train (-)	1	1	1
Number of evacuation pumps per train(-)	5	3	3
Number of parallel trains (-)	42	97	29
Process performance			
Purity (%)	94.9	95.0	95.1
Recovery (%)	91.0	90.0	91.4
Productivity ($mol\ m^{-3}\ s^{-1}$)	1.89	4.45	3.61
Compressor power (MW_e)	12.00	7.91	14.10
Blowdown power (MW_e)	4.39	8.78	1.24
Evacuation power (MW_e)	41.77	39.22	22.45
Overall power consumption (MW_e)	58.15	55.90	37.79
Specific energy consumption (kWh_e/t_{CO_2})	307.86	299.53	199.33

The VSA cycle schedule is illustrated in Fig. D.3 in Appendix D based on the opti-

mized process variables. Idle times are included wherever deemed necessary. To treat the entire dry flue gas in a continuous manner, a total of 42 parallel trains with seven columns per train, 97 parallel trains with four columns per train and 29 parallel trains with four columns per train are necessary for Zeolite 13X, UTSA-16 and IISERP MOF2 cases, respectively. Clearly, the MOFs achieved higher productivities, i.e. less adsorbent volume as compared to Zeolite 13X. For this scale of capture unit, the total power consumption based on compressors, all blowdown and evacuation vacuum pumps pertaining to all parallel trains is shown in Table 5.5. As expected, the evacuation step consumes most of the total power. UTSA-16 and Zeolite 13X require high power consumption, while IISERP MOF2 has the lowest power consumption. This observation is consistent with previous studies that have shown that this can be explained by the low N_2 affinity of an adsorbent [91, 115].

The cost breakdowns for all adsorbents corresponding to the lowest capture cost are provided in Table 5.6. In addition, other costs pertaining to flue gas pre-treatment (i.e. cooling and drying), CO_2 conditioning, transport and storage costs are also reported for all adsorbents. It is worth noting that all cost breakdowns are reported in $€/t_{CO2,\,avoided}$. Since the overall framework remains the same for all adsorbents, capture costs are compared to assess the performance of each of the adsorbents. As can be seen from the table, IISERP MOF2 is the best performing adsorbent for the VSA process. For IISERP MOF2, the capital costs constitute about 36%, where the contributions from columns (≈6%), compressors (≈5%) and vacuum pumps (≈6%) have similar magnitudes. On the other hand, the operating costs for IISERP MOF2 sum up to 64%, including both fixed and variable operating costs. As expected, the major contribution arises from power consumption (≈38% of the capture cost). It is worth noting that the fixed operating costs are dependent on the total capital requirement. UTSA-16 has the highest capture cost as compared to the other two adsorbents. This is primarily due to exorbitant adsorbent costs. Adsorbent costs constitute 20% of the

total capture costs. This is strikingly high compared to IISERP MOF2 (≈13%) and Zeolite 13X (9%) due to the presence of expensive metal source cobalt. The high adsorbent costs prohibited the optimizer from increasing the column volume, thereby increasing the number of parallel trains. This observation was corroborated by a case study in a later section where the influence of MOF prices on the capture cost was considered. In addition, high power consumption also remains a significant contributor. Zeolite 13X requires more number of columns per unit train as compared to MOFs because of the non-linear nature of the CO_2 isotherm. For this reason, huge capital is needed while relatively higher N_2 affinity increased the electricity costs.

5.4.2 Importance of process design objectives

The most common choice of process design objectives while designing or comparing optimal VSA processes for post-combustion CO_2 capture has been either energy consumption linked to the VSA or productivity or both [19, 24, 97, 102]. Besides, few studies also considered lowering total costs in their process designs [21, 48–50]. Generally, the rationale behind the choice of design objectives is that the energy consumption approximates the operating costs, and productivity gives a rough estimation of capital costs as well as operating costs related to the adsorbent. Although this might hold true when the adsorbents under consideration have similar costs and designing a single unit VSA train. The CO_2 capture problem, on the other hand, requires several VSA trains in order to treat the entire flue gas. Thus, choosing an appropriate design objective remains critical, especially when optimizing or comparing VSA with different CO_2 capture technologies. To this end, different process design objectives were examined through an optimization study to comprehend the influence of each design objective towards achieving lower cost of CO_2 capture. Three optimization problems that are commonly used in the literature were considered in addition to the minimization of CO_2 capture cost and are described below.

Table 5.6: CO_2 avoided costs breakdown of the four-step VSA cycle for different materials that were optimized for the minimum capture cost. A value of 0.0 indicates that the contribution was less than 0.1 €/$t_{CO_2,\ avoided}$.

		Base case	
Adsorbent	Zeolite 13X	UTSA-16	IISERP MOF2
Vacuum pump efficiency	Variable	Variable	Variable
Objective function	Min. cost	Min. cost	Min. cost
	€/$t_{CO_2,\ avoided}$	€/$t_{CO_2,\ avoided}$	€/$t_{CO_2,\ avoided}$
Cooling & drying	**2.8**	**2.8**	**2.8**
CAPEX cooling & drying	2.2	2.2	2.2
Fixed OPEX cooling & drying	0.3	0.3	0.3
Variable OPEX cooling & drying	0.3	0.3	0.3
VSA capture	**48.6**	**62.1**	**30.8**
CAPEX	18.6	25.1	11.1
Total direct cost	11.5	15.5	6.9
Column cost	3.8	3.6	1.7
Compressor cost	1.5	1.5	1.5
Vacuum pump cost	3.8	4.8	1.9
Heat exchanger cost	0.0	0.0	0.0
Valves cost	0.4	0.5	0.1
Initial adsorbent cost	1.9	5.1	1.6
Process contingency	1.7	2.3	1.0
Indirect cost	1.9	2.5	1.1
Project contingency	2.6	3.6	1.6
Owner cost	0.9	1.2	0.5
OPEX	30.0	37.0	19.7
Fixed OPEX	9.0	12.1	5.5
Electricity cost	18.1	17.6	11.7
Adsorbent cost	2.7	7.2	2.3
Cooling water cost	0.2	0.1	0.2
CO_2 conditioning	**8.7**	**8.8**	**8.7**
CAPEX conditioning	2.4	2.4	2.4
Fixed OPEX conditioning	0.4	0.4	0.4
Electricity cost conditioning	5.9	6.0	5.9
CO_2 pipeline	**12.2**	**12.4**	**12.2**
CAPEX pipeline	10.9	11.0	10.8
Fixed OPEX pipeline	1.3	1.4	1.4
CO_2 storage	**18.6**	**18.8**	**18.5**
CAPEX storage	15.2	15.3	15.1
Fixed OPEX storage	2.5	2.5	2.5
Variable OPEX storage	0.9	0.9	0.9
CO_2 avoided cost	**90.9**	**104.9**	**73.0**

- Problem 1: Minimization of overall power consumption
- Problem 2: Maximization of productivity
- Problem 3: Minimization of overall power consumption and maximization of productivity

Optimization runs were performed for each of these cases based on both IISERP MOF2 and Zeolite 13X as adsorbents. The reason for choosing IISERP MOF2 and Zeolite 13X for the case study is that the IISERP MOF2 provides a representative case for VSA because of its superior performance as compared to other adsorbents, and Zeolite 13X represents the case for commercial adsorbents. The base results pertaining to the minimization of the capture cost are shown in Table 5.6. Note that the optimal techno-economic performance obtained from the minimization of capture cost is referred to herein as the minimum capture cost case unless otherwise stated. After unique optimization runs, the techno-economic performances corresponding to the minimum overall power consumption and maximum productivity were evaluated and reported in Table 5.7 as Case I and Case II, respectively. Consider, for instance, the minimization of overall power consumption. For IISERP MOF2, the lowest power consumption obtained was 25.56 MW_e, notably, a 34% difference when compared to the power consumption linked to the minimum capture cost case. The optimizer selected smaller columns and small-sized vacuum pumps in order to minimize the pressure drop losses and power consumption associated with the vacuum pumps. However, the capture cost of the four-step adsorption cycle optimized based on the minimum overall power consumption was almost 184% higher than that of the reference minimum capture cost. This strikingly high capture cost comes from the enormous capital expenditure and related footprint required to treat the entire flue gas based on smaller columns. The total number of columns required was 1593, owing to which the column cost increased by $\approx$760% compared to the minimum capture cost case. Considering the scheduling, the

total number of vacuum pumps needed has also increased from 116 to 1416. While the total power consumed by all of these vacuum pumps is minimal, the capital expenditure related to these vacuum pumps has increased by ≈3.5× that of the minimum capture cost case. In addition, adsorbent, valves and fixed operating costs associated with the capital expenditure have also increased. On the other hand, the electricity costs are almost 32% lower than the minimum capture cost case. Similar observations can be made for Zeolite 13X. The capture cost related to the minimum overall power consumption is 244% more than the minimum capture cost. The power consumption lowered to ≈35 MW_e, i.e. a difference of ≈23 MW_e, at the expense of 432% more capital expenditure compared to the minimum capture cost case. Owing to the process behaviour of achieving lower overall power consumption at lower productivity, the productivity obtained in these cases will be lower than the minimum capture cost scenario. This clearly explains that the process design must not solely focus on minimization of overall power consumption but must also take into account the associated capital and operating costs.

Case II in Table 5.7 shows techno-economic performances corresponding to the maximum productivity. Again, the capture cost related to the maximum productivity remains 124% higher than the minimum capture cost for IISERP MOF2. Interestingly, the optimized column length has reached the lower bound in the optimization. This is because the optimizer selected the lowest possible adsorbent volume to increase the productivity of the process. Further, the cycle duration has also shortened, thereby facilitating the increase in productivity by reducing the number of columns per train. The overall power consumption rose to ≈53 MW_e compared to ≈38 MW_e in the minimum capture cost case, resulting in ≈44% more electricity costs. For Zeolite 13X, the capture cost corresponding to the maximum productivity was ≈124% higher than the minimum capture cost.

Figure 5.7(a) shows the Pareto solutions obtained from the multi-objective optimiza-

tion where overall power consumption was minimized simultaneously by maximizing productivity. For comparison, results obtained from minimization of CO_2 capture cost, minimization of overall power consumption, i.e. Case I, and maximization of productivity (Case II) are also shown. Generally, the Pareto solutions represent the best trade-off between the overall power consumption and productivity and provide approximations for the best cost performances. Any point below the Pareto curve remains infeasible, while any point that lies above the curve corresponds to a suboptimal point. As can be observed from the figure, the minimum capture cost lies in the suboptimal region of the Pareto plot, indicating that the multi-objective optimization formulations involving productivity and energy consumption do not provide complete information about costs. This can be clearly seen in Fig. 5.7(b). It is, therefore, clear that the best objective for optimizing VSA processes related to CO_2 capture problem is the capture cost [49].

5.4.3 Effect of overestimating the vacuum pump efficiency

Clearly, the costs linked to the electricity consumption influence the minimum overall capture cost. As the vacuum pump is a major power consumer, quantifying the realistic vacuum pump performance in terms of efficiency (η_V) is crucial. Most literature studies assume a constant theoretical $\eta_V \approx 70 - 80\%$ for VSA energy calculations, which, in practice, holds true for low to moderate vacuum levels ($\geq$0.1 bar). However, the production of high purity CO_2, at high recovery, based on VSA processes, requires deep vacuum pressures. To achieve deep vacuum ($<$0.1 bar), it was found in an earlier study that the vacuum pump performance significantly drops to a lower value [97]. This is also consistent with observations from pilot plant experiments [35]. The dependence of η_V on vacuum was regressed to formulate an efficiency function [97]. The same efficiency function was used in the present chapter, although not rigorous, captures the essential features of most of the vacuum pumps at deep vacuum.

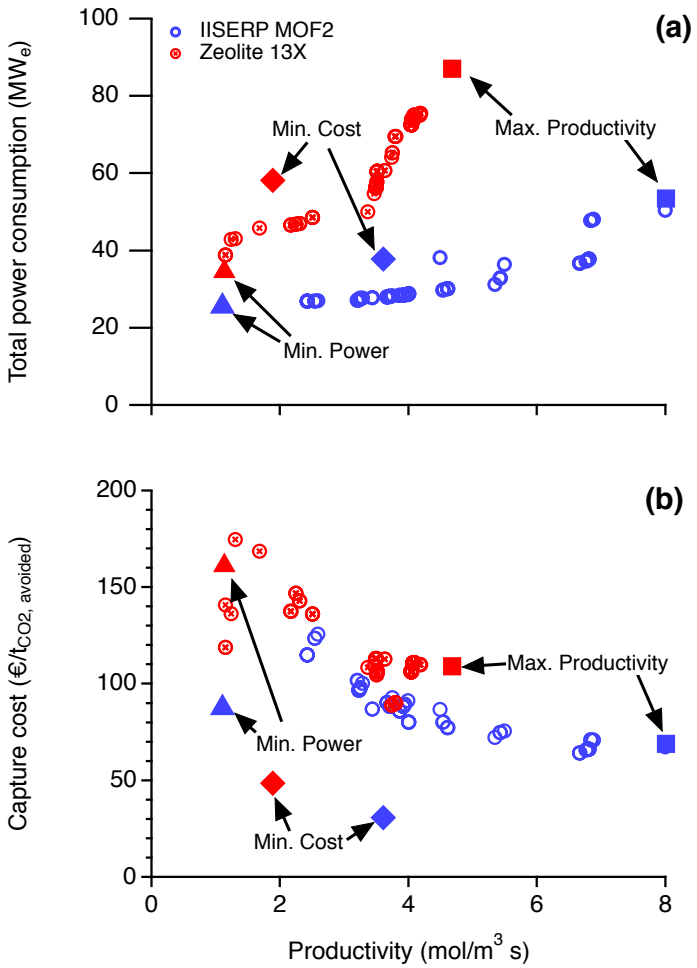

Figure 5.7: (a) Pareto solutions obtained from the multi-objective optimization and (b) the corresponding capture costs for IISERP MOF2 (blue circles) and Zeolite 13X (red circles). For comparison, optimization results pertaining to minimum capture cost (diamonds), minimum overall power consumption (triangles), maximum productivity (squares) are also illustrated.

To understand the impact of η_V on the VSA process design and minimum capture cost, two optimization cases are compared. The two cases considered are a fixed efficiency case where η_V=72% and a variable efficiency case η_V is a function of the pressure. The reference cases reported in Table 5.6 for IISERP MOF2 and Zeolite 13X are representative of variable η_V case. Independent optimization runs were performed for both IISERP MOF2 and Zeolite 13X with η_V=72%.

The minimum capture cost results pertaining to constant η_V=72% case for both IISERP MOF2 and Zeolite 13X are presented as Case III in Table 5.8. For IISERP MOF2, the

overall power consumption was estimated as 29.02 MW_e compared to 37.79 MW_e for the reference variable efficiency case. As expected, this difference primarily stems from the evacuation step and translates to roughly 24% lower electricity costs. On the other hand, the overall power consumption for Zeolite 13X in the case of η_V=72% was underestimated by ≈20 MW_e (≈35%) compared to that of the variable efficiency case. The productivity remained fairly constant as compared to reference cases for both materials. When the variable efficiency is considered for the vacuum pumps, the electricity consumption for IISERP MOF2 remained almost the same as that of the MEA-based capture case (see Table D.1 in Appendix D) while Zeolite 13X demanded almost 1.5× the electricity needed for the MEA case. On the contrary, the electricity consumption based on constant η_V=72% for IISERP MOF2 and Zeolite 13X remains ≈25% and ≈3%, respectively, lower than that of the MEA-based capture. This result corroborates the fact that the energy calculations based on theoretical vacuum pump efficiencies can optimistically lead to lower energy demands than that of MEA-based capture and, moreover, can underestimate the realistic energy consumption [10].

As can be seen from Table 5.8, the vacuum pump efficiency directly influences the minimum capture cost. Using η_V=72% reduced the overall minimum capture cost by almost 8% and 17% for IISERP MOF2 and Zeolite 13X, respectively. As expected, these savings come mainly from the reduction in OPEX related to electricity cost. While most other costs remained the same for IISERP MOF2, for Zeolite 13X, improved efficiency leads to a change in the VSA process design. It is interesting to notice that in the case of Zeolite 13X, some of the energy savings with η_V=72% goes towards increasing the column length leading to an increase in pressure drop. This leads to the reduction in the number of parallel trains and the overall capital cost. Therefore, this study highlights the fact that an appropriate quantification of vacuum pump performance is important for calculating the realistic power consumption, and thereby, costs of VSA processes.

Table 5.7: Techno-economic performances for case studies relating to the choice of objective function, i.e., overall power consumption (P_{el}) and productivity (Pr). Note that * indicates the change made with respect to reference cases in Tables 5.5 and 5.6.

	Case I	**Case I**	**Case II**	**Case II**
Adsorbent	Zeolite 13X	IISERP MOF2	Zeolite 13X	IISERP MOF2
Vacuum pump efficiency	Variable	Variable	Variable	Variable
Objective function	Min. P_{el}*	Min. P_{el}*	Max. Pr*	Max. Pr*
Operating conditions				
Adsorption time (s)	265	188	213	107
Blowdown pump flow rate ($m^3\ h^{-1}$)	355	707	3195	3040
Evacuation pump flow rate ($m^3\ h^{-1}$)	439	1045	2241	2584
Maximum feed pressure (bar)	1.30	1.24	1.17	1.22
Intermediate pressure (bar)	0.22	0.35	0.10	0.35
Low pressure (bar)	0.023	0.032	0.014	0.018
Feed velocity ($m\ s^{-1}$)	1.08	0.79	0.88	1.10
Column length (m)	3.7	5.4	3.0	3.0
Length-to-diameter ratio (-)	3.0	3.0	3.0	3.0
Train configuration				
Number of columns per train (-)	18	9	4	3
Blowdown pumps per train (-)	1	1	1	1
Evacuation pumps per train (-)	16	7	3	2
Number of parallel trains (-)	263	177	533	420
Process performance				
Purity (%)	95.0	94.9	95.0	95.0
Recovery (%)	90.2	90.0	90.8	89.9
Productivity ($mol\ m^{-3}\ s^{-1}$)	1.13	1.10	4.68	8.01
Compressor power (MW_e)	4.63	3.86	2.63	3.39
Blowdown power (MW_e)	1.19	1.33	27.12	15.85
Evacuation power (MW_e)	28.77	20.37	57.29	34.20
Overall power consumption (MW_e)	34.59	25.56	87.04	53.44
Specific energy consumption (kWh_e/t_{CO_2})	184.93	136.98	461.98	286.52
Cost performance				
CAPEX (€/$t_{CO_2,\ avoided}$)	99.0	48.7	54.7	34.5
Total direct cost (€/$t_{CO_2,\ avoided}$)	61.0	30.1	33.7	21.3
Column cost (€/$t_{CO_2,\ avoided}$)	34.4	14.6	14.1	8.4
Compressor cost (€/$t_{CO_2,\ avoided}$)	1.5	1.5	1.5	1.5
Vacuum pump cost (€/$t_{CO_2,\ avoided}$)	16.1	6.7	14.6	9.1
Heat exchanger cost (€/$t_{CO_2,\ avoided}$)	0.0	0.0	0.0	0.0
Valves cost (€/$t_{CO_2,\ avoided}$)	5.8	2.0	2.6	1.6
Initial adsorbent cost (€/$t_{CO_2,\ avoided}$)	3.2	5.3	0.8	0.7
Process contingency (€/$t_{CO_2,\ avoided}$)	9.2	4.5	5.1	3.2
Indirect cost (€/$t_{CO_2,\ avoided}$)	9.8	4.8	5.4	3.4
Project contingency (€/$t_{CO_2,\ avoided}$)	14.0	6.9	7.8	4.9
Owner cost (€/$t_{CO_2,\ avoided}$)	4.9	2.4	2.7	1.7
OPEX (€/$t_{CO_2,\ avoided}$)	62.2	38.8	54.4	34.4
Fixed OPEX (€/$t_{CO_2,\ avoided}$)	46.8	23.2	25.9	16.5
Electricity cost (€/$t_{CO_2,\ avoided}$)	10.8	8.0	27.3	16.8
Adsorbent cost (€/$t_{CO_2,\ avoided}$)	4.5	7.5	1.1	1.0
Cooling water cost (€/$t_{CO_2,\ avoided}$)	0.1	0.1	0.1	0.1
VSA capture cost (€/$t_{CO_2,\ avoided}$)	**161.2**	**87.5**	**109.1**	**68.9**

Table 5.8: Techno-economic performances for case studies relating to the impact of the vacuum pump efficiency (Case III) and the length-to-diameter ratio (Case IV). Note that * indicates the change made with respect to reference cases in Tables 5.5 and 5.6.

	Case III	**Case III**	**Case IV**	**Case IV**
Adsorbent	Zeolite 13X	IISERP MOF2	Zeolite 13X	IISERP MOF2
Vacuum pump efficiency	72%*	72%*	Variable	Variable
Objective function	Min. cost	Min. cost	Min. cost	Min. cost
Operating conditions				
Adsorption time (s)	235	117	189	119
Blowdown pump flow rate ($m^3\ h^{-1}$)	11922	4797	13549	17748
Evacuation pump flow rate ($m^3\ h^{-1}$)	19291	16638	14641	18482
Maximum feed pressure (bar)	2.14	2.00	1.69	1.97
Intermediate pressure (bar)	0.10	0.30	0.10	0.28
Low pressure (bar)	0.023	0.034	0.026	0.045
Feed velocity ($m\ s^{-1}$)	1.15	1.19	1.13	1.19
Column length (m)	8.9	8.7	6.8	8.5
Length-to-diameter ratio (-)	3.0	3.0	2.0*	2.0*
Train configuration				
Number of columns per train (-)	7	4	7	5
Blowdown pumps per train (-)	1	1	1	1
Evacuation pumps per train (-)	5	3	5	4
Number of parallel trains (-)	31	30	28	14
Process performance				
Purity (%)	94.9	95.1	95.0	95.2
Recovery (%)	90.5	91.6	89.9	90.2
Productivity ($mol\ m^{-3}\ s^{-1}$)	1.82	3.58	2.03	2.87
Compressor power (MW_e)	13.90	13.53	9.69	13.37
Blowdown power (MW_e)	4.47	1.13	5.36	2.35
Evacuation power (MW_e)	19.29	14.36	31.86	16.57
Overall power consumption (MW_e)	37.66	29.02	46.91	32.29
Specific energy consumption (kWh_e/t_{CO_2})	200.67	152.75	251.55	172.51
Cost performance				
CAPEX (€/$t_{CO_2,\ avoided}$)	17.3	11.3	15.8	10.9
Total direct cost (€/$t_{CO_2,\ avoided}$)	10.6	7.0	9.7	6.7
Column cost (€/$t_{CO_2,\ avoided}$)	3.2	1.7	3.2	1.6
Compressor cost (€/$t_{CO_2,\ avoided}$)	1.5	1.5	1.5	1.5
Vacuum pump cost (€/$t_{CO_2,\ avoided}$)	3.6	2.0	2.9	1.4
Heat exchanger cost (€/$t_{CO_2,\ avoided}$)	0.0	0.0	0.0	0.0
Valves cost (€/$t_{CO_2,\ avoided}$)	0.3	0.1	0.3	0.1
Initial adsorbent cost (€/$t_{CO_2,\ avoided}$)	2.0	1.7	1.8	2.1
Process contingency (€/$t_{CO_2,\ avoided}$)	1.6	1.0	1.5	1.0
Indirect cost (€/$t_{CO_2,\ avoided}$)	1.7	1.1	1.6	1.1
Project contingency (€/$t_{CO_2,\ avoided}$)	2.4	1.6	2.2	1.6
Owner cost (€/$t_{CO_2,\ avoided}$)	0.9	0.6	0.8	0.5
OPEX (€/$t_{CO_2,\ avoided}$)	23.1	17.0	25.0	18.6
Fixed OPEX (€/$t_{CO_2,\ avoided}$)	8.4	5.6	7.7	5.4
Electricity cost (€/$t_{CO_2,\ avoided}$)	11.7	8.9	14.7	10.1
Adsorbent cost (€/$t_{CO_2,\ avoided}$)	2.8	2.3	2.5	2.9
Cooling water cost (€/$t_{CO_2,\ avoided}$)	0.2	0.2	0.1	0.2
VSA capture cost (€/$t_{CO_2,\ avoided}$)	**40.4**	**28.3**	**40.8**	**29.5**

5.4.4 Impact of length-to-diameter ratio

In this section, the effect of the L/D ratio of adsorption columns on minimum capture cost was investigated by considering IISERP MOF2 and Zeolite 13X as case studies. While higher L/D ($\in \{4, 5\}$) could be considered for the analysis, previous simulations from the literature revealed that the high L/D might not favour the overall cost reduction [49]. Given the goal to reduce the overall CAPEX, lower L/D $\in \{2, 3\}$ were examined based on rigorous optimizations. The results shown in Table 5.6 for IISERP MOF2 and Zeolite 13X were considered as the reference for L/D=3. The minimum capture costs corresponding to L/D=2, obtained after unique optimization runs, are reported as Case IV in Table 5.8. As can be seen from the table, the size requirements of vacuum pumps have increased due to large diameters. Reducing the L/D ratio has been demonstrated to have a limited effect on the minimum capture cost when using IISERP MOF2. The total number of columns reduced from 116 to 70 while the column costs remained constant. It is interesting to notice that the vacuum pump costs have been reduced by ≈26% owing to fewer vacuum pumps. Contrarily, an increase in adsorbent volume has resulted in increase in adsorbent costs by 28%. Therefore, the CAPEX remained nearly constant. Note that the electricity costs decreased by 14% because of the reduction in the power consumption mainly from the evacuation step (since P_{L} increased to 0.045 bar from 0.034 bar in the reference L/D=3 case). Overall, changing L/D from 3 to 2 has reduced the minimum capture cost from 30.8 to 29.5 € per tonne of CO_2 avoided.

The minimum capture cost was reduced to 40.8 € per tonne (lowered by ≈16%) for Zeolite 13X when the L/D was modified from 3 to 2. Clearly, there are a number of factors contributing to the decrease in minimum capture cost. By using wider columns, the number of parallel trains reduced from 42 to 28, which also reduced the total number of columns from 294 to 196. This resulted in ≈16% reduction in column costs. Consequently, the adsorbent and valves costs have also decreased. Another

contribution comes from a fewer vacuum pumps. The vacuum pump costs have been lowered by ≈1.3× owing to 33% reduction in the total number of vacuum pumps. As a result, the CAPEX requirements were lowered by ≈15%. It is interesting to note that the overall power consumption reduced by ≈19% and also a 17% reduction in OPEX. Most industrial VSA columns in operation have reasonably large diameters indicating that wider columns can indeed be used to reduce the number of parallel trains and thereby cost of capture. Naturally, there should be caution in terms of challenges related to implementation when designing wider columns such as those pertaining to flow distribution.

5.4.5 Comparative analysis with MEA-capture

Although MEA- and adsorption-based CO_2 capture technologies are on different levels of technological readiness levels, the key economic performance indicators were determined for both based on the assumption that the technologies are mature and ready for large-scale deployment. The cost performances of both technologies for post-combustion CCS implementation in SMR plants are illustrated in Fig. 5.8. The IISERP MOF2 cost performance reported in Table 5.6 was used as a representative case for the VSA system in order to compare with the reference MEA case. In addition, Zeolite 13X was also considered for the discussion as it represents the case for commercial adsorbents. Figure 5.8 shows the breakdown of CO_2 avoided costs (€/$t_{CO2,\ avoided}$) for CCS implementation of both technologies. As can be seen from the figure, CO_2 avoided cost for VSA based on IISERP MOF2 is almost 10% higher than that of the MEA case. The VSA performance with Zeolite 13X deteriorates further with a CO_2 avoided cost of 90.9 € per tonne of CO_2 avoided. It is worth noting that the CO_2 capture remains the major contributor to CCS implementation in both technologies. For MEA-based absorption, the CO_2 capture costs were determined to be 30.1 € per tonne of CO_2 avoided [100]. The capture costs for the VSA system based on IISERP MOF2 are 12% higher than that

of MEA-based capture, whereas 71% higher when Zeolite 13X is used. Note that the capture costs for VSA also include flue gas cooling and drying costs. The CO_2 conditioning, transport and storage costs are marginally higher (i.e. <10%) for VSA because of slightly higher flow rates as compared to that of the MEA case. Upon close examination of capture costs, the components responsible for higher capture costs for the VSA system include CAPEX, fixed OPEX and costs linked to energy consumption, as illustrated in Fig. 5.8. The VSA-based capture based on IISERP MOF2 and Zeolite 13X results in 7% and 68% higher CAPEX, respectively, as compared to the MEA case, due to a large number of parallel trains and associated footprint together with flue gas pre-treatment. This shows that MOFs have ability to reduce huge capital costs significantly. The fixed operating costs, which depend on the total capital requirement, are 21% higher in the VSA system based on IISERP MOF2 compared to the reference MEA case. Finally, the costs linked to electricity consumption for capture are again 15% and 77% higher in the VSA cases for IISERP MOF2 and Zeolite 13X, respectively, which comes from the power consumption due to the requirement of low vacuum levels and a large number of vacuum pumps. This is an interesting result because VSA-based processes are often reported as low energy-intensive processes for capture. While most of the studies assume high vacuum pump efficiencies at deep vacuum, the practical limitations of vacuum pumps at deep vacuum are often overlooked. The analysis related to fixing the vacuum pump efficiency in the earlier section showed that the energy numbers for the VSA process are indeed lower than that of the MEA-based capture. Altogether, the MEA-based capture outperforms the four-step VSA process based on the adsorbents considered in terms of the CO_2 avoided cost for post-combustion CO_2 capture in SMR plants.

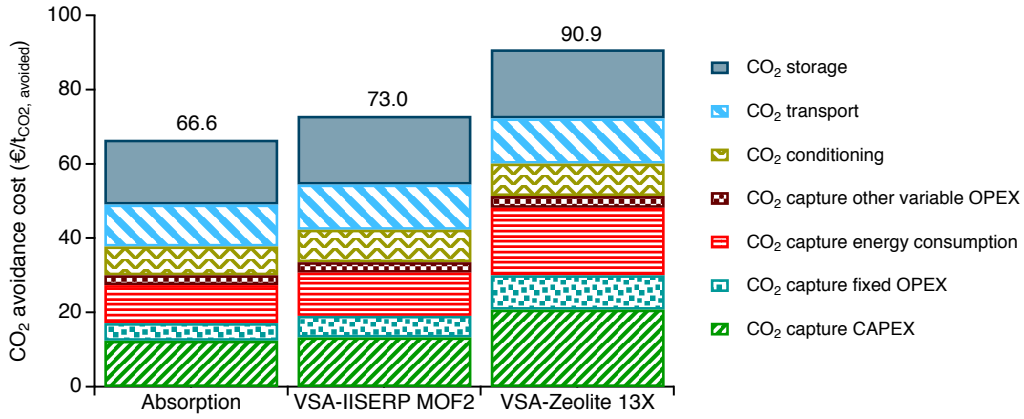

Figure 5.8: Cost performance of the VSA technology as compared to MEA solvent for CCS implementation. Note that VSA-based CO_2 capture also includes cooling and drying costs.

5.4.6 Cost of metal-organic frameworks

As mentioned earlier, given the wide uncertainties involved in the large-scale production of metal-organic frameworks, estimating an actual price remains a critical challenge while evaluating the techno-economic feasibility of MOFs for CO_2 capture. Although cost estimations based on the raw materials provide a reasonable approximation for purchase costs, the scale-up for CCS application is expected to reduce the production costs for MOFs. Given such variability of MOF prices, it is important to understand the MOF price for which adsorption processes are attractive. To this end, the influence of MOF price on the CO_2 capture cost was examined through an optimization study where the VSA process was optimized for the minimum capture cost for different MOF prices. Both UTSA-16 and IISERP MOF2 were considered for the analysis as each MOF represents a unique scenario. The synthesis of UTSA-16 involves an expensive metal source, cobalt, as the raw material, while IISERP MOF2 composes of comparatively cheaper metal, nickel. The MOF price was varied over a broad range of 0 and 10 times the cost of relative metal content. In each case, unique optimization runs were performed for both IISERP MOF2 and UTSA-16, and minimum capture costs were determined. The minimum cost performances of UTSA-16 and IISERP

MOF2 presented in Table 5.6 represent a baseline case where the MOF price assumed was twice the cost of the relative metal content in the MOF structure.

Figure 5.9 shows the overall trend of MOF price on the minimum cost of capture. Every point on the figure represents a unique optimization run. Note that optimization runs corresponding to zero MOF price are shown at the left-most portion of the plot. A MOF price of zero indicates that the MOF is available for use at no cost. Although never encountered in practice, it provides the absolute lower bound for this case study. A factor of $1\times$ represents a case where the production cost equals the cost of bulk purchase of metals, and the cost of organic linkers, solvents, and other production costs are negligible subject to the economics of scale. In other words, $1\times$ is the lowest possible estimate that can be practically achieved when the MOF price is the same as the cost of the raw materials. On the other hand, a worst-case situation involves MOF price amounting to 10 times the metal purchase cost, which is a representative case of poor scale-up. For UTSA-16, the minimum capture cost increases as the MOF price increases. As can be seen from Fig. 5.9, the UTSA-16 prices vary between 0 € and 83200 € per tonne. Clearly, higher UTSA-16 costs discourage the practical implementation in a VSA process. Such exorbitant costs can be attributed to the presence of an expensive metal source, cobalt. The advantages UTSA-16 offers in terms of process performance are limited by its expected price. As can be seen from Fig. 5.9, a slight reduction in the MOF price leads to a significant decrease in the overall capture cost. It is worth noting that the UTSA-16 performs better than commercial adsorbent like Zeolite 13X when the production costs are as close as zero but still is expensive compared to MEA-capture. For this case of zero price, it is worth mentioning that both the column length and the interstitial feed velocity have approached the upper limit as the optimizer was seeking to reduce the number of parallel trains, which otherwise was impeded by exorbitant adsorbent costs. IISERP MOF2 prices, on the other hand, were varied between 0 € and 22200 € per tonne. As expected, higher IISERP MOF2 price resulted

in gradual increase in minimum capture cost. As can be seen from Fig. 5.9, IISERP MOF2 always outperforms Zeolite 13X over this broad range. It is also interesting to notice that the IISERP MOF2 outperforms the reference MEA-capture case when the price IISERP MOF2 price is less than 1×, i.e. less than the raw materials cost. However, caution should be used in this regard as the MEA is the baseline case, although other solvents can lead to lower capture costs. The overall trend suggests that the MOF's superior technical performance outperforms the cost characteristics when the metal sources are cheap and available in abundance. The deployment of MOFs, especially with expensive metals, seems to be prohibitive. It is therefore important to search for high-performance adsorbents that are cheaply available.

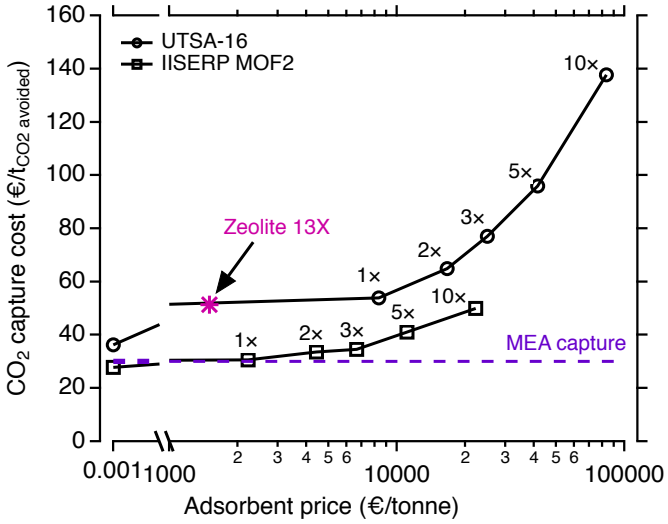

Figure 5.9: Influence of adsorbent prices on the minimum CO_2 capture cost (includes cooling and drying costs for VSA). Zeolite 13X and MEA-capture costs are shown for reference. The indicators, 1×, 2×, ..., 10×, refer to the multiplier applied to the cost of the metal in the metal-organic framework.

5.5 Conclusions

A systematic approach for the design and techno-economic assessment of vacuum swing adsorption (VSA) processes was developed. The methodology incorporates a detailed VSA process model, peripheral component models, vacuum pump per-

formance, scale-up, process scheduling and comprehensive costing model, including the cost of adsorbent. This methodology was applied to a case study on post-combustion CO_2 capture from a steam methane reformer (SMR). Here, the techno-economic methodology, consistent with best practices, combined with stochastic optimization, was used to calculate the minimum CO_2 capture cost and the corresponding process design and operating parameters. The key results of this chapter can be summarized as follows:

- Optimizing the VSA process for proxy objectives such as minimizing energy and maximizing productivity does not guarantee the minimum cost. The minimum cost configurations did not lie on the minimum-energy vs maximum-productivity Pareto curves. This arises because of the complexities that exist in the scale-up of VSA processes from single-column simulations, a technique commonly used in the literature.

- The study clearly shows that the realistic efficiencies for vacuum pumps, especially at low pressures, need to be accounted for in order to obtain better estimates of the capture cost. It was shown that efficiencies that are used in literature, typically $\approx 72\%$, can indeed underestimate the overall power consumption as much as 24- 35% resulting in 8 - 17% lower minimum capture cost for specific cases in this chapter.

- The choice of adsorbent and its cost has a major impact on the cost of CO_2 capture. Three different adsorbents that include Zeolite 13X and metal-organic frameworks, UTSA-16 and IISERP MOF2, were compared based on minimum CO_2 capture costs and benchmarked against state-of-the-art MEA-based absorption process. IISERP MOF2 was found out to be the best-performing adsorbent with a minimum CO_2 capture cost of 33.6 € per tonne of CO_2 avoided, inclusive of flue gas pre-treatment costs. The current benchmark adsorbent material, Zeolite

13X, ranked second with a minimum capture cost of 51.4 € per tonne of CO_2 avoided. Higher power consumption and lower productivity resulted in higher overall costs for Zeolite 13X. UTSA-16 remains performing poorly with a minimum capture cost 64.9 € per tonne of CO_2 avoided, primarily due to exorbitant adsorbent costs. The presence of an expensive metal source, cobalt, inhibited the superior technical performance of UTSA-16.

- Adsorbents that were found to be better candidates based on their superior energy/productivity performance did not necessarily result in lower costs. For instance, UTSA-16, which has consistently been touted as an excellent candidate for CO_2 capture compared to the benchmark material Zeolite 13X, did not provide better cost performance. This was clearly shown to be a direct result of exorbitant adsorbent cost.

- The baseline MEA outperforms the best-performing adsorbent IISERP MOF2 with 10% lower CO_2 avoided cost. The MOF prices were varied over a wide range, given the variability in MOF scale-up, to comprehend the potential production costs at which MOF gives an advantage over commercial adsorbents like Zeolite 13X and the baseline MEA process. It was shown that UTSA-16 outperforms Zeolite 13X only when its production costs are less than the costs of raw materials, a seemingly impossible proposition. On the other hand, capture costs for IISERP MOF2 are less than Zeolite 13X over the entire range considered and on par with reference MEA-capture when IISERP MOF2 prices are almost equal to the raw material costs.

Chapter 6

How much can novel solid sorbents reduce the cost of post-combustion CO_2 capture? A techno-economic investigation on the cost limits of pressure-vacuum swing adsorption

6.1 Introduction

Carbon dioxide capture and storage (CCS) from point sources are expected to play a key role in decarbonizing the global energy and industry sectors [27, 28]. The feasibility of implementing CCS may vary from one industry to the other since several factors such as CO_2 composition, pressure, the flow rate of the flue gas, system-level integration aspects etc. affect the attractiveness of CCS [29]. In the context of system-level integration, post-combustion CO_2 capture can be retrofitted into existing chemical/power plants in a rather straightforward manner without restructuring the plant layout and has been identified as one of the viable technologies in short- to medium-term [30]. While the majority of industrial sources emit CO_2-containing gases at atmospheric pressure, the variation in CO_2 composition is typically in the range of 3.5-30% across

The results presented in this chapter have been reported in: S.G. Subraveti, S. Roussanaly, R. Anantharaman, L. Riboldi, A. Rajendran. How much can novel solid sorbents reduce the cost of post-combustion CO_2 capture? A techno-economic investigation on the cost limits of pressure-vacuum swing adsorption. *Appl. Energy* **2021**, *Accepted*.

industries [116]. Although there are several CO_2 capture technologies considered for post-combustion CO_2 capture, the associated energy penalty and cost expenditure remains a barrier for the large-scale implementation [10]. Among all, solvent-based CO_2 capture is at the forefront owing to its technological maturity and commercial implementation. Adsorption-based processes are proposed as an alternative to the traditional solvents for their ability to lower the energy penalty and the costs related to the capture [10].

One of the main drivers determining the performance of adsorption processes is the choice of adsorbents. Recent developments in material science have facilitated material chemists to discover several new classes of adsorbents, such as metal-organic frameworks (MOFs), covalent-organic frameworks (COFs), etc., that can be highly tuned for CO_2 capture applications [30]. Since each class can typically consist of hundreds of thousands of materials, including both real and hypothetical structures, the selection of suitable adsorbents remains crucial for assessing the potential of adsorptive CO_2 capture. The quest for the best performing adsorbents has resulted in several *in-silico* material screening studies that use various performance metrics to rank materials [23, 45, 51, 102, 117–122]. While the initial focus primarily relied on simplified process metrics (derived under equilibrium conditions) as means to evaluate the performance of adsorbents in the real process, integration of dynamic process modelling and optimization into adsorbent screening was later identified as a reliable tool to evaluate the realistic performance of adsorbents [23, 45, 91, 101, 102, 120, 123]. As a result, studies focusing on the *multiscale screening* of known material databases have emerged wherein the adsorbent properties determined through molecular simulations are later incorporated into the process simulation and optimization routines to identify/rank top material performers based on key process-oriented metrics such as the CO_2 purity, CO_2 recovery, energy penalty, productivity or cost of the CO_2 capture [45, 91, 101, 102]. Alternatively, the problem of identifying the desirable adsorbent properties in

processes was also approached through *process inversion* [21, 24]. The *process inversion* approach focuses on determining the "ideal" adsorbent properties that result in the best process performance through an integrated adsorbent-process optimization. In other words, the adsorbent properties are simultaneously optimized along with the process variables in the optimization. This approach helps in identifying the best performance limits of adsorptive CO_2 capture [24]. Both simplified and detailed process models have been used in this approach. For instance, feature spaces of adsorbent properties such as CO_2 and N_2 adsorption isotherms, heat of adsorption, Henry's constant, etc., were probed using *process inversion* approach in order to determine the lowest energy penalty [24, 115, 124] and CO_2 capture costs [21, 51] for post-combustion adsorptive CO_2 capture. More recently, Pai *et al.* explored adsorbent properties such as CO_2 and N_2 adsorption equilibria that minimize the energy penalty and maximize the productivity for different flue gas compositions using a machine learning model [125].

In Chapter 5, it was demonstrated that the realistic performance of adsorbents should be assessed by incorporating a comprehensive techno-economic analysis framework with detailed process modelling and optimization. This is primarily because the cost assessment captures the inherent complexities associated with the scale-up of the processes for industrial applications, which otherwise are not quantified when using process performance metrics such as energy penalty or productivity.

While previous studies provide some insights into understanding the underlying relationships between the adsorbent properties and the process performance, in this chapter, the following key questions are posed:

1. If "ideal" adsorbent(s) were discovered, what are the cost limits of adsorptive post-combustion CO_2 capture from industrial flue gases?

2. How do the costs compare with the benchmark technology, i.e. absorption?

Addressing these questions is critical to understand the true potential of adsorption

processes and thus allow for advances in both material discovery and process design. This chapter aims to answer the questions mentioned above by employing a *process inversion* approach. The analysis is restricted to single-stage pressure-vacuum swing adsorption (PVSA) technology, a widely studied class of adsorption processes for CO_2 capture applications. In this chapter, the cost limits are defined as the lowest possible achievable costs for capturing CO_2 from post-combustion industrial flue gases using "ideally" desired adsorbent features in the PVSA process considered. The impact of parameters such as the vacuum level required in the process, pellet morphology and adsorbent costs on PVSA costs is also demonstrated through an optimization study. Further, a one-to-one comparison with benchmark monoethanolamine (MEA) solvent cases for various industrial applications. Finally, the cost performance of two "real" adsorbents are evaluated and compared with the limits to identify the potential for *"material innovation"*.

The present chapter is organized as follows: the next section summarises the different cases considered to encompass the wide range of industrial applications. In the computational details section, the *process inversion* approach through integrated techno-economic optimization framework is explained, and details of adsorbent properties, process model, scale-up and economic assessment are provided. The results and discussion section reports the findings obtained from optimizations and compares them with benchmark MEA-based CO_2 capture cases. The merits and demerits of PVSA for post-combustion CO_2 capture are discussed in the concluding remarks, along with some perspectives towards the advancement of adsorptive CO_2 capture.

6.2 Case study

For this study, a case matrix comprising a wide range of CO_2 compositions at different flue gas flow rates is considered to represent various industrial post-combustion flue gas sources adequately [116]. Under dry conditions, the flue gas consists of CO_2/N_2

binary mixture and the CO_2 molar compositions in the flue gas are varied between 3.5% and 30%. This range corresponds to flue gas sources from simple cycle gas turbine plants, natural gas combined cycle power plants, coal-fired power plants, cement and steel industries. Further, the analysis is extended to different flue gas flow rates ranging from 303 tonnes/h to 3696 tonnes/h to account for the effect of the scale of operation. Table 6.1 illustrates the case matrix used in this chapter. In all cases, the flue gas is available at 1 bar and 35 °C for post-combustion CO_2 capture.

The system under consideration includes CO_2 capture from dry flue gas. The following is excluded while estimating the costs: the process that emits CO_2 containing flue gas, CO_2 conditioning, CO_2 transport and CO_2 storage. The process layout of adsorptive CO_2 capture is provided in Fig. E.1 in Appendix E. The dry flue gas further undergoes compression followed by cooling to 25 °C. Multiple adsorption process trains with N columns each are employed to treat the dry flue gas. The CO_2 rich product and N_2 are collected separately using separate vacuum pumps.

Further, adsorptive CO_2 capture is benchmarked against the baseline monoethanolamine-based (MEA) technology to fully understand the potential of adsorption process technology for various industrial applications. To be consistent, the system boundaries for both PVSA- and MEA-based CO_2 capture were kept the same. The MEA-based CO_2 capture performances based on Fu et al [116] are summarized in Tables E.1 and E.2 in Appendix E.

6.3 Computational details

The cost limits of adsorptive CO_2/N_2 binary mixture separations are determined using a recently developed integrated techno-economic optimization model [88]. The computational framework integrates adsorbent, process and economic aspects to determine the cost-optimal performance of adsorptive post-combustion CO_2 capture on industrial scales, as shown in Fig. E.2 in Appendix E. Both adsorbent properties and

Table 6.1: Case matrix related to different CO_2 compositions and flue gas flow rates considered in this study. Industrial examples are also highlighted where vertical text was used to represent specific industrial cases that have similar flow rates as considered in this study, while the horizontal text was used to indicate industrial examples with similar CO_2 compositions.

CO_2 composition (%)	Flue gas flow rate (tonne h^{-1})				
	313	1159	2004	2850	3696
3.5	32 MW offshore gas turbine		Gas turbine		1000 MW coal power plant
7.5					
13			Coal-fired power plant		
20			Cement		
30			Steel		

process design parameters are simultaneously optimized herein to determine the lowest possible costs.

6.3.1 Adsorbent features

Adsorbent properties required for process modelling include CO_2 and N_2 adsorption isotherms, crystal density, isosteric heats of adsorption, pellet porosity, pellet diameter and specific heat capacity. Physicochemical properties such as CO_2 and N_2 adsorption isotherms, crystal density and isosteric heats of adsorption are inherent crystal properties, while pellet porosity, pellet diameter and specific heat capacity are properties of adsorbent within the adsorption column.

A practically deployable sorbent for CO_2 capture should have several critical features, e.g., low cost, scalability, stability, etc. However, the ability to separate CO_2 and N_2, i.e., the two key components of flue gas, is arguably the most important feature. Most practical adsorption-based CO_2 and N_2 separations exploit the differences in affinity between CO_2 and N_2 on a specific sorbent. The affinity is expressed in the form of an adsorption isotherm that relates the fluid and solid phase concentrations at equilibrium. The hypothetical CO_2 and N_2 adsorption isotherms were expressed in terms of the competitive dual-site Langmuir (DSL) isotherm model. The advan-

tages of using the competitive DSL isotherm model involve computational simplicity (because of the explicit formulation) and also the ability to adequately represent the mixture equilibrium predictions from single component parameters for many practical systems [120, 126]. The competitive DSL isotherm model (for component i) is given by,

$$q_i^* = \frac{q_{\mathrm{sb},i} b_i c_i}{1 + \sum_i b_i c_i} + \frac{q_{\mathrm{sd},i} d_i c_i}{1 + \sum_i d_i c_i} \quad i = \mathrm{CO_2}, \mathrm{N_2} \tag{6.1}$$

In Eq. 6.1, c_i is the fluid-phase concentration of the component i, q_i^* is the equilibrium solid-phase loading of the component i, $q_{\mathrm{sb},i}$ and $q_{\mathrm{sd},i}$ represent saturation capacities for the two sites and, b_i and d_i are the temperature dependent adsorption equilibrium constants defined as:

$$b_i = b_{0,i} e^{\left(-\frac{\Delta U_{\mathrm{b},i}}{RT}\right)} \tag{6.2a}$$

$$d_i = d_{0,i} e^{\left(-\frac{\Delta U_{\mathrm{d},i}}{RT}\right)} \tag{6.2b}$$

where $\Delta U_{\mathrm{b},i}$ and $\Delta U_{\mathrm{d},i}$ are the internal energies of the two sites. Different hypothetical CO_2 and N_2 adsorption isotherms can be generated by varying the parameters q_{sb}, q_{sd}, b_0, d_0, ΔU_{b} and ΔU_{d}. For many known adsorbents, CO_2 adsorption is heterogeneous and the DSL isotherm model can reasonably describe the equilibrium while N_2 adsorption is homogeneous [24]. Consequently, the DSL isotherm parameter variation was constrained such that both thermodynamic consistency and homogeneity of N_2 adsorption are maintained. This can be accomplished by describing the competition between CO_2 and N_2 between the two sites using equal energy site (EES) formulation [101]. Here, the saturation capacity of each site remains the same for both components, i.e., $q_{\mathrm{sb,CO_2}} = q_{\mathrm{sb,N_2}}$ and $q_{\mathrm{sd,CO_2}} = q_{\mathrm{sd,,N_2}}$. Also, the internal energy of adsorption and constants b_0 and d_0 for N_2 are kept identical between the two sites, i.e., $\Delta U_{\mathrm{b,N_2}} = \Delta U_{\mathrm{d,N_2}}$ and $b_{0,\mathrm{N_2}} = d_{0,\mathrm{N_2}}$. Experimental evidence also supported this type of formalism for Zeolite 13X [47]. The physicochemical properties for achieving lowest costs are examined by considering the following parameters $q_{\mathrm{sb,CO_2}}$, $q_{\mathrm{sd,CO_2}}$, $\Delta U_{\mathrm{b,CO_2}}$, $\Delta U_{\mathrm{d,CO_2}}$, $b_{0,\mathrm{CO_2}}$, $d_{0,\mathrm{CO_2}}$, $\Delta U_{\mathrm{b,N_2}}$, $b_{0,\mathrm{N_2}}$.

In a recent study, Farhamini *et al* [102] showed that both pellet porosity (ϵ_{p}) and pellet diameter (d_{p}) can significantly affect the process performance. Hence, the variation of ϵ_{p} and d_{p} was also considered in the optimization. Other properties such as crystal density and the specific heat capacity of the adsorbent are held constant to that of Zeolite 13X. While specific heat capacity can potentially impact the process performance[102], especially under adiabatic conditions, it is held constant because of lack of data.

6.3.2 Process model and economic analysis

Two pressure-vacuum swing adsorption (PVSA) cycles are considered in this chapter. The first cycle illustrated in Fig. E.3 (in Appendix E) consists of four steps:

1. Adsorption step (ADS): Feed mixture introduced in the column for a duration of t_{ADS} at high pressure (P_{H}) undergoes separation through preferential adsorption of the heavy component CO_2 while the light componentN_2 leaves the column.

2. Blowdown step (BLO): Co-current blowdown to an intermediate vacuum (P_{I}) to remove N_2 from the column. If P_{H} >1 bar, then the column pressure first reduces to atmospheric pressure using a valve and further down to P_{I} using a vacuum pump. If P_{H} =1 bar, then only vacuum pump reduces the column pressure to P_{I}.

3. Evacuation step (EVAC): Column pressure further reduced to a low vacuum (P_{L}) using a vacuum pump in the counter-current direction to collect CO_2 rich product at the feed end of the column.

4. Light product pressurization step (LPP): Light product from the adsorption column pressurizes the column back to high pressure.

Owing to its simple features, this cycle has been benchmarked by various studies [21, 24, 101, 102] and was also demonstrated at a pilot plant facility [35]. Further, a more complex six-step PVSA cycle with dual reflux (DR) is considered as the second cycle

[21, 24, 44]. The cycle schematic is shown in Fig. E.4 in Appendix E. In addition to the four steps above, this cycle comprises two reflux steps:

5. Light reflux (LR) step after the evacuation at P_{L} where the light product from the adsorption column is used as reflux to purge the column in the LR step.

6. Heavy reflux (HR) step after the adsorption step at P_{H} by using the product from the LR step in order to increase the CO_2 partial pressure in the column.

The process simulations were carried out using a non-isothermal, one-dimensional mathematical model obtained by solving mass, momentum and energy balances [19]. The model comprises a set of partial differential equations (PDEs) after incorporating the following assumptions: 1) gas-phase obeys ideal gas law, 2) axially dispersed plug flow represents the bulk flow, 3) linear driving force model characterises the solid phase mass transfer, 4) there exist no radial gradients for composition, pressure and temperature across the column, 5) Ergun's equation accounts for the pressure drop across the column, 6) adsorbent properties and bed porosity are uniform, 7) the process operation remains adiabatic and, 8) instantaneous thermal equilibrium exists between the gas and the solid. More details on the appropriate boundary conditions used for each step in the cycle and the simulation parameters can be found in Appendix E. The PDEs were numerically discretized into 30 finite volumes along the spatial domain using the finite volume method with a weighted essentially non-oscillatory (WENO) scheme [19]. The resulting ordinary differential equations (ODEs) were then integrated using *ode23tb*, a stiff ODE solver in MATLAB. The cycle simulations were carried out based on a standard uni-bed approach where a single column undergoes all cycle steps in a sequence. The column was initialized with a feed mixture at P_{L} and simulated until the process reached cyclic steady state (CSS). When the mass balance error for the PVSA process equals 1% or less was observed for five consecutive cycles, the process was considered to attain CSS. A minimum number of 50 cycles were simulated to en-

sure that the CSS criterion was adequate. For simulations where the system fails to achieve CSS, a maximum number of 500 cycles were simulated, after which it was assumed that the system attained CSS. At CSS, state variables such as composition, pressure and temperature profiles were determined to calculate key performance indicators. The process model was previously demonstrated to reproduce both lab-scale, and pilot-scale experiments [35, 47].

The column scheduling was carried out based on the method proposed by Khurana and Farooq [21] to determine the number of columns required for continuous operation. The main assumptions are reiterated as follows: 1) Continuous-feed operation with constant throughput, 2) Separate vacuum pumps used to collect CO_2 and N_2 from respective steps to avoid contamination, 3) One vacuum pump serves only one column at any given time and, 4) Coupled steps occur simultaneously to avoid using storage tanks. More details on the column scheduling are provided in Section E.3.3. The modelling of a vacuum pump performance plays a crucial role in process simulations. Two key approaches, used in Chapter 5, are incorporated here. First, the flow rate of the vacuum pump is incorporated as the boundary condition. This provides a realistic estimation of blowdown and evacuation times. Second, the efficiency of the vacuum pump is made a function of the pressure, i.e., the vacuum pump efficiency drops as per the expression provided in Appendix E. This ensures a realistic estimation of the power consumption.

The economic analysis was carried out based on the cost model developed in Chapter 5 and the cost assessment was performed on an aspirational Nth Of A Kind (NOAK) basis [127] wherein it was assumed that the adsorptive CO_2 capture is mature for commercial deployment. The cost estimates are provided in $€_{2016}$ price levels. Costs with older estimates were updated using Chemical Engineering Plant Cost Index (CEPCI) and inflation. While undertaking techno-economic analyses, the outcomes can significantly change depending on the assumptions and the design choices [128]. Hence, it is

worth noting that the techno-economic model used in this chapter obeys both technical and economic recommendations for adsorption processes [128] and are consistent with best practices [127].

6.3.3 Integrated techno-economic optimization

The integrated techno-economic optimization problem was formulated to minimize the CO_2 avoided cost (defined in Section E.5) of the PVSA technology while achieving a minimum of 95% CO_2 purity and 90% CO_2 recovery. To this end, both process and adsorbent design variables were used as decision variables in the optimization problem.

Process decision variables: adsorption step duration (t_{ADS}), high pressure (P_{H}), intermediate vacuum (P_{I}), low vacuum (P_{L}), column length (L), reflux fraction (θ_{R}), fractional duration of reflux steps (f_{t}), volumetric flow rates of blowdown (S_{B}) and evacuation (S_{E}) vacuum pumps.

Adsorbent decision variables: CO_2 DSL isotherm parameters ($q_{\mathrm{sb,CO_2}}$, $q_{\mathrm{sd,CO_2}}$, $\Delta U_{\mathrm{b,CO_2}}$, $\Delta U_{\mathrm{d,CO_2}}$, $b_{0,\mathrm{CO_2}}$, $d_{0,\mathrm{CO_2}}$), N_2 DSL isotherm parameters ($\Delta U_{\mathrm{b,N_2}}$, $b_{0,\mathrm{N_2}}$), pellet porosity (ϵ_{p}) and pellet diameter (d_{p}).

Most of the process decision variables were kept the same as that of Chapter 5. Additionally, the high pressure (P_{H}) in the adsorption step was also varied. Although feed velocity in the adsorption step can be explicitly varied in the optimization, it was not considered as a decision variable in the present chapter. This was because the optimizer in Chapter 5 always approached the upper bounds in the techno-economic optimizations in order to reduce the total number of trains required for the separation. [88] Hence, in the present chapter, the feed velocity was calculated as the minimum fluidization velocity, which is the maximum velocity at which the packed beds can operate theoretically. Since the fluidization velocity depends on the decision variables P_{H}, ϵ_{p} and, d_{p}, feed velocity can be considered as a dependent variable. Reflux fraction

(θ_{R}) was defined as the fraction of the adsorption outlet flow that goes as the feed to the LR step in the six-step DR cycle while the fractional duration of LR and HR steps relate to the LR and HR step durations as: $t_{\mathrm{i}} = f_{\mathrm{t}} t_{\mathrm{ADS}}$, where i = HR, LR. The length to diameter ratio of the adsorption columns was fixed to 3. The lower and upper bounds defined for the decision variables are provided in Table E.5 in Appendix E. A global search method, a non-dominated sorting genetic algorithm II (NSGA-II), was used to solve the constrained optimization problem in MATLAB 2018b. The constraints were handled as penalty terms in the objective function. The initial set of decision variables were generated using Latin hypercube sampling, and at least 20000 NSGA-II evaluations were carried out in each optimization to ensure that the solution has converged.

6.4 Results and discussion

6.4.1 Cost limits of four-step PVSA cycle

Unique optimizations were carried out to determine the minimum CO_2 avoided cost for each of the cases specified in Table 6.1. The optimization was performed by varying both adsorbent and process design variables simultaneously in the optimizations. Note that the requirements of minimum 95% CO_2 purity and 90% CO_2 recovery were considered as constraints for all optimizations in this chapter. The costs of adsorbents have been set to zero in these optimizations, which were based on the assumption that the "ideal" hypothetical adsorbent(s) identified using *process inversion* can be synthesized or available for zero-cost. Although not plausible practically, this assumption will determine the absolute minimum costs of building and operating simply the PVSA process alone without additional expenditures related to the adsorbent.

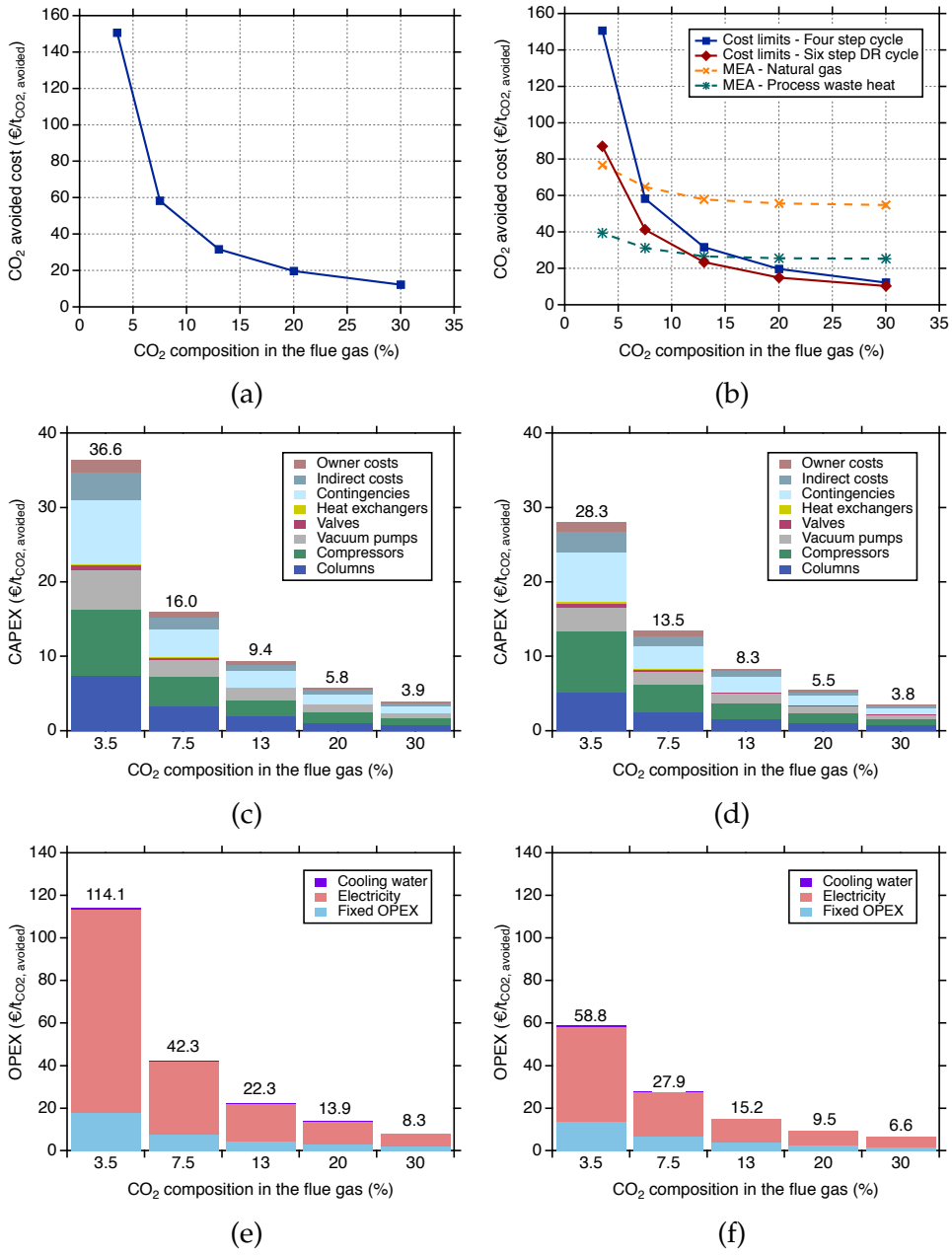

Figure 6.1: (a) Cost limits (or the lowest possible CO_2 avoided costs) of the four-step PVSA cycle at different CO_2 compositions. (b) Comparison between the cost limits of both four-step and six-step DR PVSA cycles with CO_2 avoided costs obtained using the MEA-based CO_2 capture with two steam supply scenarios (natural gas boiler and waste heat recovery). CO_2 avoided costs reported here exclude CO_2 conditioning, transport and storage. (c) Breakdown of investment costs (CAPEX) related to the cost limits of the four-step cycle. (d) Breakdown of investment costs (CAPEX) related to the cost limits of the six-step DR cycle. (e) Breakdown of operating costs (OPEX) related to the cost limits of the four-step cycle. (f) Breakdown of operating costs (OPEX) related to the cost limits of the six-step DR cycle.

Figure 6.1 (a) illustrates the minimum CO_2 avoided costs (or the cost limits) obtained over a range of CO_2 compositions for a flue gas flow rate of 2004 tonnes h^{-1} at atmospheric pressure. The CO_2 avoided costs increase with a decrease in CO_2 compositions. For instance, the minimum CO_2 avoided cost obtained for 30% CO_2 composition is 12.2 € per tonne of CO_2 avoided, and the CO_2 avoided cost increases 1135% when the CO_2 composition is reduced from 30% to 3.5%. In Fig. 6.1(c) and (e), the breakdown of the capital and operating costs that add up to the minimum CO_2 avoided costs are shown. Note that the individual cost breakdown of capital and operating costs along with optimal decision variables for all optimizations reported in this study are tabulated in Tables E.5-E.13 in Appendix E. As can be observed from Figs. 6.1(c) and (e), the capital costs contribute to about 24-32% of the avoided costs over a range of CO_2 compositions, and operating costs drive the techno-economic of PVSA. The operating costs amount to about 68% of the total costs for the case of 30% CO_2 composition, and this relative contribution increases to about 76% when the CO_2 composition is reduced to 3.5%. The major contribution to operating costs comes from electricity consumption, which varies between 77% and 84% of the operating costs. The electricity requirements cost 6.4 € per tonne of CO_2 avoided for 30% CO_2 composition case; however, when the CO_2 composition is reduced to 3.5%, the electricity costs escalate to 95.5 € per tonne of CO_2 avoided. Such high electricity demands with the decrease in CO_2 composition can be attributed to the P_{H} and P_{L} required in the process and due to low efficiency of the vacuum pumps at low pressures.

Figure 6.2 shows the optimal values of P_{H} and P_{L} obtained over a range of CO_2 compositions. The shaded region around the optimal values represents the upper and lower limits of the solutions obtained within the 5% vicinity of the minimum CO_2 avoided costs. The rationale behind this is to account for the variation of P_{H} and P_{L} on the minimum avoided cost. As expected, P_{L} decreases from $\approx$ 0.11 bar to 0.01 bar with lowering CO_2 composition from 30% to 3.5%, respectively; contrarily, P_{H} increases

from 1.8 bar to 2.9 bar. This trend is observed because the process requires a certain amount of working capacity from the adsorbent to meet the 95% CO_2 purity and 90% CO_2 recovery constraints. Hence, a higher pressure ratio, P_H / P_L is required.

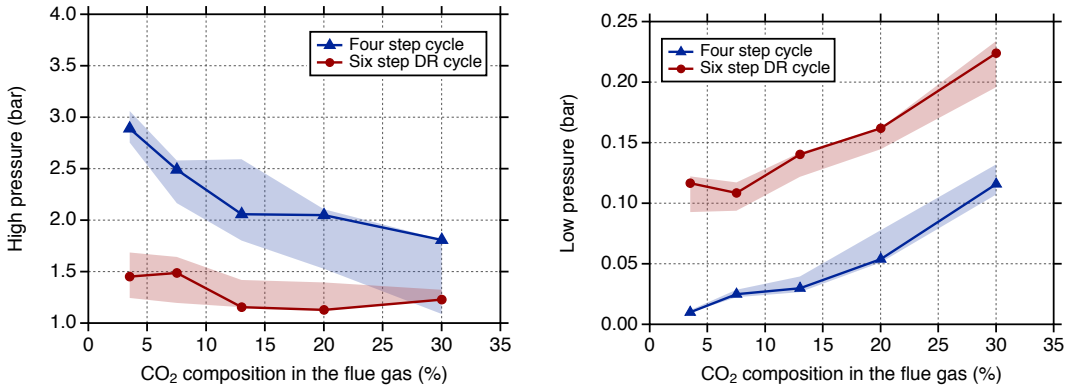

(a) (b)

Figure 6.2: Optimal high pressures (P_H) and low pressures (P_L) corresponding to the cost limits obtained at different CO_2 compositions. Shaded region represents the range of P_H and P_L within the 5% vicinity of the lowest possible CO_2 avoided costs.

Next, the adsorbent properties that link to the cost limits are considered. Figures 6.3(a)-(f) show the optimal (or "ideal") single component CO_2 and N_2 isotherms for different CO_2 compositions. The CO_2 isotherms of the ideal adsorbent (shown in red) indicate that they are all quite linear for all CO_2 compositions. The corresponding N_2 isotherms invariably converged close to zero loading. When the solutions near the minimum cost value for each case are analyzed, it was found that more than one CO_2 isotherm resulted in similar CO_2 avoided costs. Hence, in addition to the optimal CO_2 isotherms, all the corresponding CO_2 isotherms obtained within the vicinity of 5% of the minimum CO_2 avoided costs are included. These CO_2 isotherms are illustrated as Box and Whisker plots in Figs. 6.3(a)-(e) to statistically represent the entire region of distribution along with minimum and maximum values. As can be seen from Figs. 6.3(a)-(e), there is a wide range of CO_2 isotherms resulting in similar cost performance. As illustrated in the figure, this band of CO_2 isotherms is generally closer to linear with varied adsorption capacities. It is worth noting that the box and whisker plots

are obtained from CO_2 isotherms evaluated as a part of the optimization algorithm. Hence, these should be viewed as a subset of all possible isotherms that would yield cost values within 5% of the minimum value. The goal here was not to find the entire range but to highlight how widely varying CO_2 isotherms can indeed result in similar costs. Such a wide range CO_2 adsorption capacities can be attributed to trade-offs between competing capital and electricity expenditure towards overall CO_2 avoided costs. This is a key observation that points to the possibility that multiple adsorbents may be able to provide the comparable (low) cost of CO_2 capture. However, they may display widely varying CO_2 isotherms. This also highlights why the interplay between material property and process performance should be studied together. The optimal N_2 isotherms are shown in Fig. 6.3(f). Since the N_2 affinity for all cases was almost zero, the isotherms around the optimum were not considered. This again confirms that low N_2 adsorption is a very desirable property of an ideal adsorbent.

Limiting P_L to 0.1 bar. One of the challenges of large-scale implementation of PVSA involves deep vacuum ($P_L < 0.1$ bar) requirements to achieve very high CO_2 purity-recovery targets. Acknowledging the practical limitations to implement deep vacuum in industrial applications, the lower limit of P_L in the optimizations is increased from 0.01 bar to 0.1 bar and investigated the impact on cost limits. After running unique optimizations for the case of the lower limit of P_L =0.1 bar, the obtained cost limits are compared to the previous case. Figure 6.4(a) illustrates the ratio of cost limits obtained in both cases at different CO_2 compositions. For 3.5% and 7.5% CO_2 compositions, CO_2 purity-recovery constraints were not met in the optimizations and hence, these compositions are not considered for the discussion. The cost limits decreased with an increase in CO_2 compositions. The difference between two cases remains minor ($\leq$6%) for CO_2 compositions from 20% to 30% while at 13% CO_2 composition, a difference of 14% was observed. This indicates that the four-step PVSA process can still be operated

at higher P_L ($\geq$0.1 bar) for higher CO_2 compositions but requires ultra-deep vacuum for lower CO_2 compositions in order to meet purity-recovery requirements.

Effect of pellet porosity and pellet size. One set of adsorbent decision variables in the cost limit optimizations relates to adsorbent properties in the pelletized form, namely, pellet porosity and pellet diameter [102]. Here, the influence of pellet properties towards achieving the cost limits at different CO_2 compositions is investigated. This study was conducted by comparing two optimization cases: in the first case, pellet porosity and pellet diameter were treated as decision variables along with other adsorbent and process decision variables in the optimizations, while the second case involves keeping pellet porosity and pellet diameter as fixed values. The cost limits discussed earlier represent the first case; meanwhile unique optimizations were carried out for the second case using fixed values of pellet porosity (ϵ_p=0.37) and diameter (d_p=1.5 mm) from Chapter 5 representing typical experimental values [35, 47].

Figure 6.4(a) illustrates the comparison between the two cases. For the entire range of CO_2 compositions considered, the difference between the minimum CO_2 avoided costs for the two cases varies between 9 to 22%. The cost limits for fixed pellet properties are about 9-11% higher than the cost limits where pellet properties were varied at higher compositions (i.e. $\geq$13%). This difference increases to 19-22% at lower CO_2 compositions (i.e. $<$13%). The improvement in CO_2 avoided costs through optimization of pellet morphology can be attributed to the increased values of optimal ϵ_p and d_p as shown in Fig. 6.3(g)-(h). The optimal values of ϵ_p vary between 0.42 and 0.76, whereas the optimal d_p lies in between 3.0 and 5.0 mm, which are greater than the typical pellet sizes used in PVSA operations. It is worth noting that Farmahini *et al* also report similar ranges for ϵ_p and d_p in their energy-productivity optimizations [102].

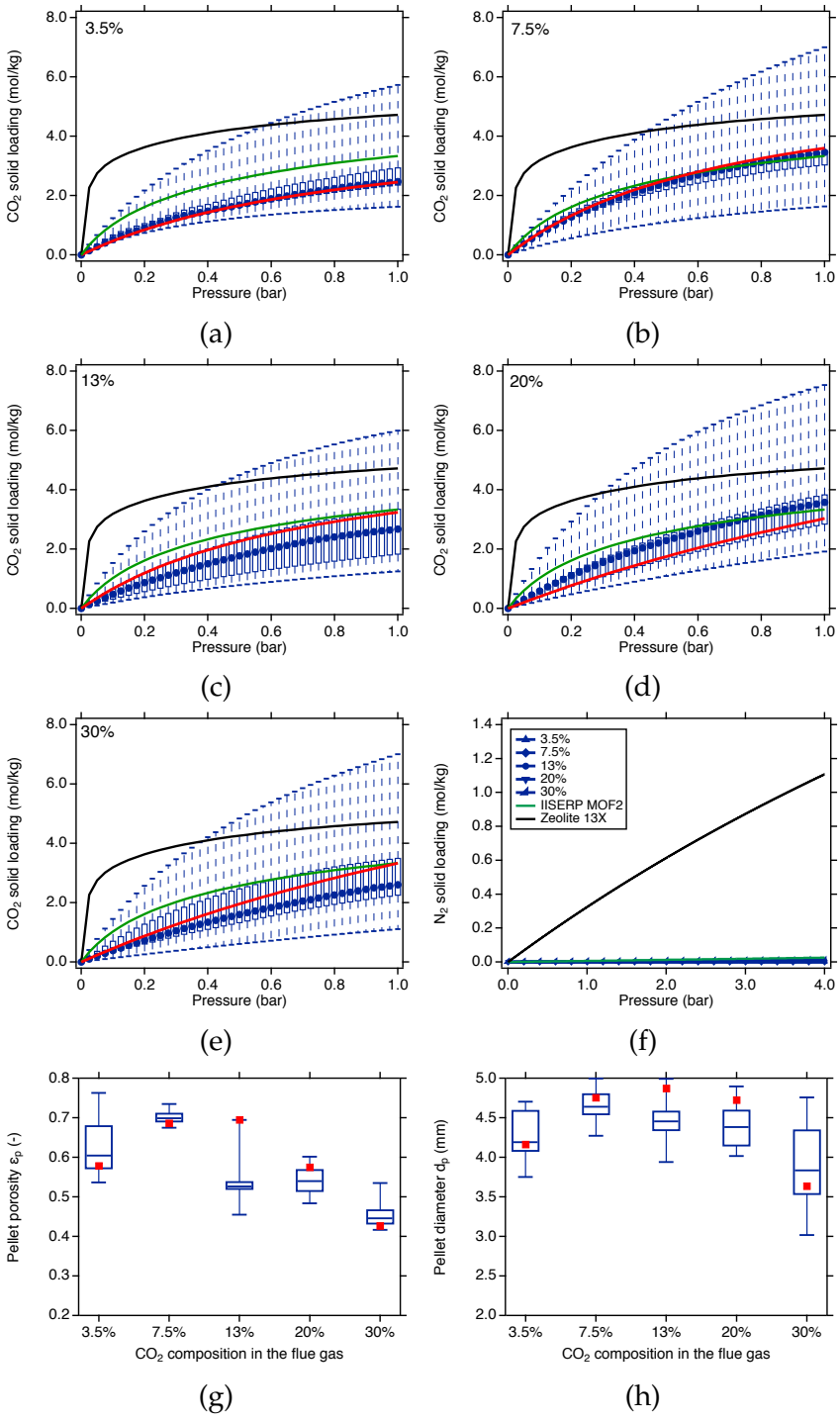

Figure 6.3: Optimal adsorbent properties corresponding to the cost limits of the four-step PVSA cycle.(a)-(e) show the optimal CO_2 adsorption isotherms (red lines) at different CO_2 compositions. Box and whisker plots in (a)-(e) represent the range of CO_2 adsorption isotherms in the 5% vicinity of the lowest possible CO_2 avoided cost. (f) the optimal N_2 adsorption isotherms at different CO_2 compositions. For comparison, CO_2 isotherms on Zeolite 13X (black lines) and IISERP MOF2 (green lines) are also shown in (a)-(e) and (f), respectively. (g) and (h) illustrate the optimal pellet porosity and diameter (red squares) along with box and whisker plots that represent the values within the 5% vicinity of the minimum CO_2 avoided costs, respectively.

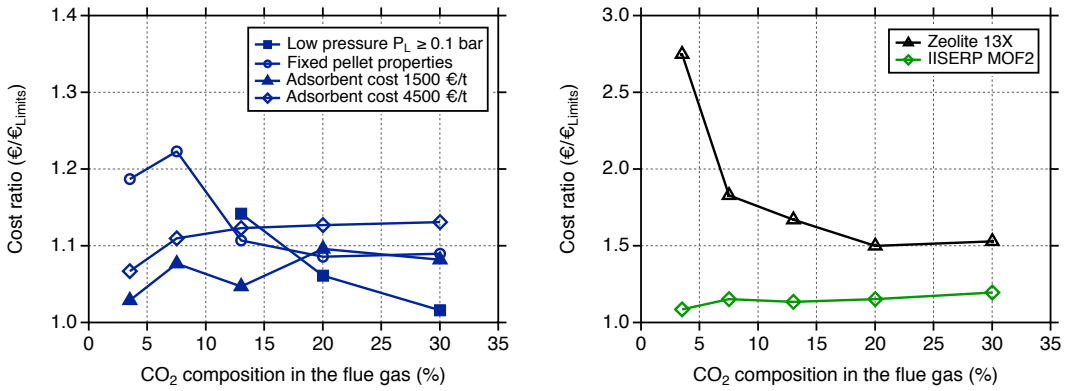

(a) (b)

Figure 6.4: (a) Impact of different process parameters on the cost limits of the four-step PVSA cycle. (b) Comparison between the cost limits of the four-step PVSA cycle with minimum CO_2 avoided costs obtained for real adsorbents (Zeolite 13X and IISERP MOF2). Note that the cost ratio was defined as the ratio between minimum CO_2 avoided costs obtained for the examined cases and the cost limits reported in Fig. 1 (a) at each CO_2 composition.

The choice of such increased values of ϵ_{p} and d_{p} by the optimizer is a result of an interplay between mass transfer characteristics and pressure drop. To elaborate, larger d_{p} favours lower pressure drop across the adsorption columns and also increases the maximum feed velocity (minimum fluidization limit) in the adsorption step. Hence, the adsorption columns can be operated at increased feed velocities with lower compression energy consumption, thereby facilitating the reduction in the number of parallel PVSA trains. Consequently, lower capital costs and compression costs are attained. Contrarily, the mass transfer is hindered by the increase in d_{p}, as given by the following relationship: $k_{\mathrm{LDF}} \propto \frac{\epsilon_{\mathrm{p}}}{d_{\mathrm{p}}^2}$, where k_{LDF} is the mass transfer coefficient. Keeping all other parameters constant, increase in d_{p}, reduces k_{LDF} which means that the mass transfer resistance is increased. This consequently increases the durations of constituent steps to meet constraints. To counter this effect, the optimizer chose high ϵ_{p} values to allow for enhanced mass transfer. As a result, there will be a lower amount of adsorbent present in the column, along with shorter PVSA cycle times. Shorter adsorption cycles lead to a fewer number of columns in a single PVSA train. This contributes to reducing

capital costs from fewer columns and vacuum pumps needed to implement the cycle scheduling. As can be seen from Fig. 6.3(g), the optimal ϵ_p values have not approached the upper limit as the adsorption column requires a certain minimum amount of adsorbent in the column to meet the CO_2 purity-recovery constraints. While higher ϵ_p and d_p are preferred theoretically, practical considerations such as the mechanical stability and the ability to synthesize high porosity pellets must be considered [102].

Influence of adsorbent costs. While an adsorbent cost of zero is interesting to understand the cost limit of PVSA, adsorbent costs cannot realistically be expected to be zero. Although the adsorbent costs are dependant on the raw materials used to synthesize them, scale-up methods, etc., the question posed is: if hypothetical adsorbents could be synthesized at similar costs as that of commercial adsorbents, what would be their contribution in bringing down CO_2 avoided costs? Hence, the influence of adsorbent costs on the cost limits is studied by considering three different adsorbent costs: 1) zero; 2) 1500 and; 4500 € per tonne of adsorbent. To provide context, commercial adsorbents like Zeolite 13X costs about 1500 € per tonne. [51, 88] Like previous case studies, unique optimizations are carried out for each case where the CO_2 avoided cost was minimized by varying both adsorbent and process decision variables. The cost limits at zero adsorbent cost serve as a reference. As can be seen from Fig. 6.4(a), the adsorbent costs considered have a marginal effect on the cost limits for all CO_2 compositions. For the case of 1500 € per tonne, the cost limits obtained are $<$10% higher than the cost limits with zero adsorbent cost, whereas 7-13% higher when the adsorbent costs are increased three times the cost of Zeolite 13X.

6.4.2 Comparison with real adsorbents

Figure 6.4(b) shows the comparison of minimum CO_2 avoided costs obtained for Zeolite 13X (black line) and IISERP MOF2 (green line) and cost limits. Of the two "real" adsorbents, Zeolite 13X always resulted in higher CO_2 avoided costs than IISERP MOF2.

At 30% CO_2 composition, the minimum CO_2 avoided cost obtained for Zeolite 13X was 18.7 € per tonne of CO_2 avoided (see Table E.11 in Appendix E) which is about 53% higher than the cost limit at the same CO_2 composition. The gap monotonically increases with reducing the CO_2 composition. For instance, the difference in CO_2 avoided costs between the Zeolite 13X and the cost limits at 3.5% CO_2 composition is approximately 175%. Higher CO_2 avoided costs for Zeolite 13X can be attributed to its non-linear CO_2 and high capacity N_2 isotherms, as shown in Fig. 6.3. While the band of hypothetical CO_2 isotherms from the cost limit optimizations are fairly linear, the non-linearity of the CO_2 isotherm for Zeolite 13X results in long blowdown and evacuation steps and, consequently, the capital costs.[88] On the other hand, previous studies have consistently shown that lower N_2 affinity significantly reduces electricity consumption. [91, 115] Since the Zeolite 13X higher N_2 affinity as compared to hypothetical N_2 isotherms, higher electricity costs are incurred compared to the "ideal" adsorbents (see Table E.11 in Appendix E).

As can be observed from Fig. 6.4(b), the marginal gap between the green line and the reference value 1.0 indicates the superior performance of IISERP MOF2, and this can be attributed to features of CO_2 and N_2 isotherms illustrated in Fig. 6.3. For all CO_2 compositions, the CO_2 isotherms of IISERP MOF2 are within the band of hypothetical CO_2 isotherms from the cost limits case. In addition, lower N_2 affinity similar to hypothetical N_2 isotherms contributed to lower electricity costs [88, 115]. Further, when the CO_2 compositions are lowered, the difference between the minimum CO_2 avoided costs of IISERP MOF2, and the cost limits also decrease non-monotonically from 20% to 9%.

Based on these results, it can be inferred that the dual-site Langmuirian-type "real" adsorbents can achieve relatively low CO_2 avoided costs at high CO_2 compositions, while their performances are discouraging at low CO_2 compositions. Conversely, the performances obtained by IISERP MOF2, an adsorbent approaching those "ideal" fea-

tures previously outlined, are consistently close to the cost limits.

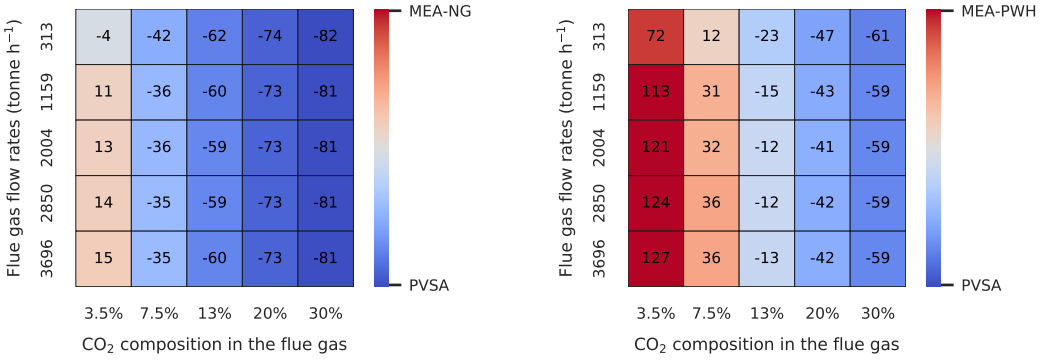

Figure 6.5: Heat maps illustrating the cost performance of the six-step DR PVSA cycle as compared to standard (a) MEA solvent using natural gas (NG) for steam generation (b) MEA solvent using process waste heat (PWH) for steam generation. The text in the heat maps represents the percentage by which the CO_2 avoided costs of PVSA are higher/lower compared to the MEA. A (+) sign indicates that the PVSA costs are higher than the MEA and a (-) indicates that the PVSA costs are lower than the MEA.

6.4.3 Cost limits of six-step DR cycle

As discussed previously, the four-step PVSA cycle relies strongly on the deep vacuum ($<$ 0.1 bar) to meet CO_2 purity-recovery constraints for CO_2 compositions lower than 30%. Although limiting the lower limit of P_L to 0.1 bar in the optimizations resulted in minimum CO_2 avoided costs slightly higher ($\leq$ 14%) than the cost limits for CO_2 compositions $\geq$ 13%, the CO_2 purity-recovery constraints were, however, not met for lower CO_2 compositions, i.e. $<$ 13%. Hence,a more complex six-step cycle with DR [21, 24, 44] is investigated by carrying out unique optimizations to determine if this cycle can yield lower cost limits than the four-step PVSA cycle while facilitating process operation at industrially feasible vacuum levels over a range of CO_2 compositions. Figure 6.1(b) shows the comparison of cost limits between the two PVSA cycles. As can be observed that the cost limits obtained for the six-step DR cycle are lower than the four-step cycle. For 30% CO_2 composition, the difference between the cost limits is 1.8 € per

tonne of CO_2 avoided (i.e. $\approx$ 15% lower for six-step DR cycle). When the CO_2 composition is lowered to 20%, the cost limits of the six-step DR cycle were found to be 24% lower than the cost limits achieved for the four-step cycle. The cost reduction ($\approx$ 42%) is more significant as the CO_2 composition is lowered from 20% to 3.5%. As can be seen from Figs. 6.1(d) and (f), the decrease in capital and, more significantly, operating costs have contributed to the cost reductions of the six-step DR cycle. As compared to the four-step cycle, the electricity costs have significantly dropped, especially at lower CO_2 compositions. This can be attributed to the optimal P_{H} and P_{L} (shown in Fig. 6.2) required to achieve the lowest CO_2 avoided costs. Optimal P_{H} for the six-step DR cycle always remained lower than that of the four-step cycle over a range of CO_2 compositions which indicate lower compression costs. Another interesting aspect remains that the six-step DR cycle can be operated with $P_{\mathrm{L}} \geq 0.1$ bar over the entire range of CO_2 compositions. This is a significant result because the industrially used vacuum pumps can now be employed. The ability to operate vacuum pumps at milder vacuum levels further entails lower electricity consumption, not only connected to the higher P_{L} but also the higher vacuum pump efficiencies. The better performance of the six-step DR cycle over the four-step cycle can be attributed to the dual reflux steps, i.e. the HR and LR steps. The LR step in the six-step DR cycle helped recover the residual CO_2 from the column after the evacuation step, and the effluent of this step was used as the heavy reflux before the depressurization steps. The HR step increased the overall CO_2 partial pressure in the column. Hence, the CO_2 purity-recovery targets can be achieved without depressurizing the column to deep vacuum levels [44].

The optimal adsorbent properties linked to the cost limits of the six-step DR cycle are shown in Fig. E.5 in Appendix E. Similar to the four-step cycle, a huge variation is noticed in CO_2 isotherms and pellet properties within a 5% range from the minimum avoided costs. The CO_2 isotherms for the six-step DR cycle were also found to be fairly linear with almost zero N_2 adsorption (see Fig. E.5 in Appendix E). For CO_2 compo-

sitions of 3.5%, 7.5% and 13%, the CO_2 isotherms of the six-step DR cycle showed a huge variation with higher loadings as compared to the four-step cycle. The band of CO_2 isotherms for both the cycles were comparable for 20% and 30% CO_2 compositions. On the other hand, the pellet diameters were closer to the upper limit of 5 mm, whereas the pellet porosity lies in the range of 0.36-0.63.

6.4.4 Comparison with MEA absorption

Here, the competitiveness of PVSA for post-combustion CO_2 capture is analyzed by comparing its cost limits with current benchmark MEA absorption. The CO_2 avoided costs for MEA obtained from two scenarios are considered: in the first scenario, the source of steam supply for MEA-based capture comes from a natural gas (NG) boiler, whereas in the second scenario, the steam is considered to be generated through heat recovery from the industrial facility. While the first scenario serves as a more general representation of standard MEA-based capture, the second scenario is highly site-specific, i.e. depends on the availability of suitable process waste heat in the industrial facility or nearby industries. The choice of these MEA scenarios comes from the fact that the steam supply source strongly affects the overall CO_2 avoided costs obtained using the MEA solvent [116]. Such variations must be considered when assessing the techno-economic performance of PVSA for a fair comparison. Figure 6.1 (b) compares the CO_2 avoided costs obtained using the MEA solvent from these scenarios at different CO_2 compositions for a constant flue gas flow rate of 2004 tonnes h^{-1}. The cost limits of both PVSA cycles are lower than the CO_2 avoided costs obtained for the MEA solvent with NG boiler case when CO_2 composition $\geq$7.5%. At 3.5% CO_2 composition, the cost limits of both PVSA cycles escalate very quickly due to significant electricity demands, thus, resulting in a poor performance as compared to the MEA absorption. The six-step DR cycle shows better cost performance than the MEA solvent with process waste heat (PWH) case for CO_2 compositions $\geq$13%. The MEA-PWH scenario,

although site-specific and subject to the availability for CO_2 capture, represents the optimistic case for the MEA. This indicates that the PVSA could potentially outperform MEA-PWH in terms of CO_2 avoided costs for all CO_2 compositions $\geq$13% should the right adsorbent be deployed.

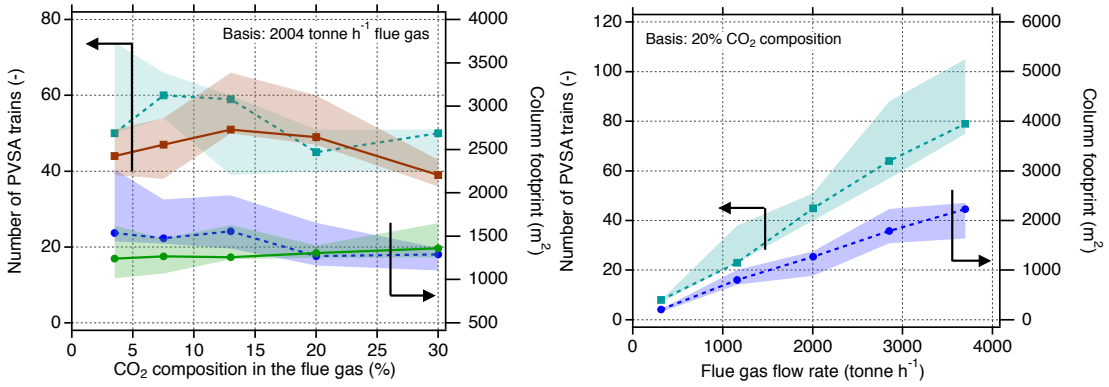

Figure 6.6: PVSA trains (squares) and column footprint (circles) required to treat (a) 2004 tonne h^{-1} flue gas at different CO_2 compositions based on the cost limits of four-step (dashed lines) and six-step DR (solid lines) cycles (b) different flue gas flow rates at 20% CO_2 composition based on the cost limits of four-step cycle. Shaded region represents the range within the 5% vicinity of the lowest possible CO_2 avoided costs.

Effect of plant scale. So far, a single flue gas flow rate of 2004 tonnes h^{-1} is considered in the analysis. Here the effect of plant size on the cost performance of the PVSA. As specified in Table 6.1, five different flue gas flow rates spanning the entire spectrum of various post-combustion industrial point sources are considered. The two MEA scenarios mentioned above are used for comparison. Given the inherent way in which the PVSA operates as multiple modules, it is expected that the overall CO_2 avoided costs will not be influenced by the plant size (or flue gas flow rate). To corroborate this assumption, optimizations are carried out to determine the cost limits of the four-step PVSA cycle at different flue gas flow rates from Table 6.1 for a fixed CO_2 composition of 20%. The results are presented in Fig. E.7 in Appendix E. As expected, the minimum CO_2 avoided costs obtained at different flue gas flow rates from unique

optimizations are almost identical (<2% difference). Based on these results, the same values of the cost limits obtained for both PVSA cycles in Fig.6.1(b) at different CO_2 compositions are extended over a range of flue gas flow rates considered without re-running the optimizations for each case. Figure 6.5 illustrates the impact of both plant size and CO_2 composition on the overall competitiveness of the PVSA. The six-step DR cycle is considered as the representative case for PVSA owing to its superior performance. The red-shaded portions of the figure indicate better performance of MEA over PVSA, while the blue-shaded portions show the superior performance of PVSA over MEA. The text in each box represents the percentage by which the CO_2 avoided costs of PVSA are higher/lower compared to the MEA. A (+) sign indicates that the PVSA costs are higher than the MEA and a (-) indicates that the PVSA costs are lower than the MEA. For the MEA-NG case as reference, the PVSA outperforms MEA for all flue gas flow rates and with CO_2 composition>3.5%. Notably, one exception was found where the PVSA performs slightly better than MEA for a flue gas flow rate of 313 tonne h^{-1} at 3.5% CO_2 composition. When MEA-PWH is considered as the basis, the PVSA results in lower costs for all flue gas flow rates with CO_2 composition$\geq$13%. These results indicate that the PVSA has a cost advantage compared to the benchmark MEA solvent for CO_2 compositions $\geq$13% over a range of flue gas flow rates provided low-cost adsorbents with appropriate separation capabilities can be developed.

Complexity of the PVSA plant. One of the challenges of the implementation of the PVSA involves integrating multiple PVSA trains. Depending on the plant size and the CO_2 composition, several PVSA trains might be needed for operation. The required number of PVSA trains are presented for both four-step cycle and six-step DR cycle in order to treat 2004 tonne h^{-1} flue gas flow rate in Fig. 6.6(a). In addition, the range within the 5% vicinity of cost limits is also shown. As can be seen from the figure, the overall trend, considering the ranges for the 5% vicinity, is that both the number

of trains and the column footprint remain fairly constant. This trend is consistent as the amount of flue gas to be treated is the same, immaterial of the CO_2 composition. The required number of PVSA trains for a fixed CO_2 composition linearly increases with the flue gas flow rates as shown in Fig. 6.6(b) (also see Table E.14 in Appendix E). For instance, 8 PVSA trains are needed to treat 313 tonne h^{-1} of flue gas at 20% CO_2 composition. On the contrary, 79 PVSA trains are required if the flow rate increases to 3696 tonne h^{-1}. Moreover, the footprint of the columns when stacked side by side for the case of the 2004 tonne h^{-1} flow rate is illustrated in Fig. 6.6(a). As can be seen from the figure, the column footprint ranges between ≈1000-2200 m^2. Over a range of flue gas flow rates at 20% CO_2 composition, the column footprint, as illustrated in Fig. 6.6(b), varies almost linearly from 209 m^2 to 2234 m^2 when the flow rate changes from 313 to 3696 tonne h^{-1}, respectively. It is to be noted that the total footprint of the plant will be higher than the values reported after adding the area occupied by compressors, vacuum pumps and piping.

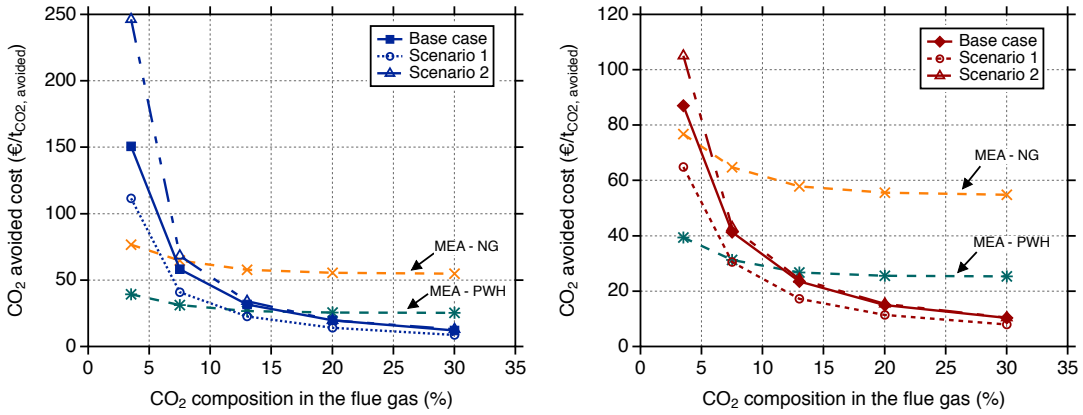

Figure 6.7: Cost limits of (a) four-step and (b) six-step DR PVSA cycles when two alternative electricity scenarios are considered: Scenario 1 - electricity price of 29.0 € per MWh and specific direct emissions of 38 kg CO_2 per MWh and; Scenario 2 - electricity price of 58.1 € per MWh and specific direct emissions of 262 kg CO_2 per MWh. The base case with the cost of electricity 58.1 € per MWh and specific direct emissions of 38 kg CO_2 per MWh is also shown.

Electricity scenarios. As previously described, the electricity demand remains the significant factor towards achieving the minimum CO_2 avoided costs for PVSA. In this chapter, the standard European electricity price of 58.1 € per MWh was used [88, 129]. For the electricity consumed, the specific direct emissions of 38 kg CO_2 per MWh are also accounted for based on the assumption that the electricity consumed by the PVSA is supplied through a deeply decarbonized power system based on a fossil-based power plant with CCS and renewables [88]. As indirect CO_2 emissions associated with electricity consumption increase the CO_2 avoidance cost [130], the premise of a deeply decarbonized power system is consistent with the search for the cost limit. Since the source of electricity generation and its characteristics depends on several parameters such as plant location and electricity mix, an optimization study is conducted with alternative scenarios to investigate the impact on PVSA cost limits. For this analysis, the electricity price of 58.1 € per MWh and the specific direct emissions of 38 kg CO_2 per MWh remain as the base case. In the first scenario, the cost of electricity is reduced to 50% of the base case while the specific direct emissions were kept the same as the base case. This scenario is representative of cases in which the PVSA facilities access low-cost renewable electricity production with preferential industrial tariffs excluding transmission costs as can happen, for example, in Norway [131]. The second scenario considers the electricity generation with higher CO_2 intensity, i.e., the cost of electricity remains the same as that of the base case while the specific direct emissions are increased to 262 kg CO_2 per MWh corresponding to the CO_2-intensity of the European average electricity mix [113, 129]. The motivation for the second scenario comes from the existing power production systems that are significantly based on fossil-fuel power plants without CCS.

The PVSA cost limits are optimized based on the two alternative electricity scenarios. Figure 6.7 illustrates the cost limits obtained for two PVSA cycles under the two alternative scenarios. As can be seen from the figure, the cost limits of both PVSA cy-

cles are lowered (≈23-32%) when the electricity prices dropped to 29.0 € per MWh in the first scenario. Under these circumstances, the six-step DR cycle outperforms MEA with NG boiler for all CO_2 compositions, whereas the four-step cycle gives lower costs for CO_2 compositions ≥7.5%. If MEA-PWH is considered as reference, then the six-step DR and four-step cycles perform better than MEA for CO_2 compositions ≥7.5% and ≥13%, respectively. On the contrary, the PVSA cost limits have either increased or remained the same when the second scenario is considered. The high CO_2 intensity in the second scenario showed a substantial effect on two PVSA cycles at a 3.5% CO_2 composition where the CO_2 avoided cost increased to 246.4 € per tonne of CO_2 avoided (64% higher than the base case) for the four-step cycle. When the six-step DR cycle is considered, the CO_2 avoided cost increased to 105.1 € per tonne of CO_2 avoided, i.e. almost 21% higher than the base case. This is because the electricity consumption is significantly higher at 3.5% CO_2 composition (see Fig. 6.1(c)-(d)) than other higher CO_2 compositions. The four-step cycle, however, obtained 68.4 € per tonne of CO_2 avoided, i.e. 17% higher costs compared to the base case at 7.5% CO_2 composition. For CO_2 compositions ≥13%, the CO_2 intensity has negligible effect on the PVSA cost limits.

6.5 Conclusions

Cost limits of two single-stage PVSA cycles for post-combustion CO_2 capture are investigated through techno-economic optimizations based on a *process inversion* approach. Using this approach, both adsorbent and process variables are simultaneously optimized based on NSGA-II algorithm to calculate the lowest possible cost of CO_2 avoided (excluding the costs of CO_2 conditioning, transport and storage) or cost limits at different flue gas flow rates and CO_2 compositions. The key results of this chapter can be summarised as follows:

- The CO_2 composition in the flue gas significantly impacts the cost limits of PVSA,

i.e., the lowest possible CO_2 avoided costs decrease with increase in CO_2 compositions. Between the two cycles considered, the six-step DR cycle achieved 15-42% lower costs compared to the four-step cycle, depending on the CO_2 composition.

- When compared with the established MEA solvent based on NG boiler as a steam source, the four-step PVSA cycle has at least 8% lower costs compared to the MEA-based CO_2 capture, whereas the six-step DR PVSA cycle has at least 35% lower costs for CO_2 compositions $\geq$7.5% over a range of flue gas flow rates.

- The optimizations indicated that the "ideal" adsorbents that facilitate lowest possible CO_2 avoided costs have fairly linear CO_2 adsorption isotherms and N_2 adsorption close to zero.

- It was found that modifying the pellet morphology can result in $\approx$9-22% lower CO_2 avoided costs based on a four-step PVSA cycle. The optimal pellet porosities and diameters were between 0.42-0.76 and 3-5 mm, respectively.

- The complexity of the PVSA plant in terms of the number of trains, equipment, piping, area, etc., significantly depends on the flue gas flow rate. The smallest plant considered in this study with a size of 313 tonne h^{-1} flue gas flow rate requires about eight PVSA trains with four columns each based on a four-step PVSA cycle. Almost 79 PVSA trains with four columns each are needed to treat a plant size of 3696 tonne h^{-1}.

Although the PVSA costs seem favourable, the practical implementation involves limitations due to the plant complexity in terms of the number of PVSA trains required to treat the flue gas, the footprint of the total plant and the associated complexities in plant integration. Some of the challenges can be offset by choosing horizontally-oriented columns instead of vertically-oriented columns, and potentially considering

hybrid processes, e.g., PVSA+cryogenic [132, 133]. Finally, the key outcome of the study is the demonstration that PVSA processes can be promising for treating flue gas streams with high CO_2 compositions, provided suitable low-cost adsorbents be developed. The fact that adsorbents with a variety of CO_2 isotherms can indeed yield similar costs is encouraging and motivates adsorbent discovery and development.

Chapter 7

Concluding remarks

The flexibility in process design makes cyclic adsorption processes attractive for industrial gas separations, particularly a potential alternative to liquid solvents for CO_2 capture. Another advantage is the minimal environmental impacts due to the use of solid adsorbents compared to the issue of solvent degradation into toxic and corrosive compounds associated with liquid solvents. However, the bottleneck for promoting innovations in the adsorption process technology has been using computationally intensive detailed mathematical models to design and optimize processes with the accuracy and reliability needed for industrial applications. With the discovery of numerous adsorbents, the current simulation and optimization tools are insufficient to design cyclic adsorption processes optimally. Moreover, the potential of adsorptive CO_2 capture is often poorly understood due to the lack of standardized techno-economic assessments that can play a significant role in evaluating both the technical and the economic viability.

The overall aim of this thesis was twofold. One, to develop machine learning-based methodologies for rapid simulation of cyclic adsorption processes. Two, to develop a rigorous techno-economic model for assessing the performance of adsorption processes for post-combustion CO_2 capture. This chapter summarizes the key outcomes achieved in this thesis. Moreover, the directions for future research are discussed to promote significant improvements in the proposed modelling strategies.

7.1 Summary

Machine learning-based process optimization. In Chapter 2, hybrid approaches were proposed to accelerate the computational speeds of PSA optimizations. The proposed approaches were implemented to maximize CO_2 purity and CO_2 recovery that can be obtained from a complex eight-step PSA cycle designed for pre-combustion CO_2 capture. The first approach, *SOpt*, exploited artificial neural networks for objective function evaluations in the multi-objective optimization routines. The neural networks are trained using the individuals evaluated by the detailed process model in the initial optimization and are utilized for function evaluations in the subsequent optimization. The Pareto front computed based on this approach overlapped with the Pareto front from the traditional optimization routine. In terms of computational speeds, this approach offered $10\times$ speed while achieving the same performance as the traditional routine. The second approach, *DROpt*, focused on reducing the dimensionality of the optimization problem. Through PLS regression, relevant variables for the optimization were identified. Based on these few relevant variables, Pareto fronts are calculated by coupling detailed process model in the multi-objection optimization. For the case considered, the dimensional reduction from eight to three doubled the computational speeds of the optimization. Finally, a combination of the first and the second approaches has also been investigated. This third approach also predicted the original Pareto front reasonably well through faster computations.

Physics-based deep learning for cycle simulation and synthesis. Leveraging the latest advances in physics-based deep learning of partial differential equations, viable methodologies are proposed for rapid adsorption cycle simulation and synthesis. Chapter 3 explored the ability of physics-based deep neural networks to predict the complex dynamics of generic pulse injections in adsorption columns. The effectiveness of the methodology was tested by investigating the impact of feed concentrations

of binary solute mixtures and injection volumes on the solute movement along the column. The deep neural networks are trained to learn the spatiotemporal dynamics for different combinations of binary feed concentrations and the pulse injection time by designing a loss function that constrains neural network predictions to match the training data while minimizing the PDE residuals. The results demonstrated that the trained model accurately predicted the solute movement in adsorption columns, capturing important features such as concentration transitions even in the absence of training data. Next, in Chapter 4, the complexity of the framework was increased by developing physics-based neural networks for rapid simulation of cyclic adsorption processes and cycle synthesis. Here individual deep neural networks are trained for each step in the adsorption cycle to learn the full spatiotemporal solutions of different state variables by obeying the underlying conservation laws of mass and momentum along with adsorption equilibria. The methodology was successfully tested and validated by constructing and simulating a four-step VSA cycle for post-combustion CO_2 capture based on individual neural network models. Next, four different VSA cycles, namely two three-step and two four-step VSA cycles with feed and light product pressurization steps, respectively, were constructed using the proposed methodology to demonstrate the cycle synthesis capabilities. The results indicated that the trained neural networks accurately simulated all the four VSA cycles.

Techno-economic assessments of P/VSA processes for post-combustion CO_2 capture. In Chapter 5, a systematic approach for the design and techno-economic assessment of VSA processes was developed. The methodology developed herein incorporated a detailed process model, vacuum pump dynamics, rational scale-up, and cost model consistent with best practices, combined with stochastic optimization to calculate the minimum CO_2 capture cost. This methodology was applied to post-combustion CO_2 capture from steam methane reformer flue gas by considering a four-step VSA process

and three different adsorbents: Zeolite 13X and metal-organic frameworks, UTSA-16 and IISERP MOF2. The results demonstrated that optimizing the VSA process using proxy objectives such as minimizing energy and maximizing productivity does not guarantee the minimum cost because of inherent complexities involved in the process scale-up. Among the three adsorbents, IISERP MOF2 showed better performance. It was also shown that the choice of adsorbent and its cost has a major impact on the cost of CO_2 capture. Finally, the baseline monoethanolamine based absorption process outperformed the best performing adsorbent IISERP MOF2 with 10% lower CO_2 avoided cost.

Chapter 6 focused on a techno-economic investigation to determine the cost limits of two PVSA cycles, namely, four-step and six-step dual reflux cycles, for post-combustion CO_2 capture. Here, a *process inversion* approach was employed, where both adsorbent and process variables are optimized simultaneously to calculate the lowest possible cost of CO_2 capture at different flue gas flow rates and CO_2 compositions. The results demonstrated that the CO_2 composition in the flue gas significantly impacts the PVSA cost limits, i.e., costs decrease with increase in CO_2 compositions. Moreover, the six-step dual reflux cycle outperformed the four-step cycle by achieving 15-42% lower costs depending on the CO_2 composition. Compared to monoethanolamine based absorption process, PVSA was found to be attractive for flue gas streams with high CO_2 compositions $\geq$7.5%. Finally, the "ideal" adsorbents facilitating lowest possible CO_2 capture costs have fairly linear CO_2 adsorption isotherms and zero N_2 adsorption.

7.2 Way forward

Towards a superstructure-based optimal cycle synthesis. Designing an optimal adsorptive gas separation process requires the right selection of adsorbents and cycle configuration. The plethora of novel adsorbents for gas separations and the flexible cycle design requires a superstructure-based approach to design an optimal cycle configura-

tion for evaluating many adsorbents. The physics-based neural network methodology developed in this thesis was demonstrated to synthesize and simulate different cycles. The next step is to extend this framework for superstructure optimization. Despite the initial success, the physics-based neural network is still in its infancy and requires further advancements before integrating with the superstructure formulation. First, the current methodology was developed based on the isothermal operation. In practice, the process is operated under adiabatic conditions. This means that the neural networks will also need to learn the conservation law of energy along with the conservation laws of mass and momentum with column temperature as an additional output. Second, a systematic study must be carried out to determine the neural network hyperparameters, such as the size of the architecture and optimal weights for the loss terms. Since the choice of weights for the loss terms can influence the overall training procedure, determining an optimal combination of weights will improve the overall accuracy of the neural network models. Third, the initial column profiles form inputs to neural networks. The initial column profiles are unknown in most cases, especially when many complex steps are included for the superstructure optimization. While a detailed process model can generate few samples of initial column profiles by simulating different cycle configurations based on heuristics, it might be a computationally desired approach. Instead, mathematical functions can be used as such or as a combination of several functions to mimic the initial column profiles typically encountered in various processes. Finally, several step models need to be trained in the future to incorporate pressure equalization steps, reflux steps, etc. The neural networks must also be trained at different step operating parameters such as column pressure, velocities, etc., to enable the variation of operating conditions in superstructure optimization.

Lessons from techno-economic assessments and future opportunities. The detailed techno-economic optimization model developed in this thesis provided several key

perspectives when designing and assessing the techno-economics of P/VSA processes for CO_2 capture. Major learning involves the requirement of deep vacuum pressures, i.e. < 0.1 bar for VSA processes, which arise from the high CO_2 purity and CO_2 recovery constraints enforced on the separation. Alternatively, pressurizing the feed to slightly higher pressures, i.e. operating as PVSA, might avoid the necessity of deep vacuum requirements depending on the CO_2 composition in the flue gas. Moreover, a more complex cycle designs like the six-step dual reflux cycle can facilitate the operation at industrial vacuum pressures.

The use of beaded adsorbents in typical adsorption processes can limit the overall process performance. This limitation comes from the maximum velocities employable for operating the P/VSA processes. As a result, the requirement of multiple P/VSA parallel trains arises. Future research on process design should focus on drastically different approaches, such as the use of monoliths or parallel-passage contacts to enable rapid cycling and increase the maximum feed velocities.

Even though PVSA costs are favourable for some cases, the practical implementation involves limitations due to the plant complexity in terms of several P/VSA trains required to treat the flue gas, total plant footprint, and the associate piping and control systems. The flow gas flow rate significantly determines the complexity of the P/VSA plant. For instance, treating flue gas flow rate of 313 tonne h^{-1} requires about eight PVSA trains with four columns each based on a four-step PVSA cycle, whereas 79 PVSA trains with four columns each are needed to treat a plant size of 3696 tonne h^{-1}. The complexity of the PVSA plant can be reduced by adopting a different design philosophy. For instance, choosing horizontally-oriented columns instead of vertically-oriented columns can decrease the number of P/VSA trains [132]. Moreover, hybrid processes, e.g., PVSA+cryogenic, should be considered for CO_2 capture as potential alternatives to reduce the plant sizes [133].

Finally, adsorbents with earth-abundant materials are critical for the large-scale im-

plementation of P/VSA processes for CO_2 capture. The cost limit analysis demonstrated that a variety of CO_2 isotherms could yield similar costs, thus encouraging the adsorbent discovery and development. However, the novel adsorbents developed for CO_2 capture should be manufactured in large-quantities for practical deployment. Future adsorbent development research must be directed towards improving: the capabilities of synthesizing adsorbent materials on a large scale, forming macroscopic shapes, and increasing the stability towards cycling and impurities to promote commercial implementation.

Bibliography

[1] S. Sircar, "Pressure swing adsorption," *Ind. Eng. Chem. Res.*, vol. 41, no. 6, pp. 1389–1392, 2002.

[2] A. Malek and S. Farooq, "Hydrogen purification from refinery fuel gas by pressure swing adsorption," *AIChE J.*, vol. 44, no. 9, pp. 1985–1992, 1998.

[3] S. Sircar and T. C. Golden, "Purification of hydrogen by pressure swing adsorption," *Sep. Sci. Technol.*, vol. 35, no. 5, pp. 667–687, 2000.

[4] S. Sircar, M. Rao, and T. Golden, "Fractionation of air by zeolites," in *Adsorption and its Applications in Industry and Environmental Protection*, vol. 120, 1999, pp. 395 –423.

[5] S. Farooq and D. Ruthven, "Numerical simulation of a kinetically controlled pressure swing adsorption bulk separation process based on a diffusion model," *Chem. Eng. Sci.*, vol. 46, no. 9, pp. 2213 –2224, 1991.

[6] A Dabrowski, "Adsorption — from theory to practice," *Adv. Colloid Interface Sci.*, vol. 93, no. 1, pp. 135 –224, 2001.

[7] A. Kapoor and R. Yang, "Kinetic separation of methane-carbon dioxide mixture by adsorption on molecular sieve carbon," *Chem. Eng. Sci.*, vol. 44, no. 8, pp. 1723 –1733, 1989.

[8] C. A. Grande and A. E. Rodrigues, "Propane/propylene separation by pressure swing adsorption using Zeolite 4A," *Ind. Eng. Chem. Res.*, vol. 44, no. 23, pp. 8815–8829, 2005.

[9] L. T. Biegler, L. Jiang, and V. G. Fox, "Recent advances in simulation and optimal design of pressure swing adsorption systems," *Sep. Purif. Rev.*, vol. 33, no. 1, pp. 1–39, 2005.

[10] M. Bui, C. S. Adjiman, A. Bardow, E. J. Anthony, A. Boston, S. Brown, P. S. Fennell, S. Fuss, A. Galindo, L. A. Hackett, J. P. Hallett, H. J. Herzog, G. Jackson, J. Kemper, S. Krevor, G. C. Maitland, M. Matuszewski, I. S. Metcalfe, C. Petit, G. Puxty, J. Reimer, D. M. Reiner, E. S. Rubin, S. A. Scott, N. Shah, B. Smit, J. P. M. Trusler, P. Webley, J. Wilcox, and N. Mac Dowell, "Carbon capture and storage (CCS): The way forward," *Energy Environ. Sci.*, vol. 11, no. 5, pp. 1062–1176, 2018.

[11] IEAGHG, "Techno-economic evaluation of SMR based standalone (merchant) plant with CCS," 2017/02, February 2017.

[12] D. M. Ruthven, S. Farooq, and K. S. Knaebel, *Pressure Swing Adsorption*. Wiley, 1994.

[13] S. Nilchan and C. Pantelides, "On the optimisation of periodic adsorption processes," *Adsorption*, vol. 4, no. 2, pp. 113–147, 1998.

[14] D. Ko and I. Moon, "Multiobjective optimization of cyclic adsorption processes," *Ind. Eng. Chem. Res.*, vol. 41, no. 1, pp. 93–104, 2002.

[15] D. Ko, R. Siriwardane, and L. T. Biegler, "Optimization of a pressure-swing adsorption process using Zeolite 13X for CO_2 sequestration," *Ind. Eng. Chem. Res.*, vol. 42, no. 2, pp. 339–348, 2003.

[16] L. Jiang, L. T. Biegler, and V. G. Fox, "Simulation and optimization of pressure-swing adsorption systems for air separation," *AIChE J.*, vol. 49, no. 5, pp. 1140–1157, 2003.

[17] D. Nikolić, E. S. Kikkinides, and M. C. Georgiadis, "Optimization of multibed pressure swing adsorption processes," *Ind. Eng. Chem. Res.*, vol. 48, no. 11, pp. 5388–5398, 2009.

[18] A. Agarwal, L. T. Biegler, and S. E. Zitney, "Simulation and optimization of pressure swing adsorption systems using reduced-order modeling," *Ind. Eng. Chem. Res.*, vol. 48, no. 5, pp. 2327–2343, 2009.

[19] R. Haghpanah, A. Majumder, R. Nilam, A. Rajendran, S. Farooq, I. A. Karimi, and M. Amanullah, "Multiobjective optimization of a four-step adsorption process for postcombustion CO_2 capture via finite volume simulation," *Ind. Eng. Chem. Res.*, vol. 52, no. 11, pp. 4249–4265, 2013.

[20] F. Capra, M. Gazzani, L. Joss, M. Mazzotti, and E. Martelli, "MO-MCS, a derivative-free algorithm for the multiobjective optimization of adsorption processes," *Ind. Eng. Chem. Res.*, vol. 57, no. 30, pp. 9977–9993, 2018.

[21] M. Khurana and S. Farooq, "Integrated adsorbent process optimization for minimum cost of electricity including carbon capture by a VSA process," *AIChE J.*, vol. 65, no. 1, pp. 184–195, 2019.

[22] N. Casas, J. Schell, L. Joss, and M. Mazzotti, "A parametric study of a PSA process for pre-combustion CO_2 capture," *Sep. Purif. Technol*, vol. 104, pp. 183–192, 2013.

[23] A. K. Rajagopalan, A. M. Avila, and A. Rajendran, "Do adsorbent screening metrics predict process performance? A process optimisation based study for post-combustion capture of CO_2," *Int. J. Greenh. Gas Control*, vol. 46, pp. 76 –85, 2016.

[24] M. Khurana and S. Farooq, "Integrated adsorbent-process optimization for carbon capture and concentration using vacuum swing adsorption cycles," *AIChE J.*, vol. 63, no. 7, pp. 2987–2995, 2017.

[25] S. G. Subraveti, K. N. Pai, A. K. Rajagopalan, N. S. Wilkins, A. Rajendran, A. Jayaraman, and G. Alptekin, "Cycle design and optimization of pressure swing adsorption cycles for pre-combustion CO_2 capture," *Appl. Energy*, vol. 254, p. 113 624, 2019.

[26] IPCC, "Climate change 2021: The physical science basis. Contribution of working group I to the sixth assessment report of the intergovernmental panel on climate change," 2021, Cambridge University Press, In press.

[27] IPCC, "Global warming of 1.5°C. An IPCC special report on the impacts of global warming of 1.5°C above pre-industrial levels and related global greenhouse gas emission pathways, in the context of strengthening the global response to the threat of climate change, sustainable development, and efforts to eradicate poverty," 2018.

[28] IEA, "Transforming industry through CCUS, IEA, Paris," 2019.

[29] IPCC, "IPCC special report on carbon dioxide capture and storage. Prepared by working group III of the intergovernmental panel on climate change," 2005.

[30] A. H. Farmahini, S. Krishnamurthy, D. Friedrich, S. Brandani, and L. Sarkisov, *Performance-based screening of porous materials for carbon capture*, arXiv. Preprint, 2020.

[31] IEAGHG, "The carbon capture project at Air Products' Port Arthur hydrogen production facility," 2018/05, December 2018.

[32] J. Schell, N. Casas, R. Pini, and M. Mazzotti, "Pure and binary adsorption of CO_2, H_2, and N_2 on activated carbon," *Adsorption*, vol. 18, no. 1, pp. 49–65, 2012.

[33] S. D. Dietz, G. Alptekin, and A. Jayaraman, *High capacity carbon dioxide sorbent*, US Patent 9,120,079, 2015.

[34] J. Zhang, R. Singh, and P. A. Webley, "Alkali and alkaline-earth cation exchanged chabazite zeolites for adsorption based CO_2 capture," *Microporous Mesoporous Mater.*, vol. 111, no. 1, pp. 478–487, 2008.

[35] S. Krishnamurthy, V. R. Rao, S. Guntuka, P. Sharratt, R. Haghpanah, A. Rajendran, M. Amanullah, I. A. Karimi, and S. Farooq, "CO_2 capture from dry flue gas by vacuum swing adsorption: A pilot plant study," *AIChE J.*, vol. 60, no. 5, pp. 1830–1842, 2014.

[36] P. Xiao, J. Zhang, P. Webley, G. Li, R. Singh, and R. Todd, "Capture of CO_2 from flue gas streams with zeolite 13X by vacuum-pressure swing adsorption," *Adsorption*, vol. 14, pp. 575–582, 2008.

[37] N. S. Wilkins and A. Rajendran, "Measurement of competitive CO_2 and N_2 adsorption on Zeolite 13X for post-combustion CO_2 capture," *Adsorption*, vol. 25, 115–133, 2019.

[38] N. S. Wilkins, J. Sawada, and A. Rajendran, "Measurement of competitive CO_2 and H_2O adsorption on Zeolite 13X for post-combustion CO_2 capture," *Adsorption*, vol. 26, 765–779, 2020.

[39] S. Reynolds, A. Mehrotra, A. Ebner, and J. Ritter, "Heavy reflux PSA cycles for CO_2 recovery from flue gas: Part I. Performance evaluation.," *Adsorption*, vol. 14, pp. 399–413, 2008.

[40] R. Haghpanah, R. Nilam, A. Rajendran, S. Farooq, and I. A. Karimi, "Cycle synthesis and optimization of a VSA process for postcombustion CO_2 capture," *AIChE J.*, vol. 59, no. 12, pp. 4735–4748, 2013.

[41] L. Wang, Z. Liu, P. Li, J. Yu, and A. E. Rodrigues, "Experimental and modeling investigation on post-combustion carbon dioxide capture using zeolite 13X-APG by hybrid VTSA process," *Chem. Eng. J.*, vol. 197, pp. 151–161, 2012.

[42] G. Xiao, P. Xiao, S. Lee, and P. A. Webley, "CO_2 capture at elevated temperatures by cyclic adsorption processes," *RSC Adv.*, vol. 2, no. 12, pp. 5291–5297, 2012.

[43] L. Joss, M. Gazzani, and M. Mazzotti, "Rational design of temperature swing adsorption cycles for post-combustion CO_2 capture," *Chem. Eng. Sci.*, vol. 158, pp. 381–394, 2017.

[44] M. Khurana and S. Farooq, "Simulation and optimization of a 6-step dual-reflux VSA cycle for post-combustion CO_2 capture," *Chem. Eng. Sci.*, vol. 152, pp. 507–515, 2016.

[45] K. T. Leperi, Y. G. Chung, F. You, and R. Q. Snurr, "Development of a general evaluation metric for rapid screening of adsorbent materials for postcombustion CO_2 capture," *ACS Sustain. Chem. Eng.*, vol. 7, no. 13, pp. 11 529–11 539, 2019.

[46] A. W. Dowling, S. R. R. Vetukuri, and L. T. Biegler, "Large-scale optimization strategies for pressure swing adsorption cycle synthesis," *AIChE J.*, vol. 58, no. 12, pp. 3777–3791, 2012.

[47] L. Estupiñan Perez, P. Sarkar, and A. Rajendran, "Experimental validation of multi-objective optimization techniques for design of vacuum swing adsorption processes," *Sep. Purif. Technol.*, vol. 224, pp. 553 –563, 2019.

[48] M. M. F. Hasan, R. C. Baliban, J. A. Elia, and C. A. Floudas, "Modeling, simulation, and optimization of postcombustion CO_2 capture for variable feed concentration and flow rate. 2. Pressure swing adsorption and vacuum swing adsorption processes," *Ind. Eng. Chem. Res.*, vol. 51, no. 48, pp. 15 665–15 682, 2012.

[49] N. Susarla, R. Haghpanah, I. Karimi, S. Farooq, A. Rajendran, L. S. C. Tan, and J. S. T. Lim, "Energy and cost estimates for capturing CO_2 from a dry flue gas using pressure/vacuum swing adsorption," *Chem. Eng. Res. Des.*, vol. 102, pp. 354–367, 2015.

[50] K. T. Leperi, R. Q. Snurr, and F. You, "Optimization of two-stage pressure/ vacuum swing adsorption with variable dehydration level for postcombustion carbon capture," *Ind. Eng. Chem. Res.*, vol. 55, no. 12, pp. 3338–3350, 2016.

[51] D. Danaci, M. Bui, N. Mac Dowell, and C. Petit, "Exploring the limits of adsorption-based CO_2 capture using MOFs with PVSA – from molecular design to process economics," *Mol. Syst. Des. Eng.*, vol. 5, pp. 212–231, 2020.

[52] C. Voss, "Applications of pressure swing adsorption technology," *Adsorption*, vol. 11, no. 1, pp. 527–529, 2005.

[53] A. Agarwal, L. T. Biegler, and S. E. Zitney, "A superstructure-based optimal synthesis of PSA cycles for post-combustion CO_2 capture," *AIChE J.*, vol. 56, no. 7, pp. 1813–1828, 2010.

[54] N. Sundaram, "Training neural networks for pressure swing adsorption processes," *Ind. Eng. Chem. Res.*, vol. 38, no. 11, pp. 4449–4457, 1999.

[55] J. Lewandowski, N. O. Lemcoff, and S. Palosaari, "Use of neural networks in the simulation and optimization of pressure swing adsorption processes," *Chem. Eng. Technol.*, vol. 21, no. 7, pp. 593–597, 1998.

[56] M. F. Hasan, I. Karimi, S. Farooq, A. Rajendran, and M. Amanullah, "Surrogate-based VSA process optimization for post-combustion CO_2 capture," in *21st European Symposium on Computer Aided Process Engineering*, vol. 29, 2011, pp. 402 –406.

[57] J. Beck, D. Friedrich, S. Brandani, S. Guillas, and E. S. Fraga, "Surrogate based optimisation for design of pressure swing adsorption systems," in *22nd European Symposium on Computer Aided Process Engineering*, vol. 30, 2012, pp. 1217 –1221.

[58] J. Beck, D. Friedrich, S. Brandani, and E. S. Fraga, "Multi-objective optimisation using surrogate models for the design of VPSA systems," *Comput. Chem. Eng.*, vol. 82, pp. 318–329, 2015.

[59] H. R. S. Anna, A. G. Barreto, F. W. Tavares, and M. B. de Souza, "Machine learning model and optimization of a PSA unit for methane-nitrogen separation," *Comput. Chem. Eng.*, vol. 104, pp. 377 –391, 2017.

[60] F. Boukouvala, M. M. F. Hasan, and C. A. Floudas, "Global optimization of general constrained grey-box models: New method and its application to constrained PDEs for pressure swing adsorption," *J. Global Optim.*, vol. 67, no. 1, pp. 3–42, 2017.

[61] Y. Jin, "A comprehensive survey of fitness approximation in evolutionary computation," *Soft Comput.*, vol. 9, no. 1, pp. 3–12, 2005.

[62] P. Pullumbi, F. Brandani, and S. Brandani, "Gas separation by adsorption: Technological drivers and opportunities for improvement," *Curr. Opin. Chem. Eng.*, vol. 24, pp. 131 –142, 2019.

[63] A. I. J. Forrester, A. Sobester, and A. J. Keane, *Engineering Design via Surrogate Modelling: A Practical Guide*. John Wiley & Sons, Ltd, 2008.

[64] A. I. Forrester and A. J. Keane, "Recent advances in surrogate-based optimization," *Prog. Aerosp. Sci.*, vol. 45, no. 1, pp. 50 –79, 2009.

[65] N. V. Queipo, R. T. Haftka, W. Shyy, T. Goel, R. Vaidyanathan, and P. K. Tucker, "Surrogate-based analysis and optimization," *Prog. Aerosp. Sci.*, vol. 41, no. 1, pp. 1 –28, 2005.

[66] A. T. Nguyen, S. Reiter, and P. Rigo, "A review on simulation-based optimization methods applied to building performance analysis," *Appl. Energy*, vol. 113, pp. 1043 –1058, 2014.

[67] S. Chen and S. A. Billings, "Neural networks for nonlinear dynamic system modelling and identification," *Int. J. Control*, vol. 56, no. 2, pp. 319–346, 1992.

[68] A. C. Zăvoianu, G. Bramerdorfer, E. Lughofer, S. Silber, W. Amrhein, and E. P. Klement, "Hybridization of multi-objective evolutionary algorithms and artificial neural networks for optimizing the performance of electrical drives," *Eng. Appl. Artif. Intell.*, vol. 26, no. 8, pp. 1781 –1794, 2013.

[69] K.-L. Du and M. N. S. Swamy, "Fundamentals of Machine Learning," in *Neural Networks and Statistical Learning*. London: Springer London, 2014, pp. 15–65.

[70] M. Kayri, "Predictive abilities of Bayesian regularization and Levenberg - Marquardt algorithms in artificial neural networks: A comparative empirical study on social data," *Math. Comput. Appl.*, vol. 21, no. 2, 2016.

[71] B. Li, J. Morris, and E. B. Martin, "Model selection for partial least squares regression," *Chemometr. Intell. Lab. Syst.*, vol. 64, no. 1, pp. 79 –89, 2002.

[72] Y. LeCun, Y. Bengio, and G. Hinton, "Deep learning," *Nature*, vol. 521, 436–444, 2015.

[73] S. G. Subraveti, Z. Li, V. Prasad, and A. Rajendran, "Machine learning-based multiobjective optimization of pressure swing adsorption," *Ind. Eng. Chem. Res.*, vol. 58, no. 44, pp. 20 412–20 422, 2019.

[74] K. N. Pai, V. Prasad, and A. Rajendran, "Experimentally validated machine learning frameworks for accelerated prediction of cyclic steady state and optimization of pressure swing adsorption processes," *Sep. Purif. Technol.*, vol. 241, p. 116 651, 2020.

[75] I. Lagaris, A. Likas, and D. Fotiadis, "Artificial neural networks for solving ordinary and partial differential equations," *IEEE Trans Neural Netw.*, vol. 9, no. 5, pp. 987–1000, 1998.

[76] I. Lagaris, A. Likas, and D. Papageorgiou, "Neural-network methods for boundary value problems with irregular boundaries," *IEEE Trans Neural Netw.*, vol. 11, no. 5, pp. 1041–1049, 2000.

[77] M. Raissi, P. Perdikaris, and G. Karniadakis, "Physics-informed neural networks: A deep learning framework for solving forward and inverse problems involving nonlinear partial differential equations," *J. Comput. Phys.*, vol. 378, pp. 686–707, 2019.

[78] G. Kissas, Y. Yang, E. Hwuang, W. R. Witschey, J. A. Detre, and P. Perdikaris, "Machine learning in cardiovascular flows modeling: Predicting arterial blood pressure from non-invasive 4D flow MRI data using physics-informed neural networks," *Comput. Methods Appl. Mech. Eng.*, vol. 358, p. 112 623, 2020.

[79] Q. Zhu, Z. Liu, and J. Yan, "Machine learning for metal additive manufacturing: Predicting temperature and melt pool fluid dynamics using physics-informed neural networks," *Comput Mech*, vol. 67, 619–635, 2021.

[80] X. Jin, S. Cai, H. Li, and G. E. Karniadakis, "NSFnets (Navier-Stokes flow nets): Physics-informed neural networks for the incompressible navier-stokes equations," *J. Comput. Phys.*, vol. 426, p. 109 951, 2021.

[81] A. Rajendran and M. Mazzotti, "Local equilibrium theory for the binary chromatography of species subject to a generalized langmuir isotherm. 2. Wave interactions and chromatographic cycle," *Ind. Eng. Chem. Res.*, vol. 50, no. 1, pp. 352–377, 2011.

[82] A. Felinger, A. Cavazzini, and G. Guiochon, "Numerical determination of the competitive isotherm of enantiomers," *J. Chromatogr. A*, vol. 986, no. 2, pp. 207–225, 2003.

[83] X. Glorot and Y. Bengio, "Understanding the difficulty of training deep feedforward neural networks," in *Proceedings of the Thirteenth International Conference on Artificial Intelligence and Statistics*, vol. 9, 2010, pp. 249–256.

[84] A. G. Baydin, B. A. Pearlmutter, A. A. Radul, and J. M. Siskind, *Automatic differentiation in machine learning: A survey*, 2018. arXiv: 1502.05767 [cs.SC].

[85] M. Abadi, P. Barham, J. Chen, Z. Chen, A. Davis, J. Dean, M. Devin, S. Ghemawat, G. Irving, M. Isard, M. Kudlur, J. Levenberg, R. Monga, S. Moore, D. G. Murray, B. Steiner, P. Tucker, V. Vasudevan, P. Warden, M. Wicke, Y. Yu, and X. Zheng, *Tensorflow: A system for large-scale machine learning*, 2016. arXiv: 1605.08695 [cs.DC].

[86] A. Paszke, S. Gross, S. Chintala, G. Chanan, E. Yang, Z. DeVito, Z. Lin, A. Desmaison, L. Antiga, and A. Lerer, *Automatic differentiation in pytorch*, 2017.

[87] Y. A. LeCun, L. Bottou, G. B. Orr, and K.-R. Müller, "Efficient backprop," in *Neural Networks: Tricks of the Trade: Second Edition*, G. Montavon, G. B. Orr, and K.-R. Müller, Eds. Berlin, Heidelberg: Springer Berlin Heidelberg, 2012, pp. 9–48.

[88] S. G. Subraveti, S. Roussanaly, R. Anantharaman, L. Riboldi, and A. Rajendran, "Techno-economic assessment of optimised vacuum swing adsorption for post-combustion CO_2 capture from steam-methane reformer flue gas," *Sep. Purif. Technol.*, vol. 256, p. 117 832, 2021.

[89] J. Xiao, C. Li, L. Fang, P. Böwer, M. Wark, P. Bénard, and R. Chahine, "Machine learning–based optimization for hydrogen purification performance of layered bed pressure swing adsorption," *Int. J. Energy Res.*, vol. 44, no. 6, pp. 4475–4492, 2020.

[90] L. M. C. Oliveira, H. Koivisto, I. G. Iwakiri, J. M. Loureiro, A. M. Ribeiro, and I. B. Nogueira, "Modelling of a pressure swing adsorption unit by deep learning and artificial intelligence tools," *Chem. Eng. Sci.*, vol. 224, p. 115 801, 2020.

[91] T. D. Burns, K. N. Pai, S. G. Subraveti, S. P. Collins, M. Krykunov, A. Rajendran, and T. K. Woo, "Prediction of MOF performance in vacuum swing adsorption systems for postcombustion CO_2 capture based on integrated molecular simulations, process optimizations, and machine learning models," *Environ. Sci. Technol.*, vol. 54, no. 7, pp. 4536–4544, 2020.

[92] M. Voldsund, K. Jordal, and R. Anantharaman, "Hydrogen production with CO_2 capture," *Int. J. Hydrogen Energy*, vol. 41, no. 9, pp. 4969–4992, 2016.

[93] IEA, "Technology roadmap - Hydrogen and fuel cells, IEA, Paris," 2015.

[94] J. Meerman, E. Hamborg, T. van Keulen, A. Ramírez, W. Turkenburg, and A. Faaij, "Techno-economic assessment of CO_2 capture at steam methane reforming facilities using commercially available technology," *Int. J. Greenh. Gas Control*, vol. 9, pp. 160–171, 2012.

[95] G. N. Nikolaidis, E. S. Kikkinides, and M. C. Georgiadis, "Model-based approach for the evaluation of materials and processes for post-combustion carbon dioxide capture from flue gas by PSA/VSA processes," *Ind. Eng. Chem. Res.*, vol. 55, no. 3, pp. 635–646, 2016.

[96] D. Yancy-Caballero, K. T. Leperi, B. J. Bucior, R. K. Richardson, T. Islamoglu, O. K. Farha, F. You, and R. Q. Snurr, "Process-level modelling and optimization to evaluate metal–organic frameworks for post-combustion capture of CO_2," *Mol. Syst. Des. Eng.*, vol. 5, no. 7, pp. 1205–1218, 2020.

[97] R. T. Maruyama, K. N. Pai, S. G. Subraveti, and A. Rajendran, "Improving the performance of vacuum swing adsorption based CO_2 capture under reduced recovery requirements," *Int. J. Greenh. Gas Control*, vol. 93, p. 102 902, 2020.

[98] S. Roussanaly, R. Anantharaman, K. Lindqvist, and B. Hagen, "A new approach to the identification of high-potential materials for cost-efficient membrane-based post-combustion CO_2 capture," *Sustain. Energy Fuels*, vol. 2, no. 6, pp. 1225–1243, 2018.

[99] M. T. Ho, G. W. Allinson, and D. E. Wiley, "Reducing the cost of CO_2 capture from flue gases using pressure swing adsorption," *Ind. Eng. Chem. Res.*, vol. 47, no. 14, pp. 4883–4890, 2008.

[100] S. Roussanaly, R. Anantharaman, and C. Fu, "Low-carbon footprint hydrogen production from natural gas: A techno-economic analysis of carbon capture and storage from steam-methane reforming," *Chem. Eng. Trans.*, vol. 81, pp. 1015–1020, 2020.

[101] A. H. Farmahini, S. Krishnamurthy, D. Friedrich, S. Brandani, and L. Sarkisov, "From crystal to adsorption column: Challenges in multiscale computational screening of materials for adsorption separation processes," *Ind. Eng. Chem. Res.*, vol. 57, no. 45, pp. 15 491–15 511, 2018.

[102] A. H. Farmahini, D. Friedrich, S. Brandani, and L. Sarkisov, "Exploring new sources of efficiency in process-driven materials screening for post-combustion carbon capture," *Energy Environ. Sci.*, vol. 13, no. 3, pp. 1018–1037, 2020.

[103] S. Xiang, Y. He, Z. Zhang, H. Wu, W. Zhou, R. Krishna, and B. Chen, "Microporous metal-organic framework with potential for carbon dioxide capture at ambient conditions," *Nat. Commun.*, vol. 3, p. 954, 2012.

[104] V. I. Agueda, J. A. Delgado, M. A. Uguina, P. Brea, A. I. Spjelkavik, R. Blom, and C. Grande, "Adsorption and diffusion of H_2, N_2, CO, CH_4 and CO_2 in UTSA-16 metal-organic framework extrudates," *Chem. Eng. Sci.*, vol. 124, pp. 159–169, 2015.

[105] S. Nandi, S. Collins, D. Chakraborty, D. Banerjee, P. K. Thallapally, T. K. Woo, and R. Vaidhyanathan, "Ultralow parasitic energy for postcombustion CO_2 capture realized in a nickel isonicotinate metal–organic framework with excellent moisture stability," *J. Am. Chem. Soc.*, vol. 139, no. 5, pp. 1734–1737, 2017.

[106] H. Jiang, A. D. Ebner, and J. A. Ritter, "Importance of incorporating a vacuum pump performance curve in dynamic adsorption process simulation," *Ind. Eng. Chem. Res*, vol. 59, no. 2, pp. 856–873, 2020.

[107] S. Roussanaly, R. Anantharaman, K. Lindqvist, H. Zhai, and E. Rubin, "Membrane properties required for post-combustion CO_2 capture at coal-fired power plants," *J. Membr. Sci.*, vol. 511, pp. 250–264, 2016.

[108] M. Haaf, R. Anantharaman, S. Roussanaly, J. Ströhle, and B. Epple, "CO_2 capture from waste-to-energy plants: Techno-economic assessment of novel integration concepts of calcium looping technology," *Resour. Conserv. Recycl.*, vol. 162, p. 104 973, 2020.

[109] NETL, "Quality guidelines for energy system studies: Cost estimation methodology for NETL assessments of power plant performance," 2011.

[110] R. Anantharaman, O. Bolland, N. Booth, E. van Dorst, C. Ekstrom, F. Franco, E. Macchi, G. Manzolini, D. Nikolic, A. Pfeffer, M. Prins, S. Rezvani, and L. Robinson, "D1.4.3 European best practice guidelines for assessment of CO_2 capture technologies (DECARBit project)," 2011. [Online]. Available: https://www.sintef.no/globalassets/project/decarbit/d-1-4-3_euro_bp_guid_for_ass_co2_cap_tech_280211.pdf.

[111] U.S. Geological Survey, "Cobalt & nickel statistics, in Kelly, T.D., and Matos, G.R., and comps., Historical statistics for mineral and material commodities in the United States (2013 version): U.S. Geological Survey Data Series," 140, 2015. Accessed June 26, 2020.

[112] J Stöcker, M Whysall, and G Miller, "30 years of PSA technology for hydrogen purification," UOP LLC, Des Plaines, IL, USA, 1998.

[113] S. O. Gardarsdottir, E. De Lena, M. Romano, S. Roussanaly, M. Voldsund, J.-F. Pérez-Calvo, D. Berstad, C. Fu, R. Anantharaman, D. Sutter, M. Gazzani, M. Mazzotti, and G. Cinti, "Comparison of technologies for CO_2 capture from cement production—Part 2: Cost analysis," *Energies*, vol. 12, no. 3, p. 542, 2019.

[114] S. Roussanaly, "Calculating CO_2 avoidance costs of carbon capture and storage from industry," *Carbon Manage.*, vol. 10, no. 1, pp. 105–112, 2019.

[115] A. K. Rajagopalan and A. Rajendran, "The effect of nitrogen adsorption on vacuum swing adsorption based post-combustion CO_2 capture," *Int. J. Greenh. Gas Control*, vol. 78, pp. 437–447, 2018.

[116] C. Fu, D. Kim, S. Roussanaly, S. Gardarsdottir, and R. Anantharaman, "Post-combustion CO_2 capture using MEA – Benchmarking performance and insights for a wide range of industrially relevant scenarios," *Submitted to Energies*, 2021.

[117] L.-C. Lin, A. H. Berger, R. L. Martin, J. Kim, J. A. Swisher, K. Jariwala, C. H. Rycroft, A. S. Bhown, M. W. Deem, M. Haranczyk, and B. Smit, "In silico screening of carbon-capture materials," *Nat. Mater.*, vol. 11, 633–641, 2012.

[118] C. E. Wilmer, O. K. Farha, Y.-S. Bae, J. T. Hupp, and R. Q. Snurr, "Structure–property relationships of porous materials for carbon dioxide separation and capture," *Energy Environ. Sci.*, vol. 5, no. 12, pp. 9849–9856, 2012.

[119] J. M. Huck, L.-C. Lin, A. H. Berger, M. N. Shahrak, R. L. Martin, A. S. Bhown, M. Haranczyk, K. Reuter, and B. Smit, "Evaluating different classes of porous materials for carbon capture," *Energy Environ. Sci.*, vol. 7, no. 12, pp. 4132–4146, 2014.

[120] M. Khurana and S. Farooq, "Adsorbent screening for postcombustion CO_2 capture: A method relating equilibrium isotherm characteristics to an optimum vacuum swing adsorption process performance," *Ind. Eng. Chem. Res.*, vol. 55, no. 8, pp. 2447–2460, 2016.

[121] J. Park, R. P. Lively, and D. S. Sholl, "Establishing upper bounds on CO_2 swing capacity in sub-ambient pressure swing adsorption via molecular simulation of metal–organic frameworks," *J. Mater. Chem. A*, vol. 5, no. 24, pp. 12 258–12 265, 2017.

[122] V. Subramanian Balashankar and A. Rajendran, "Process optimization-based screening of zeolites for post-combustion CO_2 capture by vacuum swing adsorption," *ACS Sustain. Chem. Eng.*, vol. 7, no. 21, pp. 17 747–17 755, 2019.

[123] J. Park, H. O. Rubiera Landa, Y. Kawajiri, M. J. Realff, R. P. Lively, and D. S. Sholl, "How well do approximate models of adsorption-based CO_2 capture processes predict results of detailed process models?" *Ind. Eng. Chem. Res.*, vol. 59, no. 15, pp. 7097–7108, 2020.

[124] B. J. Maring and P. A. Webley, "A new simplified pressure/vacuum swing adsorption model for rapid adsorbent screening for CO_2 capture applications," *Int. J. Greenh. Gas Control*, vol. 15, pp. 16 –31, 2013.

[125] K. N. Pai, V. Prasad, and A. Rajendran, "Practically achievable process performance limits for pressure-vacuum swing adsorption-based post-combustion CO_2 capture," *ACS Sustain. Chem. Eng.*, vol. 9, no. 10, pp. 3838–3849, 2021.

[126] J. A. Ritter, S. J. Bhadra, and A. D. Ebner, "On the use of the dual-process langmuir model for correlating unary equilibria and predicting mixed-gas adsorption equilibria," *Langmuir*, vol. 27, no. 8, pp. 4700–4712, 2011.

[127] S. Roussanaly, E. S. Rubin, M. van der Spek, G. Booras, N. Berghout, T. Fout, M. Garcia, S. Gardarsdottir, V. N. Kuncheekanna, M. Matuszewski, S. McCoy, J. Morgan, S. M. Nazir, and A. Ramirez, *Towards improved guidelines for cost evaluation of carbon capture and storage*, version 1.1, Mar. 2021. DOI: 10.5281/zenodo.4646284. [Online]. Available: https://doi.org/10.5281/zenodo.4646284.

[128] D. Danaci, P. A. Webley, and C. Petit, "Guidelines for techno-economic analysis of adsorption processes," *Front. Chem. Eng.*, vol. 2, p. 30, 2021.

[129] M. Voldsund, S. O. Gardarsdottir, E. De Lena, J.-F. Pérez-Calvo, A. Jamali, D. Berstad, C. Fu, M. Romano, S. Roussanaly, R. Anantharaman, H. Hoppe, D. Sutter, M. Mazzotti, M. Gazzani, G. Cinti, and K. Jordal, "Comparison of technologies for CO_2 capture from cement production—Part 1: Technical evaluation," *Energies*, vol. 12, p. 559, 2019.

[130] S. Roussanaly, N. Berghout, T. Fout, M. Garcia, S. Gardarsdottir, S. M. Nazir, A. Ramirez, and E. S. Rubin, "Towards improved cost evaluation of carbon capture and storage from industry," *Int. J. Greenh. Gas Control*, vol. 106, p. 103 263, 2021.

[131] J. Jakobsen, S. Roussanaly, and R. Anantharaman, "A techno-economic case study of CO_2 capture, transport and storage chain from a cement plant in Norway," *J. Clean. Prod.*, vol. 144, pp. 523–539, 2017.

[132] A. Wright, Personal Communication, Dec. 20, 2020.

[133] A. Wright, *Integrating oxyfuel CO_2 purification technologies with a post-combustion capture adsorption unit*, Mar. 2017.

[134] M. Paliwal and U. A. Kumar, "Neural networks and statistical techniques: A review of applications," *Expert Syst. Appl.*, vol. 36, no. 1, pp. 2 –17, 2009.

[135] D. M. Himmelblau, "Accounts of experiences in the application of artificial neural networks in chemical engineering," *Ind. Eng. Chem. Res.*, vol. 47, no. 16, pp. 5782–5796, 2008.

[136] D. Marquardt, "An algorithm for least-squares estimation of nonlinear parameters," *SIAM J. Appl. Math.*, vol. 11, no. 2, pp. 431–441, 1963.

[137] M. T. Hagan and M. B. Menhaj, "Training feedforward networks with the Marquardt algorithm," *IEEE Trans. Neural Networks*, vol. 5, no. 6, pp. 989–993, 1994.

[138] F. Dan Foresee and M. T. Hagan, "Gauss-newton approximation to Bayesian learning," in *Proceedings of International Conference on Neural Networks (ICNN'97)*, vol. 3, 1997, pp. 1930–1935.

[139] D. J. C. MacKay, "Bayesian interpolation," *Neural Comput.*, vol. 4, no. 3, pp. 415–447, 1992.

[140] S. Wold, M. Sjöström, and L. Eriksson, "PLS-regression: A basic tool of chemometrics," *Chemometr. Intell. Lab. Syst.*, vol. 58, no. 2, pp. 109 –130, 2001.

[141] H. Deng, S. Roussanaly, and G. Skaugen, "Techno-economic analyses of CO_2 liquefaction: Impact of product pressure and impurities," *Int. J. of Refrig.*, vol. 103, pp. 301–315, 2019.

[142] E Lemmon, M Huber, and M McLinden, "NIST standard reference database 23: Reference fluid thermodynamic and transport properties-REFPROP, Version 9.1," 2013.

[143] S Roussanaly, A. L. Brunsvold, and E. S. Hognes, "Benchmarking of CO_2 transport technologies: Part II – Offshore pipeline and shipping to an offshore site," *Int. J. Greenh. Gas Control*, vol. 28, pp. 283–299, 2014.

[144] S Roussanaly, A. A. Grimstad, and E. S. Hognes, "The economic value of CO_2 for EOR applications," *Energy Procedia*, vol. 63, pp. 7836–7843, 2014.

[145] G. Skaugen, S. Roussanaly, J. Jakobsen, and A. Brunsvold, "Techno-economic evaluation of the effects of impurities on conditioning and transport of CO_2 by pipeline," *Int. J. Greenh. Gas Control*, vol. 54, pp. 627–639, 2016.

[146] M. Knoope, W. Guijt, A. Ramírez, and A. Faaij, "Improved cost models for optimizing CO_2 pipeline configuration for point-to-point pipelines and simple networks," *Int. J. Greenh. Gas Control*, vol. 22, pp. 25–46, 2014.

[147] E. T. P. for Zero Emission Fossil Fuel Power Plants (ZEP)", "The costs of CO_2 storage, post-demonstration CCS in the EU, Brussels, Belgium," 2011.

[148] C. T. Choi and H. Wen-Chung, "Incorporation of a valve equation into the simulation of a pressure swing adsorption process," *Chem. Eng. Sci.*, vol. 49, pp. 75–84, 1994.

Appendix A: Modelling of cyclic adsorption processes

A one-dimensional mathematical model is used to describe adsorption column dynamics in cyclic adsorption processes. The following general assumptions are incorporated into the model:

1. Axially dispersed plug flow model to describe the bulk gas phase.
2. The gas-phase behaves ideally.
3. No radial gradients exist for composition, pressure and temperature across the column.
4. The mass transfer resistance is mainly due to macropore diffusion and described by the linear driving force (LDF) model
5. Instantaneous thermal equilibrium between the gas and the solid phases.
6. Bed properties along the column remain uniform.
7. Pressure drop calculations are based on Ergun's equation for long columns (>1 m) and Darcy's law for shorter columns ($\leq$1 m).

A.1 Model equations

Based on the above assumptions, the following system of coupled nonlinear PDEs based on the conservation of mass, momentum, and energy can be derived:

Component mass balance:

$$\frac{\partial y_i}{\partial t} + \frac{y_i}{T}\frac{\partial P}{\partial t} - \frac{y_i}{P}\frac{\partial T}{\partial t} = \frac{T}{P} D_{\mathrm{L}} \frac{\partial}{\partial z}\left(\frac{P}{T}\frac{\partial y_i}{\partial z}\right) - \frac{T}{P}\frac{\partial}{\partial z}\left(\frac{y_i P}{T} v\right) - \frac{RT}{P}\frac{1-\varepsilon}{\varepsilon}\frac{\partial q_i}{\partial t} \tag{A.1}$$

Total mass balance:

$$\frac{1}{P}\frac{\partial P}{\partial t} - \frac{1}{T}\frac{\partial T}{\partial t} = -\frac{T}{P}\frac{\partial}{\partial z}\left(\frac{P}{T} v\right) - \frac{RT}{P}\frac{1-\varepsilon}{\varepsilon}\sum_{i=1}^{n_{\mathrm{comp}}}\frac{\partial q_i}{\partial t} \tag{A.2}$$

Column energy balance:

$$\begin{aligned}\left[\frac{1-\varepsilon}{\varepsilon}\left(\rho_{\mathrm{s}} C_{\mathrm{p,s}} + C_{\mathrm{p,a}}\sum_{i=1}^{n_{\mathrm{comp}}} q_{\mathrm{i}}\right)\right]\frac{\partial T}{\partial t} &= \frac{K_{\mathrm{z}}}{\varepsilon}\frac{\partial^2 T}{\partial z^2} - \frac{C_{\mathrm{p,g}}}{R}\frac{\partial P}{\partial t} - \frac{C_{\mathrm{p,g}}}{R}\frac{\partial}{\partial z}(vP) \\ &\quad - \frac{1-\varepsilon}{\varepsilon} C_{\mathrm{p,a}} T \sum_{i=1}^{n_{\mathrm{comp}}}\frac{\partial q_{\mathrm{i}}}{\partial t} + \frac{1-\varepsilon}{\varepsilon}\sum_{i=1}^{n_{\mathrm{comp}}}\left(\Big(-\Delta H\Big)\frac{\partial q_{\mathrm{i}}}{\partial t}\right)\end{aligned} \tag{A.3}$$

Pressure drop (Ergun's equation):

$$-\frac{\partial P}{\partial z} = \frac{150}{4}\frac{1}{r_{\mathrm{p}}^2}\Big(\frac{1-\varepsilon}{\varepsilon}\Big)^2 \mu v + \frac{1.75}{2}\frac{1}{r_{\mathrm{p}}}\Big(\frac{1-\varepsilon}{\varepsilon}\Big)\rho|v|v \tag{A.4}$$

Linear driving force model:

$$\frac{\partial q_i}{\partial t} = k_i(q_i^* - q_i) \tag{A.5}$$

Mass transfer coefficient (macropore controlled):

$$k_i = \frac{c_i}{q_i^*}\frac{15\varepsilon_{\mathrm{p}} D_{\mathrm{p}}}{r_{\mathrm{p}}^2} \tag{A.6}$$

Adsorption equilibria (generalized form):

$$q_i^* = f(c_i, T) \tag{A.7}$$

Ideal gas law:

$$c_i = \frac{y_i P}{RT} \tag{A.8}$$

A.2 Initial and boundary conditions

For simulating cyclic adsorption processes, the above mentioned system of PDEs and algebraic equations are solved together with appropriate initial and boundary conditions. For initializing the cycle simulations, it is convenient to assume that the bed of

the first step is equilibrated with feed mixture at specified temperature and pressure. Subsequently, the final condition of one step will be the initial condition of the subsequent step. The boundary conditions in cyclic adsorption process can be generalized based on the position of the valves at two ends of the adsorbent bed as: open-open, open-closed, and closed-open.

Open-open. Here both valves are open and represent a constituent step in which an inlet stream is conveyed through the column and an outlet stream exiting from the other column end. Dankwert's boundary conditions for a dispersed plug flow system apply to component mass and energy balances. For the total mass balance, the flow rate (in terms of velocity) at the inlet and the exit pressure at the outlet are controlled. The boundary conditions can be written as,

$$D_{\mathrm{L}} \frac{\partial y_i}{\partial z} \bigg|_{z=0} = -v \mid_{z=0} \left(y_{\mathrm{in}} - y_i \mid_{z=0} \right) \tag{A.9}$$

$$\frac{\partial y_{\mathrm{i}}}{\partial z} \bigg|_{z=L} = 0 \tag{A.10}$$

$$K_z \frac{\partial T}{\partial z} \bigg|_{z=0} = -\varepsilon \rho_{\mathrm{g}} C_{\mathrm{p,g}} v \mid_{z=0} \left(T_{\mathrm{in}} - T \mid_{z=0} \right) \tag{A.11}$$

$$\frac{\partial T}{\partial z} \bigg|_{z=L} = 0 \tag{A.12}$$

$$v \mid_{z=0} = v_{\mathrm{in}} \tag{A.13}$$

$$P \mid_{z=L} = P_{\mathrm{out}} \tag{A.14}$$

Open-closed. Here the column inlet is open and the column outlet is closed. Equations A.9-A.12 remain valid. Depending on the constituent step, $v \mid_{z=0}$ can be calculated based on either Eq. A.13 or change in pressure at the column inlet. Equation A.14 changes to:

$$\frac{\partial P}{\partial z} \bigg|_{z=L} = 0 \tag{A.15}$$

Closed-open. Here the column inlet is closed and the column outlet is open. Equations A.10, A.12 remain valid while Eqs. A.9, A.11, A.13 reduce to:

$$\left.\frac{\partial y_i}{\partial z}\right|_{z=0} = 0 \tag{A.16}$$

$$\left.\frac{\partial T}{\partial z}\right|_{z=0} = 0 \tag{A.17}$$

$$v\,\big|_{z=0} = 0 \tag{A.18}$$

Depending on the dynamics of the constituent step at the column outlet, the boundary condition for the total mass balance can be implemented either in terms of pressure profile or constant velocity, i.e.,

$$P\,\big|_{z=L} = P(t) \quad \text{or,}$$

$$v\,\big|_{z=L} = v_{\text{out}} \tag{A.19}$$

Appendix B: Supplementary material for Chapter 2

B.1 Adsorption equilibria

The Sips isotherm model used to describe the adsorption equilibria of CO_2 and H_2 on activated carbon is given by

$$q_i^* = \frac{q_{\text{sat},i} \left(k_i p_i\right)^{s_i}}{1 + \left(k_i p_i\right)^{s_i}} \tag{B.1}$$

where $q_{\text{sat,i}}$ is the temperature dependent saturation solid phase concentration, k_i is the adsorption equilibrium constant, s_i is a parameter which can take values between 0 and 1 and, p_i is the partial pressure of component i. The quantities $q_{\text{sat,i}}$, k_i and p_i are defined as follows:

$$q_{\text{sat},i} = \omega_i e^{-\frac{\psi_i}{RT}} \tag{B.2}$$

$$k_i = \theta_i e^{-\frac{\phi_i}{RT}} \tag{B.3}$$

$$s_i = s_{1,i} \arctan(s_{2,i}(T - T_{\text{ref}})) + s_{\text{ref},i} \tag{B.4}$$

The parameters used for CO_2 were obtained from previous publication [25] and are as follows: ω_{CO_2}=3.74 mol kg^{-1}; ψ_{CO_2}=-7.87 kJ mol^{-1}; θ_{CO_2} =26.9 $\times$ 10^{-9} Pa^{-1}; ϕ_{CO_2}=-2.05 kJ mol^{-1}; s_{1,CO_2}=0.136; s_{2,CO_2}=0.110; s_{ref,CO_2}=0.760 and; T_{ref,CO_2}=281 K. The H_2 parameters used were obtained from literature [32] and are: ω_{H_2}=6.66 mol kg^{-1}; ψ_{H_2}=0.0 kJ mol^{-1}; θ_{H_2} =0.7 $\times$ 10^{-9} Pa^{-1}; ϕ_{H_2}=-9.83 kJ mol^{-1}; s_{1,H_2}=0; s_{2,H_2}=0; s_{ref,H_2}=0.956 and; T_{ref,H_2}=273 K. The extended Sips isotherm model used to predict the multi-component

behavior is as follows:

$$q_i^* = \frac{q_{\text{sat},i}\,(k_i p_i)^{s_i}}{1 + \sum_{i=1}^{n_{\text{comp}}} (k_i p_i)^{s_i}} \tag{B.5}$$

where n_{comp} is the total number of components in the multi-component system.

B.2 Artificial neural networks

Feed-forward neural networks (as shown in Fig. B.1) were used as ANN models owing to their applicability to a variety of problems [134, 135]. The network architecture illustrated in Fig. B.1 consists of one input layer, one hidden layer and one output layer. A distinct neural network was developed for each output, and the mathematical representation can be written as

$$\hat{u} = f(\bar{x}) = f_2\left(\sum_{k=1}^{n} w_k^{(2)} f_1\left(\sum_{j=1}^{p} w_{kj}^{(1)} x_j + \theta_j\right) + \phi + \epsilon\right) \tag{B.6}$$

where f_1 is an activation function of the hidden layer; f_2 is an activation function of the output layer; $w_k^{(2)}$ is the weight parameter between neuron k in the hidden layer and the output neuron; θ corresponds to the bias in the hidden layer; ϕ is the bias of the output neuron and ϵ is a random error with zero mean. In this work, the activation function of the hidden layer was a tan-sigmoid transfer function:

$$f_1(x) = \frac{(e^x - e^{-x})}{(e^x + e^{-x})} \tag{B.7}$$

A linear transfer function was considered as the activation function of the output layer:

$$f_2(x) = x \tag{B.8}$$

The weights and bias in Eq. B.6 were determined during the neural network training process. In the training process, the networks were modified using supervised learning algorithms by adjusting the weights and bias based on the inputs presented to the network along with the output so that the network attempts to produce the desired

output. Conventional ANN training methods such as back-propagation of errors involve providing a set of input-output data to the network and minimizing the mean squared error (MSE) between the predicted and actual outputs of the network using first-order or second-order optimization methods. However, this procedure often leads to issues of overfitting the ANN model [69]. To overcome this, Bayesian regularization was applied to the training data to minimize the model errors and avoid overfitting problems.

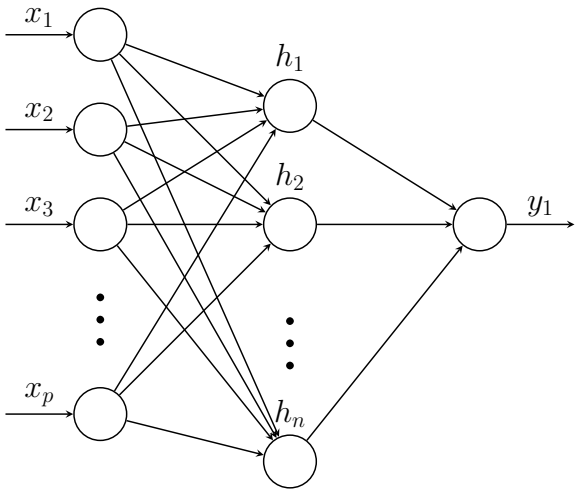

Figure B.1: Neural network architecture

B.3 Bayesian regularization

In this analysis, Bayesian regularization was implemented using the Levenberg-Marquardt algorithm [136, 137], a second-order optimization method, for minimizing both errors and weights. To improve the generalization ability, the performance function is modified by adding a term E_{w} that consists of a MSE of the network weights as shown below:

$$F = \beta E_{\mathrm{D}} + \alpha E_{\mathrm{w}} \tag{B.9}$$

where α and β are hyperparameters or regularization parameters [138]. The network error, E_{D}, is the MSE and can be expressed as follows:

$$E_{\mathrm{D}} = \frac{1}{M_{\mathrm{Samples}}} \sum_{k=1}^{M_{\mathrm{Samples}}} \left(\hat{y}_{k,\,\mathrm{ANN}} - y_{k,\,\mathrm{DM}} \right)^2 \tag{B.10}$$

where M_{Samples} is the number of samples; $\hat{y}_{k,\,\mathrm{ANN}}$ is the predicted value of the ANN model and $y_{k,\,\mathrm{DM}}$ is the actual value from the detailed PSA model. The MSE of network weights, E_{w}, is given by

$$E_{\mathrm{w}} = \frac{1}{m} \sum_{i=1}^{m} w_i^2 \tag{B.11}$$

In the Bayesian learning framework, the optimal weights and performance function parameters α, β are obtained in the training process [139]. For detailed discussions on BR, the readers are referred to elsewhere in the literature [138, 139]. The learning-validation procedure was repeated for 50 times until the lowest performance function, F, was achieved.

B.4 Partial least squares

The theory of partial least squares (PLS) regression is well documented in the literature [140]. In this section, a brief overview of the technique is provided. PLS is a multivariate linear regression technique that aims to describe the relationship between the input and output variables by projecting them onto a new space of latent variables that are linear combinations of the original variables. The latent variables (or principal components) are extracted from the standardized data sets containing the original variables $x_{\mathbf{s}} \in \Re^{N \times P}$ and $y_{\mathbf{s}} \in \Re^{N \times M}$ through singular value decomposition [140] of the respective data matrices as shown below:

$$x_{\mathbf{s}} = tp' + e_x \tag{B.12}$$

$$y_{\mathbf{s}} = sq' + e_y \tag{B.13}$$

where t=[t_1,t_2,..t_d] $\in \Re^{N \times d}$ and s=[s_1,s_2,..s_d] $\in \Re^{N \times d}$ are the scores (or latent variables) of $x_{\mathbf{s}}$ and $y_{\mathbf{s}}$, respectively, p=[p_1,p_2,..p_d] $\in \Re^{P \times d}$ and q=[q_1,q_2,..q_d] $\in \Re^{M \times d}$ are the load-

ings for $x_{\mathbf{s}}$ and $y_{\mathbf{s}}$, respectively, e_x and e_y are the model residuals of $x_{\mathbf{s}}$ and $y_{\mathbf{s}}$, respectively, and d is the number of latent variables. Scores, which are also known as PLS components, form a set of uncorrelated variables orthogonal to each other. The latent representation allows the PLS model to explain most of the variability of both input and output variables using fewer latent variables.

Finally, the PLS model can be expressed in compact form as

$$y_{\mathbf{s}} = x_{\mathbf{s}} b_{\mathrm{PLS}} + R \tag{B.14}$$

where b_{PLS} is the PLS regression coefficient matrix relating to $x_{\mathbf{s}}$ and $y_{\mathbf{s}}$. The key idea behind obtaining PLS regression coefficients involves maximization of the covariance between the score vectors t and s subject to: $\|w\|$=1 and $\|c\|$=1, where w and c are the input and output weights, respectively.

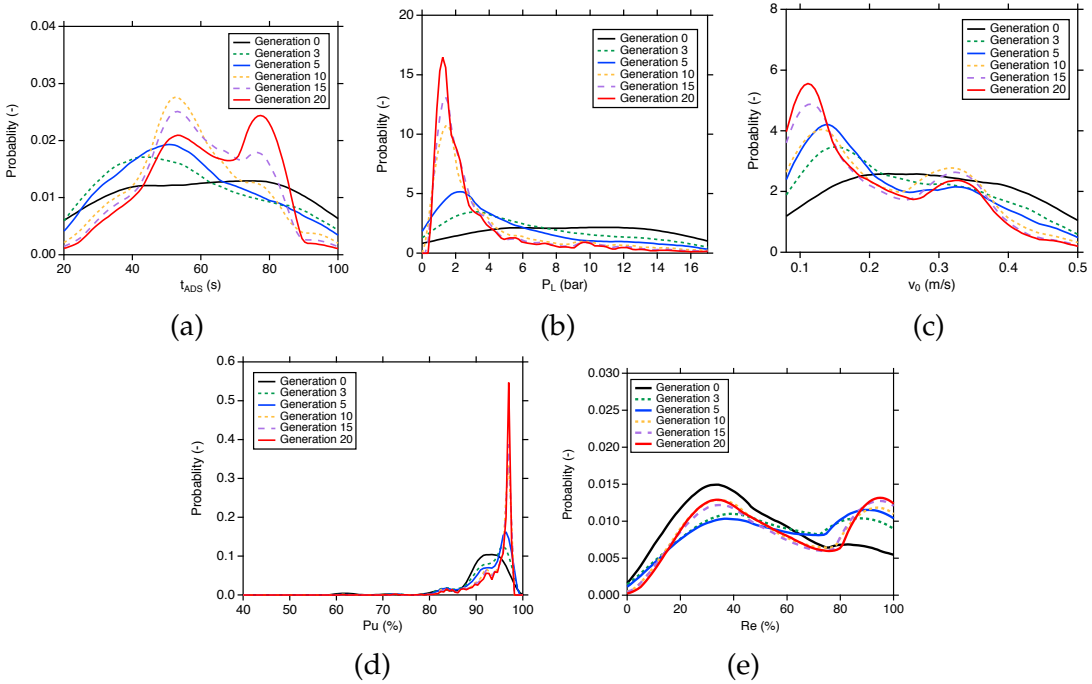

Figure B.2: Probability distributions of (a) adsorption time (t_{ADS}), (b) low pressure (P_{L}), (c) feed velocity (v_0), (d) purity (Pu) and, (e) recovery (Re) for different number of generations i. Note: All individuals after generation i from *TradOpt* implementation were used to plot the probability distributions. The distributions are obtained using kernel density estimation.

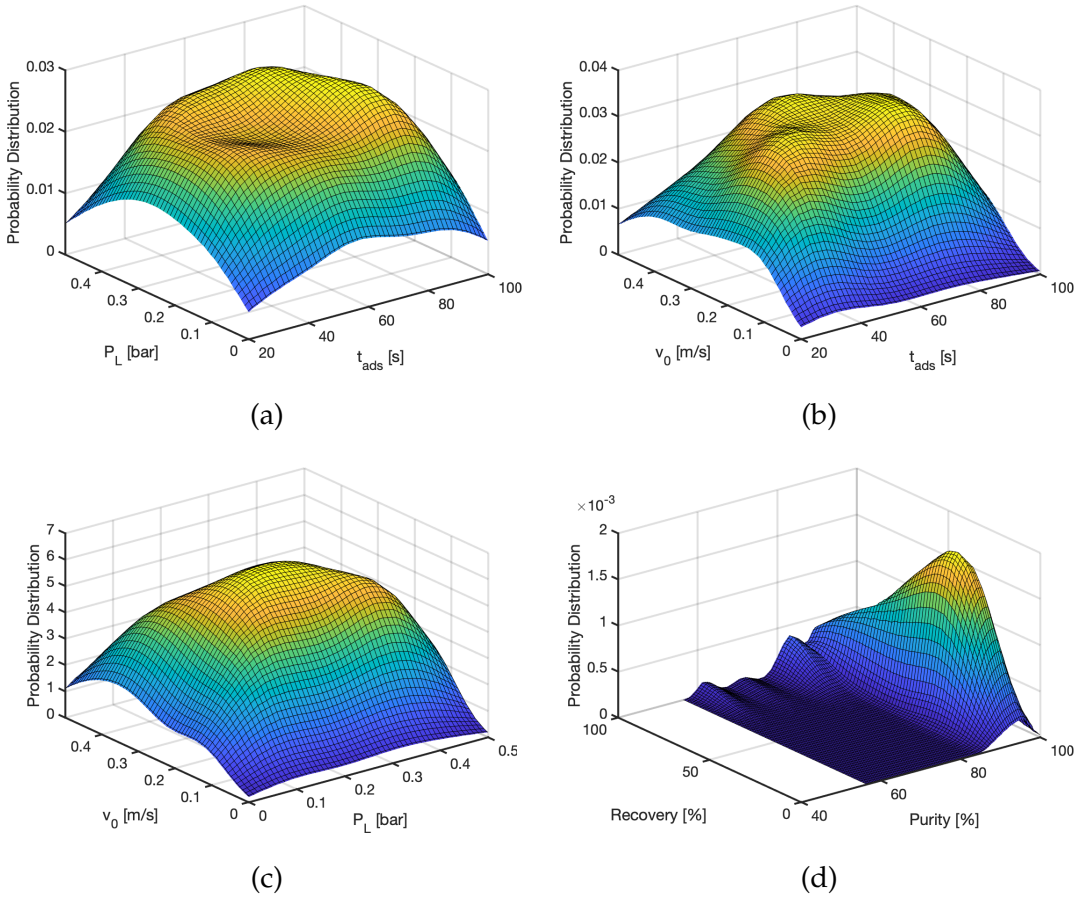

Figure B.3: Bivariate distribution plots of key input and output variables in the initial population of *TradOpt*. The distributions are obtained using kernel density estimation.

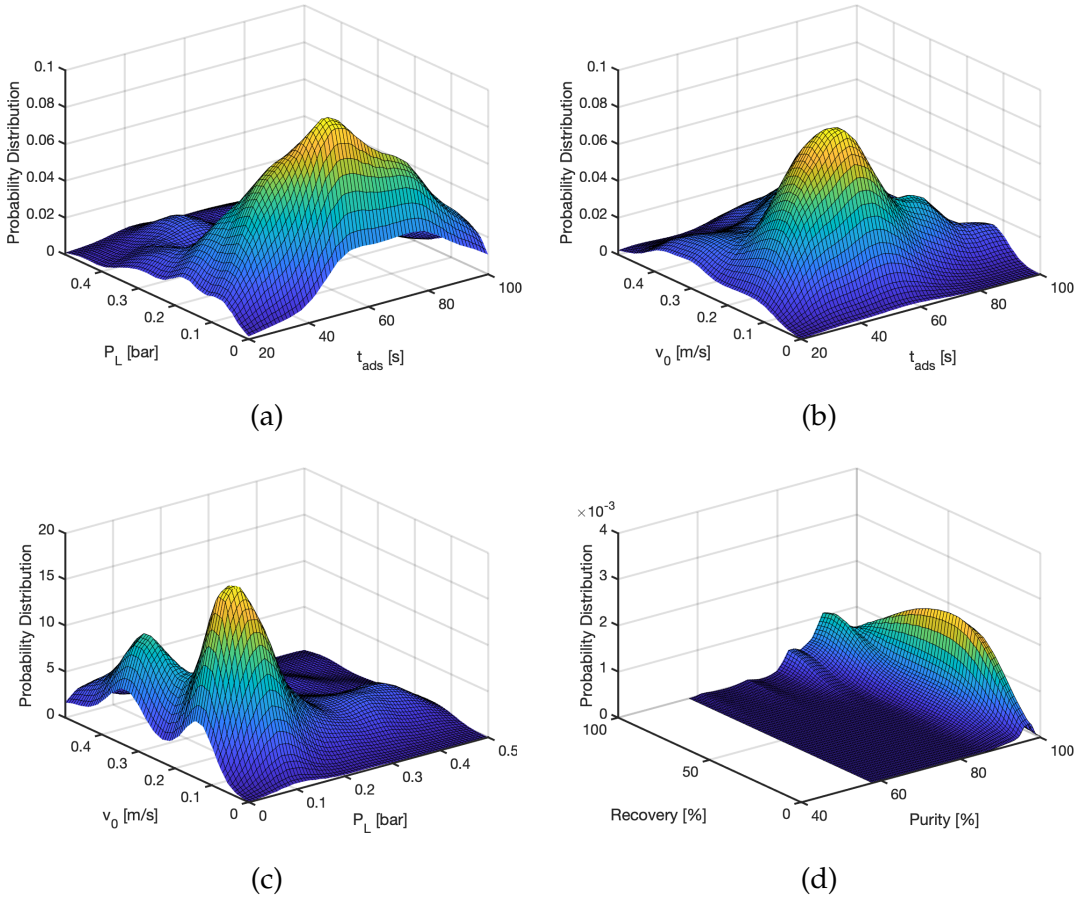

Figure B.4: Bivariate distribution plots of key input and output variables at the end of generation 5 in *TradOpt*. The distributions are obtained using kernel density estimation.

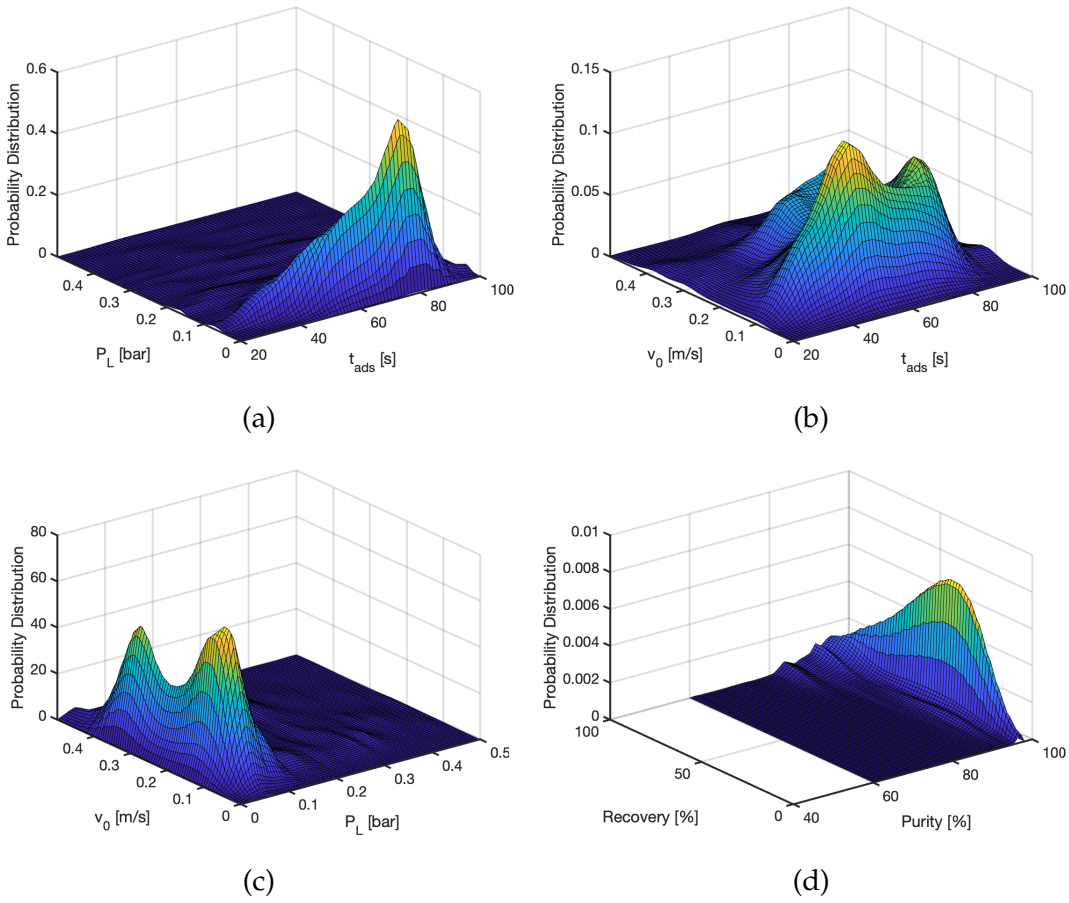

Figure B.5: Bivariate distribution plots of key input and output variables at the end of generation 20 in *TradOpt*. The distributions are obtained using kernel density estimation.

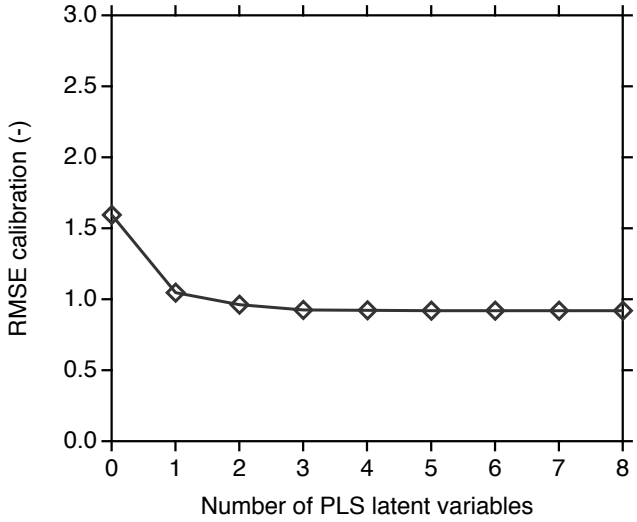

Figure B.6: RMSE of the PLS calibration model as a function of the number of latent variables.

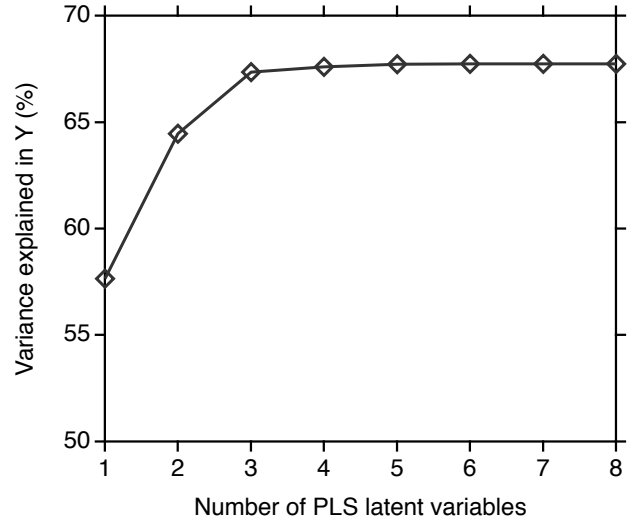

Figure B.7: Cumulative contribution of each latent variable to the percentage variance of Y that is explained.

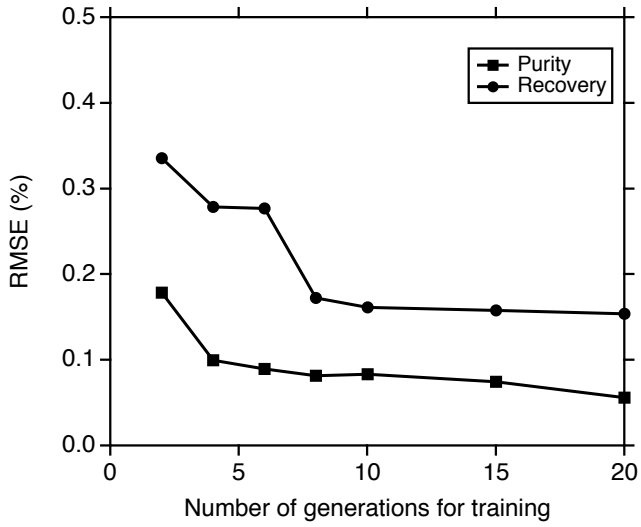

Figure B.8: RMSE of purity and recovery as a function of the number of generations for determining an adequate value of N in *DR-SOpt*.

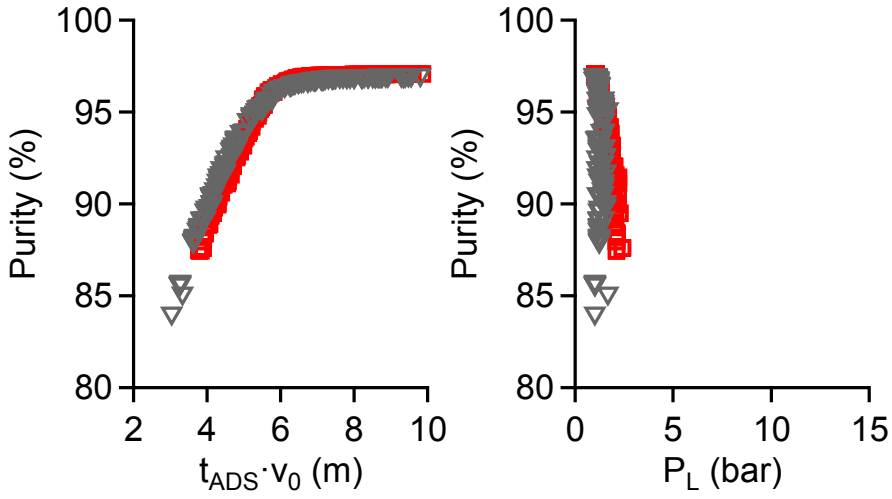

Figure B.9: Comparison of optimal decision variables obtained using *DR-SOpt* (inverted triangles) and *TradOpt* (squares).

Table B.1: Selected optimal solutions obtained for *TradOpt*.

t_{ADS} [s]	t_{PREQ1} [s]	t_{PREQ2} [s]	t_{CnBLO} [s]	t_{PUR} [s]	P_{L} [bar]	v_0 [m s^{-1}]	v_{PUR} [m s^{-1}]	Pu [%]	Re [%]
45.5	67.8	91.5	73.8	45.9	2.2	0.09	0.2	90.4	99.8
40.7	67.4	87.6	69.0	49.9	2.1	0.10	0.1	88.4	99.9
60.3	69.8	103.9	88.2	33.6	1.6	0.09	0.4	94.8	98.6
50.0	69.0	94.9	78.5	42.3	1.8	0.09	0.3	91.9	99.7
42.1	67.5	88.7	70.2	48.8	2.0	0.10	0.1	88.9	99.9
70.5	74.3	112.8	102.4	24.7	1.2	0.09	0.6	96.5	93.7
71.4	72.3	112.9	100.9	24.1	1.3	0.08	0.4	96.5	93.8
62.7	81.0	106.6	100.2	31.1	1.2	0.09	0.5	95.7	97.7
65.1	77.9	108.4	100.3	29.4	1.2	0.09	1.0	96.4	94.6
61.6	70.4	105.0	90.6	32.3	1.5	0.09	0.4	95.2	98.3
70.2	74.9	112.5	101.8	25.0	1.2	0.09	0.5	96.5	93.8
70.2	74.9	112.5	101.8	25.0	1.2	0.09	0.5	96.5	93.8
64.0	80.0	107.6	100.7	29.9	1.1	0.09	0.5	96.1	96.6
64.0	80.0	107.6	100.7	29.9	1.1	0.09	0.5	96.1	96.6
70.5	75.3	112.8	102.4	24.7	1.2	0.09	0.6	96.5	93.7
81.0	74.7	121.7	111.3	15.9	1.0	0.10	0.7	97.1	69.2
79.5	73.2	120.1	109.2	17.2	1.1	0.08	0.7	96.9	88.8
81.5	73.4	121.8	111.1	15.6	1.0	0.08	0.7	96.9	87.7
80.9	75.2	122.0	111.2	15.8	1.0	0.11	0.8	97.1	65.7
81.0	74.2	121.5	111.2	15.8	1.0	0.10	0.7	97.1	69.2

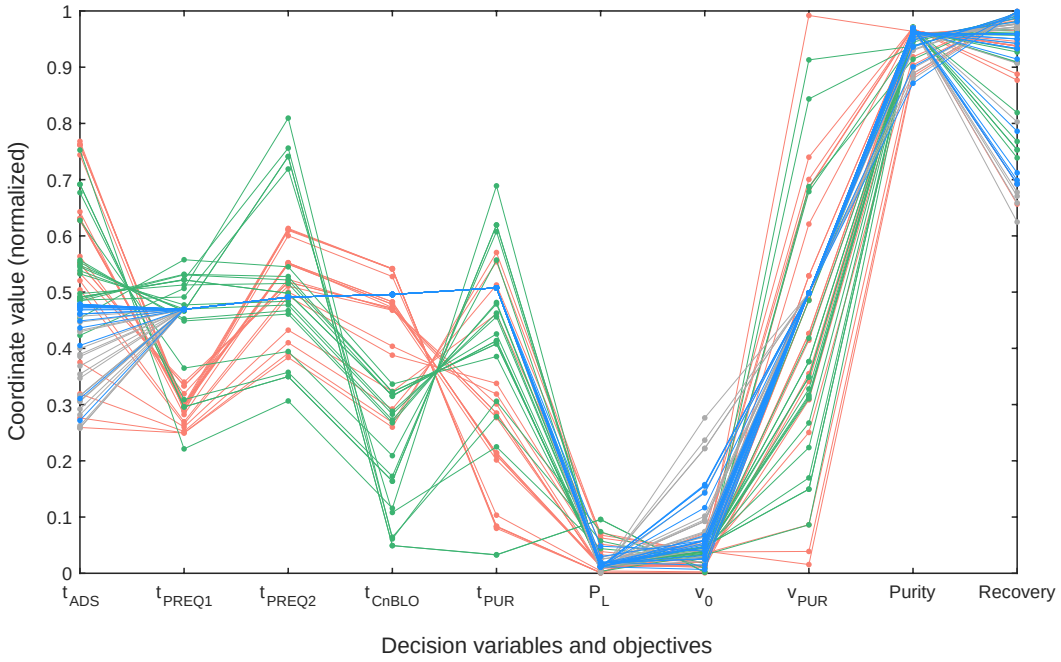

Figure B.10: Parallel coordinate representation of selected optimal solutions obtained using *TradOpt* (red), *SOpt* (green), *DROpt* (blue) and *DR-SOpt* (gray) optimization approaches. The ranges for the decision variables (x) used in the optimization were as follows: t_{ADS} [s]: 20-100, t_{PREQ1} [s]: 30-180, t_{PREQ2} [s]: 30-180, t_{CnBLO} [s]: 30-180, t_{PUR} [s]: 10-80, P_{L} [bar]: 1-17.3, v_0 [ms^{-1}]: 0.08-0.5 and v_{PUR} [ms^{-1}]: 0.1-1. The coordinate values represented in the figure were normalized using: $\bar{x}$ = $(x - \min x)/(\max x - \min x)$.

Appendix C: Direct cost functions for process equipment

The direct costs of individual process equipment were estimated using Aspen Economic Process Analyzer®. Several economic evaluations were performed for each equipment based on a wide range of key design characteristics in order to develop reliable direct cost functions for the optimization. DataFit was used to carry out the regression and it was ensured that the obtained direct cost functions are continuous in the ranges used for the optimization. It is worth mentioning that a design margin of 1.1 in the flows was used at the desired pressure and temperature for the evaluations. However, the regressions are always related to operating conditions without design margins. More details on the regression including the adjusted coefficient of multiple determination (R^2_{ADJ}), average absolute error (avg. abs. error) and maximum absolute error (max. abs. error) are summarized below.

C.1 Columns

In an attempt to develop a generic direct cost function for columns, 156 cases with a wide range of characteristics were considered. Economic evaluations were performed for different diameters, length-to-diameter (L/D) ratios and pressures. The direct cost function based on three variables is given in Eq. C.1. The obtained regression parameters are provided in Table C.1. Figure C.1 illustrates the regression.

$$\text{Column direct cost (€)} = \exp(a \cdot \text{diameter (m)} + b \cdot \text{L/D (-)} + c \cdot \text{pressure (bar)} + d) \quad \text{(C.1)}$$

Table C.1: Regression characteristics of columns

Parameter	**Column**
Coefficient a	0.4148138
Coefficient b	0.0738133
Coefficient c	0.0231138
Coefficient d	10.807870
R^2_{ADJ}	0.986
Avg. abs. error (%)	4.71
Max. abs. error (%)	15.74
Number of cases evaluated	156
Diameter range (m)	1-5
Length-to-diameter ratio range (-)	2-6
Pressure range (bar)	1-4

C.2 Compressors

Based on 63 evaluations, a two-variable direct cost function was obtained for single-stage compressors as shown in Eq. C.2. Actual inlet volumetric flow rate and outlet pressure were varied to represent accurate cost estimations for compressors. The obtained regression parameters and characteristics are listed in Table C.2, while Fig. C.2 shows the regression.

$$\text{Compressor direct cost (€)} = a \cdot \left(\text{Inlet flow rate (m}^3\text{ h}^{-1}\text{)}\right)^b \cdot c^{\text{Pressure (bar)}} \tag{C.2}$$

C.3 Vacuum pump

For a reliable vacuum pump direct cost estimation, 19 cases were considered for economic evaluation in Aspen Economic Process Analyzer®. The key design characteristics of the vacuum pump include the volumetric flow rate and the suction pressure. The cases are representative of a wide span of volumetric flow rates. For all the cases, the suction pressure operating range remains the same, between 0.01 bar and 1 bar.

Table C.2: Regression characteristics of rotating equipment

Parameter	Compressor	Vacuum pump
Coefficient a	121.412	423.900
Coefficient b	0.900	0.653
Coefficient c	1.032	30000.000
R^2_{ADJ}	0.998	0.999
Avg. abs. error (%)	1.43	0.61
Max. abs. error (%)	3.95	1.94
Number of cases evaluated	63	19
Flow range ($m^3\ h^{-1}$)	100000-500000	250-20000
Pressure range (bar)	1-4	0.01-1

Hence, a direct cost function with volumetric flow rate was regressed as shown in Eq. C.3. The regression parameters and characteristics can be found in Table C.2, while the regression is shown in Fig. C.3.

$$\text{Vacuum Pump direct cost (€)} = a \cdot \left(\text{Inlet flow rate } (m^3\ h^{-1})\right)^b + c \tag{C.3}$$

C.4 Heat exchangers

The direct cost function of heat exchangers with both heat exchange area and pressure as variables was obtained from Deng et. al [141]. Suitable factors were used to update costs to €$_{2016}$ using Chemical Engineering Plant Cost Index (CEPCI) and inflation. The two-variable cost function is shown in Eq. C.4 and the regression parameters are provided in Table C.3.

$$\text{Heat exchanger direct cost (€)} = a \cdot \left(\text{Area } (m^2)\right)^b \cdot c^{\text{Pressure (bar)}} \tag{C.4}$$

C.5 Switching valves

Owing to the cyclic nature of the VSA operation, switching valves are essential to implement the cycle sequence. Based on the VSA cycle considered, the number of switch-

Table C.3: Regression characteristics of heat exchangers [141].

Parameter	**Heat exchanger**
Coefficient a	12003
Coefficient b	0.603
Coefficient c	1.011187
R^2_{ADJ}	0.959
Avg. abs. error (%)	14.2
Max. abs. error (%)	32.6
Number of cases evaluated	53
Area range (m^2)	30-4000
Pressure range (bar)	2.7-81

ing valves required per column was estimated to be 3. Given the several number of columns required to capture the flue gas, the cost of valves will no longer be insignificant. Hence, the direct cost of each valve was set to 6000 €. Note that the valves related to the control and instrumentation are accounted for in the indirect costs of process equipment.

C.6 Adsorbent costs

The adsorbent direct costs comprise purchase costs (PC) and transport and installation costs (TIC) and were calculated as follows:

$$\text{Adsorbent direct cost (€)} = M \cdot N \cdot \text{Column volume} \cdot (1-\varepsilon) \cdot \rho_{\mathrm{s}} \cdot (PC + TIC) \quad \text{(C.5)}$$

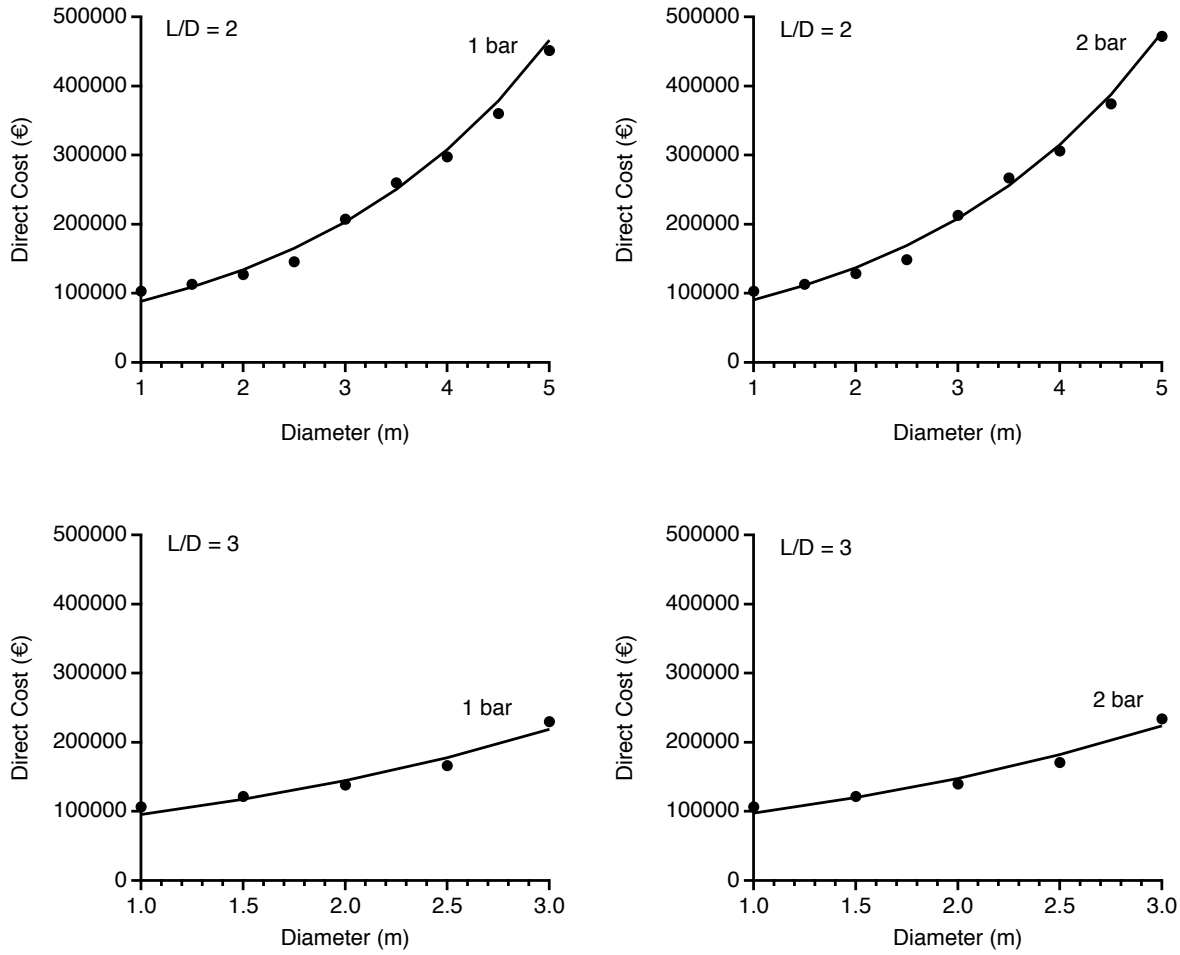

Figure C.1: Direct cost regression of columns. Note that the points represent the Aspen Economic Process Analyzer® evaluations and the lines are regressed cost functions.

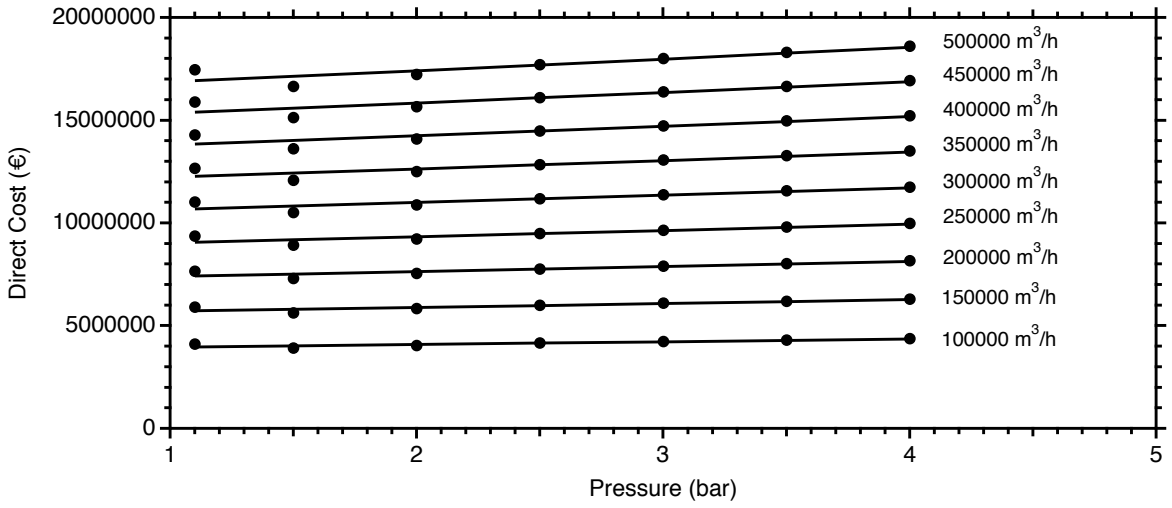

(a)

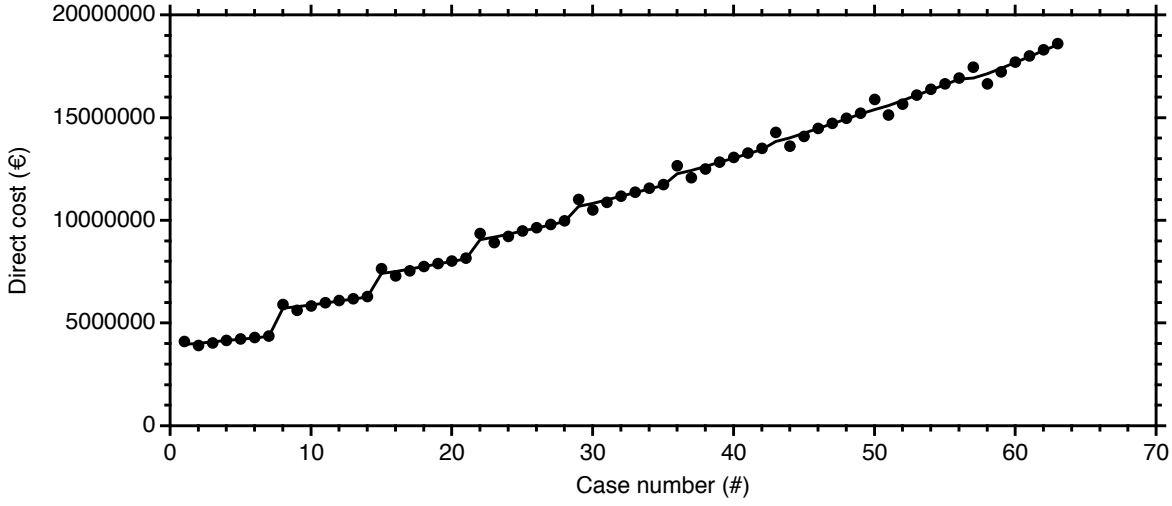

(b)

Figure C.2: Direct cost regression of compressors. Note that the points represent the Aspen Economic Process Analyzer® evaluations and the lines are regressed cost functions.

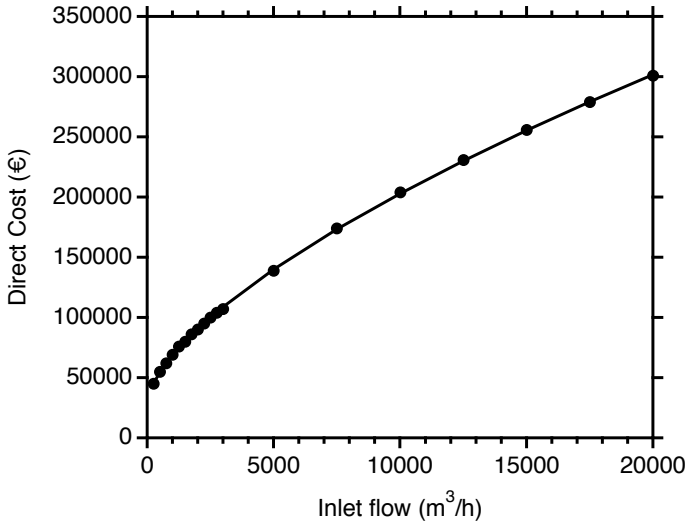

Figure C.3: Direct cost regression of vacuum pumps. Note that the points represent the Aspen Economic Process Analyzer® evaluations and the lines are regressed cost functions.

Appendix D: Supplementary material for Chapter 5

D.1 Baseline MEA-based CO_2 capture

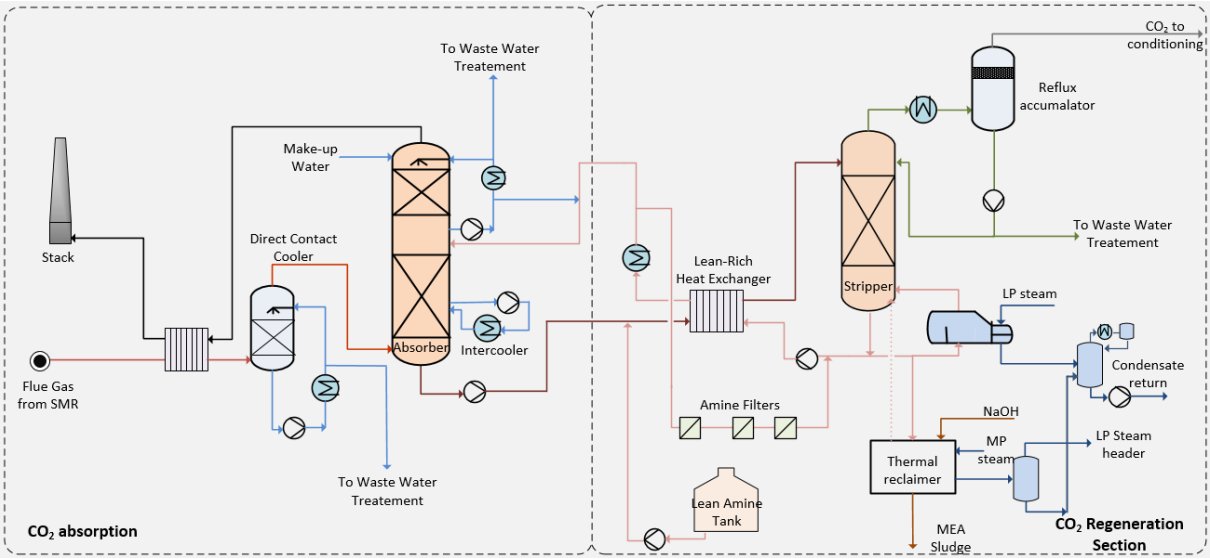

Figure D.1: Detailed process flow diagram of the MEA-based CO_2 capture process for the hydrogen production plant with CO_2 capture [11].

Table D.1: Key performances of hydrogen production plant without and with MEA-based CCS [100].

Parameter	**Without CCS**	**With CCS**
Natural gas to feedstock (t h^{-1})	51.66	51.66
Natural gas to fuel (t h^{-1})	26.59	26.59
Natural gas LHV (MJ kg^{-1})	46.49	46.49
Total energy input (MW)	1010	1010
H_2 to battery limit (t h^{-1})	18.77	18.77
H_2 to battery limit (Nm^3 H_2 h^{-1})	208700	208700
Total energy in H_2 product (MW)	626	626
Gross power output from steam cycle (MW_e)	123.8	91.6
H_2 plant and co-generation power consumption (MW_e)	-3.5	-3.5
CO_2 capture plant (MW_e)	-	-6.7
CO_2 conditioning plant (MW_e)	-	-18.3
Net power output (MW_e)	120.3	63.1
Total energy in H_2 product compared to total energy input (%)	61.9	61.9
Total energy in H_2 and electricity produced compared to total energy input (%)	73.8	68.2
Emissions (kg_{CO_2} Nm^{-3} H_2)	0.994	0.100
Levelized cost of hydrogen (c€Nm^{-3} H_2)	12.20	18.07
CO_2 avoidance cost (€/$t_{CO_2,avoided}$)	-	66.6
CO_2 capture cost (€/$t_{CO_2,avoided}$)	-	30.1

D.2 Adsorbent materials

Table D.2: Dual-site Langmuir isotherm parameters.

	Zeolite 13X [19]	**UTSA-16** [104]	**IISERP MOF2** [91]
CO_2			
q_{sb} (mol kg^{-1})	3.09	4.08	3.29
q_{sd} (mol kg^{-1})	2.54	1.29	1.89
b_0 (m^3 mol^{-1})	8.65×10^{-7}	2.52×10^{-7}	9.39×10^{-8}
d_0 (m^3 mol^{-1})	2.63×10^{-8}	1.75×10^{-9}	5.23×10^{-7}
ΔU_{b} (J mol^{-1})	-36641	-32800	-31135
ΔU_{d} (J mol^{-1})	-35690	-35040	-31135
N_2			
q_{sb} (mol kg^{-1})	3.09	1.33	3.29
q_{sd} (mol kg^{-1})	2.54	1.77	1.89
b_0 (m^3 mol^{-1})	2.69×10^{-6}	9.17×10^{-5}	2.55×10^{-7}
d_0 (m^3 mol^{-1})	2.69×10^{-6}	9.42×10^{-9}	2.55×10^{-7}
ΔU_{b} (J mol^{-1})	-15710	-7500	-11890
ΔU_{d} (J mol^{-1})	-15710	-27760	-11890

D.3 Technical modelling of vacuum swing adsorption

D.3.1 Design of a unit train

The procedure proposed by Khurana and Farooq [21] was used to determine the column scheduling. Each train comprises minimum number of columns and vacuum pumps necessary for a continuous operation. The minimum number of columns per train was calculated as follows:

$$N = \text{ceiling}\left(\frac{\sum_{i=\text{steps}} t_i}{t_{\text{ADS}}}\right) \tag{D.1a}$$

t_i represents the duration of step i in the cycle. The minimum number of blowdown/evacuation vacuum pumps required is given by,

$$N_{\text{V},j} = \text{ceiling}\left(\frac{t_j}{t_{\text{ADS}}}\right) \quad j = \text{blowdown/evacuation} \tag{D.1b}$$

If sum of the individual steps in a cycle is not a multiple of the adsorption time, an idle step has to be included after evacuation step so that the bed profiles are least affected

Table D.3: Boundary conditions for the 4-step VSA cycle.

Step	z=0	z=L
Adsorption	$v\|_{z=0} = v_{\text{feed}}$	$P\|_{\text{z=L}} = P_{\text{H}}$
	$D_{\text{L}}\ \frac{\partial y_i}{\partial z}\big\|_{\text{z=0}} = -v\|_{\text{z=0}}\,(y_{i,\text{feed}} - y_i\|_{\text{z=0}})$	$\frac{\partial y_i}{\partial z}\big\|_{\text{z=L}} = 0$
	$\frac{\partial T}{\partial z}\big\|_{\text{z=0}} = -\varepsilon\ v\|_{\text{z=0}}\,\rho_{\text{g}} C_{p,\text{g}}(T_{\text{feed}} - T\|_{\text{z=0}})$	$\frac{\partial T}{\partial z}\big\|_{\text{z=L}} = 0$
Blowdown	$\frac{\partial P}{\partial z}\big\|_{\text{z=0}} = 0$	$v\|_{\text{z=L}} = v_{\text{vac.pump}}$
	$\frac{\partial y_i}{\partial z}\big\|_{\text{z=0}} = 0$	$\frac{\partial y_i}{\partial z}\big\|_{\text{z=L}} = 0$
	$\frac{\partial T}{\partial z}\big\|_{\text{z=0}} = 0$	$\frac{\partial T}{\partial z}\big\|_{\text{z=L}} = 0$
Evacuation	$v\|_{\text{z=0}} = v_{\text{vac.pump}}$	$\frac{\partial P}{\partial z}\big\|_{\text{z=L}} = 0$
	$\frac{\partial y_i}{\partial z}\big\|_{\text{z=0}} = 0$	$\frac{\partial y_i}{\partial z}\big\|_{\text{z=L}} = 0$
	$\frac{\partial T}{\partial z}\big\|_{\text{z=0}} = 0$	$\frac{\partial T}{\partial z}\big\|_{\text{z=L}} = 0$
Light Product Pressurisation	$\frac{\partial P}{\partial z}\big\|_{\text{z=0}} = 0$	$v\|_{\text{z=L}} = \frac{v_{\text{ADS}} P_{\text{ADS}}\|_{\text{z=L}}}{P\|_{\text{z=L}}}$
	$\frac{\partial y_i}{\partial z}\big\|_{\text{z=0}} = 0$	$D_{\text{L}}\ \frac{\partial y_i}{\partial z}\big\|_{\text{z=L}} = -v\|_{\text{z=L}}\,(y_{i,\text{feed}} - y_i\|_{\text{z=L}})$
	$\frac{\partial T}{\partial z}\big\|_{\text{z=0}} = 0$	$\frac{\partial T}{\partial z}\big\|_{\text{z=L}} = -\varepsilon\ v\|_{\text{z=L}}\,\rho_{\text{g}} C_{p\text{g}}(T_{\text{feed}} - T\|_{\text{z=L}})$

[21]. The duration of an idle step was calculated as follows:

$$t_{\text{IDLE}} = N t_{\text{ADS}} - \sum_{i=\text{steps}} t_i \tag{D.1c}$$

D.3.2 Parallel trains

A single VSA train might not be sufficient to treat the large volume of flue gas. Hence, several trains of VSA units in parallel are required to capture 90% CO_2 [21, 49]. The number of parallel trains can be calculated as:

$$M = \text{ceiling}\left(\frac{\dot{F}_{\text{flue}}}{\dot{F}_{\text{train}}}\right) \tag{D.2}$$

Here $\dot{F}_{\text{flue}}$ is the total flue gas flow rate in kmol h^{-1} and $\dot{F}_{\text{train}}$ is the average molar flow rate of the feed to each train in kmol h^{-1}. It is worth mentioning that the inlet

Table D.4: VSA simulation parameters.

Parameter	Value
Column properties	
Particle diameter, d_{p} (mm)	1.5
Column void fraction, ϵ_{B} (-)	0.37
Particle void fraction, ϵ_{P} (-)	0.35
Tortuosity, τ (-)	3
Operating conditions	
Adsorption pressure, P_{H} (bar)	1.02
Inlet feed composition, $y_{\mathrm{CO_2}}/y_{\mathrm{N_2}}$ (-)	0.2/0.8
Inlet feed temperature, T_{feed} (K)	298.15
Physical properties	
Adsorbent density, ρ_{s} (kg m^{-3})	
Zeolite 13X	1130.0 [19]
UTSA-16	1171.0 [104]
IISERP MOF2	937.7 [91]
Molecular diffusivity, D_{m} (cm^2 s^{-1})	0.16
Fluid viscosity, μ (cP)	0.0172
Specific heat capacity of adsorbent, $C_{\mathrm{p,s}}$ (J kg^{-1} K^{-1})	
Zeolite 13X	1070.0
UTSA-16	1070.0
IISERP MOF2	1070.0
Specific heat capacity of gas phase, $C_{\mathrm{p,g}}$ (J mol^{-1} K^{-1})	30.7
Specific heat capacity of adsorbed phase, $C_{\mathrm{p,a}}$ (J mol^{-1} K^{-1})	30.7
Inside heat transfer coefficient, h_{in} (J m^{-2} K^{-1} s^{-1})	0
Outside heat transfer coefficient, h_{out} (J m^{-2} K^{-1} s^{-1})	0
Effective gas thermal conductivity, K_{z} (J m^{-1} K^{-1} s^{-1})	0.09
Universal gas constant, R (m^3 Pa mol^{-1} K^{-1})	8.314

pressure varies over the duration of the adsorption step owing to the constant velocity boundary condition at the feed end. Therefore, the average molar flow rate of feed to each train was calculated based on an integral average of the molar flow rate over the duration of the adsorption step (shown in Eq. E.2e) and then, used to calculate the

number of parallel trains.

$$\dot{F}_{\text{train}} = \frac{1}{t_{\text{ADS}}} \int_0^{t_{\text{ADS}}} \dot{F} dt \tag{D.3}$$

D.4 Technical modelling of peripheral units

The implementation of CO_2 capture using VSA technology requires several peripheral units extending from flue gas pre-treatment to CO_2 conditioning. In this section, the technical modeling related to each component unit is discussed below.

Flue gas cooling and drying. The wet flue gas was first cooled to 313.15 K by a direct contact cooler and then dehydrated using a molecular sieve 3Å [98].

Compressors. Single-stage compressors were modeled as an isoentropic compression process. The motor efficiency was assumed to be 100%. The energy consumption was calculated as follows:

$$E_{\text{C}}\ (\text{J}_\text{e}) = \frac{1}{\eta_{\text{C}}} \frac{\gamma}{\gamma - 1} \int_{t=0}^{t=t_{\text{ADS}}} QP \left[\left(\frac{P}{P_{\text{ref}}} \right)^{\frac{\gamma-1}{\gamma}} - 1 \right] \text{d}t \tag{D.4a}$$

Here η_{C} is the compression efficiency which was assumed to be 80%, γ is the adiabatic constant obtained from a linear regression as a function of CO_2 composition (see Fig. D.2), P is the pressure, P_{ref} is the reference pressure of flue gas, t_{ADS} is the adsorption step time and Q is the volumetric flow rate of the feed mixture.

Vacuum pumps. The energy consumption by a vacuum pump was modeled as an isentropic expansion process as given by,

$$E_{\text{V}}\ (\text{J}_\text{e}) = \frac{1}{\eta_{\text{V}}} \frac{\gamma}{\gamma - 1} \int_{t=0}^{t=t_{\text{step}}} QP \left[\left(\frac{P_{\text{atm}}}{P} \right)^{\frac{\gamma-1}{\gamma}} - 1 \right] \text{d}t \tag{D.4b}$$

In the above equation, t_{step} is the step duration of blowdown/evacuation step, η_{V} is the vacuum pump efficiency.

Heat exchangers. Two identical counter-current heat exchangers were considered to cool the dry flue gas after compression to 298.15 K. The design was evaluated based on the cooling duty and the log-mean temperature difference (LMTD) for the counter-current flow. The dry flue gas represents the hot side of the heat exchangers while the cooling water is the cold side. To determine the cooling duty, input and output stream characteristics of the hot dry flue gas were used. While the mass flow rate, input and output temperatures of the dry flue gas were known, the specific heat capacity was obtained from the National Institute of Standards and Technology (NIST) REFPROP v.9 database [142]. The mass flow rate of the cooling water was then determined by dividing the cooling duty by the heat capacity [142] and an allowable temperature increase of the cooling water. The inlet and outlet temperatures of cooling water were set to 283.15 K and 291.5 K, respectively. The heat exchanger area (A_{EX}) was obtained using,

$$A_{\mathrm{EX}} = \frac{\dot{Q}_{\mathrm{EX}}}{U_{\mathrm{EX}}\mathrm{LMTD}} \tag{D.5}$$

where Q_{EX} is the cooling duty (W) and U_{EX} is the overall heat transfer coefficient which is assumed to be around 1000 W m^{-2} K^{-1} for all process heat exchangers [141].

CO_2 conditioning. The CO_2 after capture undergoes compression from 1 bar, 298.15 K to offshore pipeline transport conditions at 200 bar and 318.15 K. The CO_2 conditioning before pipeline transport was modelled as a four-stage compression system with intercoolers and a pump to deliver the CO_2 at desired pressure in Aspen HYSYS. The readers are referred elsewhere [100] for detailed modeling of CO_2 conditioning.

CO_2 transport and storage. The costs of the transport and storage are assessed using the iCCS tool developed by SINTEF Energy Research [131] and previously documented [143–145]. The transport cost model relies on the pipeline cost model developed by Knoope et al. [146] and the storage cost model relies on the Zero Emission Platform for Zero Emission Fossil Fuel Power Plants [147].

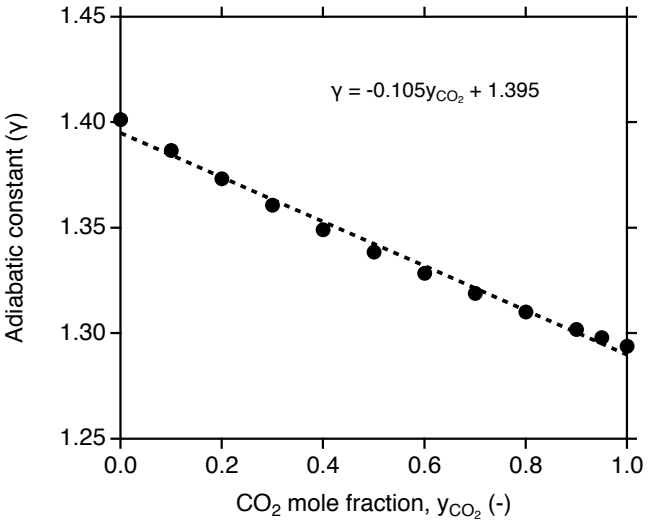

Figure D.2: Linear dependence of adiabatic constant (γ) as a function of CO_2 mole fraction. Note that the γ values were obtained from NIST database [142].

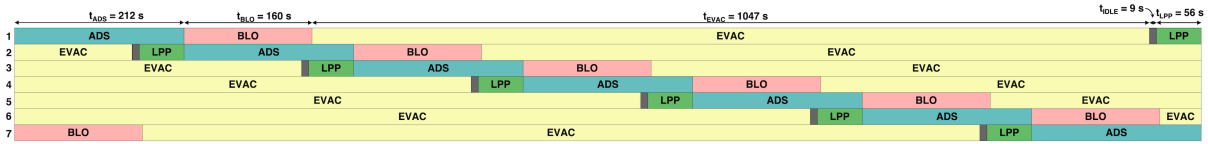

(a) Zeolite 13X

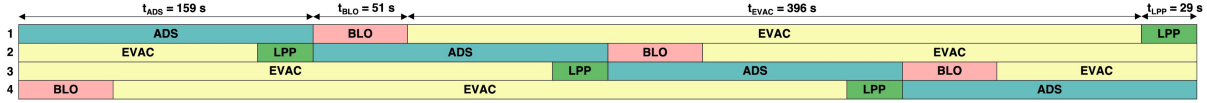

(b) UTSA-16

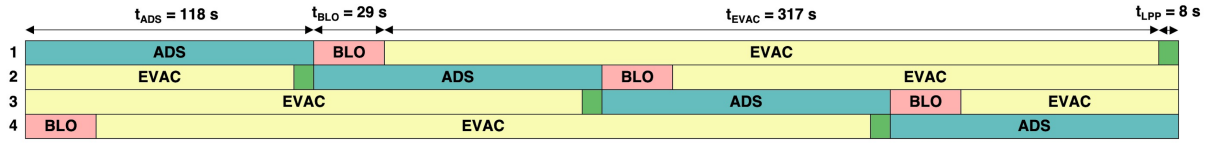

(c) IISERP MOF2

Figure D.3: Optimal cycle schedules for all three adsorbents.

Appendix E: Supplementary material for Chapter 6

E.1 PVSA plant layout

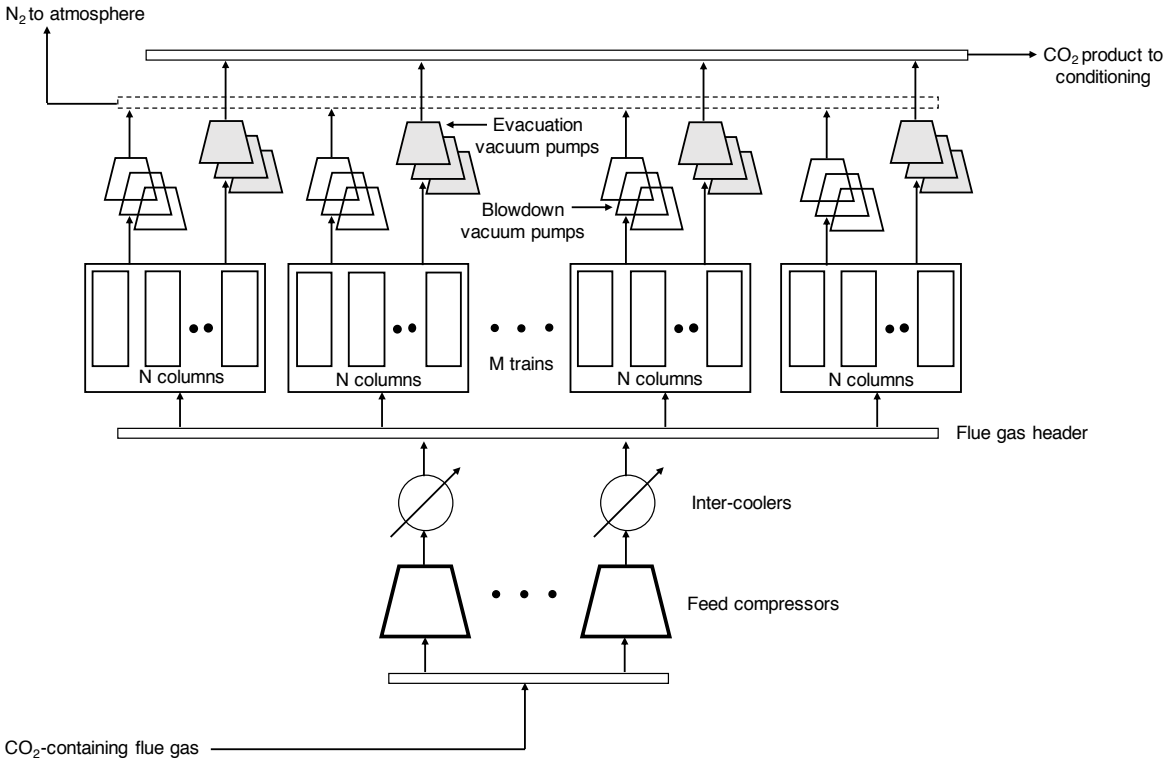

Figure E.1: PVSA process layout [88] that represents the scope of the study.

E.2 MEA-based cost performances

Table E.1: CO_2 avoided costs (€/$t_{CO_2\ avoided}$) obtained for MEA-based CO_2 capture at different CO_2 compositions and flue gas flow rates [116]. The steam for MEA-based CO_2 capture is generated using natural gas boiler.

CO_2 composition (%)	Flue gas flow rate (tonne h^{-1})				
	313	1159	2004	2850	3696
3.5	91.2	78.7	76.8	76.3	75.5
7.5	71.8	65.0	64.8	63.7	63.7
13	62.5	59.2	57.9	57.7	58.2
20	58.8	56.5	55.7	56.0	56.1
30	56.3	55.2	54.8	54.9	54.7

Table E.2: CO_2 avoided costs (€/$t_{CO_2\ avoided}$) obtained for MEA-based CO_2 capture at different CO_2 compositions and flue gas flow rates [116]. The steam for MEA-based CO_2 capture is generated using process waste heat.

CO_2 composition (%)	Flue gas flow rate (tonne h^{-1})				
	313	1159	2004	2850	3696
3.5	50.5	40.8	39.4	38.9	38.3
7.5	36.9	31.5	31.3	30.5	30.5
13	30.4	27.8	26.7	26.6	27.0
20	28.1	26.2	25.6	25.9	25.9
30	26.5	25.6	25.4	25.4	25.2

E.3 Techno-economic optimization model

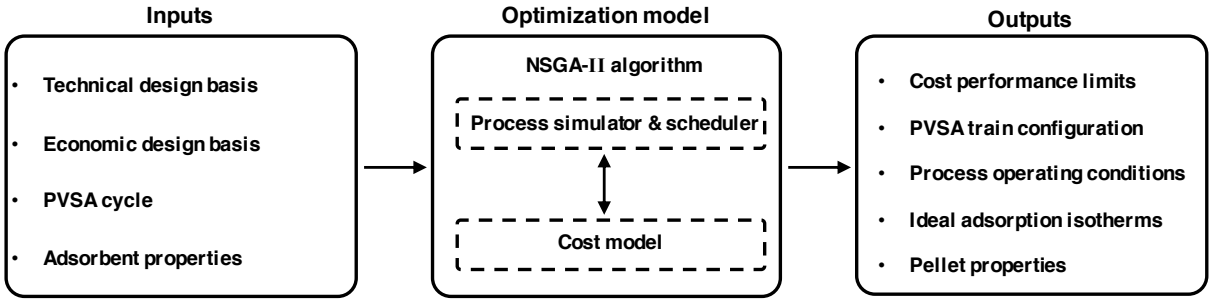

Figure E.2: Integrated techno-economic optimization methodology [88].

E.3.1 PVSA cycle

Four-step cycle

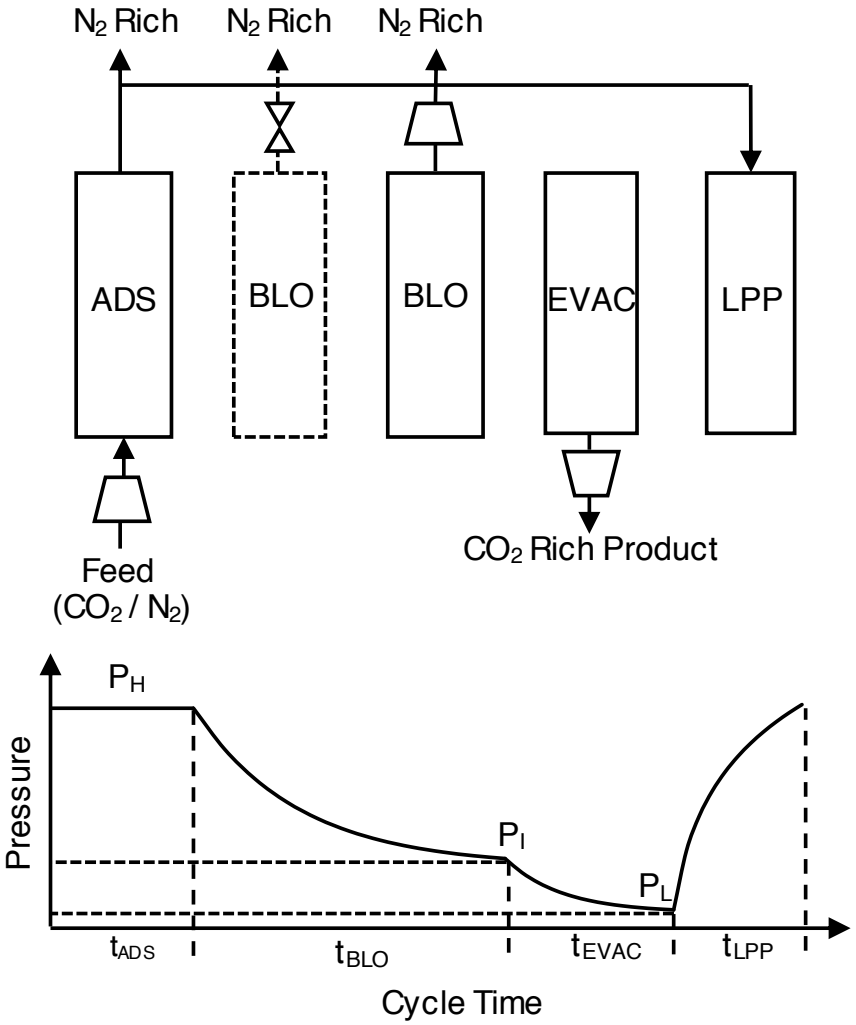

Figure E.3: Four-step PVSA cycle schematic.

Six-step DR cycle

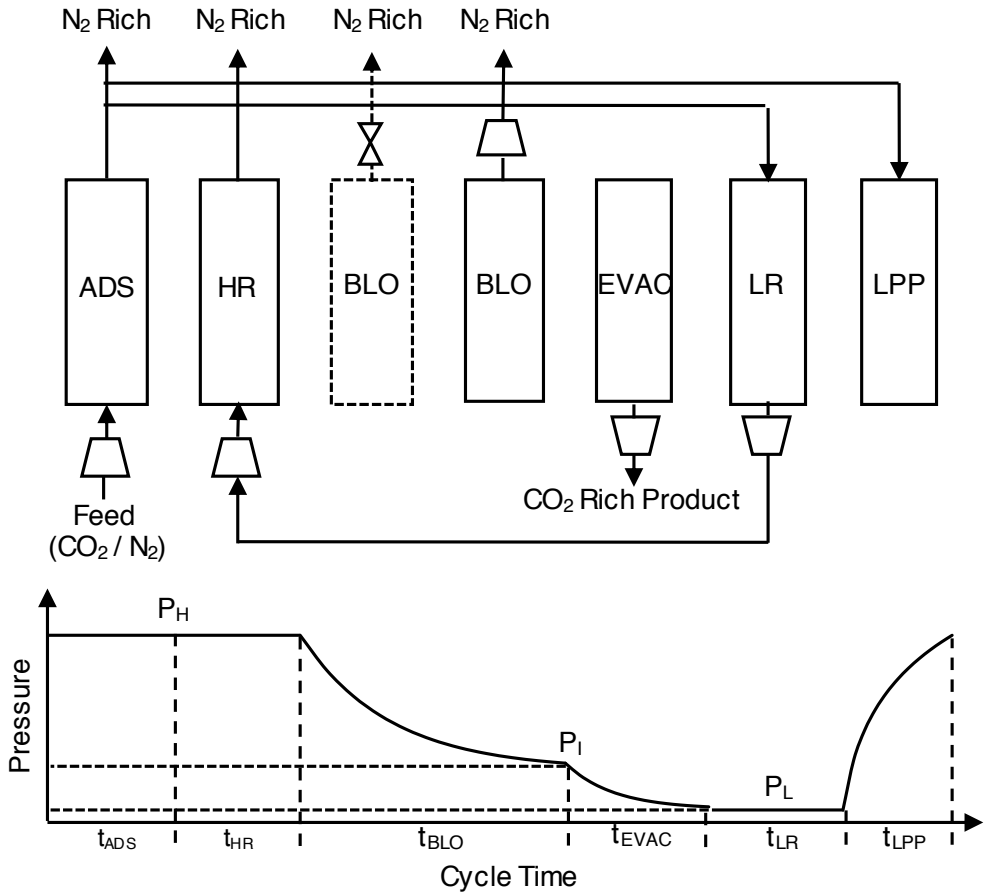

Figure E.4: Six-step DR PVSA cycle schematic.

E.3.2 Boundary conditions

Table E.3: Boundary conditions used for PVSA cycles.

Step	z=0	z=L
Adsorption	$v\|_{z=0} = v_{\text{feed}}$	$P\|_{\text{z=L}} = P_{\text{H}}$
	$D_{\text{L}} \left.\frac{\partial y_i}{\partial z}\right\|_{\text{z=0}} = -v\|_{\text{z=0}} \left(y_{i,\text{feed}} - y_i\|_{\text{z=0}}\right)$	$\left.\frac{\partial y_i}{\partial z}\right\|_{\text{z=L}} = 0$
	$\left.\frac{\partial T}{\partial z}\right\|_{\text{z=0}} = -\varepsilon\, v\|_{\text{z=0}}\, \rho_{\text{g}} C_{p,\text{g}} (T_{\text{feed}} - T\|_{\text{z=0}})$	$\left.\frac{\partial T}{\partial z}\right\|_{\text{z=L}} = 0$
Blowdown	$\left.\frac{\partial P}{\partial z}\right\|_{\text{z=0}} = 0$	$v\|_{\text{z=L}} = v^*_{\text{BLO}}$
	$\left.\frac{\partial y_i}{\partial z}\right\|_{\text{z=0}} = 0$	$\left.\frac{\partial y_i}{\partial z}\right\|_{\text{z=L}} = 0$
	$\left.\frac{\partial T}{\partial z}\right\|_{\text{z=0}} = 0$	$\left.\frac{\partial T}{\partial z}\right\|_{\text{z=L}} = 0$
Evacuation	$v\|_{\text{z=0}} = v_{\text{vac.pump}}$	$\left.\frac{\partial P}{\partial z}\right\|_{\text{z=L}} = 0$
	$\left.\frac{\partial y_i}{\partial z}\right\|_{\text{z=0}} = 0$	$\left.\frac{\partial y_i}{\partial z}\right\|_{\text{z=L}} = 0$
	$\left.\frac{\partial T}{\partial z}\right\|_{\text{z=0}} = 0$	$\left.\frac{\partial T}{\partial z}\right\|_{\text{z=L}} = 0$
Light Product Pressurisation	$\left.\frac{\partial P}{\partial z}\right\|_{\text{z=0}} = 0$	$v\|_{\text{z=L}} = \frac{v_{\text{ADS}} P_{\text{ADS}}\|_{\text{z=L}}}{P\|_{\text{z=L}}}$
	$\left.\frac{\partial y_i}{\partial z}\right\|_{\text{z=0}} = 0$	$D_{\text{L}} \left.\frac{\partial y_i}{\partial z}\right\|_{\text{z=L}} = -v\|_{\text{z=L}} \left(y_{i,\text{feed}} - y_i\|_{\text{z=L}}\right)$
	$\left.\frac{\partial T}{\partial z}\right\|_{\text{z=0}} = 0$	$\left.\frac{\partial T}{\partial z}\right\|_{\text{z=L}} = -\varepsilon\, v\|_{\text{z=L}}\, \rho_{\text{g}} C_{pg} (T_{\text{feed}} - T\|_{\text{z=L}})$
Heavy Reflux	$v\|_{z=0} = v_{\text{HR}}$	$P\|_{\text{z=L}} = P_{\text{H}}$
	$D_{\text{L}} \left.\frac{\partial y_i}{\partial z}\right\|_{\text{z=0}} = -v\|_{\text{z=0}} \left(y_{i,\text{feed}} - y_i\|_{\text{z=0}}\right)$	$\left.\frac{\partial y_i}{\partial z}\right\|_{\text{z=L}} = 0$
	$\left.\frac{\partial T}{\partial z}\right\|_{\text{z=0}} = -\varepsilon\, v\|_{\text{z=0}}\, \rho_{\text{g}} C_{p,\text{g}} (T_{\text{feed}} - T\|_{\text{z=0}})$	$\left.\frac{\partial T}{\partial z}\right\|_{\text{z=L}} = 0$
Light Reflux	$P\|_{\text{z=0}} = P_{\text{L}}$	$v\|_{\text{z=L}} = \frac{\theta_{\text{R}} v_{\text{ADS}} P_{\text{ADS}}\|_{\text{z=L}}}{P\|_{\text{z=L}}}$
	$\left.\frac{\partial y_i}{\partial z}\right\|_{\text{z=0}} = 0$	$D_{\text{L}} \left.\frac{\partial y_i}{\partial z}\right\|_{\text{z=L}} = -v\|_{\text{z=L}} \left(y_{i,\text{feed}} - y_i\|_{\text{z=L}}\right)$
	$\left.\frac{\partial T}{\partial z}\right\|_{\text{z=0}} = 0$	$\left.\frac{\partial T}{\partial z}\right\|_{\text{z=L}} = -\varepsilon\, v\|_{\text{z=L}}\, \rho_{\text{g}} C_{p,\text{g}} (T_{\text{feed}} - T\|_{\text{z=L}})$

*The velocity boundary condition at z=L for the blowdown step was defined as:

$$v_{\mathrm{BLO}} = \begin{cases} v_{\mathrm{valve}} & \text{if} \quad 1\ \text{bar} < P \leq P_{\mathrm{H}} \\ v_{\mathrm{vac.pump}} & \text{else if} \quad P \leq 1\ \text{bar} \end{cases} \tag{E.1}$$

where P is the column pressure at z=L; $v_{\mathrm{vac.pump}}$ is the velocity of the vacuum pump and; v_{valve} is the velocity of gas leaving blowdown step when $P_{\mathrm{H}} > 1$ bar and modelled using a valve equation as recommended by Fluids Control Institute Inc [148].

Table E.4: PVSA simulation parameters.

Parameter	**Value**
Column Properties	
Column void fraction, ϵ_{B} (-)	0.37
Tortuosity, τ (-)	$1/\epsilon_{\mathrm{p}}$ [102]
Operating Conditions	
Adsorption pressure, P_{H} (bar)	1.02
Inlet feed temperature, T_{feed} (K)	298.15
Physical Properties	
Adsorbent crystal density, ρ_{s} (kg m^{-3})	
Hypothetical materials	1738.5
Zeolite 13X	1738.5 [19]
IISERP MOF2	1442.6 [91]
Molecular diffusivity, D_{m} (cm^2 s^{-1})	0.16
Fluid viscosity, μ (cP)	0.0172
Specific heat capacity of adsorbent, $C_{\mathrm{p,s}}$ (J kg^{-1} K^{-1})	1070.0
Specific heat capacity of gas phase, $C_{\mathrm{p,g}}$ (J mol^{-1} K^{-1})	30.7
Specific heat capacity of adsorbed phase, $C_{\mathrm{p,a}}$ (J mol^{-1} K^{-1})	30.7
Inside heat transfer coefficient, h_{in} (J m^{-2} K^{-1} s^{-1})	0
Outside heat transfer coefficient, h_{out} (J m^{-2} K^{-1} s^{-1})	0
Effective gas thermal conductivity, K_{z} (J m^{-1} K^{-1} s^{-1})	0.09
Universal gas constant, R (m^3 Pa mol^{-1} K^{-1})	8.314

E.3.3 Column scheduling and parallel trains

Column scheduling was determined based on the procedure proposed by Khurana and Farooq [21]. The minimum number of columns and vacuum pumps needed in

each PVSA train for a continuous operation are calculated as follows:

$$N = \text{ceiling}\left(\frac{\sum_{i=\text{steps}} t_i}{t_{\text{ADS}}}\right) \tag{E.2a}$$

N is the minimum number of columns per train and t_i represents the step duration i in the cycle. Idle step is included after the evacuation step when the sum of the individual steps in a cycle is not a multiple of the adsorption time and the idle step duration was calculated as follows:

$$t_{\text{IDLE}} = N t_{\text{ADS}} - \sum_{i=\text{steps}} t_i \tag{E.2b}$$

$$N_{\text{V},j} = \text{ceiling}\left(\frac{t_j}{t_{\text{ADS}}}\right) \quad j = \text{blowdown/evacuation/lightreflux} \tag{E.2c}$$

$N_{\text{V},j}$ is the minimum number of blowdown/evacuation/light reflux vacuum pumps per train.

The number of PVSA parallel trains are calculated as:

$$M = \text{ceiling}\left(\frac{\dot{F}_{\text{flue}}}{\dot{F}_{\text{train}}}\right) \tag{E.2d}$$

where $\dot{F}_{\text{flue}}$ represents the total flue gas flow rate (kmol h^{-1}) and $\dot{F}_{\text{train}}$ represents the average molar flow rate of the feed to each train (kmol h^{-1}) defined as follows:

$$\dot{F}_{\text{train}} = \frac{1}{t_{\text{ADS}}} \int_0^{t_{\text{ADS}}} \dot{F} dt \tag{E.2e}$$

E.4 Modelling of other equipment

Rotating equipment

The energy consumed by compressors was determined by assuming single-stage isoentropic compression with 100% motor efficiency as follows:

$$E_{\text{C}}\ (\text{J}_{\text{e}}) = \frac{1}{\eta_{\text{C}}} \frac{\gamma}{\gamma - 1} \int_{t=0}^{t=t_{\text{ADS}}} QP\left[\left(\frac{P}{P_{\text{ref}}}\right)^{\frac{\gamma-1}{\gamma}} - 1\right] \text{d}t \tag{E.3a}$$

where η_{C}=80% is the compression efficiency; γ represents adiabatic constant defined as a linear function of CO_2 composition (see Eq. E.3c) [88]; Q is the volumetric flow rate

of the feed mixture; P is the pressure; reference pressure P_{ref}=1.02 bar and; t_{ADS} is the adsorption step time.

The vacuum pump energy consumption was calculated assuming an isentropic expansion process and is given by,

$$E_{\text{V}}\ (\text{J}_{\text{e}}) = \frac{1}{\eta_{\text{V}}} \frac{\gamma}{\gamma - 1} \int_{t=0}^{t=t_{\text{step}}} QP \left[\left(\frac{P_{\text{atm}}}{P} \right)^{\frac{\gamma-1}{\gamma}} - 1 \right] \text{d}t \tag{E.3b}$$

η_{V} is the vacuum pump efficiency defined in Eq. E.3d and; t_{step} is the step duration of blowdown/evacuation step.

$$\gamma = -0.105 y_{\text{CO}_2} + 1.395 \tag{E.3c}$$

$$\eta_{\text{V}} = \frac{15.84P}{1 + 19.80P} \tag{E.3d}$$

where P, in bar, is the suction pressure. The efficiency, η_{V}, includes that of the driver.

Heat exchangers

Counter-current heat exchangers were used to cool the flue gas after compression to 298.15 K. The heat exchanger area was determined using Eq. E.4.

$$A_{\text{EX}} = \frac{\dot{Q}_{\text{EX}}}{U_{\text{EX}} \text{LMTD}} \tag{E.4}$$

where Q_{EX} is the cooling duty (W); LMTD is the log-mean temperature difference for the counter-current flow and; U_{EX}=1000 W m^{-2} K^{-1} was assumed for the overall heat transfer coefficient [88]. It is worth noting that the inlet and outlet temperatures of cooling water were fixed to 283.15 K and 291.5 K, respectively in order to determine the cooling duty.

E.5 CO_2 avoided cost

The CO_2 avoided cost, in €/$t_{CO_2\ \text{avoided}}$ (where $t_{CO_2\ \text{avoided}}$ is metric tonnes of CO_2 avoided) is defined as shown below:

$$\text{CO}_2 \text{ Avoided Cost} = \frac{\sum_i \frac{\text{TCR}_{\text{PVSA capture plant}}\ (i) + \text{Annual OPEX}_{\text{PVSA capture plant}}\ (i)}{(1+d)^i}}{\sum_i \frac{\text{Annual amount of CO}_2 \text{ emissions avoided by PVSA capture plant } (i)}{(1+d)^i}} \tag{E.5}$$

where i is the year index (-). The amount of CO_2 emissions avoided by PVSA capture plant is the difference of annual amount of CO_2 captured by PVSA process and direct emissions due to electricity consumption in the PVSA plant. It is assumed that the electricity consumed by the PVSA is supplied through a deeply decarbonized power system based on a fossil-based power plant with CCS and renewable [88]. Since the direct emissions due to electricity consumption increase the CO_2 avoided cost, the premise of a deeply decarbonized power system remains consistent, given the goal is to determine the cost limits of PVSA. Note that CO_2 avoided cost excludes CO_2 conditioning, transport and storage [130].

E.6 Optimization

Table E.5: Lower and upper bounds of decision variables used in the optimizations.

Decision variable	**Lower bound**	**Upper bound**
Adsorption time, t_{ADS} (s)	50	400
Blowdown vacuum pump flow rate, S_{B} (m^3 h^{-1})	1500	20000
Evacuation vacuum pump flow rate, S_{E} (m^3 h^{-1})	1500	20000
High pressure, P_{H} (bar)	1	3.6
Intermediate pressure, P_{I} (bar)	P_{L} + 0.01	0.99
Low pressure, P_{L} (bar)	0.01	0.2
Column length, L (m)	6	9
Reflux fraction, θ_{R} (-)	0.008	0.08
Fractional reflux duration, f_{t} (-)	0.1	0.9
Saturation capacity for b site, q_{sb} (mol kg^{-1})	0.1	8
Saturation capacity for d site, q_{sd} (mol kg^{-1})	0.1	8
CO_2 equilibrium constant for b site, $b_{0,\mathrm{CO_2}}$ (m^3 mol^{-1})	1×10^{-11}	1×10^{-5}
CO_2 equilibrium constant for d site, $d_{0,\mathrm{CO_2}}$ (m^3 mol^{-1})	1×10^{-11}	1×10^{-5}
CO_2 internal energy for b site, $\Delta U_{\mathrm{b,CO_2}}$ (J mol^{-1})	-7000	-46000
CO_2 internal energy for d site, $\Delta U_{\mathrm{d,CO_2}}$ (J mol^{-1})	-7000	-46000
N_2 equilibrium constant, $b_{0,\mathrm{N_2}}$ (m^3 mol^{-1})	1×10^{-12}	1.58×10^{-6}
N_2 internal energy, $\Delta U_{\mathrm{b,N_2}}$ (J mol^{-1})	-5000	-17000
Pellet porosity, ϵ_{p} (-)	0.2	0.8
Pellet diameter, d_{p} (mm)	1	5

Table E.6: Techno-economic performances of the four-step PVSA cycle optimized for cost limits at a constant flue gas flow rate of 2004 t h^{-1} over a range of CO_2 compositions. A value of 0.0 indicates that the contribution was less than 0.1 €/$t_{CO_2,\ avoided}$.

	3.5%	**7.5%**	**13%**	**20%**	**30%**
Operating conditions					
Adsorption time (s)	111	94	105	142	58
Blowdown pump flow rate ($m^3\ h^{-1}$)	1649	1686	1623	2592	3415
Evacuation pump flow rate ($m^3\ h^{-1}$)	12143	15004	19234	14699	17523
High pressure (bar)	2.89	2.49	2.06	2.05	1.81
Intermediate pressure (bar)	0.12	0.18	0.32	0.76	0.56
Low pressure (bar)	0.010	0.025	0.030	0.054	0.116
Feed velocity ($m\ s^{-1}$)	1.29	1.26	1.36	1.58	1.63
Column length (m)	8.4	8.4	8.7	9.0	8.6
Particle porosity (-)	0.58	0.69	0.69	0.57	0.43
Particle diameter (mm)	4.2	4.8	4.9	4.7	3.6
Train configuration					
Number of columns per train (-)	5	4	4	4	4
Blowdown pumps per train (-)	1	1	1	1	1
Evacuation pumps per train (-)	3	2	2	3	2
Number of parallel trains (-)	50	60	59	45	50
Process performance					
Purity (%)	95.1	95.3	94.9	95.2	94.9
Recovery (%)	90.1	90.1	92.2	90.6	90.4
Productivity ($mol\ m^{-3}\ s^{-1}$)	0.98	2.16	3.32	5.84	8.63
Compressor power (MW_e)	84.23	68.06	52.81	53.37	44.90
Blowdown power (MW_e)	1.59	1.70	1.28	0.59	1.50
Evacuation power (MW_e)	64.76	47.74	51.37	41.80	33.70
Overall power consumption (MW_e)	150.59	117.50	105.47	95.75	80.09
Specific energy consumption (kWh_e/t_{CO_2})	1547.3	576.1	300.3	187.1	109.9
Cost performance					
CAPEX (€/$t_{CO_2,\ avoided}$)	36.6	16.0	9.4	5.8	3.9
Total direct cost (€/$t_{CO_2,\ avoided}$)	22.5	9.9	5.8	3.6	2.4
Column cost (€/$t_{CO_2,\ avoided}$)	7.3	3.2	1.9	1.0	0.7
Compressor cost (€/$t_{CO_2,\ avoided}$)	9.0	4.0	2.2	1.5	1.0
Vacuum pump cost (€/$t_{CO_2,\ avoided}$)	5.3	2.3	1.5	1.0	0.6
Heat exchanger cost (€/$t_{CO_2,\ avoided}$)	0.2	0.1	0.1	0.0	0.0
Valves cost (€/$t_{CO_2,\ avoided}$)	0.6	0.3	0.1	0.1	0.1
Initial adsorbent cost (€/$t_{CO_2,\ avoided}$)	0.0	0.0	0.0	0.0	0.0
Process contingency (€/$t_{CO_2,\ avoided}$)	3.4	1.5	0.9	0.5	0.3
Indirect cost (€/$t_{CO_2,\ avoided}$)	3.6	1.6	0.9	0.6	0.4
Project contingency (€/$t_{CO_2,\ avoided}$)	5.2	2.2	1.3	0.8	0.6
Owner cost (€/$t_{CO_2,\ avoided}$)	1.8	0.8	0.5	0.3	0.2
OPEX (€/$t_{CO_2,\ avoided}$)	114.1	42.3	22.3	13.9	8.3
Fixed OPEX (€/$t_{CO_2,\ avoided}$)	17.7	7.8	4.5	2.8	1.9
Electricity cost (€/$t_{CO_2,\ avoided}$)	95.5	34.2	17.6	11.0	6.4
Adsorbent cost (€/$t_{CO_2,\ avoided}$)	0.0	0.0	0.0	0.0	0.0
Cooling water cost (€/$t_{CO_2,\ avoided}$)	0.9	0.3	0.2	0.1	0.0
CO_2 avoided cost (€/$t_{CO_2,\ avoided}$)	**150.7**	**58.3**	**31.7**	**19.7**	**12.2**

Table E.7: Techno-economic performances of the four-step PVSA cycle optimized for cost limits with $P_L \geq 0.1$ bar at a constant flue gas flow rate of 2004 t h^{-1} over a range of CO_2 compositions. A value of 0.0 indicates that the contribution was less than 0.1 €/$t_{CO_2, avoided}$.

	3.5%	**7.5%**	**13%**	**20%**	**30%**
Operating conditions					
Adsorption time (s)	-	-	64	80	67
Blowdown pump flow rate (m^3 h^{-1})	-	-	5167	2001	2762
Evacuation pump flow rate (m^3 h^{-1})	-	-	11784	10430	14236
High pressure (bar)	-	-	3.59	3.13	2.52
Intermediate pressure (bar)	-	-	0.26	0.51	0.87
Low pressure (bar)	-	-	0.10	0.12	0.14
Feed velocity (m s^{-1})	-	-	0.89	0.93	1.49
Column length (m)	-	-	9.0	9.0	8.3
Particle porosity (-)	-	-	0.47	0.66	0.50
Particle diameter (mm)	-	-	2.3	3.4	4.5
Train configuration					
Number of columns per train (-)	-	-	4	4	4
Blowdown pumps per train (-)	-	-	1	1	1
Evacuation pumps per train (-)	-	-	2	2	2
Number of parallel trains (-)	-	-	50	54	45
Process performance					
Purity (%)	-	-	95.0	94.9	94.9
Recovery (%)	-	-	90.3	90.6	90.4
Productivity (mol m^{-3} s^{-1})	-	-	3.55	4.85	10.43
Compressor power (MW_e)	-	-	96.37	78.33	61.65
Blowdown power (MW_e)	-	-	4.40	1.12	0.39
Evacuation power (MW_e)	-	-	32.09	26.20	25.37
Overall power consumption (MW_e)	-	-	132.87	105.65	87.41
Specific energy consumption (kWh_e/t_{CO_2})	-	-	386.45	206.46	119.96
Cost performance					
CAPEX (€/$t_{CO_2, avoided}$)	-	-	8.8	5.8	3.6
Total direct cost (€/$t_{CO_2, avoided}$)	-	-	5.4	3.6	2.2
Column cost (€/$t_{CO_2, avoided}$)	-	-	1.7	1.2	0.7
Compressor cost (€/$t_{CO_2, avoided}$)	-	-	2.4	1.5	1.0
Vacuum pump cost (€/$t_{CO_2, avoided}$)	-	-	1.1	0.7	0.5
Heat exchanger cost (€/$t_{CO_2, avoided}$)	-	-	0.1	0.0	0.0
Valves cost (€/$t_{CO_2, avoided}$)	-	-	0.1	0.1	0.1
Initial adsorbent cost (€/$t_{CO_2, avoided}$)	-	-	0.0	0.0	0.0
Process contingency (€/$t_{CO_2, avoided}$)	-	-	0.8	0.5	0.3
Indirect cost (€/$t_{CO_2, avoided}$)	-	-	0.9	0.6	0.4
Project contingency (€/$t_{CO_2, avoided}$)	-	-	1.3	0.8	0.5
Owner cost (€/$t_{CO_2, avoided}$)	-	-	0.4	0.3	0.2
OPEX (€/$t_{CO_2, avoided}$)	-	-	27.4	15.1	8.8
Fixed OPEX (€/$t_{CO_2, avoided}$)	-	-	4.3	2.8	1.7
Electricity cost (€/$t_{CO_2, avoided}$)	-	-	22.8	12.1	7.0
Adsorbent cost (€/$t_{CO_2, avoided}$)	-	-	0.0	0.0	0.0
Cooling water cost (€/$t_{CO_2, avoided}$)	-	-	0.3	0.2	0.1
CO_2 avoided cost (€/$t_{CO_2, avoided}$)	**-**	**-**	**36.2**	**20.9**	**12.4**

Table E.8: Techno-economic performances of the four-step PVSA cycle optimized for cost limits with fixed pellet properties at a constant flue gas flow rate of 2004 t h^{-1} over a range of CO_2 compositions. A value of 0.0 indicates that the contribution was less than 0.1 €/$t_{CO_2,\ avoided}$.

	3.5%	**7.5%**	**13%**	**20%**	**30%**
Operating conditions					
Adsorption time (s)	103	155	86	103	123
Blowdown pump flow rate ($m^3\ h^{-1}$)	5139	2552	2360	1731	1693
Evacuation pump flow rate ($m^3\ h^{-1}$)	6190	8326	12957	11663	16125
High pressure (bar)	3.50	2.62	2.14	2.00	2.76
Intermediate pressure (bar)	0.06	0.17	0.22	0.40	0.84
Low pressure (bar)	0.016	0.023	0.055	0.074	0.17
Feed velocity ($m\ s^{-1}$)	0.75	0.83	0.88	0.89	0.78
Column length (m)	8.9	8.5	9.0	9.0	8.6
Particle porosity (-)	0.35	0.35	0.35	0.35	0.35
Particle diameter (mm)	1.5	1.5	1.5	1.5	1.5
Train configuration					
Number of columns per train (-)	6	5	4	4	3
Blowdown pumps per train (-)	1	1	1	1	1
Evacuation pumps per train (-)	4	3	2	2	1
Number of parallel trains (-)	60	76	72	74	72
Process performance					
Purity (%)	95.1	94.9	95.1	94.9	94.9
Recovery (%)	90.1	90.9	89.9	90.6	90.2
Productivity ($mol\ m^{-3}\ s^{-1}$)	0.56	1.33	2.44	3.56	7.91
Compressor power (MW_e)	105.14	81.49	67.28	58.57	70.01
Blowdown power (MW_e)	7.67	3.43	2.66	1.53	0.47
Evacuation power (MW_e)	57.70	53.44	41.65	35.89	23.00
Overall power consumption (MW_e)	170.51	138.36	111.59	95.99	93.47
Specific energy consumption (kWh_e/t_{CO_2})	1752.4	672.54	325.80	187.52	128.52
Cost performance					
CAPEX (€/$t_{CO_2,\ avoided}$)	46.5	20.9	10.6	6.9	3.8
Total direct cost (€/$t_{CO_2,\ avoided}$)	28.7	12.9	6.5	4.3	2.4
Column cost (€/$t_{CO_2,\ avoided}$)	11.6	5.1	2.4	1.7	0.8
Compressor cost (€/$t_{CO_2,\ avoided}$)	9.4	4.0	2.3	1.5	1.0
Vacuum pump cost (€/$t_{CO_2,\ avoided}$)	6.5	3.2	1.5	1.0	0.4
Heat exchanger cost (€/$t_{CO_2,\ avoided}$)	0.3	0.1	0.1	0.0	0.0
Valves cost (€/$t_{CO_2,\ avoided}$)	0.9	0.4	0.2	0.1	0.1
Initial adsorbent cost (€/$t_{CO_2,\ avoided}$)	0.0	0.0	0.0	0.0	0.0
Process contingency (€/$t_{CO_2,\ avoided}$)	4.3	1.9	1.0	0.6	0.4
Indirect cost (€/$t_{CO_2,\ avoided}$)	4.6	2.1	1.1	0.7	0.4
Project contingency (€/$t_{CO_2,\ avoided}$)	6.6	3.0	1.5	1.0	0.5
Owner cost (€/$t_{CO_2,\ avoided}$)	2.3	1.0	0.5	0.3	0.2
OPEX (€/$t_{CO_2,\ avoided}$)	132.6	50.5	24.5	14.5	9.5
Fixed OPEX (€/$t_{CO_2,\ avoided}$)	22.4	10.0	5.1	3.4	1.9
Electricity cost (€/$t_{CO_2,\ avoided}$)	109.1	40.1	19.2	11.0	7.5
Adsorbent cost (€/$t_{CO_2,\ avoided}$)	0.0	0.0	0.0	0.0	0.0
Cooling water cost (€/$t_{CO_2,\ avoided}$)	1.1	0.4	0.2	0.1	0.1
CO_2 avoided cost (€/$t_{CO_2,\ avoided}$)	**179.1**	**71.4**	**35.1**	**21.4**	**13.3**

Table E.9: Techno-economic performances of the four-step PVSA cycle optimized for cost limits with an adsorbent cost of 1500 € per tonne at a constant flue gas flow rate of 2004 t h^{-1} over a range of CO_2 compositions. A value of 0.0 indicates that the contribution was less than 0.1 €/$t_{CO_2,\ avoided}$.

	3.5%	**7.5%**	**13%**	**20%**	**30%**
Operating conditions					
Adsorption time (s)	164	100	64	112	74
Blowdown pump flow rate ($m^3\ h^{-1}$)	1727	1768	2881	2586	2520
Evacuation pump flow rate ($m^3\ h^{-1}$)	17589	19296	19330	14063	14293
High pressure (bar)	3.07	2.57	2.08	2.96	2.35
Intermediate pressure (bar)	0.14	0.21	0.25	0.69	0.71
Low pressure (bar)	0.011	0.019	0.042	0.102	0.144
Feed velocity ($m\ s^{-1}$)	1.11	1.24	1.47	1.11	1.34
Column length (m)	8.9	9.0	8.7	8.6	8.8
Particle porosity (-)	0.72	0.68	0.61	0.64	0.65
Particle diameter (mm)	4.9	4.5	4.5	4.1	5.0
Train configuration					
Number of columns per train (-)	4	4	4	4	4
Blowdown pumps per train (-)	1	1	1	1	1
Evacuation pumps per train (-)	2	2	2	2	2
Number of parallel trains (-)	51	51	53	52	49
Process performance					
Purity (%)	95.0	94.9	94.9	94.9	94.9
Recovery (%)	90.2	91.6	91.1	90.0	90.9
Productivity ($mol\ m^{-3}\ s^{-1}$)	1.01	2.07	3.71	5.74	8.13
Compressor power (MW_e)	85.22	71.12	55.99	74.63	54.80
Blowdown power (MW_e)	1.68	1.47	2.24	0.92	0.76
Evacuation power (MW_e)	67.11	54.78	45.67	33.96	27.87
Overall power consumption (MW_e)	154.00	127.38	103.90	109.51	83.43
Specific energy consumption (kWh_e/t_{CO_2})	1581.20	614.41	299.47	215.31	113.84
Cost performance					
CAPEX (€/$t_{CO_2,\ avoided}$)	36.4	16.6	9.9	6.3	4.2
Total direct cost (€/$t_{CO_2,\ avoided}$)	22.5	10.3	6.1	3.9	2.6
Column cost (€/$t_{CO_2,\ avoided}$)	6.4	2.9	1.7	1.1	0.8
Compressor cost (€/$t_{CO_2,\ avoided}$)	9.1	4.0	2.2	1.5	1.0
Vacuum pump cost (€/$t_{CO_2,\ avoided}$)	4.6	2.2	1.4	0.8	0.5
Heat exchanger cost (€/$t_{CO_2,\ avoided}$)	0.2	0.1	0.1	0.0	0.0
Valves cost (€/$t_{CO_2,\ avoided}$)	0.5	0.2	0.1	0.1	0.1
Initial adsorbent cost (€/$t_{CO_2,\ avoided}$)	1.6	0.9	0.6	0.3	0.2
Process contingency (€/$t_{CO_2,\ avoided}$)	3.4	1.5	0.9	0.6	0.4
Indirect cost (€/$t_{CO_2,\ avoided}$)	3.6	1.7	1.0	0.6	0.4
Project contingency (€/$t_{CO_2,\ avoided}$)	5.2	2.4	1.4	0.9	0.6
Owner cost (€/$t_{CO_2,\ avoided}$)	1.8	0.8	0.5	0.3	0.2
OPEX (€/$t_{CO_2,\ avoided}$)	118.6	46.3	23.4	16.3	9.0
Fixed OPEX (€/$t_{CO_2,\ avoided}$)	17.6	8.1	4.8	3.1	2.0
Electricity cost (€/$t_{CO_2,\ avoided}$)	97.7	36.6	17.6	12.6	6.6
Adsorbent cost (€/$t_{CO_2,\ avoided}$)	2.3	1.2	0.8	0.5	0.3
Cooling water cost (€/$t_{CO_2,\ avoided}$)	0.9	0.4	0.2	0.1	0.1
CO_2 avoided cost (€/$t_{CO_2,\ avoided}$)	**155.0**	**62.9**	**33.3**	**22.6**	**13.2**

Table E.10: Techno-economic performances of the four-step PVSA cycle optimized for cost limits with an adsorbent cost of 4500 € per tonne at a constant flue gas flow rate of 2004 t h^{-1} over a range of CO_2 compositions. A value of 0.0 indicates that the contribution was less than 0.1 €/$t_{CO_2,\ avoided}$.

	3.5%	**7.5%**	**13%**	**20%**	**30%**
Operating conditions					
Adsorption time (s)	198	110	122	137	95
Blowdown pump flow rate ($m^3\ h^{-1}$)	1610	1934	5165	2520	2387
Evacuation pump flow rate ($m^3\ h^{-1}$)	12281	18082	19283	14063	14313
High pressure (bar)	3.37	2.42	2.43	2.98	2.70
Intermediate pressure (bar)	0.14	0.21	0.39	0.75	0.96
Low pressure (bar)	0.016	0.020	0.043	0.098	0.156
Feed velocity (m s^{-1})	0.87	1.30	1.28	1.07	1.18
Column length (m)	8.8	8.7	8.8	8.9	8.9
Particle porosity (-)	0.80	0.69	0.68	0.70	0.69
Particle diameter (mm)	4.7	4.9	4.8	4.6	5.0
Train configuration					
Number of columns per train (-)	4	4	4	3	4
Blowdown pumps per train (-)	1	1	1	1	1
Evacuation pumps per train (-)	2	2	2	2	2
Number of parallel trains (-)	62	55	53	51	48
Process performance					
Purity (%)	95.2	94.9	95.1	94.9	94.9
Recovery (%)	90.1	91.0	90.3	90.2	90.2
Productivity (mol $m^{-3}\ s^{-1}$)	0.85	2.10	3.50	7.01	7.87
Compressor power (MW_e)	90.59	66.19	63.91	73.99	63.37
Blowdown power (MW_e)	1.96	1.69	3.44	0.69	0.15
Evacuation power (MW_e)	57.61	53.17	48.97	33.49	26.97
Overall power consumption (MW_e)	150.16	121.05	116.32	108.17	90.49
Specific energy consumption (kWh_e/t_{CO_2})	1543.30	587.48	338.03	212.32	124.49
Cost performance					
CAPEX (€/$t_{CO_2,\ avoided}$)	40.9	18.3	10.9	6.0	4.5
Total direct cost (€/$t_{CO_2,\ avoided}$)	25.2	11.3	6.7	3.7	2.8
Column cost (€/$t_{CO_2,\ avoided}$)	7.8	3.0	1.8	0.9	0.8
Compressor cost (€/$t_{CO_2,\ avoided}$)	9.1	4.0	2.3	1.5	1.0
Vacuum pump cost (€/$t_{CO_2,\ avoided}$)	4.7	2.3	1.5	0.8	0.5
Heat exchanger cost (€/$t_{CO_2,\ avoided}$)	0.3	0.1	0.1	0.0	0.0
Valves cost (€/$t_{CO_2,\ avoided}$)	0.6	0.3	0.1	0.1	0.1
Initial adsorbent cost (€/$t_{CO_2,\ avoided}$)	2.8	1.6	1.0	0.5	0.4
Process contingency (€/$t_{CO_2,\ avoided}$)	3.8	1.7	1.0	0.6	0.4
Indirect cost (€/$t_{CO_2,\ avoided}$)	4.1	1.8	1.1	0.6	0.4
Project contingency (€/$t_{CO_2,\ avoided}$)	5.8	2.6	1.5	0.9	0.6
Owner cost (€/$t_{CO_2,\ avoided}$)	2.0	0.9	0.5	0.3	0.2
OPEX (€/$t_{CO_2,\ avoided}$)	119.9	46.4	26.8	16.2	10.2
Fixed OPEX (€/$t_{CO_2,\ avoided}$)	19.7	8.8	5.3	2.9	2.2
Electricity cost (€/$t_{CO_2,\ avoided}$)	95.3	34.9	19.9	12.4	7.3
Adsorbent cost (€/$t_{CO_2,\ avoided}$)	3.9	2.3	1.4	0.7	0.6
Cooling water cost (€/$t_{CO_2,\ avoided}$)	1.0	0.3	0.2	0.1	0.1
CO_2 avoided cost (€/$t_{CO_2,\ avoided}$)	**160.8**	**64.7**	**37.7**	**22.2**	**14.7**

Table E.11: Techno-economic performances of the four-step PVSA cycle optimized for the minimum CO_2 avoided cost with Zeolite 13X as an adsorbent at a constant flue gas flow rate of 2004 t h^{-1} over a range of CO_2 compositions. A value of 0.0 indicates that the contribution was less than 0.1 €/$t_{CO_2,\ avoided}$.

	3.5%	**7.5%**	**13%**	**20%**	**30%**
Operating conditions					
Adsorption time (s)	185	217	122	133	104
Blowdown pump flow rate ($m^3\ h^{-1}$)	5738	12317	9659	7948	5540
Evacuation pump flow rate ($m^3\ h^{-1}$)	2461	11418	13646	16748	19000
High pressure (bar)	3.65	1.78	2.89	2.01	2.61
Intermediate pressure (bar)	0.028	0.057	0.129	0.266	0.459
Low pressure (bar)	0.010	0.011	0.035	0.036	0.087
Feed velocity ($m\ s^{-1}$)	0.92	1.30	1.05	1.49	1.23
Column length (m)	8.9	8.9	9.0	8.7	8.7
Particle porosity (-)	0.69	0.69	0.65	0.63	0.52
Particle diameter (mm)	3.8	4.0	3.6	4.8	3.5
Train configuration					
Number of columns per train (-)	26	8	7	6	5
Blowdown pumps per train (-)	2	1	1	1	1
Evacuation pumps per train (-)	23	6	4	4	3
Number of parallel trains (-)	53	68	53	52	46
Process performance					
Purity (%)	94.3	95.2	94.9	94.9	95.2
Recovery (%)	89.6	89.9	91.0	90.9	90.6
Productivity ($mol\ m^{-3}\ s^{-1}$)	0.15	0.79	1.91	3.73	7.09
Compressor power (MW_e)	100.85	47.67	78.20	51.78	66.06
Blowdown power (MW_e)	17.49	15.50	9.91	6.00	2.88
Evacuation power (MW_e)	141.86	113.53	82.51	77.1	60.76
Overall power consumption (MW_e)	260.21	176.70	170.62	134.90	129.69
Specific energy consumption (kWh_e/t_{CO_2})	2687.2	867.9	492.3	262.7	177.6
Cost performance					
CAPEX (€/$t_{CO_2,\ avoided}$)	150.2	34.8	14.9	9.0	5.2
Total direct cost (€/$t_{CO_2,\ avoided}$)	92.6	21.4	9.2	5.5	3.2
Column cost (€/$t_{CO_2,\ avoided}$)	46.4	7.8	3.2	1.7	0.9
Compressor cost (€/$t_{CO_2,\ avoided}$)	9.7	4.0	2.3	1.5	1.0
Vacuum pump cost (€/$t_{CO_2,\ avoided}$)	20.1	6.8	2.3	1.7	0.8
Heat exchanger cost (€/$t_{CO_2,\ avoided}$)	0.3	0.1	0.1	0.0	0.0
Valves cost (€/$t_{CO_2,\ avoided}$)	3.6	0.6	0.3	0.1	0.1
Initial adsorbent cost (€/$t_{CO_2,\ avoided}$)	12.5	2.2	1.0	0.6	0.4
Process contingency (€/$t_{CO_2,\ avoided}$)	13.9	3.2	1.4	0.8	0.5
Indirect cost (€/$t_{CO_2,\ avoided}$)	14.9	3.5	1.5	0.9	0.5
Project contingency (€/$t_{CO_2,\ avoided}$)	21.3	4.9	2.1	1.3	0.7
Owner cost (€/$t_{CO_2,\ avoided}$)	7.5	1.7	0.7	0.4	0.3
OPEX (€/$t_{CO_2,\ avoided}$)	263.9	72.1	37.9	20.6	13.5
Fixed OPEX (€/$t_{CO_2,\ avoided}$)	71.1	16.6	7.1	4.3	2.5
Electricity cost (€/$t_{CO_2,\ avoided}$)	173.9	52.1	29.1	15.4	10.4
Adsorbent cost (€/$t_{CO_2,\ avoided}$)	17.8	3.1	1.4	0.8	0.5
Cooling water cost (€/$t_{CO_2,\ avoided}$)	1.1	0.3	0.2	0.1	0.1
CO_2 avoided cost (€/$t_{CO_2,\ avoided}$)	**414.1**	**106.9**	**52.8**	**29.6**	**18.7**

Table E.12: Techno-economic performances of the four-step PVSA cycle optimized for the minimum CO_2 avoided cost with IISERP MOF2 as an adsorbent at a constant flue gas flow rate of 2004 t h^{-1} over a range of CO_2 compositions. A value of 0.0 indicates that the contribution was less than 0.1 €/$t_{CO_2,\ avoided}$.

	3.5%	**7.5%**	**13%**	**20%**	**30%**
Operating conditions					
Adsorption time (s)	106	135	80	91	52
Blowdown pump flow rate ($m^3\ h^{-1}$)	5365	3440	3000	1883	4284
Evacuation pump flow rate ($m^3\ h^{-1}$)	19752	17503	15983	17057	14607
High pressure (bar)	2.76	2.68	2.48	2.70	2.50
Intermediate pressure (bar)	0.08	0.24	0.28	0.58	0.69
Low pressure (bar)	0.011	0.024	0.050	0.076	0.132
Feed velocity ($m\ s^{-1}$)	1.21	1.15	1.21	1.23	1.47
Column length (m)	8.8	8.9	8.9	8.9	7.8
Particle porosity (-)	0.67	0.73	0.64	0.67	0.54
Particle diameter (mm)	4.5	4.9	4.0	4.8	4.8
Train configuration					
Number of columns per train (-)	4	4	4	4	4
Blowdown pumps per train (-)	1	1	1	1	1
Evacuation pumps per train (-)	2	2	2	2	2
Number of parallel trains (-)	52	55	54	48	52
Process performance					
Purity (%)	95.1	95.1	95.0	95.1	95.0
Recovery (%)	90.0	90.0	90.7	91.2	91.0
Productivity (mol $m^{-3}\ s^{-1}$)	1.02	1.97	3.43	5.68	10.91
Compressor power (MW_e)	78.55	72.70	66.56	68.41	60.28
Blowdown power (MW_e)	5.63	2.99	2.37	0.79	1.47
Evacuation power (MW_e)	71.38	54.56	41.59	38.46	31.69
Overall power consumption (MW_e)	155.57	130.25	110.53	107.65	93.44
Specific energy consumption (kWh_e/t_{CO_2})	1601.00	639.26	319.95	208.86	127.35
Cost performance					
CAPEX (€/$t_{CO_2,\ avoided}$)	40.1	18.2	10.6	6.5	4.4
Total direct cost (€/$t_{CO_2,\ avoided}$)	24.7	11.2	6.5	4.0	2.7
Column cost (€/$t_{CO_2,\ avoided}$)	6.5	3.2	1.8	1.1	0.7
Compressor cost (€/$t_{CO_2,\ avoided}$)	9.0	4.0	2.3	1.5	1.0
Vacuum pump cost (€/$t_{CO_2,\ avoided}$)	5.4	2.4	1.3	0.8	0.6
Heat exchanger cost (€/$t_{CO_2,\ avoided}$)	0.2	0.1	0.1	0.0	0.0
Valves cost (€/$t_{CO_2,\ avoided}$)	0.5	0.3	0.1	0.1	0.1
Initial adsorbent cost (€/$t_{CO_2,\ avoided}$)	3.1	1.3	0.9	0.5	0.4
Process contingency (€/$t_{CO_2,\ avoided}$)	3.7	1.7	1.0	0.6	0.4
Indirect cost (€/$t_{CO_2,\ avoided}$)	4.0	1.8	1.0	0.6	0.4
Project contingency (€/$t_{CO_2,\ avoided}$)	5.7	2.6	1.5	0.9	0.6
Owner cost (€/$t_{CO_2,\ avoided}$)	2.0	0.9	0.5	0.3	0.2
OPEX (€/$t_{CO_2,\ avoided}$)	123.6	49.0	25.4	16.2	10.2
Fixed OPEX (€/$t_{CO_2,\ avoided}$)	19.4	8.8	5.1	3.1	2.2
Electricity cost (€/$t_{CO_2,\ avoided}$)	99.0	38.1	18.8	12.2	7.4
Adsorbent cost (€/$t_{CO_2,\ avoided}$)	4.4	1.8	1.3	0.8	0.5
Cooling water cost (€/$t_{CO_2,\ avoided}$)	0.9	0.3	0.2	0.1	0.1
CO_2 avoided cost (€/$t_{CO_2,\ avoided}$)	**163.7**	**67.2**	**36.0**	**22.7**	**14.6**

Table E.13: Techno-economic performances of the six-step DR PVSA cycle optimized for cost limits at a constant flue gas flow rate of 2004 t h^{-1} over a range of CO_2 compositions. A value of 0.0 indicates that the contribution was less than 0.1 €/$t_{CO_2,\ avoided}$.

	3.5%	**7.5%**	**13%**	**20%**	**30%**
Operating conditions					
Adsorption time (s)	260	268	174	112	71
Blowdown pump flow rate ($m^3\ h^{-1}$)	1701	1812	1663	5115	1694
Evacuation pump flow rate ($m^3\ h^{-1}$)	7071	11380	14155	19852	13287
LR pump flow rate ($m^3\ h^{-1}$)	19752	19761	18954	17841	15109
High pressure (bar)	1.45	1.49	1.16	1.13	1.23
Intermediate pressure (bar)	0.36	0.62	0.69	0.74	0.90
Low pressure (bar)	0.12	0.11	0.14	0.16	0.22
Feed velocity ($m\ s^{-1}$)	2.01	1.98	2.23	2.25	2.36
Reflux time (s)	234	239	154	99	64
Reflux fraction (-)	0.06	0.05	0.08	0.07	0.07
Column length (m)	9.0	8.8	8.4	8.7	8.9
Particle porosity (-)	0.57	0.56	0.53	0.53	0.41
Particle diameter (mm)	5.0	5.0	4.8	4.9	4.9
Train configuration					
Number of columns per train (-)	4	4	4	4	5
Blowdown pumps per train (-)	1	1	1	1	1
Evacuation pumps per train (-)	1	1	1	1	2
LR pumps per train (-)	1	1	1	1	1
HR blowers per train (-)	1	1	1	1	1
Number of parallel trains (-)	44	47	51	49	39
Process performance					
Purity (%)	95.0	95.3	96.0	95.1	94.9
Recovery (%)	92.1	94.0	91.9	94.1	92.7
Productivity (mol $m^{-3}\ s^{-1}$)	1.16	2.48	4.30	6.05	7.97
Compressor power (MW_e)	48.18	45.58	34.71	27.80	31.47
Blowdown power (MW_e)	0.89	0.62	0.51	1.32	0.15
Evacuation power (MW_e)	5.76	9.62	12.14	16.03	15.85
LR power (MW_e)	16.64	17.78	17.11	15.45	10.70
HR power (MW_e)	2.40	2.72	1.47	1.30	2.25
Overall power consumption (MW_e)	73.86	76.32	65.95	61.90	60.43
Cost performance					
CAPEX (€/$t_{CO_2,\ avoided}$)	28.3	13.5	8.3	5.5	3.8
Total direct cost (€/$t_{CO_2,\ avoided}$)	17.5	8.3	5.1	3.4	2.3
Column cost (€/$t_{CO_2,\ avoided}$)	5.1	2.5	1.5	1.0	0.7
Compressor cost (€/$t_{CO_2,\ avoided}$)	8.2	3.7	2.2	1.4	0.9
Vacuum pump cost (€/$t_{CO_2,\ avoided}$)	3.2	1.7	1.2	0.9	0.5
Heat exchanger cost (€/$t_{CO_2,\ avoided}$)	0.2	0.1	0.1	0.0	0.0
Valves cost (€/$t_{CO_2,\ avoided}$)	0.6	0.3	0.2	0.1	0.1
Initial adsorbent cost (€/$t_{CO_2,\ avoided}$)	0.0	0.0	0.0	0.0	0.0
Process contingency (€/$t_{CO_2,\ avoided}$)	2.6	1.2	0.8	0.5	0.3
Indirect cost (€/$t_{CO_2,\ avoided}$)	2.8	1.3	0.8	0.5	0.4
Project contingency (€/$t_{CO_2,\ avoided}$)	4.0	1.9	1.2	0.8	0.5
Owner cost (€/$t_{CO_2,\ avoided}$)	1.4	0.7	0.4	0.3	0.2
OPEX (€/$t_{CO_2,\ avoided}$)	58.8	27.9	15.2	9.5	6.6
Fixed OPEX (€/$t_{CO_2,\ avoided}$)	13.8	6.6	4.0	2.7	1.8
Electricity cost (€/$t_{CO_2,\ avoided}$)	44.4	21.1	11.0	6.8	4.7
Adsorbent cost (€/$t_{CO_2,\ avoided}$)	0.0	0.0	0.0	0.0	0.0
Cooling water cost (€/$t_{CO_2,\ avoided}$)	0.5	0.2	0.1	0.1	0.0
CO_2 avoided cost (€/$t_{CO_2,\ avoided}$)	**87.1**	**41.4**	**23.5**	**15.0**	**10.4**

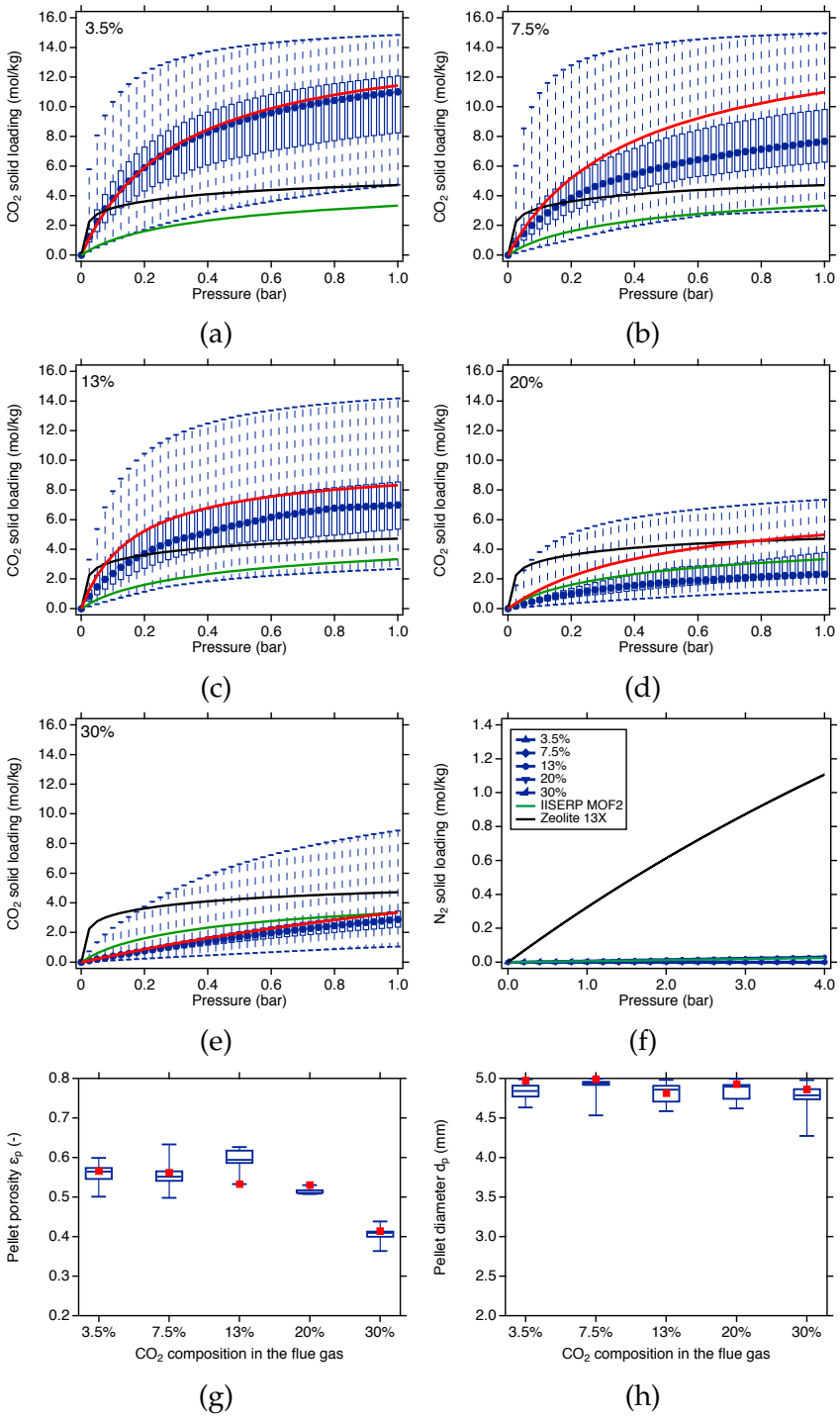

Figure E.5: Optimal adsorbent properties corresponding to the cost limits of six-step DR cycle.(a)-(e) show the optimal CO_2 adsorption isotherms at different CO_2 compositions. Box and whisker plots in (a)-(e) represent the range of CO_2 adsorption isotherms in the 5% vicinity of the lowest possible CO_2 avoided cost. (f) show the optimal N_2 adsorption isotherms at different CO_2 compositions. For comparison CO_2 and N_2 adsorption isotherms of Zeolite 13X (black lines) and IISERP MOF2 (green lines) are also shown in (a)-(e) and (f), respectively. (g) and (h) illustrate the optimal pellet porosity and diameter, respectively, corresponding to the cost limits of six-step DR cycle.

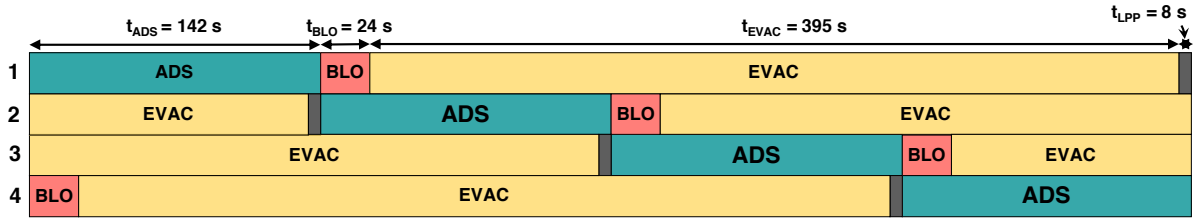

(a) Four step cycle

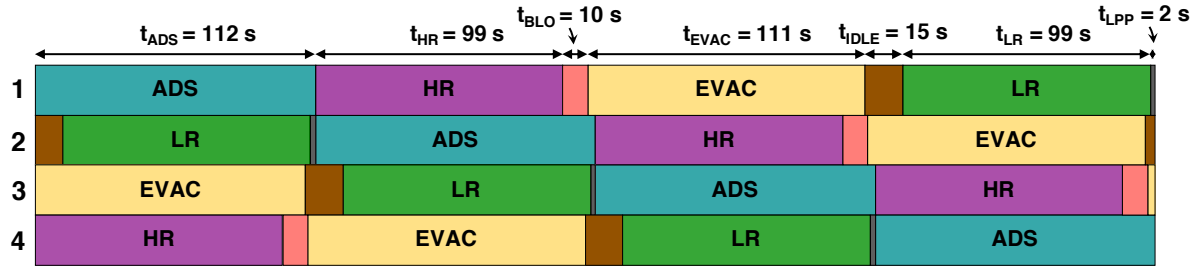

(b) Six step DR cycle

Figure E.6: Sample optimal cycle schedules corresponding to the cost limits of (a) four-step cycle and (b) six-step DR cycle at 20% CO_2 composition and 2004 t h^{-1} flue gas flow rate.

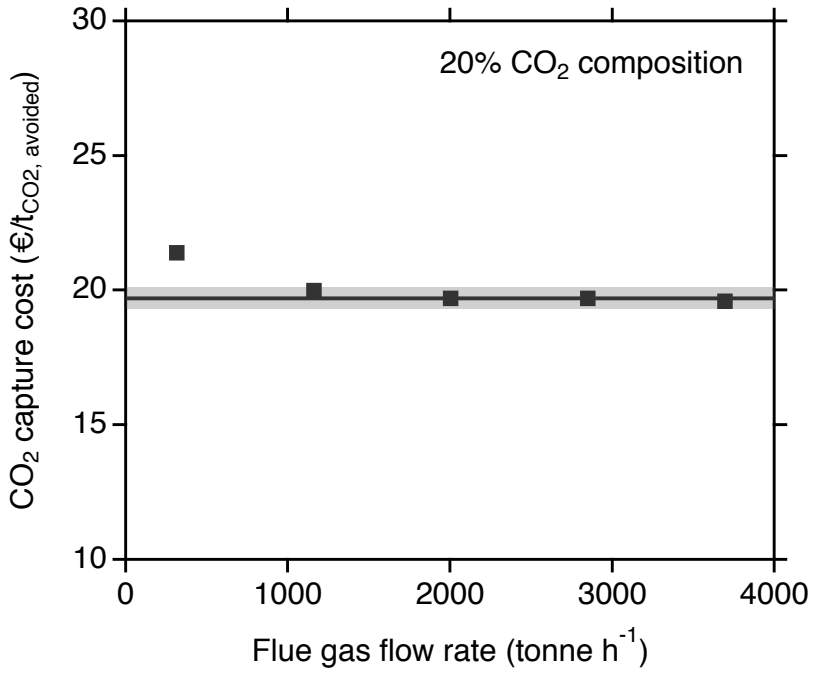

Figure E.7: Effect of plant size (or flue gas flow rates) on the cost limits of the four-step PVSA cycle for a fixed CO_2 composition of 20%.

Table E.14: Summary of train configuration and techno-economic performances of the four-step PVSA cycle optimized for cost limits at 20% CO_2 composition over a range of flue gas flow rates.

Flue gas flow rate (tonne h^{-1})	**313**	**1159**	**2004**	**2850**	**3696**
Column length (m)	8.7	8.9	9.0	8.9	9.0
Number of columns per train (-)	4	5	4	4	4
Number of parallel trains (-)	8	23	45	64	79
Purity (%)	94.9	95.0	95.2	95.0	94.9
Recovery (%)	91.2	90.7	90.6	90.9	90.6
Productivity (mol m^{-3} s^{-1})	5.74	5.35	5.84	5.92	6.10
Overall power consumption (MW_e)	15.59	56.42	95.75	144.97	180.16
CO_2 avoided cost (€/$t_{CO_2,\ avoided}$)	21.6	20.0	19.7	19.7	19.6